Experimental and theoretical study of the uptake of peroxy radicals by organic aerosol surfaces

Roose Antoine

Université de Lille

IMT Lille Douai
École Mines-Télécom
IMT-Université de Lille

Ecole Doctorale Science de la Matière, du Rayonnement et de l'Environnement

Thèse de doctorat

Présentée par

Antoine ROOSE

En vue d'obtenir le titre de

Docteur en physique de l'université de Lille

Experimental and theoretical study of the uptake of peroxy radicals by organic aerosol surfaces

Etude expérimentale et théorique de la capture de radicaux peroxy par la surface d'aérosols organiques

Thèse dirigée par Denis DUFLOT et Véronique RIFFAULT

Préparée aux laboratoires PhLAM et SAGE

Date de soutenance le 18 décembre 2019 devant le jury d'examen :

Président : Yuri BEDJANIAN – Directeur de recherches CNRS (U. Orléans, ICARE)

Rapporteurs : Manuel RUIZ-LOPEZ – Directeur de recherches CNRS (U. Lorraine, LPCT)

Barbara NOZIERE – Directrice de recherches CNRS (U. Lyon, IRCELYON)

Examinateurs : Delphine VARDANEGA – Maitre de conférences (U. Franche-Comté, UTINAM)

Directeur de Thèse : Denis DUFLOT – Maitre de conférences HDR (U. Lille, PhLAM)

Co-directrice de Thèse : Véronique RIFFAULT - Professeure (IMT Lille Douai, SAGE)

Encadrants : Céline TOUBIN – Professeure (U. Lille, PhLAM)

Sébastien DUSANTER – Maitre-Assistant (IMT Lille Douai, SAGE)

"*They've learned to realize that whether they like a theory or they don't like a theory is not the essential question. Rather, it is whether or not the theory gives predictions that agree with experiment. It is not a question of whether a theory is philosophically delightful, or easy to understand, or perfectly reasonable from the point of view of common sense. […]. So I hope you can accept Nature as She is—absurd*."

Richard P. Feynman – QED the strange theory of light and matter

"*God made the bulk; surfaces were invented by the devil*"

Wolfgang Pauli

ACKNOWLEDGMENT

Je tiens tout d'abord à remercier M. Bedjanian d'avoir accepté de présider ma soutenance de thèse ainsi que Mme. Nozière et M. Ruiz-Lopez d'avoir accepté de lire et évaluer ce manuscrit et enfin, Mme. Vardanega d'avoir examiné mes travaux. Merci pour les discussions scientifiques et les remarques judicieuses apportées lors de la soutenance.

Cette thèse a été menée conjointement au sein de deux laboratoires, le laboratoire de Physique des Lasers, Atomes et Molécules ainsi que le laboratoire de Sciences de l'Atmosphère et Génie de l'Environnement. Je tiens donc à remercier Marc Douay et Patrice Coddeville de m'avoir accueilli au sein de leur groupe de recherche.

Cette thèse n'aurait pu être ce qu'elle est sans la direction de Denis et Véronique ainsi que la supervision de Céline et Sébastien.

Merci à Denis pour ces nombreuses discussions scientifiques ou non, son soutien que ce soit moral, scientifique ou administratif.

Merci à Véronique pour tous ses conseils et également pour avoir organisé les rassemblements de ses doctorants et post-doctorants autour de plusieurs repas.

Merci à Sébastien pour ses conseils et son soutien tout au long du développement du réacteur.

Merci à Céline pour son attention et pour son encadrement qui est toujours efficace.

Merci à vous quatre pour m'avoir fait confiance pendant ces 3 ans.

Mes travaux expérimentaux n'auraient pas été possibles sans le support de tous les techniciens et ingénieurs de Douai. Je tiens donc à les remercier et tout particulièrement Emmanuel Tison pour son aide pour les réparations du CPC.

Je remercie également Florent et Valérie pour la gestion du cluster du PhLAM, vous êtes toujours disponibles pour apporter votre aide, c'est très appréciable. Je remercie également Denis et André pour la gestion des allocations d'heures sur les clusters nationaux.

Sans une bonne ambiance de travail, il est plus difficile de mener une thèse à son terme. Je tiens donc à remercier tous mes collègues qui ont participé à cette ambiance qu'ils soient permanents, post-doctorants, doctorants ou stagiaires. Je remercie notamment les habitués du Black night (ils se reconnaitront) avec qui j'ai eu de nombreuses discussions animées. Je remercie également Ahmad, Marius et Asma pour l'ambiance au sein du laboratoire réactivité.

Je tiens également à remercier ma famille pour leur soutien tout au long de mes études.

Enfin, je remercie Pauline pour son soutien et sa patience tout au long de ces 3 ans. Merci de partager ma vie.

TABLE OF CONTENTS

Table of contents

LIST OF FIGURES

LIST OF TABLES

LIST OF ABREVIATIONS

AA-MD: All Atom Molecular Dynamics

ACS: American Chemical Society

AFT: Aerosol Flow Tube

AIMD: *Ab Initio* Molecular Dynamics

AMBER: Assisted Model Building with Energy Refinement

AO: Atomic Orbital

AU: Atomic Units

BD: Brownian Dynamics

BEARPEX: Biosphere Effects on Aerosol and Photochemistry Experiment

BVOC: Biogenic Volatile Organic Compounds

CABINEX: Community Atmosphere Biosphere Interactions Experiment

CAPS: Cavity Attenuated Phase Shift

CC: Coupled Cluster

CCD: Coupled Cluster Doubles

CCN : Cloud Condensation Nuclei

CCSD: Coupled Cluster Single and Doubles

CCSDT: Coupled Cluster Single, Doubles and Triples

CCSD(T): Coupled Cluster Single, Doubles with Triples treated perturbatively

CG-MD: Coarse Grain Molecular Dynamics

CHARMM: Chemistry at HARvard Macromolecular Mechanics

CIMS: Chemical Ionization Mass Spectrometry

CL: Chain Length

CM: Continuum Mechanics

COM: Center Of Mass

CPC: Condensation Particle Counter

CPU: Central Processing Unit

DFT: Density Functional Theory

DFTB: Density Functional Tight Binding

DMA: Differential Mobility Analyzer

ECHAMP: Ethane-based Chemical AMPlification

EE: Electronical Embedding

Exp: Experimental

FAGE: Fluorescent Assay by Gas Expansion

FF: Force Field

FMO: Fragment Molecular Orbital

GA: Glutaric Acid

GAFF: General Amber Force Field

GGA: Generalized Gradient Approximation

GP: Generation Process

GTO: Gaussian Type Orbital

HF: Hartree-Fock

HUMPPA-COPEC : Hyytiälä United Measurements of Photochemistry and Particles in Air-Comprehensive Organic Precursor Emission and Concentration study

IPCC: International Panel on Climate Change

IS-MD: Implicit Solvent Molecular Dynamics

LCAO: Linear Combination of (non-orthogonal) Atomic Orbitals

LDA: Local Density Approximation

LIF-FAGE: Laser Induced Fluorescence – Fluorescence Assay by Gas Expansion

LINCS: LINear Constraint Solver

LJ: Lennard Jones

LPM: Liter Per Minute

LSDA: Local Spin Density Approximation

MCM: Master Chemical Mechanism

MD: Molecular Dynamics

ME: Mechanical Embedding

MFC: Mass Flow Controller

MIESR: Matrix Isolation Electron Spin Resonance

MO : Molecular Orbital

MP2 : second order Møller-Plesset perturbation

MP4: fourth order Møller-Plesset perturbation

NPT: fixed Number, Pressure and Temperature

NVT: fixed Number, Volume and Temperature

ONIOM: Own N-layered molecular Orbital Molecular Mechanics

OPLS/AA: Optimized Potential for Liquid simulations/All Atoms

OVOC: Oxygenated Volatile Organic Compound

PC: Product Complex

PERCA: PEroxy Radical Chemical Amplifier

PES: Potential Energy Surface

PFA: PerFluoroAlkoxy

PM: Particulate Matter

PROPHET: Program for Research on Oxidants: Photochemistry, Emissions, and Transport

PTR-TOFMS: Proton Transfer Reaction Time Of Flight Mass Spectrometer

QCISD: Quadratic Configuration Interaction Single and Doubles

QM: Quantum Mechanics

QM/MM: Quantum Mechanics/Molecular Mechanics

RACM: Regional Atmospheric Chemistry Mechanism

RC: Reactive Complex

RDF: Radial Distribution Function

RESP: Restrained Electrostatic Potential Fit

RH: Relative Humidity

SCF: Self-Consistent Field

SLPM: Standard Liter Per Minute

SMPS: Scanning Mobility Particle Sizer

SOA: Secondary Organic Aerosols

SR: Short Range

STO: Slater Type Orbital

TS: Transition State

TST: Transition State Theory

UMP2: Unrestricted second order Møller-Plesset perturbation

UV: Ultra Violet

VA: Valeric Acid

VOC: Volatile Organic Compound

V-rescale: Velocity rescale

wc-AFT: wall coated Aerosol Flow Tube

ZPE : Zero Point (vibrational) Energy

INTRODUCTION

The Earth atmosphere is composed (in numbers of molecules) of 78% of N_2, 21% of O_2 and 0.9% of Ar, the remaining tenth of percent being mainly trace gases such as carbon dioxide, nitrous oxide, methane or ozone. Water can also be found in the atmosphere but its concentration varies with the position on Earth and the time of the day. Finally, aerosols, a suspension of solid or liquid particles in gas, are also a part of the atmosphere. Their size is comprised between nanometers to tens of micrometers in diameter. There are formed by nucleation or condensation of vapor species but can also be emitted directly in the atmosphere (primary aerosol). They can come from natural sources (volcanic dust, sea salt, biogenic particles, etc.) or from anthropogenic ones (soot, industrial dust, etc.)[1]

The atmosphere is composed of several layers (Figure 1) characterized by variations in temperature and pressure. The temperature profile along the altitude is used to delimit each layer. The layers are the following:

- Troposphere: the lowest layer goes up to 10-15 km altitude depending on latitude and time of year. The temperature decreases rapidly in this region. Within this layer, the boundary layer can be found between the surface and an altitude of 1 to 2 km. In this layer, the ground has a direct influence on the atmosphere.
- Stratosphere: from the troposphere, up to 50 km approximatively. In this region, temperature increases with altitude. Within this region one can find the ozone layer where about 90% of the atmospheric ozone can be found. This ozone is produced by the photolysis of O_2 molecules by solar UV radiation (Chapman cycle).
- Mesosphere: This layer is comprised between the stratosphere and 80 – 100 km altitude. The temperature decreases in this region.
- Thermosphere: This layer goes from the mesosphere up to 600 km altitude. The temperature increases in this region due to the absorption of short-wavelength radiation by N_2 and O_2.
- Exosphere: the last region of the atmosphere is above the thermosphere. In this region, molecules with sufficient energy can escape from Earth gravitational forces.

The pressure decreases exponentially as the altitude increases, if the hydrostatic equilibrium is assumed. [2–4]

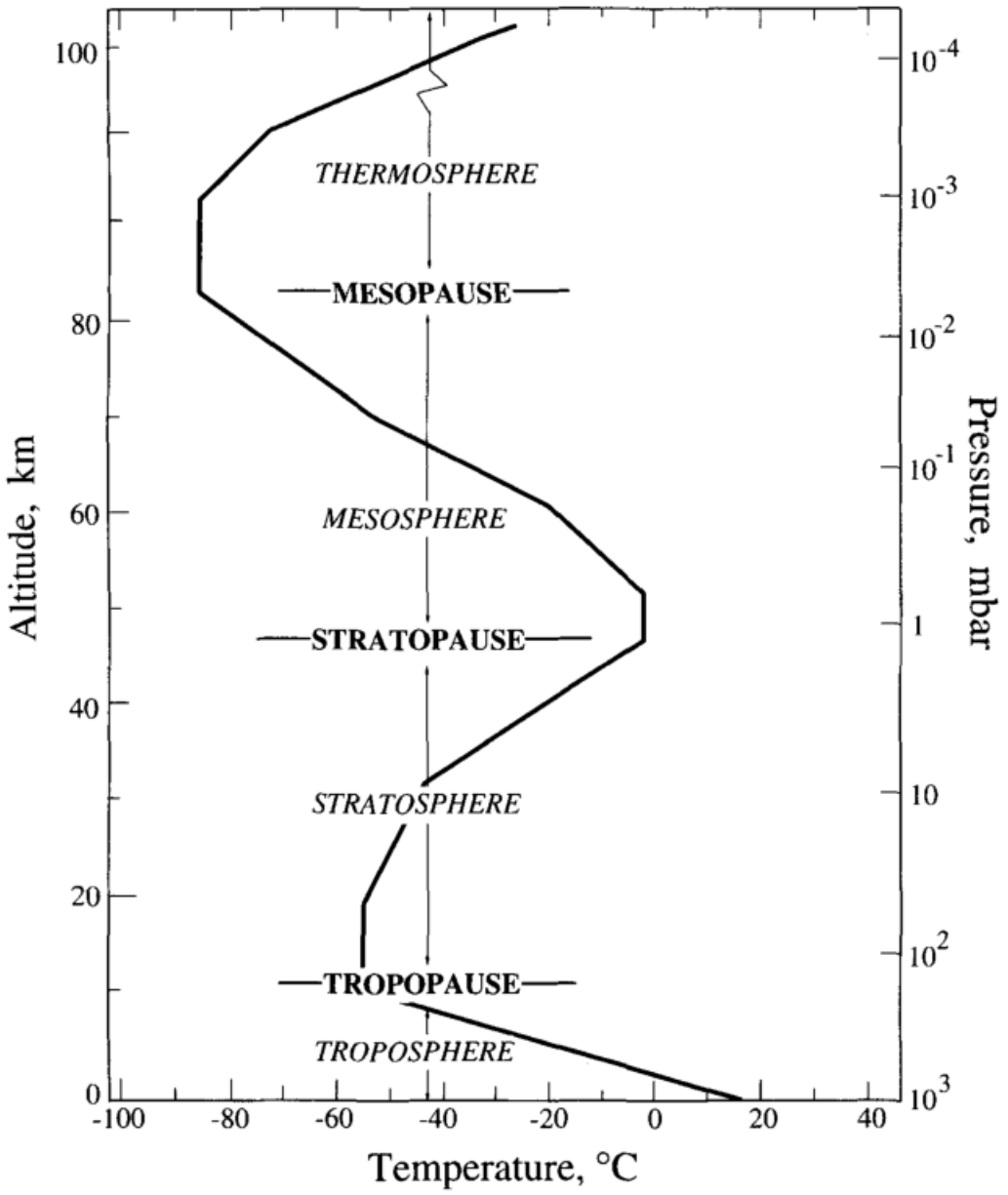

Figure 1: Layers of the atmosphere.[2]

Trace gases and particles emitted from both natural and anthropogenic sources have a large impact on the composition of the atmosphere and thus on human health[5] and Earth's climate.[2,6] The removal of these pollutants can be done by wet or dry deposition or by chemical transformations initiated by oxidant species (O_3, NO_3, OH) during their transport in the atmosphere (Figure 2).

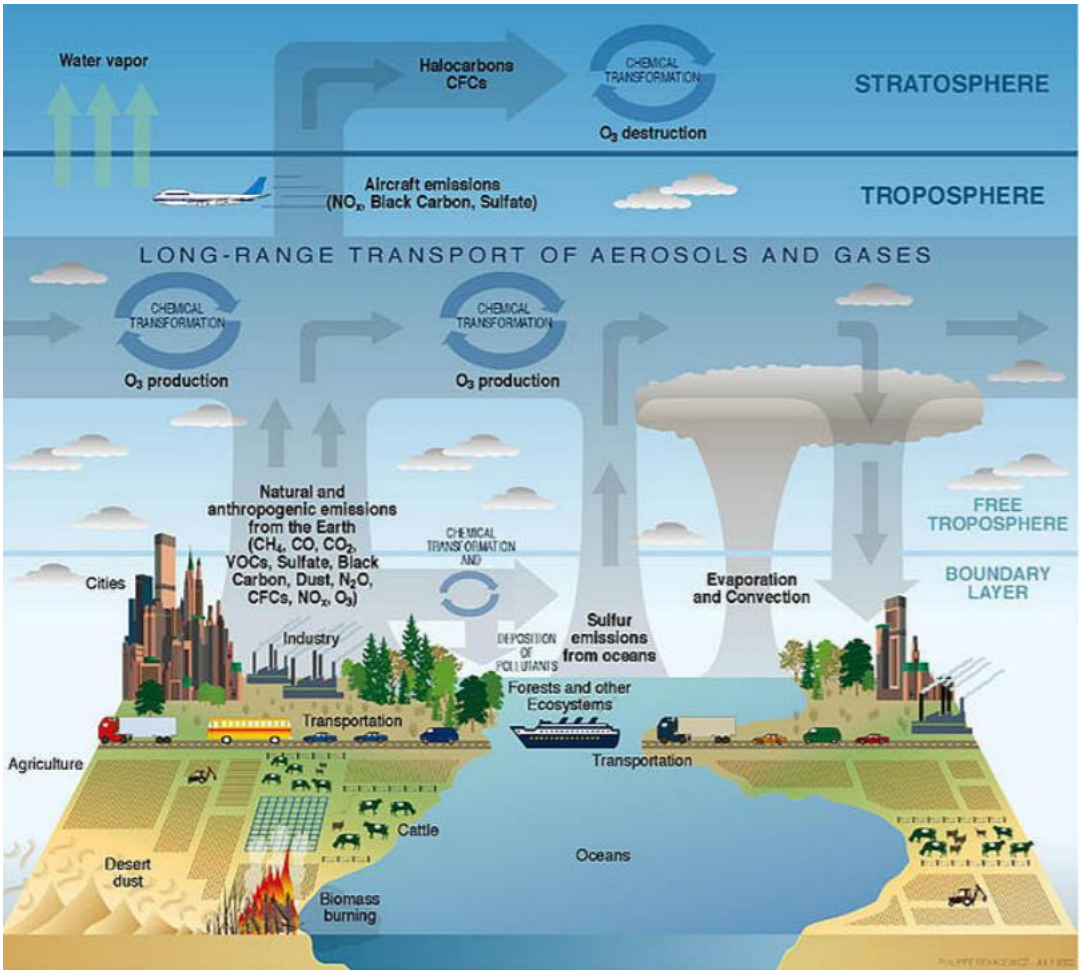

Figure 2: Schematic of chemical and transport processes related to atmospheric composition[7]

The oxidation of primary pollutants (directly emitted from the source) can leads to the formation of secondary pollutants such as O_3 with the NOx cycle and Secondary Organic Aerosols (SOA). Indeed, the oxidation of Volatile Organic Compounds (VOCs) usually leads to less volatile compounds, which can then nucleate and condense to form organic aerosols. However, the formation of these pollutants is still not completely understood.[8,9]

It has been shown that gaseous pollutants and aerosols can have an impact on human health.[5] For example, Heo et al. (2016)[10] have estimated that the aggregate social costs for year 2005 due to the PM2.5 (particulate matter with a diameter lower than 2.5 µm) and inorganics pollutant emissions within a 36 km×36 km area in United States were 1.0 trillion dollars. This epidemiological study reveals an association between the particulate air pollution and the daily mortality stronger in winter than in summer. High PM in summer is often associated with the production of SOA, so SOA may have an impact on health also but more studies have yet to be carried out.[9]

Some pollutants (CH_4, N_2O, Chlorofluorocarbons, etc…) can play the role of greenhouse gases and impact the climate. Even if greenhouse gases are needed to form a climate suitable for human life (otherwise the mean surface temperature of the Earth would be -18 °C), the increasing release of these compounds in the atmosphere since 1750 has contributed to a global warming effect.[11]

The consequences of global warming could be catastrophic (increase of sea level, intensity and frequency of cyclones and storms, etc.). It is the reason why the International Panel on Climate Change (IPCC), [11] a group of scientific experts, tries to estimate among many other things what will happen in case of an increase of the temperature of several degrees according to several scenarios.

For this, they need to know exactly what is the radiative forcing of each atmospheric species. However, even if the impact of some gaseous pollutants is well known (see for instance CO_2, CH_4, N_2O in Figure 3), there are still large uncertainties associated to the aerosol impacts.

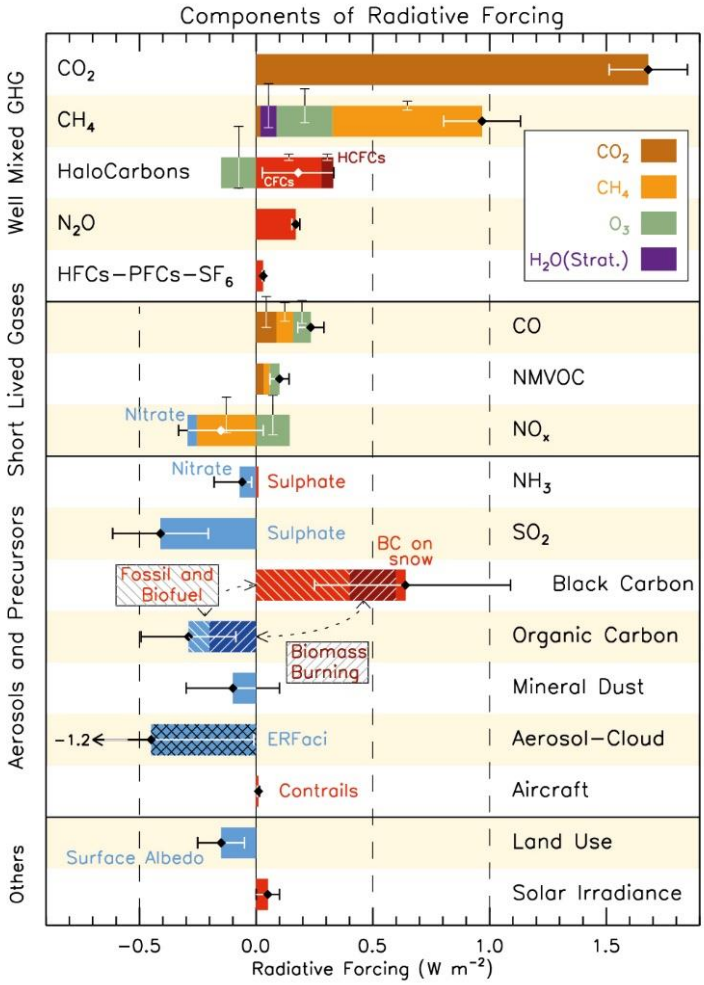

Figure 3: Radiative forcing for the period 1750-2011.[11]

To check the reliability of atmospheric models, simulations are often compared to field measurements; but some reaction mechanisms are still missing.[8,12–14] This is why laboratory measurements are important to study specific mechanisms. An example of mechanism could be the reactivity of primary species with gas-phase oxidants under specific conditions characteristic of different environments (urban, rural, forested, remote). The uptake coefficient of a gas species on environmental surfaces such as aerosols, providing the proportion of a gas species captured by the surface after collision could be another example. When the experiments are impossible to conduct due to hazardousness (radionuclides), technical difficulties or a large experimental cost, simulation tools at the molecular level can be used. They are able to provide

kinetic data of reactions, structural information and thermodynamical observables. As the experiments give only a macroscopic description of the studied system, simulation tools can also be used to understand and describe mechanisms occurring at the molecular level.

The RO_X ($OH + HO_2 + RO_2$) family is one of the major groups of free radicals in the atmosphere. The OH radical is involved in the removal of many atmospheric pollutants[15] (e.g. NO_X, SO_X, VOC). In particular, the comparison between atmospheric models and field measurements in forested areas have shown some discrepancies in OH and HO_2 concentrations,[13,14,16,17] with the latter being one of the main sources of OH radicals. One reason for the model-measurement difference may be an incomplete description of HO_2 uptake on organic aerosols in the models.

The uptake process of HO_2 and other organic peroxy radicals (RO_2) has not been precisely characterized yet during laboratory experiments or by numerical simulations even if some macroscopic models of uptake have been developed to obtain a better description of the real processes[18]. The influence of some parameters such as temperature and relative humidity (RH) is not well understood and while the catalytic impact of copper and iron in the aerosol phase has been highlighted,[19] measurements of their concentrations in aerosols have not been made concomitantly with HO_2 and OH. The latter may lead to a variability within one order of magnitude for the HO_2 uptake on aerosols of the same nature.

During this thesis, the peroxy radical uptake on organic aerosols has been studied by both laboratory experiments and molecular-level simulations (using quantum mechanics as well as classical molecular mechanics).

The first chapter introduces the chemistry of ROx in the atmosphere, the model used and the discrepancies between them and field measurements. Then the uptake coefficient is defined and a statement on the parameters that affect the uptake is made. The state of the art concerning the HO_2 uptake coefficient, HO_2 reactivity and then mass accommodation coefficient will be introduced. Finally, the objectives of the work will be explained.

The methodology used will be introduced in chapter 2. Firstly, each part of the experimental setup (the aerosol flow tube AFT and each instrument used for the generation and the detection of aerosol and peroxy radicals) will be detailed. The computational method used for the molecular dynamics and the quantum mechanics study will be introduced as well.

Chapter 3 introduces the main characterization done on the experimental setup. Then measurement of peroxy radical uptake will be given and compared to the values in the literature. Chapter 4 will introduce the computation done for the benchmark of the force field and the method used for the generation of particles. The formed particles will be characterized. Then the computation of HO_2 mass accommodation coefficient will be discussed with the difficulty to treat the heterogeneous reactivity. Finally a conclusion on the work will be done and the perspective will be presented.

CHAPTER 1: CONTEXT AND OBJECTIVES

I Chemistry of RO_x radicals

The RO_x family consists of hydrogen (H), hydroxyl (OH), hydroperoxyl (HO_2), organic peroxyl (RO_2) and alkoxyl (RO) radicals (with R=CH_3, Phenyl, etc.).[19] In the atmosphere, their concentrations are about 10^6 cm^{-3} for OH radicals, from 10^7 cm^{-3} to 10^9 cm^{-3} depending on NO_x concentrations for HO_2[2] and about 10^9 cm^{-3} for RO_2 radicals.[20]

Since RO_x species are amongst the most important free radicals in the atmosphere, it is crucial to well characterize their sources, their sinks and their reactivity. As mentioned in the introduction section, these species are involved in the removal of gaseous pollutants such as volatile organic compounds (VOCs),[21] thus controlling their lifetime, and are involved in the formation of SOA or ozone,[22] two secondary pollutants impacting both air quality and climate.

I.1 Radical sources

The major source of OH on a global scale is the photolysis of O_3 through the formation of excited atoms of oxygen, $O(^1D)$ and their subsequent reaction with water:[23]

$$O_3 + h\nu\ (\lambda < 336\ nm) \rightarrow O(^1D) + O_2 \quad (R1)$$

$$O(^1D) + H_2O \rightarrow 2\ OH \quad (R2)$$

OH can also be produced in urban and forested areas from HONO (reservoir species) and H_2O_2 photolyses, the former being sometimes the main source of OH:[23]

$$HONO + h\nu\ (\lambda < 400\ nm) \rightarrow OH + NO \quad (R3)$$

$$H_2O_2 + h\nu\ (\lambda < 370\ nm) \rightarrow 2\ OH \quad (R4)$$

In the presence of NO concentrations larger than 10 ppt, HO_2 is also an important source of OH since it reacts with NO to propagate the radical chain:[23]

$$HO_2 + NO \rightarrow OH + NO_2 \quad (R5)$$

In marine areas, halogens (X = I, F, Cl, Br) can also act as catalysts to produce OH from the reaction of ozone with hydroperoxyl radicals (R6-R7).[24] This chemistry leads to the formation of a photolabile HOX species which is then photolyzed to produce OH (R8).

$$X + O_3 \rightarrow XO + O_2 \quad (R6)$$

$$XO + HO_2 \rightarrow HOX + O_2 \quad (R7)$$

$$HOX + h\nu \rightarrow OH + X \quad (R8)$$

Finally, the ozonolysis of unsaturated compounds such as alkenes can be also an important source of OH as well as HO_2 and RO_2 during both daytime and nighttime (R9).[22] This chemistry involves the formation of Criegee radicals which then decompose to produce RO_x species.[23] For instance, the ozonolysis of alpha-pinenes and other cyclic terpenes with one double bond leads to the formation of 0.85 HO, 0.10 HO_2 and 0.62 RO_2 on average[25].

$$O_3 + \text{alkene} \rightarrow \alpha\ OH + \beta\ HO_2 + \gamma\ RO_2 + \text{products} \quad (R9)$$

Because of the light dependence of the OH sources mentioned above (R1-R2, R3, R4, R8), OH is considered as the major oxidant of the atmosphere primarily during daylight hours. Additional non-photolytic sources of OH are also operating in the atmosphere through the ozonolysis of unsaturated organics (R9) or nighttime reactions of NO_3 with organics. However, photolytic sources are predominant during daytime.

Indeed, any reaction that produces H or HCO in the troposphere acts as a HO_2 source:

$$H + O_2 + M \rightarrow HO_2 \quad (R10)$$

$$HCO + O_2 \rightarrow HO_2 + CO \quad (R11)$$

The major source of HO_2 is the photolysis of aldehydes[22] (R12). For instance, formaldehyde (HCHO) is photolyzed at wavelengths lower than 370 nm to produce H and HCO, which in turn propagate to HO_2 ((R10) and (R11)).

$$RCHO + h\nu \rightarrow R + HCO \quad (R12)$$

It is interesting to note that RO_2 radicals are formed through the reaction of alkyl radicals R with dioxygen[6] (R13). The photolysis of carbonyl compounds (aldehydes and ketones) is also a source of RO_2 radicals in the atmosphere.

$$R + O_2 \rightarrow RO_2 \quad (R13)$$

OH radicals can also generate RO_2 and HO_2 radicals (propagation) by reacting with volatile organic compounds (VOC) ((R14) and (R13)) and with CO ((R15) and (R10)), HCHO ((R16), (R11) and (R10)) and H_2 ((R17) and (R10)) respectively.

$$OH + RH \rightarrow R + H_2O \quad (R14)$$

$$CO + OH \rightarrow CO_2 + H \quad (R15)$$

$$HCHO + OH \rightarrow HCO + H_2O \quad (R16)$$

$$H_2 + OH \rightarrow H_2O + H \quad (R17)$$

Organic peroxyl radicals (RO_2) are quickly converted into alkoxyl radicals (RO) through their reaction with NO (R18) as well as self- and cross-reactions under low NO_x concentrations (R19):

$$RO_2 + NO \rightarrow RO + NO_2 \quad (R18)$$

$$RO_2 + RO_2 \rightarrow RO + RO + O_2 \quad (R19)$$

Then the reactions of alkoxyl radicals RO (e.g. CH_3O, C_2H_5O, etc.) lead to the formation of HO_2 through their reaction with molecular oxygen (R20) as well as isomerization and decomposition reactions (not shown):

$$RO + O_2 \rightarrow R_{(-H)}O + HO_2 \quad (R20)$$

The thermal decomposition of species such as HO_2NO_2 [23] (reservoir molecule of HO_2) or peroxy acyl nitrate species (reservoir molecule of RO_2) such as $CH_3C(O)OONO_2$ [23] can also lead to the formation of HO_2 and RO_2:

$$HO_2NO_2 \rightleftharpoons HO_2 + NO_2 \quad \text{(R21)}$$

$$CH_3C(O)OONO_2 + M \rightleftharpoons CH_3C(O)O_2 + NO_2 + M \quad \text{(R22)}$$

I.2 Radical sinks

Concerning the sink of RO_x radicals, in a high NO_x environment, the reactions of the peroxy and hydroxyl radicals with NO and NO_2 lead to the formation of alkyl nitrate $RONO_2$ (R23) and nitric acid HNO_3 ((R24) and (R25)), respectively.

$$RO_2 + NO \rightarrow RONO_2 \quad \text{(R23)}$$

$$HO_2 + NO \rightarrow HNO_3 \quad \text{(R24)}$$

$$OH + NO_2 \rightarrow HNO_3 \quad \text{(R25)}$$

Furthermore, the peroxy radicals can react with themselves and lead to the formation of hydroperoxydes through reactions (R26) and (R27). These reactions are in competition with the reaction with NO ((R23) and (R24)) when the concentration of NO_x is low.

$$HO_2 + HO_2 \rightarrow H_2O_2 + O_2 \quad \text{(R26)}$$

$$RO_2 + HO_2 \rightarrow RO_2H + O_2 \quad \text{(R27)}$$

Heterogeneous processes also lead to the sink of peroxy radicals. Indeed, the reaction with atmospheric particles generally leads to the removal of HO_2 and OH ((R28) and (R29)).

$$HO_2 + \text{aerosol} \rightarrow \text{loss} \quad \text{(R28)}$$

$$OH + \text{aerosol} \rightarrow \text{loss} \quad \text{(R29)}$$

By reacting with VOCs, OH can propagate to RO_2 as explained in section I.1 (Reactions (R14) and (R13)). Then RO_2 can propagate to HO_2 by reacting with NO:

$$RO_2 + NO \rightarrow RO + NO_2 \quad \text{(R30)}$$

Then RO can react with O_2 (reaction (R20)) to form HO_2. Finally, HO_2 propagates to form OH by reacting with NO:

$$HO_2 + NO \rightarrow NO_2 + OH \quad \text{(R31)}$$

The propagation of all the RO_x can also be done with O_3 by the following reactions:

$$HO_2 + O_3 \rightarrow OH + 2\,O_2 \quad \text{(R32)}$$

$$OH + O_3 \rightarrow HO_2 + O_2 \quad \text{(R33)}$$

As listed before, there are many reactions in which HO_2 and RO_2 are involved and that contribute to the regulation of the oxidative capacity of the atmosphere.

I.3 Radical chemistry in various areas

Both the sources and sinks of RO_x radicals vary according to the nature of the area (forested, marine, urban, arctic, etc.). A distinction is made below between the **initiation, termination**

and **propagation** reactions of RO_x radicals to discuss the specific chemistry occurring in these different environments. An **initiation** reaction is a reaction transforming a closed-shell molecule into a radical. A **propagation** reaction transforms a radical into another radical. **The recycling cycle** is composed of all the propagation reactions. A **termination** reaction transforms a radical species into a closed-shell molecule. **Loss** processes include termination and propagation reactions while **formation** pathways involve both initiation and propagation reactions.

Whalley *et al.* (2010)[24] have studied the HO_x (OH + HO_2) budget (Figure 4) and chemistry (Figure 5) in a marine area. The main initiation pathways for the radicals are the photolysis of water in the case of OH radicals and the reaction of OH with CO for the production of HO_2. The main loss pathways are due to the heterogeneous uptake of HO_2 at the aerosol surface and HO_2 and RO_2 self- and cross-reactions to form peroxides. Furthermore, the uptake of RO_x on aerosol is an indirect sink of RO_x radicals since RO_x are reservoir species of OH. In the study of Whalley *et al.*,[24] the uptake by aerosol surfaces accounts for 23% of the total loss rate of HO_2 if an uptake coefficient of 0.1 is assumed.

The HO_x species reactivity forms a recycling cycle as shown in Figure 5. The main propagation reactions involved in this cycle are the formation of RO_x species followed by the photolysis of RO_x which leads to the formation of OH. Then OH propagates to HO_2 through reaction with CO or ozone. In the case of HO_2, it propagates to OH by reacting with NO or ozone. More recently, it has also been shown that the reaction between OH and CH_3O_2 in this type of environment leads to a decrease of RO_2 and to the formation of HO_2 radicals.[26–28]

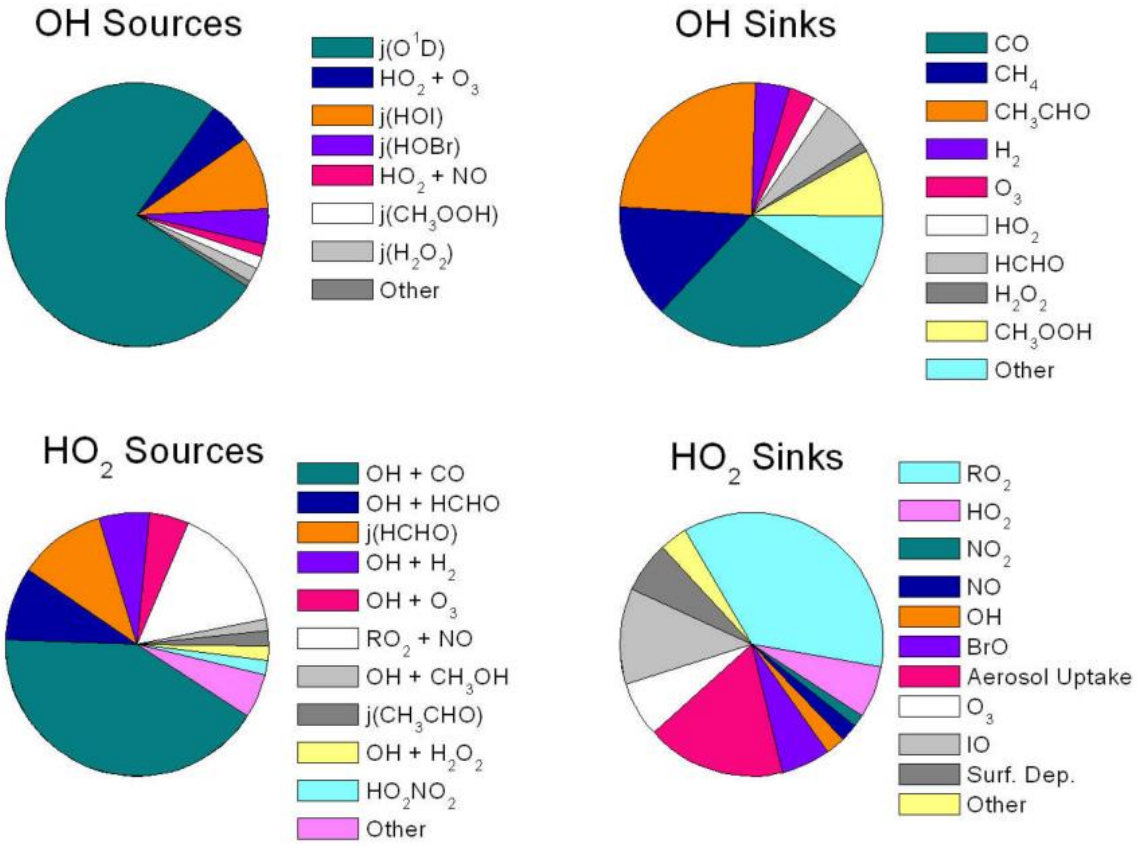

Figure 4: Pie charts showing the average diurnal modeled OH and HO_2 sources and sinks between 12:00 and 13:00 over the tropical Atlantic ocean. Figure taken from Whalley et al. (2010)[24]

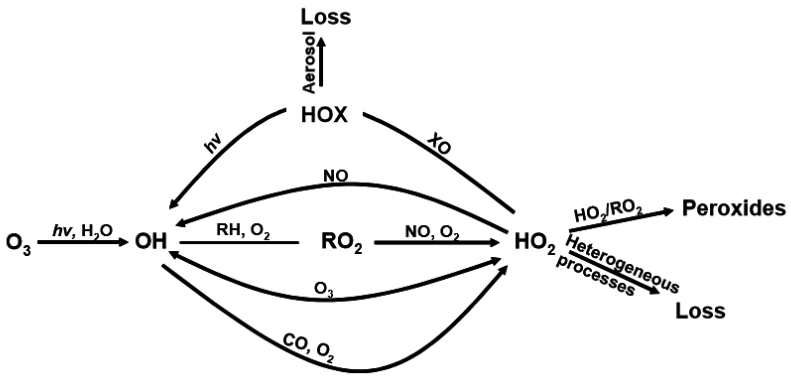

Figure 5: Chemical reaction scheme showing the reactions affecting OH and HO_2 concentrations. X=I, Br and R= alkyl group. Figure taken from Whalley et al. (2010) [24]

Similar chemical schemes can be found for polluted areas as reported in the study of Xue *et al.* (2016).[29] In Figure 6, the red arrows show the initiation reaction of RO_x radicals. The main sources of RO_x species are the photolysis of species such as HONO, HCHO, OVOC and ozone. The reaction of NO_3 with VOC leads also to the formation of RO_2.

The blue arrows represent the termination processes of HO_x species. In urban areas, the two main processes leading to HO_x destruction are the reactions of RO_2 and OH with NO_2 forming peroxy acyl nitrates (RO_2NO_2) and nitric acid (HNO_3), respectively. Then, some reactions involving NO can also lead to the formation of nitrous acid (HONO) from OH+NO and organic nitrates ($RONO_2$) from RO_2+NO. HONO and RO_2NO_2 are molecular reservoirs of OH and RO_2, respectively, since their photolysis or their thermal decomposition can reform the radicals. Finally, the self- and cross-reactions of peroxy radicals and the heterogeneous uptake of HO_2 on aerosols also act as termination reactions. However, the contribution of the latter ones in urban environments (implying high concentrations of NO and NO_2) is negligible.

The green arrows show the recycling cycle of RO_x radicals. The main reactions involved in the recycling process are the reactions of HO_2 and RO_2 with NO, since these areas are characterized by large NO_x emissions. These reactions lead to the propagation of HO_2 into OH and RO_2 to HO_2, with the concomitant formation of NO_2 and thus ozone from the subsequent photolysis of NO_2.

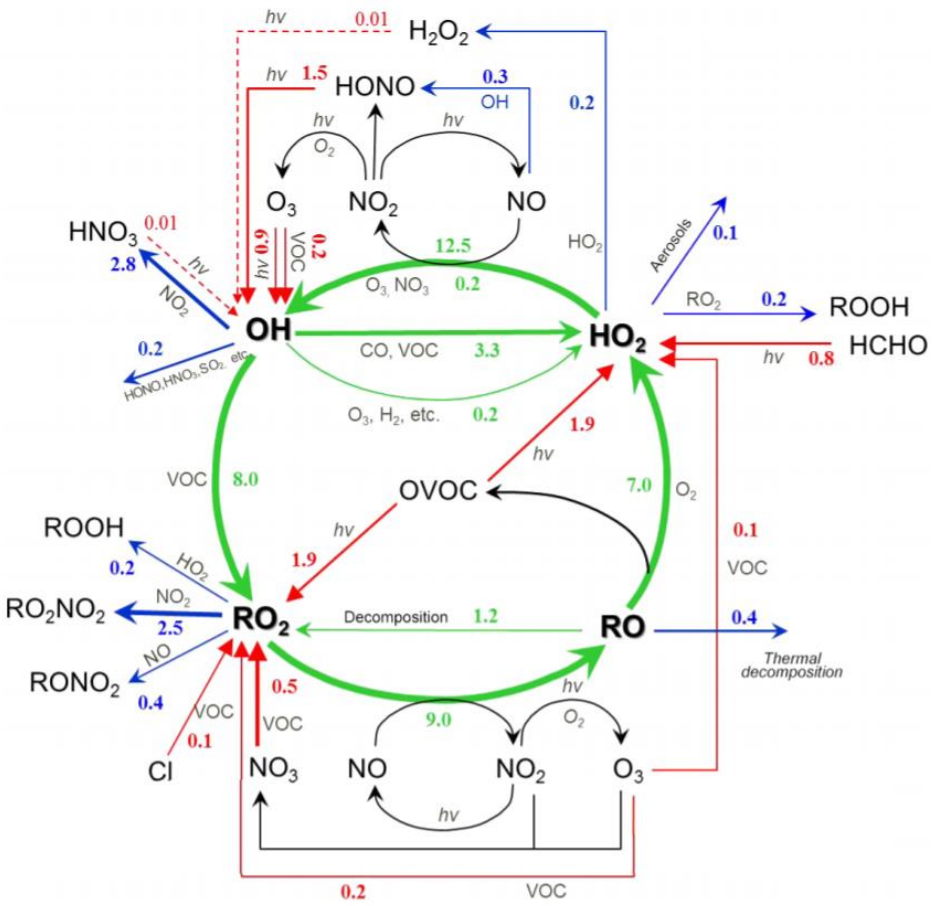

Figure 6: Daytime average RO_x budget at Tung Chung (China) on 25 August 2011. The unit is ppb h^{-1}. The red, blue and green lines indicate the initiation, termination and propagation pathways of radicals, respectively.[29]

Another reactive scheme has been proposed by Hens *et al.*[13] for forested areas. This environment is characterized by low NO_x (NO + NO_2) and high Biogenic Volatile Organic Compound (BVOC) concentrations, the major BVOC being isoprene followed by different monoterpenes. As seen in Figure 7, the initiation processes (green arrows) are the photolysis reactions of HONO, H_2O_2, HCHO and acetone. Then the reaction of ozone with some VOCs leads to the formation of OH and RO_2. The termination processes (red arrows) are due to the reaction of RO_x radicals with NO_x and their self- and cross-reactions. The recycling cycle (blue arrows) is largely driven by the reactions of OH with VOCs and is limited by ambient NO.

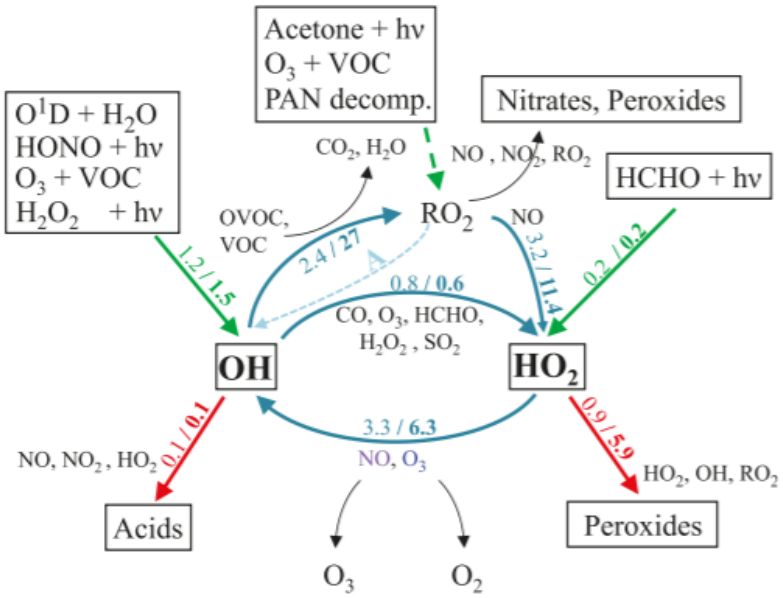

Figure 7: HO_x budget in a boreal forest. Radical production (green), recycling (blue), and loss (red) pathways are indicated by bold arrows. All rates are given in 10^6 molecule cm^{-3} s^{-1}.[13]

I.4 Current understanding of atmospheric RO_x chemistry

Many of the advances in our understanding of the atmosphere have arisen from field measurements of trace gases and their comparison to simulations from atmospheric models.[21] However, comparisons of model simulations of RO_x species to field observations have shown serious discrepancies, suggesting that the RO_x chemistry implemented in models is incomplete.

I.4.1 Comparison of RO_x measurements to atmospheric modeling

Many field campaigns have been performed to test the reliability of atmospheric oxidation mechanisms. Stone *et al.*[30] and Heard *et al.*[31] published a critical review of field campaigns carried out between 1995 and 2009 that were compared to zero-dimensional (0-D) box modelling using chemical mechanisms such as the Master Chemical Mechanism MCMv3.2 (MCM,[32] http://mcm.leeds.ac.uk/MCM) and the Regional Atmospheric Chemistry Mechanism (RACM, Stockwell *et al.*[33]).

These authors have shown that current mechanisms of atmospheric chemistry implemented in 0-D models can reasonably reproduce radical measurements performed in the marine boundary layer, even if there is still a gap in our knowledge for higher altitudes above the ocean.[30] Indeed, OH is generally overestimated at higher altitude.[30] In polluted urban regions (exhibiting high levels of NO_x and anthropogenic VOCs), model-measurement comparisons are in reasonable agreement (within 7%). However, there is sometime significant missing OH sinks (less than 54%) in the model and multifunctional VOC degradation mechanisms are still not well understood.[30] The models also tend to underpredict HO_x concentrations (including peroxy radicals) under high NO_x levels, suggesting an unknown source of RO_x.

The worst agreement with models occurs in forested regions characterized by high emissions of biogenic VOCs and low NO_x levels.[22,30] In these regions, OH reactivity measurements show that significant OH sinks are still missing in the models (up to 300% of the measured OH

reactivity). These missing sinks may be due to unmeasured primary VOC emissions or the presence of unmeasured secondary species (mono- and multifunctional oxygenated VOCs produced during the oxidation of primary VOCs).[22] A missing OH sink due to VOCs in models would likely lead to an underestimation of peroxy radicals since the propagation rate of OH to both HO_2 and RO_2 is underestimated. However, measured HO_2 concentrations were 6 to 8 times lower than model results in some field campaigns.[12,30]

During the PROPHET (Program for Research on Oxidants: PHotochemistry, Emissions, and Transport) campaign in 1998, Tan *et al.*[16] and Sillman *et al.*[14] reported some model/measurement comparisons. They found, using two different models, a modelled daytime OH concentration which was approximately 2.7 times lower than the measured values, while the modeled HO_2 concentration was 30% higher than the measured one. During nighttime, the modeled HO_2+RO_2 was also higher than the measurements by a factor of ~10 in the presence of terpenes. While the disagreement for OH seems to be due to measurement artifacts,[34] the disagreement observed for peroxy radicals suggests a missing sink of these radicals in forested areas. It is worth noting that a FAGE (Fluorescent Assay by Gas Expansion) instrument was used to measure HO_2 during PROPHET 1998. This type of instrument was recently shown to be prone to interferences from RO_2 radicals. FAGE instruments therefore measure HO_2 plus a fraction of RO_2 radicals, suggesting that the disagreement observed between modeled and measured HO_2 during PROPHET 1998 is even larger.

Griffith *et al.*[17] have also compared different models and two field measurement campaigns (Program for Research on Oxidants: PHotochemistry, Emissions, and Transport - PROPHET 2008, and the Community Atmosphere-Biosphere Interactions Experiment - CABINEX 2009). The FAGE instrument used in this study did not exhibit any interference for OH during the campaign, leading to an observed-to-modeled ratio close to unity. However, the modeled sum of HO_2 and isoprene-based peroxy radicals were generally higher than the measurements by a factor of 1.3-2.5, confirming results from PROPHET 1998. Mao *et al.*[34] also made similar observations during the Biosphere Effects on Aerosols and Photochemistry Experiment II (BEARPEX09) field campaign in a pine plantation in the Sierra Nevada Mountains, California, as shown in Figure 8. The modelled concentration of HO_2 was 1.3 times larger than the measurements.

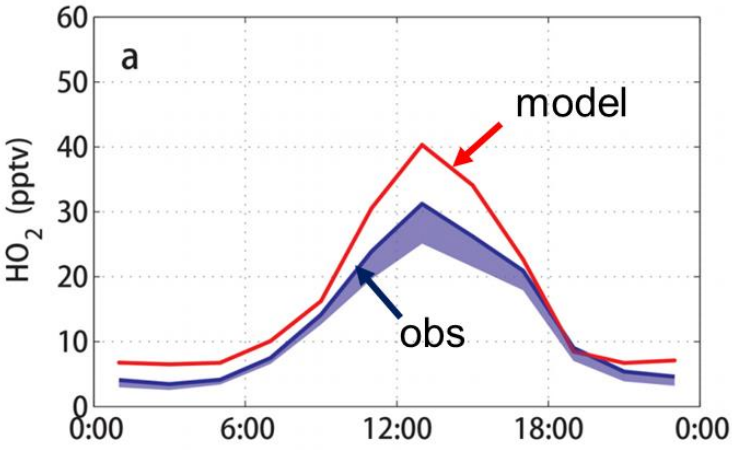

Figure 8: Diurnal cycle of HO_2 between 20 June and 30 July 2009 during the BEARPEX09 field campaign. Modeled HO_2 concentration is represented in red and observed HO_2 concentration is represented in blue. The interferences coming from FAGE are marked by the shaded area.[34]

Hens *et al.*[13] in 2014 came to different conclusions during the HUMPPA-COPEC-2010 (Hyytiälä United Measurements of Photochemistry and Particles in Air-Comprehensive Organic Precursor Emission and Concentration study) field campaign in a pine-dominated forest in Finland. Their measurements of hydroxyl radicals were in agreement with models but this time the HO_2 mixing ratio was significantly underpredicted, suggesting a missing source of peroxy radicals in this forest. The measured OH reactivity was also different from the observed one. These differences may come from missing reactions of OH with VOC and could explain the missing sources of HO_2.

In conclusion for the forested areas (high BVOC concentrations, low NO_x levels), even if the latest studies performed with interference-free OH instruments seem to indicate that OH concentrations observed during field campaigns may be reproduced by atmospheric models, there is a disagreement between measured and modeled HO_2 or HO_2 + RO_2 concentrations, suggesting a lack of understanding concerning the sources, sinks and reactivity of these species. As for the sinks, one possible origin for the missing loss in models could be the HO_2 (and RO_2) uptake on atmospheric aerosols.

I.4.2 Impact of the HO_2 uptake on the RO_x chemistry

The uptake of HO_2 on aerosols has the potential to significantly change the composition of the atmosphere since less oxidative species will be available (less OH recycling, less O_3 production) to oxidize ambient trace gases. The uptake of HO_2 has already been taken into account in some models. Nevertheless, the parameterization of this uptake is not well defined and the mechanisms underlying the uptake process are still uncertain.

To take into account the uptake process, a reactive first-order rate coefficient k can be defined by equation 1, where a is the particle radius, D_g the gas-phase diffusion coefficient of the targeted species, $\bar{c}$, A the particle surface concentration and γ the uptake coefficient.[35]

$$k = \left(\frac{a}{D_g} + \frac{4}{\bar{c}\gamma} \right)^{-1} A \qquad 1$$

Here the uptake coefficient γ represents the probability that a radical species will be captured when it collides with the surface.

For example, a low value of 0.2 was first recommended by Jacob (2000)[35] for γ_{HO2} in marine environments based on laboratory data for aqueous aerosols (cloud, aqueous aerosol containing inorganics such as sulfate or nitrate, γ values ranging from 0.05-0.2), which contrasts to results from model-observation comparisons suggesting higher values of 0.2-1.[36–39] However, according to Macintyre and Evans (2011),[36] the higher values required in models to reproduce ambient observations of RO_x radicals may in fact reflect the omission of halogen chemistry which cycles HO_2 back to OH (R6-R8)[40,41] and hence decreases HO_2 concentrations at the global scale. Thornton *et al.* 2008[42] proposed a parameterization for γ_{HO2} as a function of temperature, for all types of aerosols except dust. The γ_{HO2} value is set to 1 below 260 K and decreases above this temperature (Figure 15 in section II.2.1). Macintyre and Evans[36] further developed this parameterization as seen in Table 1.

Table 1: Uptake coefficients for HO_2 used in the Macintyre and Evans (2011) study[36]

Aerosol	Reaction probability (γ)[a]	Reference
Sulfate	$\alpha \times \beta$ where	
	$\alpha = 5.14545 \times 10^{-4} \exp(1560/T)$	Remorov et al. (2002)[b]
	$\beta = (-26.1818 \exp(-0.078 \times \mathrm{RH}) + 1.74545)$	Taketani et al. (2008)[c]
Organic carbon	0.025	Ivanov et al. (1999)[d]
Black carbon	0.01	Saathoff et al. (2001).
NaCl	$5.66 \times 10^{-5} \exp(1560/T)$ (RH < 62 %)	Remorov et al. (2002).
	0.05 (RH ≥ 62 %)	Taketani et al. (2007).
Dust	0.1 (RH ≥ 50 %); 0.05 (RH < 50 %)	Hänel (1976) reported in Dentener et al. (1996)

[a] T: temperature in K, RH: Relative Humidity in %. [b] Temperature dependent relationship as for NaCl, as fits data from Hanson et al. (1992)[43], Cooper and Abbatt (1996)[44] and Thornton and Abbatt (2005).[45] [c] Exponential fit to available data; [d] 10^{-4} to 5 × 10^{-2} reported at room temperature. Mid value of the range is used.

Figure 7 reports the impact of changing the HO_2 uptake in the Macintyre and Evans model from a constant γ_{HO2} value of 0.2 to the parameterization shown in Table 1. As can be seen, an increase of the HO_2 concentration by approximately a factor of 2 (case of the Chinese coast) leads to an increase of both OH and O_3 by 31% and 27%, respectively. It also leads to a significant decrease in H_2O_2 concentration, which in turn leads to a longer lifetime for SO_2 since the reaction of H_2O_2 with SO_2 in cloud droplets leads to the formation of SO_4^{2-}. Its transport to higher altitudes, due to a longer lifetime, can then lead to the production of sulfate which is known to have a cooling effect on climate. There is a small impact at the global scale (increase in the production of sulfate is mostly positive at each longitude) but the impact is more significant regionally (e.g. OH and O_3 production over Chinese regions).

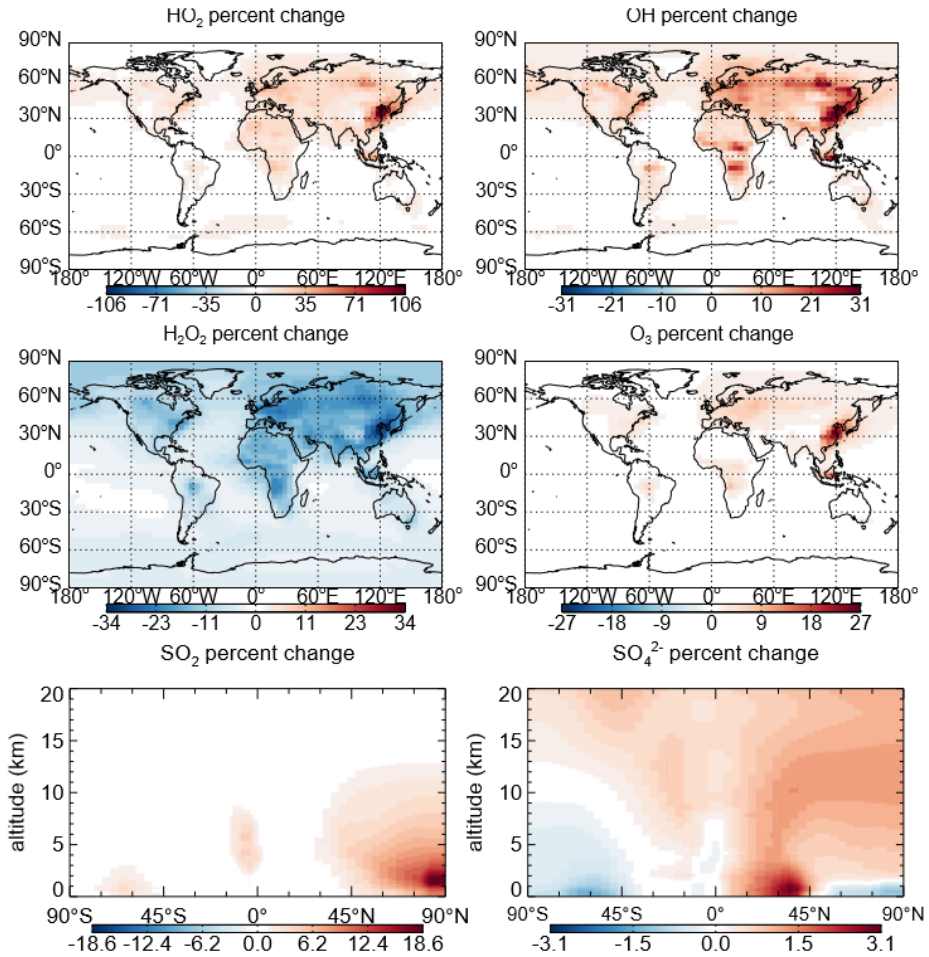

Figure 9: Impact on the annual mean concentrations of oxidants and sulfur species when moving from a γ(HO_2) value of 0.2 (Jacob,2000)[35] to the scheme presented in Table 1 (global mean γ(HO_2) of 0.028)[36]

This modeling shows the importance to better understand the uptake processes of HO_2 and the necessity to conduct laboratory experiments and numerical simulations to quantify the uptake coefficient for different types of aerosols. It is also worth noting that models do not consider an uptake of RO_2 radicals. However, mono- and multifunctional RO_2 radicals, such as isoprene- or monoterpene-derived peroxy radicals, may be efficiently captured by aerosols. This lack of knowledge significantly impedes our ability to perform reliable forecasting of atmospheric composition.

II Study of uptake processes

As discussed above, the uptake of RO_x radicals on aerosols, and more generally of trace gases, is an important process in the atmosphere.[46] Indeed, it is one of the process leading to the removal of gaseous pollutants (e.g. uptake of SO_2 and NH_3 on water droplets, which leads to the formation of acid rains).[2] The uptake could also lead to a modification of the aerosol properties (light absorption and scattering, bioaccessibility, etc.). In addition, a modification of the chemical properties at the surface may enhance the production of cloud condensation nuclei. These changes in properties can be due to the adsorption of new closed-shell species at the

surface or to an alteration of its chemical nature through surface and bulk reactions involving radical species. [47–50]

II.1 Theoretical models of uptake

Liquid or solid particles can interact with gas phase species either in the atmosphere[18,19,36,43–45,51–77] or even in the interstellar medium where some reactions occur after adsorption at the surface of interstellar grains (ice, dust).[78] As mentioned previously, the uptake coefficient is the probability that a molecule will be lost from the gas phase – at least, temporarily – after colliding with the surface.

The uptake of a species on an aerosol particle can be considered as a convolution of three types of processes (Figure 10):

- Gas diffusion
- Adsorption, and eventually surface reaction
- Bulk diffusion, and eventually reaction in the bulk

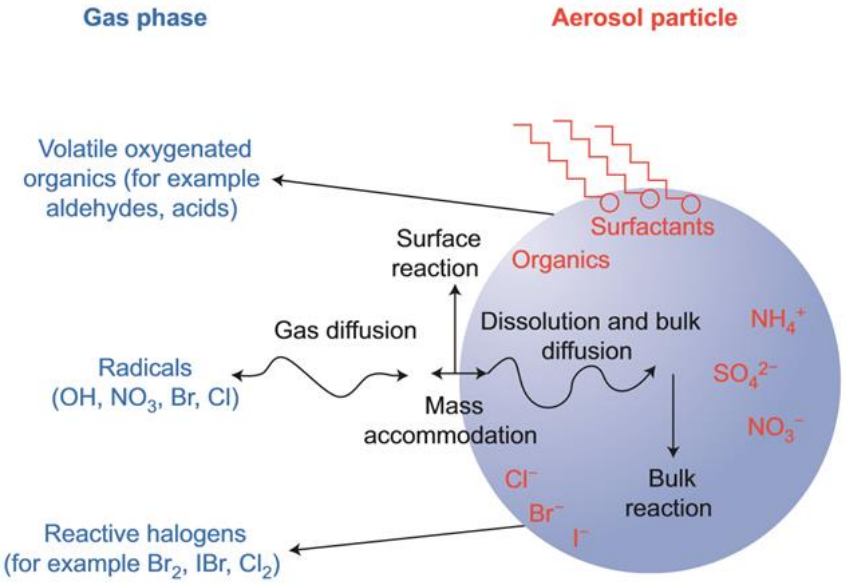

Figure 10: Schematic of the processes that govern heterogeneous radical uptake by aerosol particles.[79]

The species will first diffuse in the gas phase and will be transported near the aerosol surface. A dynamic exchange will occur between the gaseous and particulate phases through adsorption/desorption processes. The mass accommodation coefficient, i.e the proportion of near-surface species which are adsorbed on the aerosol, will only depend on the adsorption rate, while the uptake coefficient will depend on the difference between the adsorption, bulk diffusion and desorption rates, the adsorption rate being larger when an uptake is observed. This process will induce a loss of this species in the gas phase.

Surface processes contributing to the consumption of the adsorbed species will lead to a higher uptake since it will result in a decrease of the desorption rate. Such processes involve reactions between the captured species and other adsorbed molecules at the surface and reactions with the aerosol surface itself. The adsorbed species can also diffuse in the aerosol bulk, leading to

a renewal of the surface, and possibly further reaction with other species present in the bulk, leading to an enhancement of the uptake.

Three phenomenological models of uptake have been proposed until now:[18]

a) The continuum flux model based on the coupling of differential rate equations of mass and heat transport, with corrections applied for gas-surface interactions[80,81]
b) The kinetic resistance model based on the linear combination of flux resistances (by analogy to electrical resistances[72])
c) The kinetic flux model based on the coupling of differential rate equations of mass transport and chemical reactions using gas kinetics formulations, corrected for gas diffusion[70,82–84]

II.1.1 Continuum flux model

For the continuum flux model, the accommodation coefficient α is determined by the theory of droplet growth. Droplet growth is controlled by both mass and heat transfers which are coupled. In this model we define two accommodation coefficients, the mass accommodation α_M and the thermal accommodation α_T, which depend on the mass flux and the temperature gradient, respectively. Further details concerning this model are given in Appendix A.

This model can be used only in the case where the aerosol radius increases sufficiently to allow the detection of the increase, as can be the case for water condensation during the formation of a droplet. However, a limitation of this model is that chemical reactions are not taken into account. Thus this model is not suitable for reactive system.[80,81]

II.1.2 Kinetic resistance model

For the kinetic resistance model, the net uptake coefficient of a trace gas with liquids or solids is computed by equation 2:

$$\gamma = \frac{4J}{n_g \bar{c}} \qquad 2$$

where J is the gas-phase flux of the trace gas towards the condensed phase, n_g the concentration of the trace gas far from the surface, and $\bar{c}$ its average molecular speed. However, when diffusion processes and reactions occur, the uptake can be considered as a sum of resistances and the well-known resistor combination rules can thus be applied to derive the uptake coefficient.

When no reaction occurs, the uptake coefficient is only limited by three processes (Figure 11.A; equation 3):

$$\frac{1}{\gamma} = \frac{1}{\Gamma_{diff}} + \frac{1}{\alpha} + \frac{1}{\Gamma_{sat}} \qquad 3$$

with $1/\Gamma_{diff}$ the gas-phase diffusion resistance and $1/\Gamma_{sat}$ the bulk diffusion resistance. However, when chemical reactions occur at the surface or in the bulk, other resistances appear (see Figure 11.b).

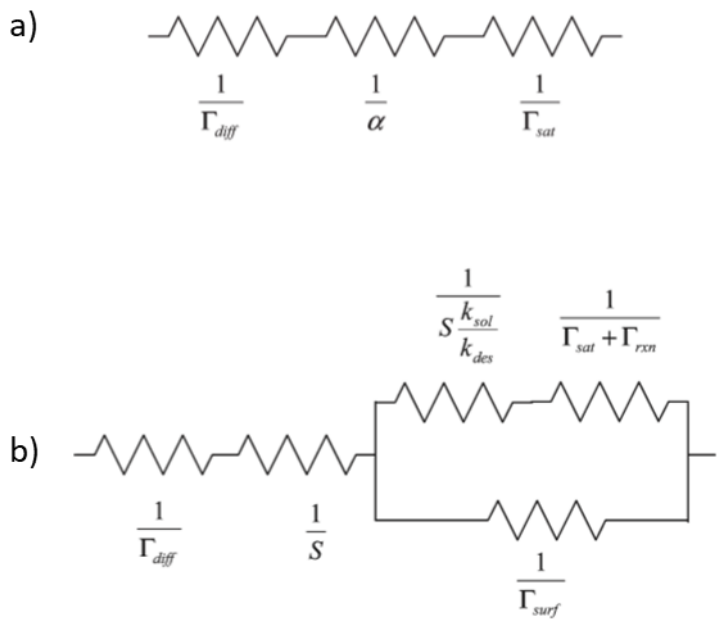

Figure 11: a) Resistor model for an uptake limited by gas-phase diffusion, mass accommodation, and solubility. b) Resistor model for an uptake limited by gas-phase diffusion, mass accommodation, solubility, liquid-phase reaction and surface reaction.[72]

Indeed when surface reactions occur, the mass accommodation coefficient α has to be split into two parts, because once a molecule is adsorbed, it can either enter the bulk or it can react at the surface. The term accounting for the particles adsorbing at the surface is called S (sticking coefficient). To compute the fraction of molecules diffusing in the bulk, we use the ratio of the kinetic coefficient of desorption k_{des} over the kinetic coefficient of solvation k_{sol}, known as the equilibrium ratio $K = \frac{k_{des}}{k_{sol}}$. So α can be expressed as in equation 4.

$$\frac{1}{\alpha} = \frac{1}{S} + \frac{1}{S\frac{k_{des}}{k_{sol}}} = \frac{1}{S} + \frac{1}{SK} = \frac{1}{S}\left(1 + \frac{1}{K}\right) \quad (4)$$

So, for the resistor model described in Figure 11.B accounting for bulk processes, we get the uptake coefficient γ by computing equation 5:

$$\frac{1}{\gamma} = \frac{1}{\Gamma_{diff}} + \frac{1}{S} + \frac{1}{\frac{1}{\frac{1}{SK} + \frac{1}{\Gamma_{sat} + \Gamma_{rxn}}} + \frac{1}{\Gamma_{surf}}} \quad (5)$$

with $\Gamma_{sat} + \Gamma_{rxn}$ the bulk processes resistance (diffusion, reaction) and Γ_{surf} the surface reaction resistance. For the gas-phase diffusion resistance, an empirical formula[85] of the isothermal diffusive transport function of the Knudsen number can be used (equation 6):

$$\frac{1}{\Gamma_{diff}} = \frac{0.75 + 0.238Kn}{Kn(1+Kn)} \quad (6)$$

where the Knudsen number Kn is equal to the mean free path λ of the species over the radius of the particle $r_p = d_p/2$:

$$\lambda = \frac{3D_g}{\bar{c}} \quad (7)$$

with D_g ($cm^2\ s^{-1}$) the gas-phase diffusion coefficient.

The surface reaction resistance can also be computed by equation 8:

$$\frac{1}{\Gamma_{surf}} = \frac{\bar{c}}{4k_{surf}b'} \quad (8)$$

where *b'* (cm) is the surface adsorption/desorption equilibrium constant, and k_{surf} the reaction rate of surface reactions (s^{-1}).

The bulk process resistance is computed by equation 9:

$$\frac{1}{\Gamma_{sat} + \Gamma_{rxn}} = \frac{1}{\frac{4HRT\sqrt{D}}{\bar{c}}\left(\sqrt{k} + \sqrt{\frac{1}{\pi t}}\right)} \quad (9)$$

where H ($mol\ L^{-1}\ atm^{-1}$) is the Henry's law constant, R ($atm\ L\ mol^{-1}\ K^{-1}$) the ideal gas constant, T (K) the temperature, t (s) the gas-liquid interaction time, D ($cm^2\ s^{-1}$) the bulk diffusion coefficient and k the reaction rate (s^{-1}).[72]

II.1.3 Kinetic flux model

The last model was developed by Pöschl, Rudich and Ammann[82] and is called the kinetic flux model or PRA (for Pöschl, Rudich, Amman) model. In this model, the uptake coefficient is described by a ratio of the net molecular flux from the gas-phase to the condensed-phase J_{net} over the gas kinetic flux colliding the surface J_{coll} (equation 10):

$$\gamma = \frac{J_{net}}{J_{coll}} \quad (10)$$

Based on the gas kinetic theory, the colliding flux can be computed by equation 11, assuming a homogeneous concentration $[X_i]_g$ for the targeted trace gas:

$$J_{coll} = [X_i]_g \frac{\bar{c}}{4} \quad (11)$$

However, a large uptake will lead to a depletion of the trace gas near the surface. The near-surface concentration thus becomes $[X_i]_{gs} < [X_i]_g$ and some corrections due to the gas diffusion need to be performed.

Compared to the kinetic resistance model, the uptake coefficient γ_{eff} in this model corresponds to the processes at the surface and in the bulk (equation 12):

$$\frac{1}{\gamma_{eff}} = \frac{1}{\alpha} + \frac{1}{\Gamma_{bulk}} \quad (12)$$

The whole system is divided in n layers as shown in Figure 12. All the elementary processes (reactivity and diffusion) between these layers are taken into account for the computation of the uptake coefficient. More details for this model are given in Appendix B.

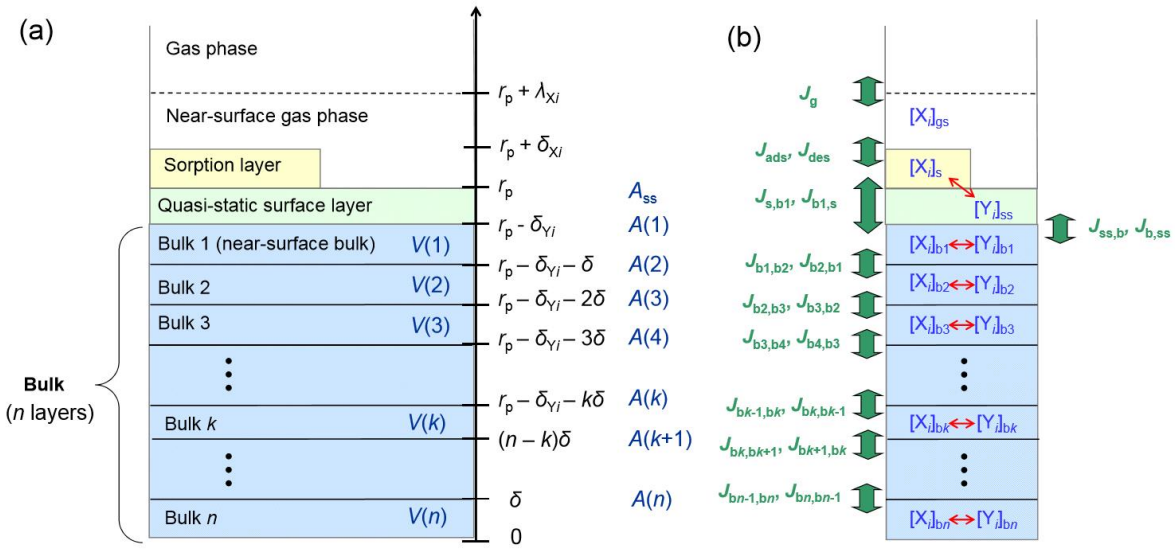

Figure 12: Kinetic multi-layer model (KM-SUB): (a) Model compartments and layers with corresponding distances from particle center ($r_p \pm x$), surface area (A) and volumes (V); λ_{Xi} is the mean free path of X_i in the gas-phase; δ_{Xi} and δ_{Yj} are the thickness of sorption and quasi-static bulk layers, respectively; δ is the bulk layer thickness. (b) Transport fluxes (green arrows) and chemical reactions (red arrows).[83]

II.1.4 Summary

The continuum flux model which was first described is the only one which takes into account the droplet growth but is not really precise and requires experiments in a cloud chamber. The kinetic resistance model is more precise than the first one and is quite easy to apply using an aerosol flow tube. The third model (kinetic flux model) is the most accurate but the number of parameters is large and a more advanced experimental setup is needed. **The kinetic resistance model will therefore be used in this study to interpret our laboratory experiments obtained with an aerosol flow tube.**

II.2 Experimental investigation of HO_2 uptake

As discussed above, measurements of HO_2 uptakes on various types of aerosols are needed to critically assess their significance and potentially implement the corresponding process in atmospheric models. In addition, the influence of environmental parameters such as temperature, pressure, RH and chemical composition of the aerosol has to be taken into account. In this section, the main uptake measurement apparatus will be introduces and studies reporting HO_2 uptake measurements are reviewed.

II.2.1 Laboratory apparatus

In the literature, several types of experimental setups have been used to measure uptake coefficients of trace gases. Among them, the paragraphs below will detail the principle, advantages and limitations of the Knudsen cell, the droplet flow reactor, the aerosol flow tube, the cloud chamber and the wall coated aerosol flow tube.

I) The Knudsen cell (Figure 13.A)
Principle: surface uptake study at P < 10 mTorr to avoid gas diffusion effects (mean free path of a molecule three times larger than the diameter of the exit orifice). Trace gas concentration measured in the presence and absence of a surface, which could lead to surface accommodation or surface reaction. Uptake coefficient derived from the difference in concentrations observed with and without the surface. Detection of reactant gas species by mass spectrometry.
Examples of investigated trace gases: water, N_2O_5, HNO_3, O_3, NO_3, etc.
Range of measurable uptake coefficients: 1 to 10^{-5}
Advantage: avoid gas diffusion effect
Drawback: cannot study high pressure effects at the surface

II) The droplet flow reactor (Figure 13.B)
Principle: study of uptake coefficients on liquid droplets whose size ranges from 50 to 200 µm. A droplet generation chamber creates droplets of uniform size and spacing via a vibrating orifice. Pressure in the 6-20 Torr range and temperature within 260-290 K. Trace gas can enter the flow tube at different positions and the concentration difference with and without droplets can be measured by infrared or mass spectroscopy. Droplets can also be further analyzed for both physical and chemical characterization.
Examples of investigated trace gases: water, HCl, H_2SO_4, O_3, etc.
Range of measurable uptake coefficients: 1 to 10^{-3}
Advantages: Environmental parameters (temperature, pressure, relative humidity, etc.) can be controlled; an accuracy of 10^{-5} on uptake coefficient can be reached
Drawbacks: need to correct for gas-phase diffusion to get accurate values of uptake. Uptake measurements limited to liquid aerosols.

III) The Aerosol Flow Tube (AFT) (Figure 13.C)
Principle: study the uptake of a trace gas on liquid or solid particles inside a flow tube by varying the contact time between both phases using a sliding injector. Aerosols produced by nebulization and passed through a conditioner where they equilibrate under the operating conditions (temperature and humidity) then can be size-selcted by a differential mobility analyzer (typically a few tens of nanometers). A suitable gas analyzer can be set at the end of the AFT to monitor the trace gas. Aerosols can also be collected and further analyzed.
Examples of investigated trace gases: HO_2, OH, HCl, HSO_4, etc.
Range of measurable uptake coefficients: 1 to 10^{-4}
Advantages: Aerosol particles can be in liquid or solid state. Experimental conditions closer to atmospheric conditions than other techniques.
Drawbacks: Fresh (charged) particles need to be neutralized. Flow needs to be laminar. Gas-phase diffusion needs to be taken into account.

IV) The cloud chamber (Figure 13.D)

Principle: investigate droplet formation and growth under thermophysical conditions to derive mass accommodation coefficients. Chamber loaded by a monodispersed aerosol. Vapor saturation established inside the chamber by adiabatic expansion. Droplet growth quantified using the constant angle Mie scattering method, which consists in monitoring light fluxes transmitted through the system and scattered by the particle under a selectable, constant scattering angle during particle growth. Experimental curves of scattered light flux vs. time compared to theoretical ones computed by means of the Mie theory[86]. Mass and thermal accommodation coefficients (see section II.1) determined from quantitative comparison of experimental and theoretical droplet growth curves.
Examples of investigated trace gases: water, HNO_3, HO_2, etc.
Range of measurable uptake coefficients: 0.01 to 1
Advantage: operating conditions close to atmospheric conditions. Independent determination of mass accommodation and heat accommodation.
Drawback: Mass and heat fluxes need to be corrected. Cumbersome setup.

V) The wall-coated Flow Tube (wc-FT) (Figure 13.E)

Principle: setup quite similar to the AFT except that instead of suspended aerosol, the system of study is coated on the wall of the tube.
Examples of investigated trace gases: HO_2, O_3, water, etc.
Range of measurable uptake coefficients: 0.2 to 10^{-5}
Advantages: can measure the surface coverage at saturation. Uptake measurement limited by gas diffusion only.
Drawbacks: Flow needs to be laminar. Gas-phase diffusion needs to be taken into account. Measurement can be limited if there is a significant surface saturation. Measurement performed on a macroscopic surface which may not be representative of the real system.

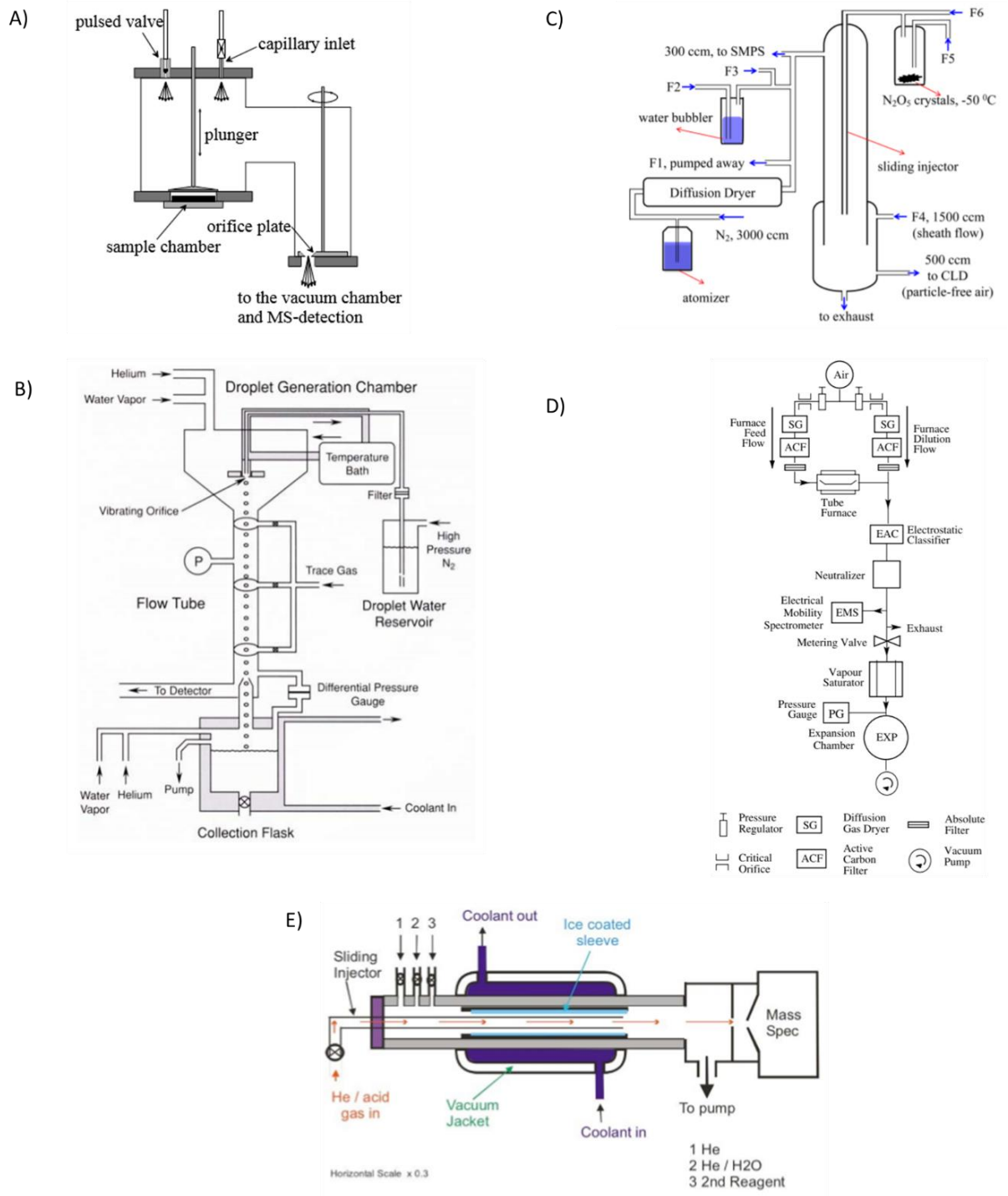

Figure 13: Different types of reactors to study gas-aerosol interactions. A) Knudsen cell reactor;[87] B) Droplet flow reactor;[88] C) Aerosol Flow tube reactor;[89] D) Cloud chamber system;[90] E) Wall coated flow tube[91]

II.2.2 Dependence of the HO_2 uptake on aerosol composition and temperature

The uptake of HO_2 has been investigated on various surfaces (macroscopic surfaces or aerosols) in the past using the Aerosol Flow Tube (AFT),[51,54,58] wall coated Flow Tube (wc-FT)[55,60] or Cloud chamber[53,64] techniques. In most of the studies, the impact of various parameters such as temperature and Relative Humidity (RH) was studied. Figure 15 shows HO_2 uptake coefficients measured on various inorganic aerosols using the AFT or wc-FT apparatus as a function of

temperature.[36] It is clear that the nature of the surface has a large influence on the HO_2 uptake with values ranging from 0.002 for natural seawater particles to 0.4 for Cu-doped sulfate aerosols. Figure 14 shows that even for organic aerosols, the uptake coefficient can vary by more than one order of magnitude as a function of the nature of the organics.

It is important to note that HO_2 uptakes reported for organic particles have been performed by only two groups with large discrepancies (more than one order of magnitude) between the two datasets for the species in common (glutaric acid). Additional measurements are thus needed to provide confidence on uptake values to be implemented in atmospheric models.

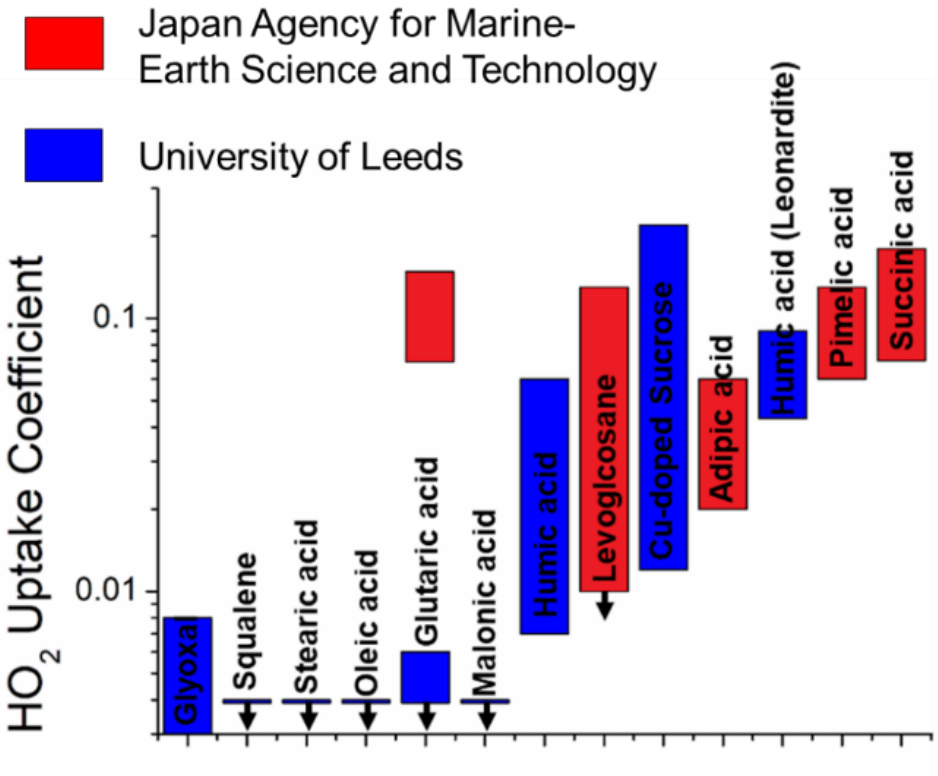

Figure 14: Measurements of HO_2 uptake on organic particles.[51–54] These measurements were performed by the Research Institute for Global Change of the Japan Agency for Marine-earth Science and Technology in Yokohoma (red) and by the School of Chemistry, of the University of Leeds, England (blue).

The impact of temperature also depends on the nature of the surface. Generally, an increase of temperature tends to decrease the HO_2 uptake, except for salts. However, most of the studies were carried out at ambient temperature and there is a lack of measurements at other atmospherically-relevant temperatures. The first parametrization made by Jacob et al.[35] was not taking into account the influence of temperature (black dotted line in Figure 15), which was not the case in the subsequent parametrizations of Mao et al.[92] (black dashed line) and Macyntire and Evans[36] (red dot-dash line).

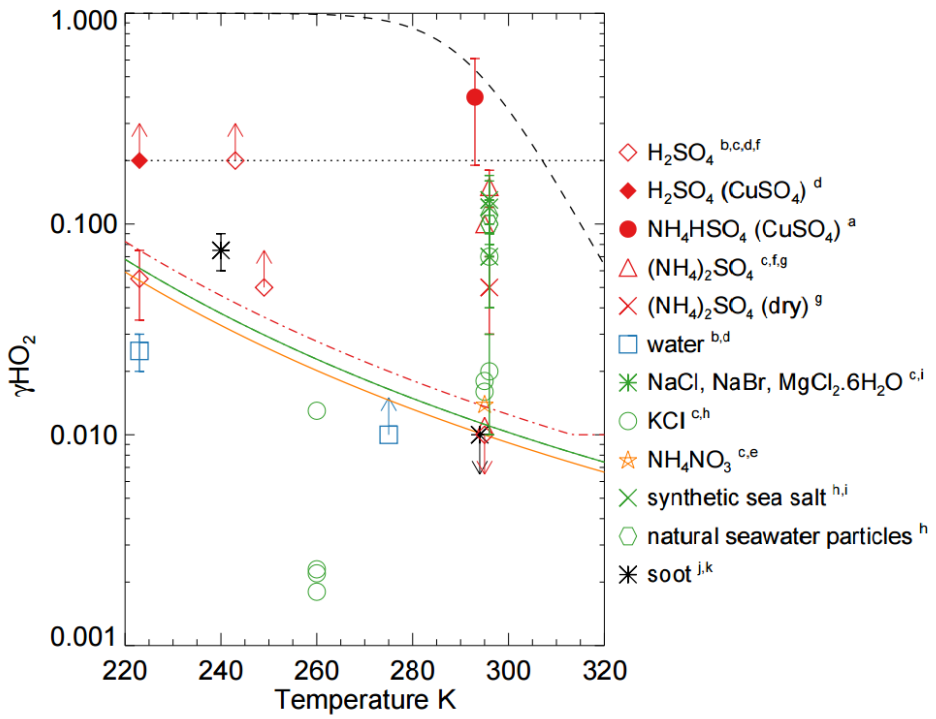

Figure 15: Summary of laboratory data for γHO_2 plotted as a function of temperature. Filled symbols denote that the aerosol was doped with Cu. Colors refer to composition as follows: red, sulfur-containing aerosols; green, Cl- (or Br-) containing salts, i.e. sea salt; black, soot; yellow, ammonium nitrate; blue, water. Solid lines indicate temperature dependencies for NH_4NO_3 (Gershenzon et al., 1999[93]), and for solid NaCl (Remorov et al., 2002[63]), respectively. Error bars as quoted in the references and arrows indicate greater than or less than. The red dot-dash line indicates the temperature dependence of the parameterization assumed in Macintyre and Evans, 2011[36] (assuming 50% of relative humidity). The black dotted line indicates a value of 0.2, as recommended by Jacob (2000)[35], and the dashed black line reports the parameterization of Thornton et al. (2008)[42] (assuming pH = 5, r = 100 nm, α = 1, $[HO_2] = 10^8$ cm^{-3}), used by Mao et al. (2010)[92] to fit model based on laboratory data with ARCTAS observation. Letters indicate references as follows: [a] Mozurkewich et al., 1987,[62] [b] Hanson et al., 1992,[43] [c] Gershenzon et al., 1995,[59] [d] Cooper and Abbatt, 1996,[44] [e] Gershenzon et al., 1999,[93] [f] Thornton and Abbatt, 2005,[94] [g] Taketani et al., 2008,[68] [h] Taketani et al., 2009,[67] [i] Loukhovitskaya et al., 2009,[60] [j] Bedjanian et al., 2005,[55] [k] Saathoff et al., 2001.[64] Figure taken from Macintyre and Evans, 2011[36].

Another parameter that impacts HO_2 uptake is the copper concentration, and to a lesser extent the iron concentration. Indeed, several studies have shown that the presence of copper and iron strongly impacts the reactivity of HO_2 within the aerosol bulk, and as a consequence impacts the uptake coefficient.[19,53,62,65,68,94] Figure 16 clearly shows that when particles are doped with Cu(II), the uptake coefficient is considerably increased at given RH and temperature. This is explained by a rapid consumption of HO_2 in the bulk due to the following mechanism for copper:[53]

$$HO_2(g) \rightleftharpoons HO_2(aq) \quad \text{(R34)}$$

$$HO_2(aq) \rightleftharpoons H^+(aq) + O_2^-(aq) \quad \text{(R35)}$$

$$Cu^{2+}(aq) + HO_2(aq) \rightarrow O_2(aq) + Cu^+(aq) + H^+(aq) \quad \text{(R36)}$$

$$Cu^+(aq) + HO_2(aq) + H_2O(l) \rightarrow H_2O_2(aq) + Cu^{2+}(aq) + OH^-(aq) \quad \text{(R37)}$$

$$Cu^{2+}(aq) + O_2^-(aq) \rightarrow O_2(aq) + Cu^+(aq) \quad \text{(R38)}$$

$$Cu^{+}(aq) + O_2^{-}(aq) + 2H_2O(l) \rightarrow H_2O_2(aq) + Cu^{2+}(aq) + 2OH^{-}(aq) \quad (R39)$$

The copper in aerosol allows the removal of resistances due to bulk and surface reactivity. Thus the resistance depending on bulk or surface becomes equal to unity in equation 3, allowing to determine the mass accommodation coefficient to some extent.

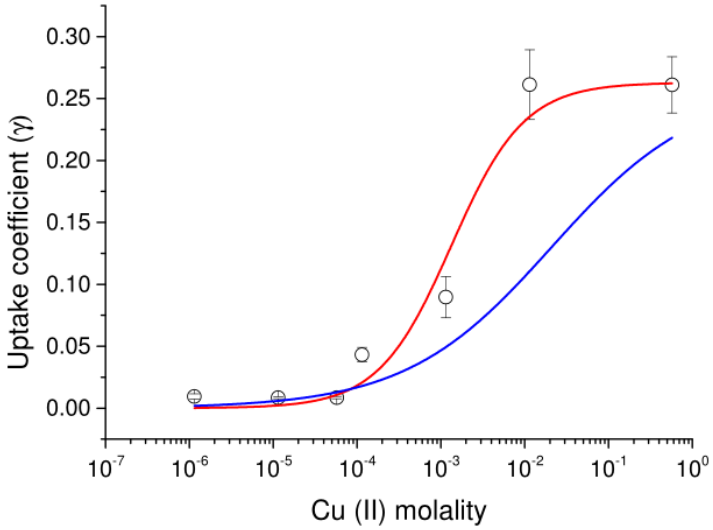

Figure 16: HO_2 uptake coefficient as a function of the estimated Cu(II) molality for ammonium sulfate aerosols at 65 % RH and 293 ± 2 K. The error bars are 2 standard deviations. Red line: fitting of $1/\gamma = 1/\alpha + 1/(A.[Cu])$ with $\alpha = 0.26$ and $A = 197$ L mol^{-1}. Blue line: fitting of $1/\gamma = 1/0.26 + 1/(B.[Cu]^{0.5})$ where $B = 1.8$ (mol L)$^{-(1/2)}$. Figure taken from Matthews 2014, experimental data obtained by Dr. Ingrid George.[95]

As seen in Table 2, the HO_2 uptake coefficient on glutaric acid is not well defined. Lakey *et al.*[51] have measured the uptake coefficient at low copper and iron concentrations and have found a very low value. However, in the study of Taketani *et al.*,[54] the values are one order of magnitude larger than in Lakey *et al.* One potential reason for the disagreement is a contamination of the samples used by Taketani *et al.* by copper or iron ions.

Table 2: Value of HO_2 uptake onto glutaric acid found in the literature[51,54]

RH (%)	Uptake	uncertainties	[HO_2] (molecules.cm^{-3})	[Cu] (M)	[Fe] (M)	References
32	<0.004	N/A	10^9	$(0.7 - 1.3).10^{-7}$	$(1.7 - 3.4).10^{-3}$	Lakey et al. 2015
54	0.006	0.002				
76	<0.004	N/A				
28	0.07	0.03	10^8	N/A		Taketani et al. 2013
68	0.15	0.04				

II.2.3 Impact of Relative Humidity (RH)

Relative humidity has an influence on the HO_2 uptake coefficient as shown in Figure 17 for measurements performed on Arizona Test Dust by Bedjanian *et al.*[56] In this study it is clear that the uptake coefficient decreases with higher RH. However, this dependence is less obvious from Matthews *et al.* [61]. This discrepancy can be explained by differences between the two studies: Bedjanian *et al.*[56] used macroscopic surfaces and high concentrations of HO_2 (10^{12} molecule cm^{-3}) to determine initial uptakes (γ_0), whereas uptakes were measured on a longer

time scale on submicronic aerosols with low concentrations of HO_2 (10^8 to 10^9 molecule cm^{-3}) in Matthews *et al.*[61] Additional work spanning the whole range of operating conditions described above is needed to elucidate this aspect.

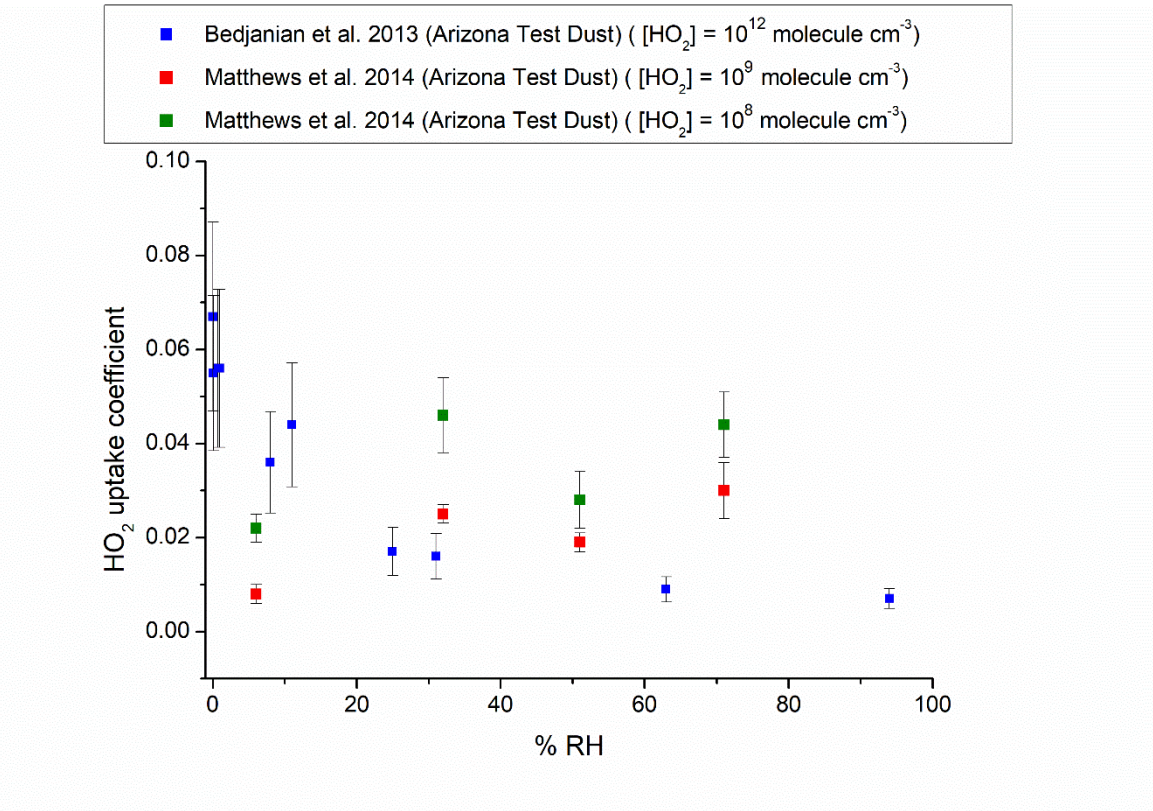

Figure 17: Influence of RH on the HO_2 uptake for Arizona Test Dust.[56,61]

Taketani *et al.*[54] have also shown that an increase in RH can lead to an increase in the uptake of HO_2 on organic compounds (Table 3). Indeed, the uptake coefficient of some dicarboxylic acids has increased by a factor larger than 2 with an increase of RH from 28% to 68%.

Table 3: Summary of HO_2 uptake coefficients for dicarboxylic acids and their dependence on RH at room temperature (from Taketani et al.[54])

	Uptake Coefficient	
Compound	RH 28%	RH 68%
Succinic acid[a]	0.07 ± 0.02	0.18 ± 0.07
Glutaric acid[a]	0.07 ± 0.03	0.15 ± 0.04
Adipic acid[a]	0.02 ± 0.01	0.06 ± 0.01
Pimelic acid[a]	0.06 ± 0.03	0.13 ± 0.04

Another study carried out by Lakey *et al.*[52] has evidenced the effect of RH for copper-doped sucrose aerosol. At low RH, the diffusion coefficient in the condensed phase decreases, which in turn leads to a lower uptake coefficient. Indeed, an uptake coefficient of 0.012 ± 0.007 was found at 17 ± 2 %RH while an uptake coefficient of 0.22 ± 0.06 was found at 65 % RH. At low RH, the uptake coefficient mainly depends on the surface reactivity.

The aqueous phase can lead to an increase of the uptake coefficient by increasing the diffusivity in the bulk.[52] Indeed, as shown in Figure 18, the increase in the relative humidity leads to an increase of the diffusion coefficient and thus of the uptake.

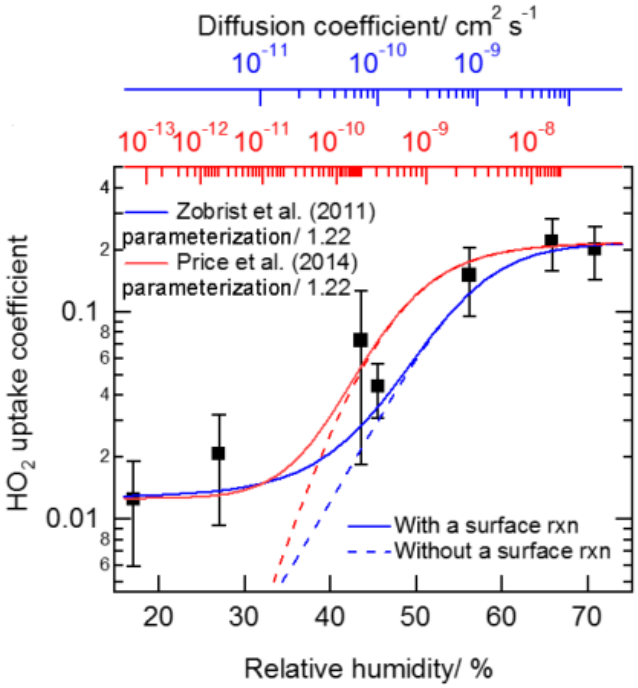

Figure 18: HO_2 uptake coefficient onto Cu(II)-doped sucrose aerosol particles as a function of relative humidity. Figure taken from Lakey et al.[52]

II.2.4 Impact of pH

The pH of the aerosol can also impact the uptake. For example, as HO_2 is considered a weak acid (pK_a = 4.7), the increase in pH tends to facilitate reaction (R35). Then O_2^- can react with another peroxy radical in order to form hydrogen peroxide according to reaction (R40):

$$O_2^- (aq) + HO_2 (aq) + H_2O(l) \rightarrow H_2O_2 + OH^- + O_2 \qquad (R40)$$

The equilibrium is fast at pH > 4 and an effective Henry's law constant shown in equation 13 has to be used to take into account the resulting higher solubility of HO_2:

$$H^{eff} = H\left(1 + \frac{K_{eq}}{[H^+]}\right) \qquad 13$$

where H^{eff} is the effective Henry's law constant, H the Henry's law constant of the species (estimated at 4000 M atm^{-1} for HO_2 at 298 K), K_{eq} the equilibrium constant of reaction (R35) and $[H^+]$ the proton concentration in the bulk phase.

The influence of pH on HO_2 uptake is shown Figure 19. The uptake increases continuously when pH increases from 2 to 8.[95]

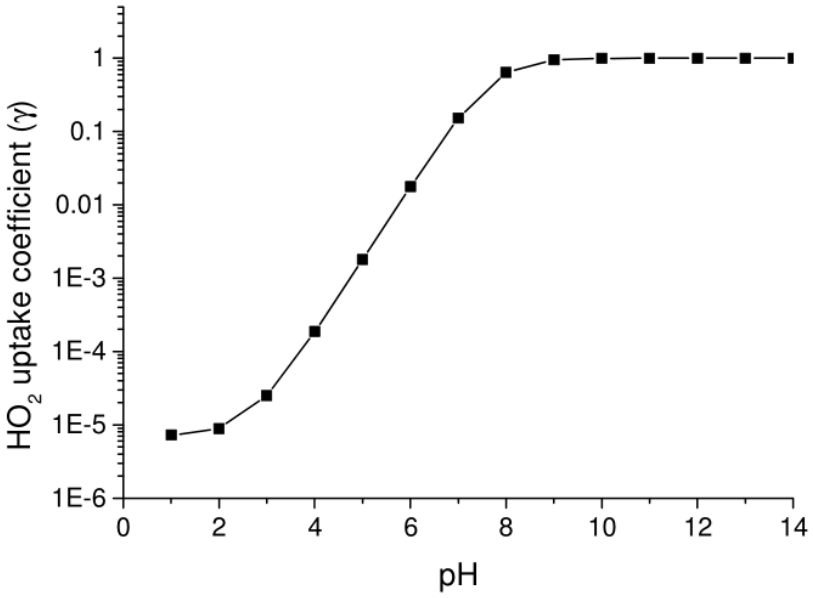

Figure 19: Theoretical HO_2 uptake coefficient as a function of aerosol pH for an aerosol radius of 100 nm, a temperature of 293 K and a HO_2 concentration of 5×10^8 molecule cm^{-3}. Figure taken from Matthews [95]

II.2.5 Review of uptake measurements reported in the literature

The following tables summarize uptake measurements of HO_2 on inorganic (Table 4), organic (Table 5) and mixed organic/inorganic (Table 6) particles or macroscopic surfaces. OH uptakes are also reported for comparison. Measurements performed on macroscopic surfaces were performed using wc-AFT and values reported for aerosol particles were obtained using AFT.

These measurements were almost all performed at room temperature and under a wide range of RH conditions. The uptake of HO_2 is generally lower than the OH one. Indeed the HO_2 uptakes range between 10^{-3} and 10^{-1} compared to 10^{-3} to 2 (meaning that secondary process happens) for OH.

Concerning the uptake of RO_2 radicals, it is worthy of note that only few values are available in the literature (Table 7). Therefore experimental determinations are strongly desirable to assess whether RO_2 uptake could act as an important sink of radicals in marine and forested areas.

Table 4: Uptake values for inorganic particles and surfaces[43,44,56,58,60,61,63,67,68,94,96–100]

Type of surfaces	Uptake coefficients		$[RO_x]$	T	Reference
	OH	**HO_2**	(10^9 cm^{-3})	(K)	
Inorganic Particles					
H_2SO_4 (55% wt)		<0.01	25-50	295	Thornton et al. 2005
$(NH_4)_2SO_4$		<0.01 (wet)	25-50	295	Thornton et al. 2005
		<0.004 (dry); 0.003-0.01 (wet)	0.1 - 1	Room	George et al. 2013
		0.04-0.05 (dry); 0.11-0.19 (wet)	<0.1	296	Taketani et al. 2008
NaCl		<0.01 (dry); 0.09-0.11 (wet)	<0.1	296	Taketani et al. 2008
		<0.004 (dry); 0.016-0.01 (wet)	0.1 - 1	Room	George et al. 2013
KCl		0.02 (dry); 0.09-0.11 (wet)	<0.1	296	Taketani et al. 2009
Synthetic sea salt		0.07-0.13 (wet)	<0.1	296	Taketani et al. 2009
Natural sea salt		0.10-0.11 (wet)	<0.1	296	Taketani et al. 2009
NH_4NO_3		0.005±0.002	0.1 - 1	Room	George et al. 2013
Cu(II)-doped $(NH_4)_2SO_4$		0.4±0.3	0.1 - 1	Room	George et al. 2013
Arizona test dust		0.018-0.031	0.3	Room	Matthews et al. 2014
Forsterite		0.004	1.6	Room	James et al. 2017
Olivine		0.069	1.6	Room	James et al. 2017
Fayalite		0.073	1.6	Room	James et al. 2017
TiO_2		0.021 - 0.037	1.6	Room	Moon et al. 2018
Macroscopic inorganic surfaces					
Water ice	0.03±0.02	0.025±0.005 (223 K)	0.3-50	205-230	Cooper et al. 1996
Water	0.0035	>0.01	50-300	275	Hanson et al. 1992
H_2SO_4 (28% wt)	>0.08	>0.05	50-300	249	Hanson et al. 1992
$(NH_4)HSO_4$ & $(NH_4)_2SO_4$	<0.03 (dry)		0.3-50	296	Cooper et al. 1996
NH_4NO_3		$5.4x10^{-5}exp[(1540±200)/T]$	500		Remorov et al. 2002
NaCl		$5.7x10^{-5}exp[(1560±140)/T]$	40-500	243-300	Remorov et al. 2002
		$2.2x10^{-8}exp[(3340±180)/T]$	200-900	240-310	Loukhovitskaya et al. 2009
	0.0046±0.0007 (dry)		≈400	Room	Park et al. 2008
NaBr		$1.2x10^{-8}exp[(3570±180)/T]$	200-900	240-330	Loukhovitskaya et al. 2009
KCl	0.0055±0.0011 (dry)		≈400	Room	Park et al. 2008
Na2SO4	0.0035±0.0004 (dry)		≈400	Room	Park et al. 2008
$MgCl_2$	0.0061±0.0012 (dry)		≈400	Room	Park et al. 2008
$MgCl_2.6H_2O$		$3.8x10^{-5}exp[(1710±60)/T]$	200-900	240-240	Loukhovitskaya et al. 2009
$CaCl_2$	0.0039±0.0004 (dry)		≈400	Room	Park et al. 2008
Synthetic sea salt	0.0035±0.0004 (dry)		≈400	Room	Park et al. 2008
		$3.1x10^{-9}exp[(3990±200)/T]$	200-900	240-310	Loukhovitskaya et al. 2009
Al_2O_3	0.11-0.44		0.1	Room	Bertram et al. 2001
	0.045±0.005 (dry)		≈400	Room	Park et al. 2008
SiO_2	0.032±0.007 (dry)		≈400	Room	Park et al. 2008
Arizona test dust	$1.2/(1+RH^{0.36})$		400-5200	275-320	Bedjanian et al. 2013
		$1.2/(18.7+RH^{1.1})$	350-3300	275-320	Bedjanian et al. 2013

Table 5: Uptake values for organic particles and surfaces[51,52,54,66,99–106]

Type of surfaces	Uptake coefficients		$[RO_x]$	T	Reference
	OH	**HO_2**	($10^9 cm^{-3}$)	(K)	
Organic particles					
Levoglucosan		<0.01-0.13	<0.1	296	Taketani et al. 2010
Pure Palmitic acid	0.8-1		15-30		McNeill et al. 2009
Coated Palmitic acid	0.05-0.3		15-30		McNeill et al. 2009
n-alkanes, Hopanes, Steranes	1.2-9		0.01-0.04		Lambe et al. 2009
Squalene	0.51		0.1-0.7	298	Che et al. 2009
	0.3		1	308	Smith et al. 2009
		<0.004	1	Room	Lakey et al. 2015
(2-ethylhexyl) sebacate	2		up to 3		Hearn et al. 2006
	1.3			297	George et al. 2007
n-hexacosane	1.04		0.4-0.8		Lambe et al. 2007
Glutaric acid		<0.004-0.006	1	Room	Lakey et al. 2015
		0.07-0.15	0.1	Room	Taketani et al. 2013
Glyoxal		0.003-0.008	1	Room	Lakey et al. 2015
Humic acid (Acros Organics)		0.007-0.06	1	Room	Lakey et al. 2015
Humic acid (Leonardite)		0.043-0.09	1	Room	Lakey et al. 2015
Malonic acid		<0.004	1	Room	Lakey et al. 2015
Oleic acid		<0.004	1	Room	Lakey et al. 2015
Stearic acid		<0.004	1	Room	Lakey et al. 2015
Cu(II)-doped sucrose		0.012-0.2	1	Room	Lakey et al. 2016b
Succinic acid		0.07-0.18	0.1	Room	Taketani et al. 2013
Pimelic acid		0.06-0.13	0.1	Room	Taketani et al. 2013
Adipic acid		0.02-0.06	0.1	Room	Taketani et al. 2013
Macroscopic organic surfaces					
Halocarbon wax	0.0006		0.1	Room	Bertram et al. 2001
Paraffin wax	0.16-1		0.1	Room	Bertram et al. 2001
	0.03-1 (dry)		≈400	Room	Park et al. 2008
Stearic acid / Palmitic acid	0.14-1		0.1	Room	Bertram et al. 2001
Glutaric acid	0.03-1 (dry)		≈400	Room	Park et al. 2008
Pyrene	0.15-1		0.1	Room	Bertram et al. 2001
	0.03-1 (dry)		≈400	Room	Park et al. 2008
CH_3 terminated monolayer	0.14-1		0.1	Room	Bertram et al. 2001
Vinyl terminated monolayer	0.25-1		0.1	Room	Bertram et al. 2001

Table 6: Uptake values for mixed inorganic and organic particles and soot macroscopic surfaces.[53,55,99,107]

Type of surfaces	Uptake coefficients		$[RO_x]$	T	Reference
	OH	**HO_2**	($10^9 cm^{-3}$)	(K)	
Mixed organic and inorganic particles					
Cu(II)-doped $(NH_4)_2SO_4$ / 1,2-diaminomethane (10:1 org/Cu)		0.24	1	293	Lakey et al. 2016
Cu(II)-doped $(NH_4)_2SO_4$ / 1,2-diaminomethane (2:1 org/Cu)		0.32	1	293	Lakey et al. 2016
Cu(II)-doped $(NH_4)_2SO_4$ / citric acid (10:1 org/Cu)		0.31	1	293	Lakey et al. 2016
Cu(II)-doped $(NH_4)_2SO_4$ / citric acid (2:1 org/Cu)		0.17	1	293	Lakey et al. 2016
Cu(II)-doped $(NH_4)_2SO_4$ / malonic acid (10:1 org/Cu)		0.28	1	293	Lakey et al. 2016
Cu(II)-doped $(NH_4)_2SO_4$ / malonic acid (2:1 org/Cu)		0.32	1	293	Lakey et al. 2016
Cu(II)-doped $(NH_4)_2SO_4$ / oxalic acid (10:1 org/Cu)		0.003	1	293	Lakey et al. 2016
Cu(II)-doped $(NH_4)_2SO_4$ / oxalic acid (2:1 org/Cu)		0.17	1	293	Lakey et al. 2016
Cu(II)-doped $(NH_4)_2SO_4$ / tartronic acid (10:1 org/Cu)		0.19	1	293	Lakey et al. 2016
Cu(II)-doped $(NH_4)_2SO_4$ / tartronic acid (2:1 org/Cu)		0.24	1	293	Lakey et al. 2016
Soot					
Soot (methane flame)	0.5-1		0.1	Room	Bertram et al. 2001
Soot (toluene flame)		0.075±0.015	130-2000	240-350	Bedjanian et al. 2005
Soot (kerosene flame)	0.19±0.03		340-2500	290	Bedjanian et al. 2010
		0.075±0.015	130-2000	240-350	Bedjanian et al. 2005

Table 7: RO_2 uptake values for inorganic and organic macroscopic surfaces.[108]

Type of surfaces	Uptake coefficients	$[RO_x]$	T	Reference
	RO_2	($10^9 cm^{-3}$)	(K)	
$CH_3C(O)O_2$ on water	0.0043±0.0024	≤100	271-277	Villalta et al. 1996
$CH_3C(O)O_2$ on water	0.0041±0.0023	≤100	275	Villalta et al. 1996
$CH_3C(O)O_2$ on Ascorbic acid 0.18M	0.0058±0.0035	≤100	275	Villalta et al. 1996
$CH_3C(O)O_2$ on 34 wt% H_2SO_4	0.0027±0.0015	≤100	246	Villalta et al. 1996
$CH_3C(O)O_2$ on 51 wt% H_2SO_4	0.0009±0.0005	≤100	273	Villalta et al. 1996
$CH_3C(O)O_2$ on 71 wt% H_2SO_4	0.0014±0.0007	≤100	298	Villalta et al. 1996

III Aerosol simulations at the molecular level

Laboratory experiments only provide a macroscopic view of the uptake process, which does not allow deconvolving the different elementary steps discussed in chapter 1 section II.1. The simulation methods can fill this gap by modelling the uptake process at the molecular level.

During the last decade, the development of computation technologies as well as the increasing performance of simulation programs has made accessible the study of more and more complex systems in various fields of research (biochemistry, materials, etc.). Indeed, simulations can provide time-resolved thermodynamical and kinetic data, as well as spectra of molecules (IR spectra, etc.) when experiments are not doable due to technical limitations, hazardousness or high cost. They can be classified in two main types, depending on the use of a classical (molecular dynamics - MD) or a quantum (quantum mechanics - QM) description of the system interactions.

III.1 Molecular dynamics (MD) studies

MD is a useful tool to provide data which are difficult to determine experimentally. For example, a study made by Tong *et al.* in 2004 was performed using both MD and QM methods to determine thermodynamical data such as liquid vapor pressure, enthalpy of vaporization, heats of sublimation, which are required to determine the gas – particle partitioning of organic compounds.[109] It can also provide models of some atmospheric processes such as surface activity and surface tension of cloud condensation nuclei (CCN),[110] stability of clusters,[111] particle nucleation,[112] reactivity at the aerosol surface (combined with some QM calculations).[113,114] There are also some computations of the free energy of solvation which is related to Henry's law constant.[18] MD gives access to the structure, energetics (e.g. free energy profile, surface tension, and surface potential) and dynamics (e.g. gas/surface collisions and bulk liquid/surface exchange).

As described in the objective section later (section IV), one of the aims of this PhD work was to create a model mimicking as close as possible the laboratory experiments performed on glutaric acid aerosols. In the following, we therefore review theoretical studies focusing on organic acid – water aerosols.[115–119]

Recent studies (Vardanega *et al.* 2014;[118] Radola *et al.* 2015[119]) have shown an important impact of temperature and relative humidity on the behavior of organic aerosols made of carboxylic monoacids (formic, acetic and propionic acids). Starting from an organic aerosol of 120 carboxylic acid molecules (described with the OPLS/AA Force field (FF)), different amounts of water molecules (TIP5P FF) have been added. The impact of water has been investigated for a wide range of temperatures from 100 to 250 K (Figure 20), not entirely relevant for atmospheric (tropospheric) conditions. Their first conclusions based on radial distribution calculations were: (i) at higher temperature (200 K) and low water content (50 mole% of water), there is a partial mixing at the surface of the organic aerosol; (ii) at moderate temperature (150 K) a partial deliquescence is obtained; (iii) some water islands can also be observed at the surface of the organic aerosols at low temperature (100 K).

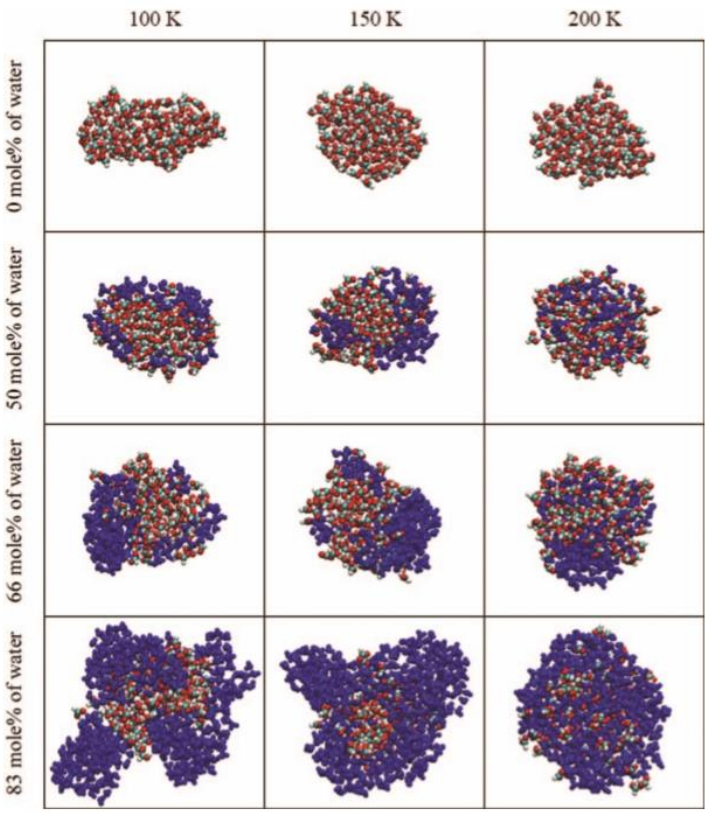

Figure 20: Equilibrium snapshots of formic acid aggregates at 100, 150 and 200 K (left, middle, and right) and for 0, 50, 66, and 83 mol. % water concentrations (from top to bottom) (Vardanega et al. 2014).[118]

Another study carried out by Darvas *et al.*[116,117] on dicarboxylic acids (malonic and oxalic acids) has also shown that pressure (in the range 0.01-1 bar) has no strong influence on the mixing state of the aggregates.

Ma *et al.*[115] used an inverted micelle model as the starting point to generate an aerosol by adding a layer of dicarboxylic acids (from C3 to C9 and C9-branched) on a droplet of water (described with the SPC/E model; see chapter 2 section II.1.2). At the end of the equilibration run, only malonic acid (C3) was dissolved into the water core. The other acids formed two separate phases: a core of water with an acid shell deposited on it. Unfortunately, no comparison with experimental data was done. Furthermore, no simulation have considered the co-condensation of water and organic acids.

Concerning the uptake theory, many studies reporting mass accommodation coefficients were done onto planar surfaces or slabs (mainly aqueous interfaces).[120–124] The surface and bulk accommodation coefficients were both calculated with equations 14 and 15, respectively, where p_k (defined by equation 16) is a factor used to correct for the limited simulation time:

$$\alpha_{m,s} = \frac{n_{absorb} + n_{adsorb} + n_{desorb}}{n_{total}} \quad (14)$$

$$\alpha_{m,b} = \frac{n_{absorb} + p_k n_{adsorb}}{n_{total}} \quad (15)$$

$$p_k = \frac{n_{absorb}}{n_{absorb} + n_{desorb}} \quad (16)$$

Mass accommodation coefficients are often close to 1 for aqueous aerosols. Morita *et al.* (2004)[122] created a slab (Figure 21.A) of 1000 water molecules and calculated 250 trajectories. On each trajectory, they added two HO_2 radicals with a velocity oriented towards the two surfaces of the slab at time 0 and 10 ps of the simulation, respectively. Using these 500 HO_2 trajectories, the authors computed a probability that the molecule accommodates on the slab close to unity but calculated values were in conflict with experimental data. Indeed, the value exceed the values of $\alpha = 0.2$ found by Mozurkewich et al.[62] and $\alpha = 0.01$ found by Hanson et al[43]. The discrepancy may come from the decomposition (process) of the uptake coefficient found by experimentation. But most probably from the facts that the MD uptake simulation was done on too few molecules and with not enough time.[125]

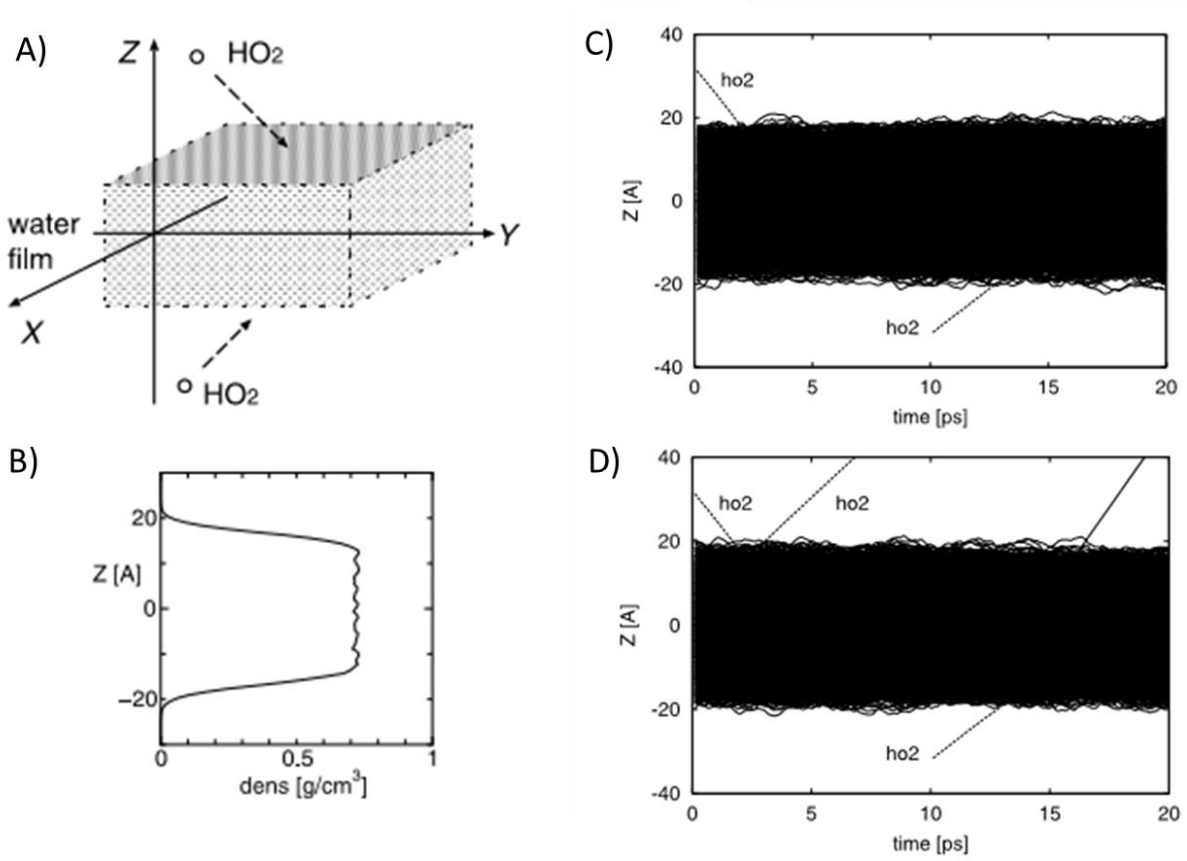

Figure 21: A) Schematic of MD scattering simulation; B) Calculated density profile of the liquid film of water (Motsuoka –Clementi-Yoshimine model of water); C and D) Two examples of MD scattering trajectories during 20ps. The solid lines denote the Z coordinates of water molecules, and the dashed lines with the label "ho2" denote two HO_2 radicals scattering onto the liquid water surface. Note that the solid region in -20Å<Z<20Å corresponds to the slab of water.[122]

Some studies were also carried out on desorption and absorption rate coefficients of a surface-active solute molecule. Surface-active solute molecules have a lower free energy when the molecules are adsorbed at the interface than in the gas- or bulk-phases. To compute those values, the transition state theory has to be used to save computational time.[125]

In the work of Julin *et al.*,[124] the mass accommodation coefficient of water vapor on a slab and a droplet of water was computed using MD at different temperatures. It was found that the droplet size has a small effect on mass accommodation. Temperature effects were shown to trigger off smaller mass accommodation coefficient. With MD simulations, the authors were

also able to provide an average desorption lifetime (few ps) which is a parameter in the kinetic flux model of uptake.

III.2 Quantum Mechanical studies

Some Density Functional Theory (DFT; see chapter 2 section II.2.2.5) calculations have been carried out by Xu and Zhang[126] on dicarboxylic acids (oxalic, malonic, maleic, phthalic and succinic acids). By using the B3LYP/6-311++G(2d,2) and the PW91PW91/6-311++G(3df,3pd) functionals, the authors have computed the free energies of formation of heterodimers and mixed clusters of dicarboxylic acids that can serve as common atmospheric aerosol nucleation precursors (sulfuric acid, ammonia, water). The obtained energies suggest that dicarboxylic acids play a role on the aerosol nucleation process.

Another simulation on dicarboxylic acid clusters was carried out by Hou *et al.*[127] but on singly deprotonated homodimer complexes (Figure 22). They used the B3LYP functional with some Dunning basis sets corrected by a single point energy calculation M06-2X (M06-2X/maug-cc-pVT(+d)Z //B3LYP/aug-cc-pVDZ). The simulations were compared with some negative ion photoelectron spectroscopy experiments. This work confirmed that dicarboxylic acids of the homodimers interact with strong hydrogen bonds which is in agreement with the experiments. The complexes are also very stable and thermodynamically favorable to form. Optimized structures were also given at B3LYP/aug-cc-pVDZ for the diacid monomer going from C_2 to C_{14} (Figure 22).

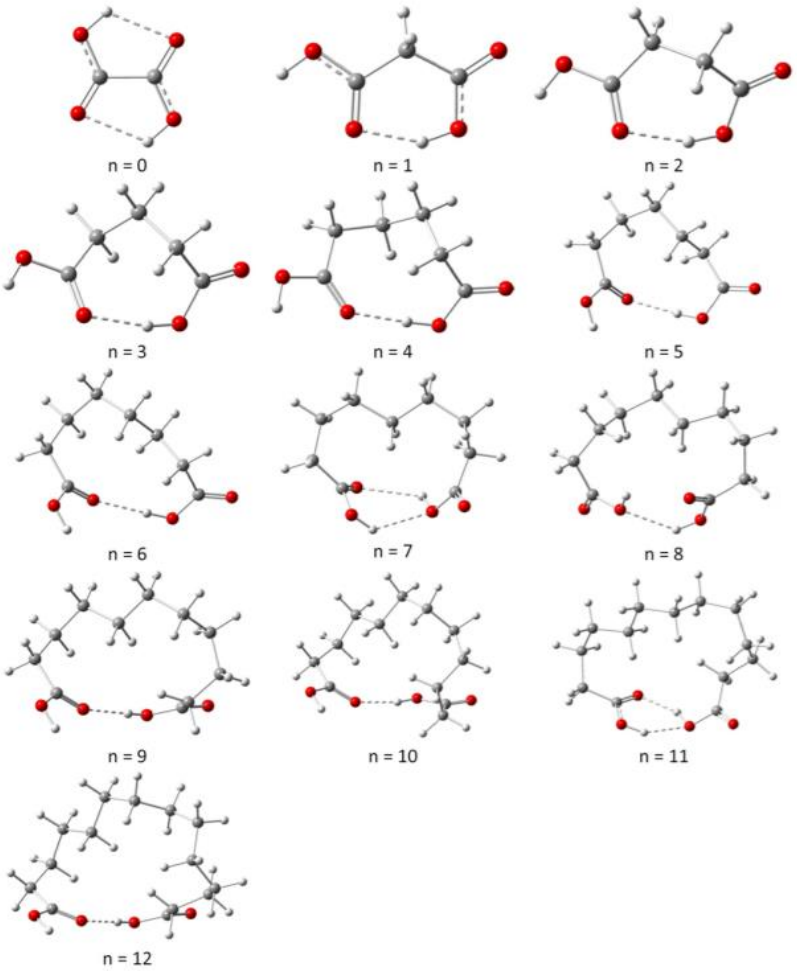

Figure 22: Optimized B3LYP/aug-cc-pVDZ dicarboxylic acid H_2DC_n (n = 0-12) structures.[127]

III.3 Studies investigating the reactivity of HO_2

Only a few studies have been carried out on HO_2 and its reactivity. Aloisio and Francisco (1997) performed an *ab initio* study on the formation of the $HO_2.H_2O$ complex. The geometry was optimized by UMP2 and B3LYP methods with various Pople basis sets (6-31G(d), 6-31++G(d), 6-311++G(d), 6-311++G(d,p),6-311++G(2d,2p), 6-311++G(2df,2p), and 6-311++G(3df,3pd)) and then the single point energy was refined at the CCSD(T) level. Frequencies and harmonic vibrational Zero Point Energies (ZPE) were computed at MP2 and B3LYP levels. The enthalpy of formation have been found to be equal to -7.6 kcal mol^{-1} and the entropy to -25.5 kcal $mol^{-1}.K^{-1}$. The equilibrium constant has been computed using partition functions (Figure 23), which could be used to quantify the proportion of complex formed in the atmosphere based on the temperature, relative humidity and HO_2 concentration.[128] The same kind of study has been done on RO_2- water complexes by Clark *et al.* in 2008.[129]

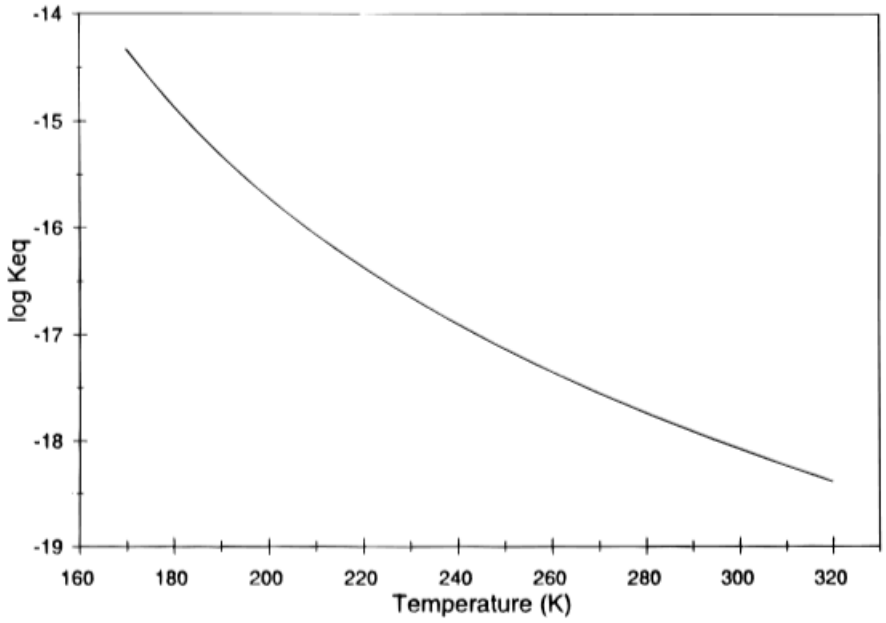

Figure 23: $HO_2.H_2O$ equilibrium constant as a function of temperature. K_{eq} is in units of cm^3 $molecule^{-1}$ taken from Aloisio and Francisco.[128]

Tachikawa and Abe[130] have also studied the stability and geometry of HO_2 complexed with one or two water molecules using QCISD and CCSD methods with a 6-311++G(d,p) basis set. Tachikawa[131] also studied the reactivity described by reaction (R41):

$$HO_2(H_2O)_n \ (n=2 \text{ or } 4) \rightarrow H_2O_2.OH(H_2O)_{n-1} \qquad \text{(R41)}$$

They showed that the H_2O_2 molecule can be formed by the electron capture of HO_2. The process may happen on ice as cosmic rays can generate an excess electron, thus this effect could be significant in the stratosphere. The reaction model is illustrated in Figure 24, and in this case, HO_2 would approach with water molecules as a proton acceptor.

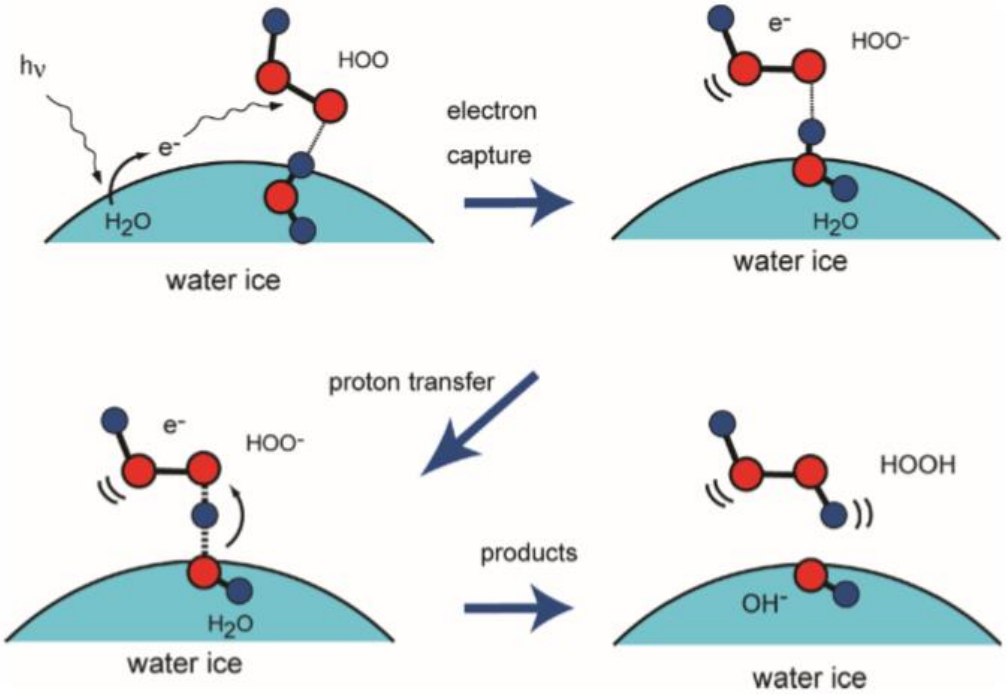

Figure 24: Reaction model of electron capture of HOO on ice taken from Tachikawa .[131]

Torrent-Sucarrat *et al.* [132] studied HO_2 adsorption and deprotonation on clusters of water $(H_2O)_{20}$ and $(H_2O)_{21}$ using B3LYP/6-311+G(d) for the geometry and MP2/6-311+G(2df,2p) for energies. They found that the deprotonation of HO_2 induced by the water molecule goes first through a hydrogen transfer between the water molecules.[132]

Martins-Costa *et al.* (2012) studied the behavior of the radical with or without its deprotonation. They used MD combined with a quantum/classical force field (FF). The solute was treated by QM (B3LYP/6-311+G* or B3LYP/aug-cc-pVTZ) while the solvent was treated using a TIP3P model (FF model). The radical was initially placed at the air/water interface. They observed that, while HO_2 stays at the interface, O_2^- is characterized by a very fast migration into the bulk as emphasized by its density profile (Figure 25).[133]

Several other reactions have been studied such as HO_2 + OH,[134,135] HO_2 self-reaction[136,137] and HO_2 + RO_2.[136,138] For example, Zhang *et al.* studied the two last ones using a CCSD(T)/6-311++G(3d,2p)//B3LYP/6-311G(2d,2p) level of theory with or without a single water molecule. While the absence of water in the CH_3O_2 + HO_2 reaction leads preferentially to the formation of $^3O_2$, the presence of water leads to the formation of O_3. However, this is not the case for the HO_2 self-reaction which leads to the formation of $^3O_2$ and H_2O_2 in both cases. An increase of the rate of HO_2 self-reaction has been observed in the presence of water but not in the case of HO_2 + CH_3O_2.[136]

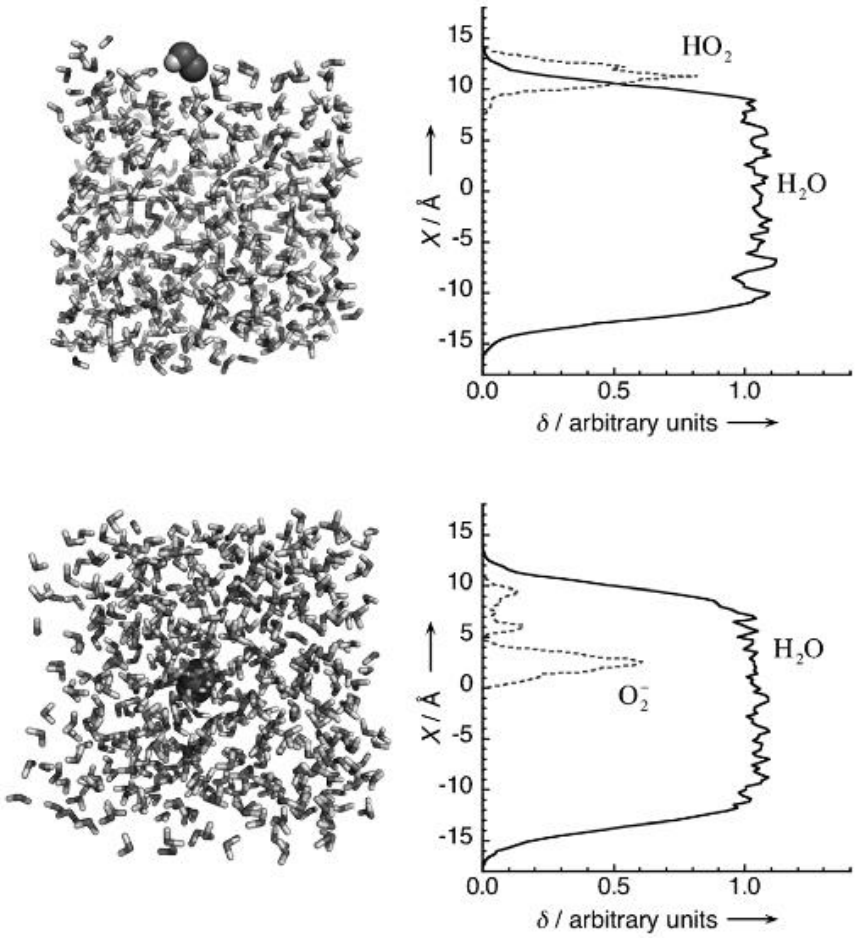

Figure 25: Unconstrained 50 ps MD simulations with the radicals initially placed at the air-water interface. Left: Snapshot at the end of the simulation showing HO_2 at the air-water interface (upper) and O_2^- in bulk water (lower). Right: Density profiles for the radicals and water (X=0 corresponds to the center of the simulation box or the water slab) taken from Martins-Costa et al.[133]

Despite those studies, there is still much to learn to improve our understanding of HO_2 and RO_2 uptake and heterogeneous reactivity at the aerosols surface. Indeed, the problem being complex in terms of variables to take into account, the impact of only a few parameters (RH, temperature, etc.) on the uptake has been investigated with both experiments and simulations. Concerning aerosol formation, some processes like the co-condensation of diacids and water, have not yet been studied. Calculations treating the reactive uptake of HO_2 on organic aerosols are still missing. The influence of the possible adsorption sites (water or organics) also needs to be investigated. The use of hybrid quantum/classical methods such as ONIOM to investigate the reactivity within or at the surface of the aerosol is a promising direction not fully explored to date.

IV Objectives and strategy

As mentioned previously, field measurements have shown that there are significant discrepancies between modeled (0-D modelling) and observed concentrations of HO_2 and RO_2 radicals in forested areas where the lifetime of peroxy radicals is long enough (low NO) to promote radical-aerosol interactions. The observed discrepancies can be due to missing reactions in the mechanisms taken into account, including the heterogeneous loss of HO_2 and RO_2 species on atmospheric aerosols. However, it is not straightforward to parameterize this process in chemical models due to uptake coefficients that are not well defined and measured. It is therefore important to better characterize this loss pathway of RO_x radicals as these species play a central role for the oxidative capacity of the atmosphere, which drives the removal and the formation of atmospheric pollutants.

While macroscopic models have been proposed to describe the uptake of trace gases on aerosols (chapter 1 section II.1), it is still difficult to study this process experimentally for radical species. The effects of ambient parameters such as temperature or relative humidity are not completely understood (chapter 1 sections II.2.2 to II.2.4), and some species such as copper and iron can promote the reactivity of HO_2 on/in the aerosol, which in turn can enhance the uptake rate. There are also some discrepancies in the literature about HO_2 uptake coefficients on organic aerosols such as glutaric acid aerosols (chapter 1 section II.2.5). In addition, little is known about the uptake process at the molecular level.

Combining laboratory experiments and simulation tools at the molecular level should allow a better characterization of some aspects of the uptake process (mass accommodation, desorption lifetime, impact of water, kinetic data, etc.). For instance, the aggregation of water on organic aerosols, which cannot be investigated experimentally, has been investigated using simulation tools. However, the co-condensation of organics and water molecules has yet to be performed. Concerning the uptake of trace gases on aerosols, most studies have determined the mass accommodation coefficient on a liquid water slab and only a few studies have modeled a more realistic aerosol particle.

The main objective of this Ph.D. work is to improve our understanding of the peroxy radical uptake on organic aerosols. It consisted in (i) developing an aerosol flow tube for measuring uptake coefficients of peroxy radicals on organic aerosols, (ii) measuring the uptake coefficient of HO_2 (and one RO_2) on organic aerosols, and (iii) simulating the uptake of HO_2 at the molecular level on model organic aerosols.

More specifically, we studied the uptake coefficient of HO_2 on glutaric acid ($C_5H_8O_4$) which is an organic diacid. Glutaric acid has a practical aspect as it is solid at ambient temperature, soluble in water and is not really hazardous. It will allow easy handling for the experiment. But it has also a number of atoms which is small enough to ensure a small enough computational cost. In the atmosphere, glutaric acid is produced by the oxidation of cyclohexene by ozone. It is detected with concentrations around 2 mol/m^3 in urban/continental environment and about 1.5 mol/m^3 in remote marine environment[7] This acid has often been observed in urban and suburban environments as mentioned in Mirivel *et al.* in 2011 or Crenn *et al.* in 2017.[139,140]

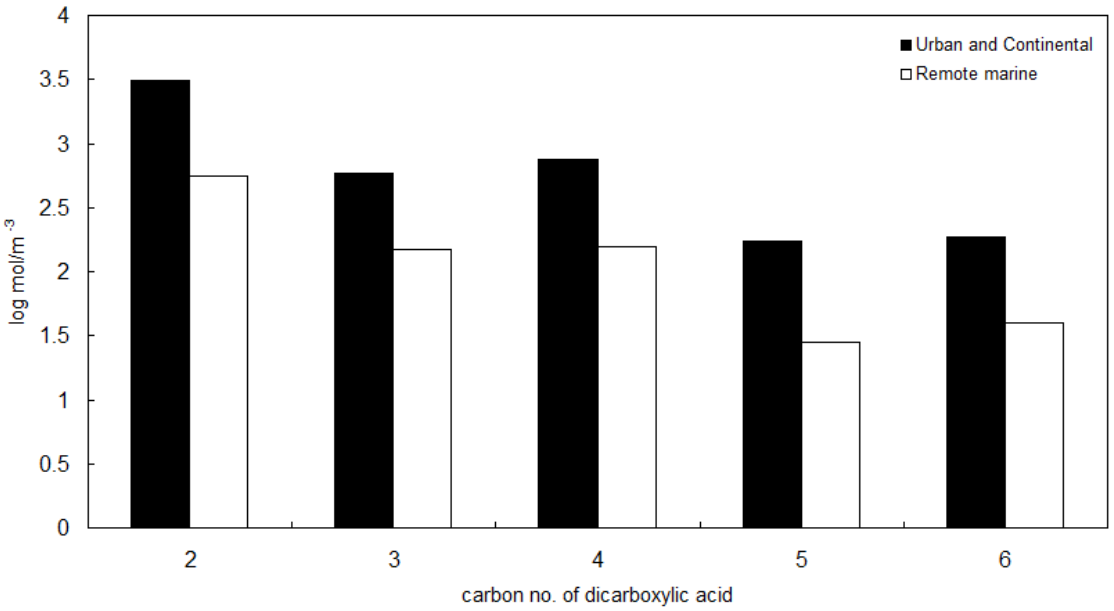

Figure 26: Comparison of dicarboxylic acids distribution in urban/continental and remote marine areas[7]

As discussed previously in chapter 1 section II.2.2, Discrepancies are observed between the measurements of two groups, concerning the HO_2 uptake coefficient onto glutaric acid.

The Ph.D. was divided into two parts, an experimental part where a new laboratory apparatus is developed and used to measure uptake coefficients of peroxy radicals, and a theoretical part where computational tools are tested and used to investigate the molecular structure of organic aerosols and the uptake of HO_2 on these aerosols.

The experimental part consisted in:

- Designing and building an Aerosol Flow Tube (AFT), combined with two aerosol generation units, and a source of peroxy radicals
- Coupling the AFT to a custom-made peroxy radical analyzer developed by Ahmad LAHIB during his Ph.D. at IMT Lille Douai (2016-2019)
- Characterizing the experimental setup, including aerosol generation, radical production, wall losses for aerosols and radicals, and the contact time between aerosols and radicals in the AFT
- Measuring the uptake of HO_2 on glutaric acid aerosols and copper-doped aerosols to validate the setup and investigating the disagreement reported in Table 2.
- Measuring the uptake of isoprene-based RO_2 radicals on glutaric acid aerosols.

The theoretical part consisted in:

- Validating the force field that describes properly the HO_2-aerosol system, using quantum mechanical computations. HO_2 parameters proposed by Vàcha et al.[141] and Chalmet and Ruiz Lopez.[142] were used for this study.
- Generating and characterizing different sizes of pure glutaric acid aerosols and mixed water/acid aerosols using classical molecular dynamics (MD)
- Computing the mass accommodation coefficient of HO_2 from MD trajectories
- Studying the reactivity of HO_2 on/in the aerosol using the ONIOM method[143]

Finally, experiments and theory have been compared with emphasis of the differences in terms of time and size scales.

The following chapter will introduce the various methods used during this PhD research project.

CHAPTER 2: METHODOLOGY

The experimental apparatus dedicated to uptake measurements has been set up during this thesis in the Science de l'Atmosphère et Génie de l'Environnement (SAGE) department of IMT Lille Douai. It is composed of an Aerosol Flow Tube (AFT), a system for generating HO_2 (and RO_2) radicals, two aerosol generators, and several analyzers for measuring peroxy radicals and aerosol concentrations and size. In this chapter, a description of every part of the setup will be given.

The simulations at the molecular level have been performed in the Physique des Lasers Atomes et Molécules (PhLAM) laboratory at the University of Lille. Classical molecular dynamics trajectories have been performed to calculate uptake coefficients on a model aerosol with different amounts of water (water added either by co-condensation or on a pure organic aerosol). Quantum calculations have also been performed to characterize the reactivity of HO_2 with the organic molecules (for a reduced system). Finally, a hybrid QM/MM (ONIOM) method has been used to determine the reactivity of HO_2 at the aerosol surface. The second part of this chapter will introduce the different theoretical methods that have been used.

I Experimental apparatus for measuring uptake coefficients

To measure the HO_2 uptake coefficient, an experimental apparatus has been developed. As mentioned above, this system is composed of an Aerosol Flow Tube (AFT), two generators for particles and one for RO_X radicals, and measurement systems to monitor RO_X and aerosols. In this section, the aerosol flow tube, the measurement tools as well as the HO_2 and aerosol generation system will be briefly introduced. Further details concerning there characterization are provided in chapter 3.

I.1 Aerosol Flow Tube (AFT) design

The aerosol flow tube (Figure 27) has been custom-made in Pyrex based on two laboratory apparatus published by other groups.[58,68] Its length L_R is about 1.3 m with an external diameter $\Theta_{Rea,ext}$ of 70 mm and an internal diameter $\Theta_{Rea,int}$ of 60 mm. This flow tube has been equipped with an injector in its center, whose length L_I is 1.5 m and whose diameter Θ_{Inj} is 12.7 mm. The generation of RO_x radicals is performed at the top of the injector through the photolysis of water-vapor in a quartz cell (length L_Q of 20 cm and diameter Θ_{Qua} of 19.05 mm) using a mercury pen-lamp (UVP PenRay® Lamp (11SC-1) analytikjena). The injection system for aerosols is at the top of the flow tube and consists of four 6.35 mm inlets. A Pyrex disk with multiples holes (3.18 mm) placed at a distance L_C of 1.25 m of the outlets will help induce a flatter front for the air flow and will speed up the development of a laminar regime. This should help avoiding aerosol coagulation from turbulent mixing. Finally, two sets of two outlets (one set of 12.7 mm–diameter tubes and one set of 6.35 mm-diameter tubes) have been placed at the bottom of the flow tube at 90° of each other to connect the analytical instruments (PERCA and SMPS).

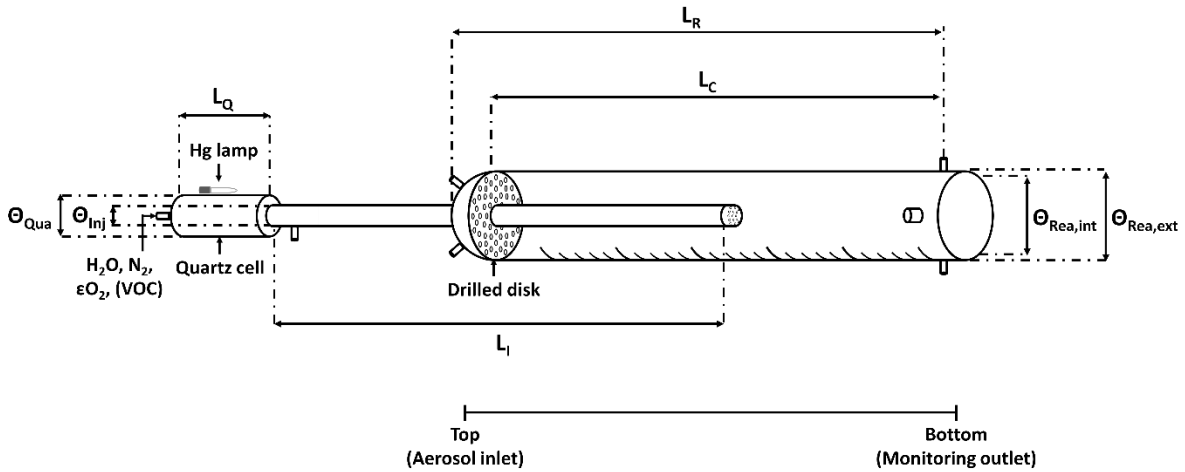

Figure 27: Schematic of the Aerosol Flow tube constructed in the SAGE department.

The aerosols are introduced through the top of the reactor and peroxy radicals are directly generated in the injector. The measurement apparatus for RO_x and aerosols sample at the end of the AFT. The injector can be translated in the reactor in order to increase or decrease the contact time between peroxy radicals and aerosols. This contact time depends on the distance between the tip of the injector and the RO_x sampling point and the flow velocity in the reactor.

A schematic and a picture of the whole setup are shown in Figure 28 and Figure 29. Total flow rates ranging from 4 to 10 LPM (Liter Per Minute) were tested to operate the aerosol flow tube, leading to residence times ranging from 55 down to 22 seconds, respectively. The flow rate through the injector where peroxy radicals are produced, is set at 1.3 LPM. The flow rates through the nucleation system and the nebulization system (see section I.2) are set at 0.5 and 1 LPM, respectively, when used to generate organic aerosols. An additional dilution flow rate of dry zero air is adjusted depending on the aerosol generation system used (see section I.2). At the outlet, the PERCA system samples at 1.3 LPM, the SMPS at 0.6 LPM and the hygrometer at 0.5 LPM. The excess of air is sent to an exhaust line fixed at the end of the AFT. The diameter of the exhaust line is the same as the AFT to avoid turbulences and gas recirculation in the measurement zone.

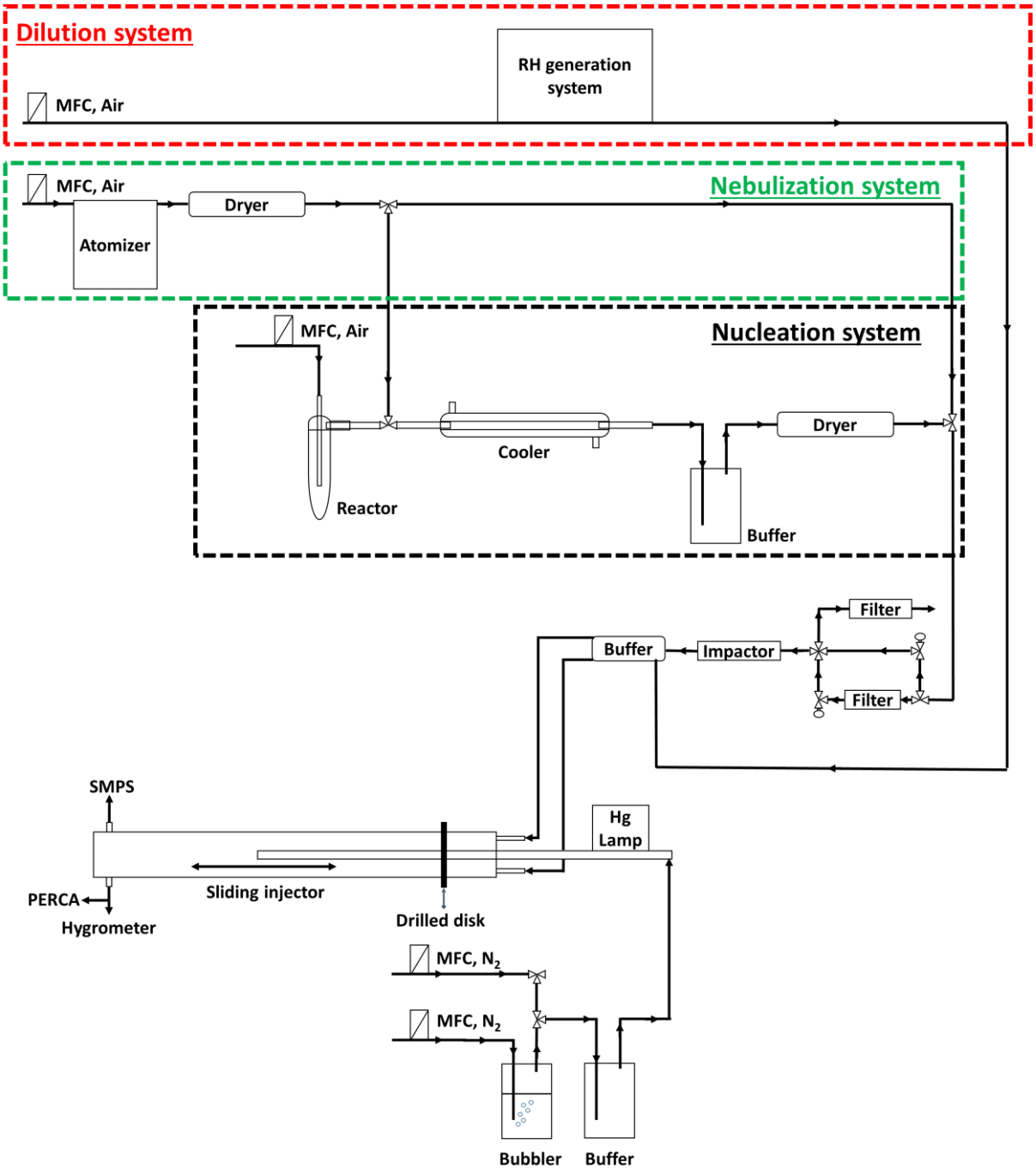

Figure 28: Schematic of the whole AFT setup (MFC: Mass flow controller). The impactor used has a 0.071 cm diameter nozzle.

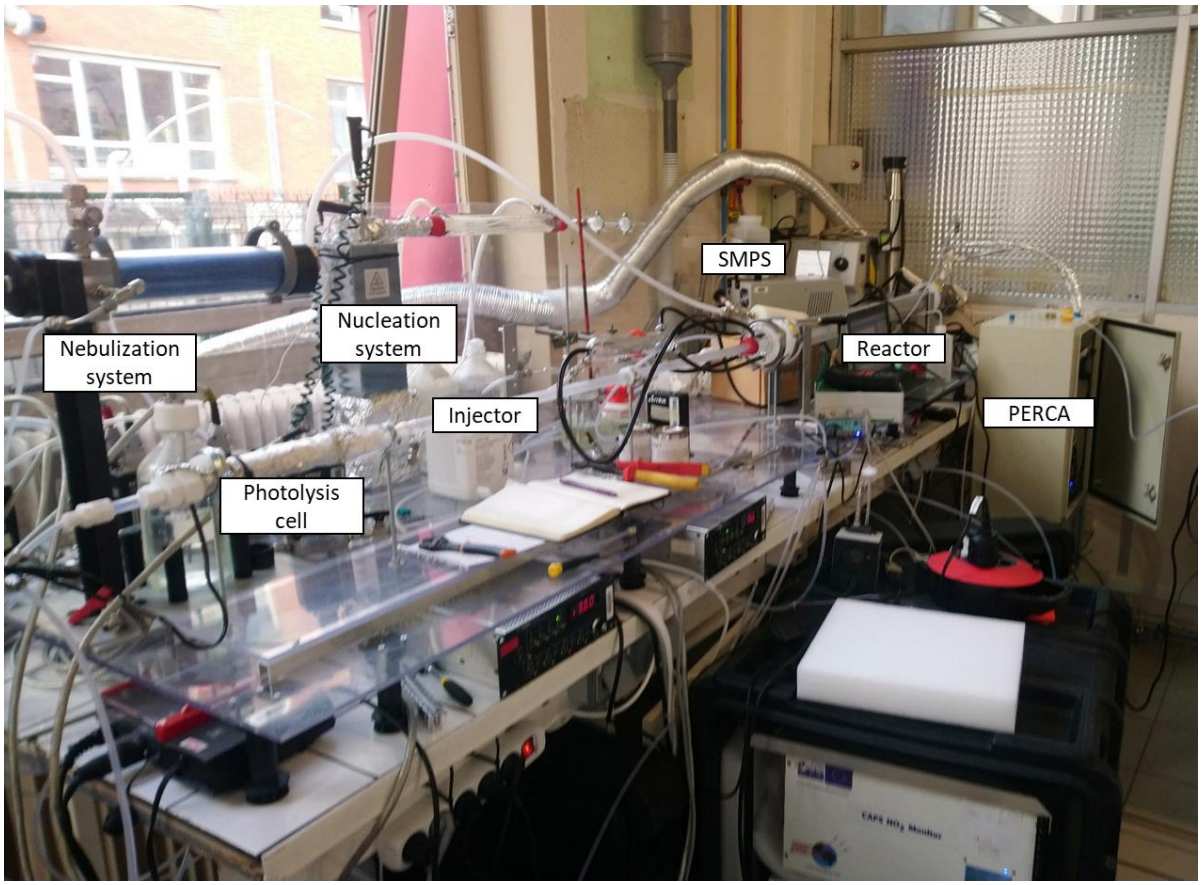

Figure 29: Picture of the AFT setup.

Within the reactor, three kinds of flow regime can be developed:

- A laminar flow operating at a Reynolds number (Re) lower than 2000
- A turbulent flow operating at Re > 4000
- A transition flow operating at Re comprised between 2000 and 4000

The Reynolds number Re can be computed by the following equation[144]:

$$\mathrm{Re} = \frac{\rho v d}{\mu} \qquad 17$$

where ρ is the fluid density (kg m^{-3}), v the fluid velocity (m s^{-1}), d the diameter of the tube (m), and μ the fluid viscosity (kg m^{-1} s^{-1}). For air, the fluid density and viscosity at 300 K are equal to 1.184 kg m^{-3} and 1.87×10^{-5} kg m^{-1} s^{-1}, respectively.

A turbulent flow implies a better mixing state within the aerosol flow tube, however it tends to increase the coagulation rate of aerosols.[2] To reach a turbulent flow, the total flow rate required in our reactor would be about 179 LPM, which corresponds to a contact time of ~1 s while contact times of at least several seconds are necessary to observe an experimental uptake. Considering the issue of aerosol coagulation and the short contact time, we have decided to work under laminar flow conditions. This kind of flow induces a gradient of velocity from the centre to the wall of the tube (Figure 30).

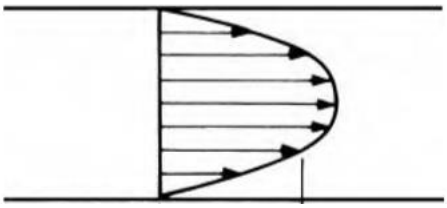

Figure 30: Schematic of the velocity gradient for laminar flow conditions.

The velocity gradient implies that the contact time is different along the radial distribution, with concentrations near the wall lower than in the center since the reaction time is longer. This phenomenon tends to form a concentration gradient which also increases if wall losses of the radical species occur. To correct this effect, Brown[145] has developed an algorithm that takes into account the wall losses as well as the diffusion of the reactive species and computes the true first order rate constant.

Mixing along the axial distribution is only due to diffusion. To compute the time needed for mixing, we can use the following equation according to Keyser[146]:

$$t = \frac{r^2}{5D_g} \qquad 18$$

where r is the flow tube radius (cm) and D_g is the gas-phase diffusion coefficient ($cm^2\ s^{-1}$) of the radical species. In the case of HO_2, according to Mozurkewich[62] (1987), $D_{g,HO2} = 0.25\ cm^2\ s^{-1}$, which leads to a mixing time of about 7 s.

I.2 Aerosol generation

Two aerosol generation systems have been built and characterized in chapter 3 section I.2. These generation systems have to fulfil some requirements like the generation of a high enough surface concentration of particles with a size of the order of the nanometer to measure the uptake coefficient. Flow rate of generation has to be of the order of a few tenths of liter per minute.

- For the first system, submicron aerosols are produced by atomizing an aqueous solution of glutaric acid (Figure 31). A diluted solution of glutaric acid is vaporized through a high-velocity jet produced by a critical orifice. The pressure at the entrance of this critical orifice controls the concentration of particles produced, however high pressure could lead to multi charged particles which could lead to detection bias. The aerosols then go through a denuder containing a dryer to reduce humidity, which implies the removal of a large fraction of the aerosol water. The amount of water removed by the dryer is shown in Table 8 and depends on how it is used. This system can provide a log normal distribution centered around 100 nm.

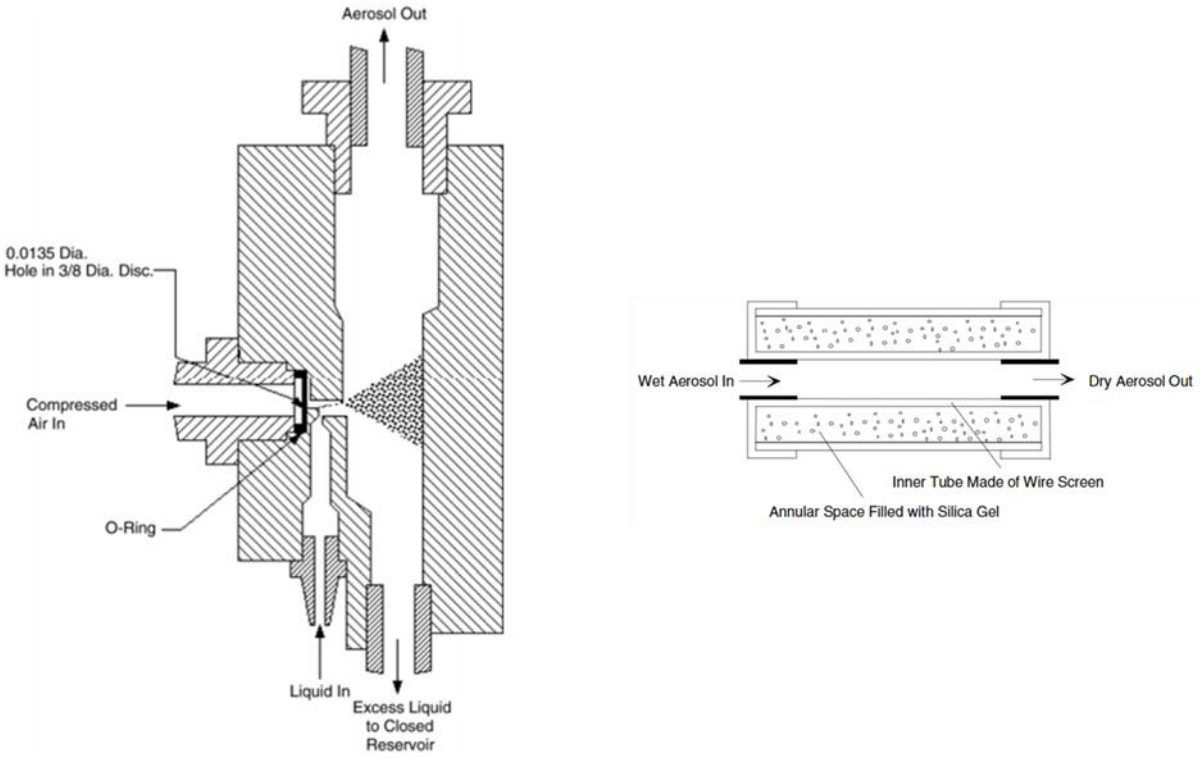

Figure 31: Schematic of the nebulizer (left) and the denuder (right).[147]

Table 8: Efficiency of the diffusion dryer.[147]

How Used	Measured Relative Humidity at Exit (%)
No diffusion dryer	60
With one Model 3062	20
With two Model 3062s (in series)	8
With one Model 3062 but after one hour of operation	28
After shaking the Model 3062 to rearrange the silica gel crystals	20

- Another way to generate submicron aerosols is to heat a solution of pure glutaric acid to produce organic vapors, which then nucleate by cooling down in a water condenser (Figure 32).[148] However, the organic compounds have to be volatile enough to vaporize without degradation. For glutaric acid, the vapor pressure is about 10^{-3} Pa at 298 K[149] and is high enough (>2.10^{-5} Pa,[150]) when its fusion point of 371 K[151] is reached. This type of setup can produce a lognormal aerosol distribution centered around a few hundred of nanometer depending on the compound used.[148]

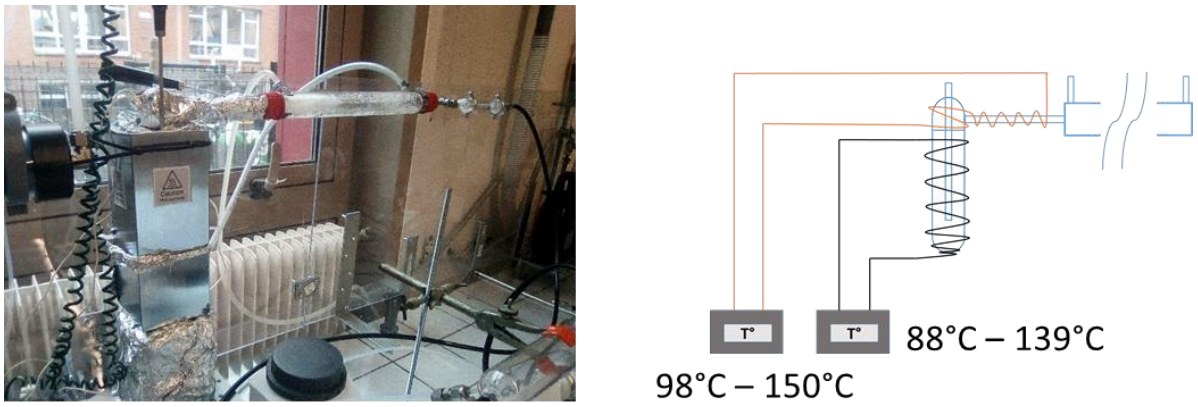

Figure 32: Picture (left) and schematic (right) of the aerosol generation setup based on the nucleation of organic vapors. Red and black lines represent the heating wires that are controlled by both temperature controller.

I.3 Peroxy radical (HO_2, RO_2) generation

HO_2 radicals are produced in the injector by the photolysis of water at 184.9 nm in a flow of N_2 (Messer 5.0) containing traces of O_2. Water is introduced in the injector by passing the N_2 flow through a water bubbler (100% Relative Humidity, RH) and by mixing it with dry N_2 to adjust RH (Figure 33). A mercury Penlamp (UVP PenRay® Lamp (11SC-1) analytikjena) emitting photons at 184.9 nm is used inside the injector to photolyze H_2O as shown in reaction (R42).

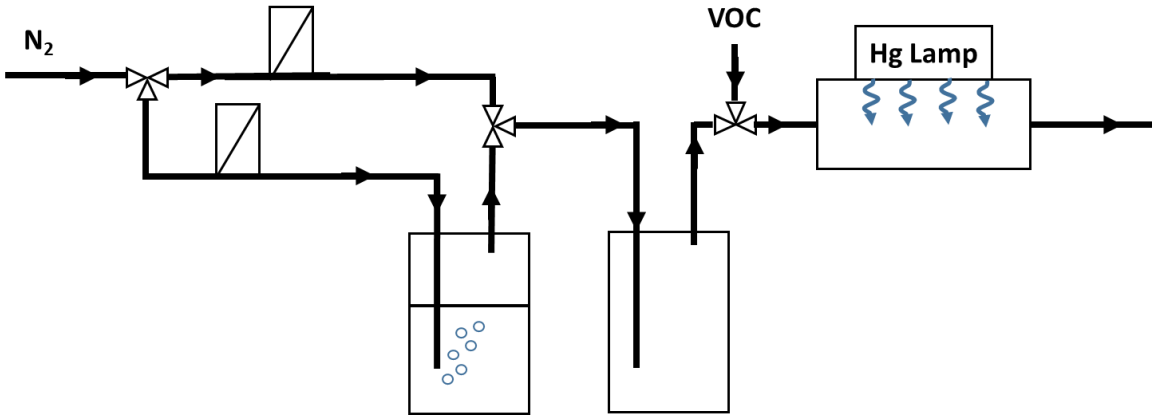

Figure 33: Schematic of the peroxy radical generation system.

H atoms produced in (R42) subsequently react with O_2 to produce HO_2 (R43).

$$H_2O + h\nu\ (185\ nm) \rightarrow OH + H \qquad (R42)$$

$$H + O_2 + M\ (N_2 \text{ or } O_2) \rightarrow HO_2 + M \qquad (R43)$$

O_2 impurities contained in the N_2 cylinder are sufficient to convert H atom into HO_2. The photolysis of O_2 at 184.9 nm can lead to the formation of a few ppb of O_3. Note that OH radicals are highly reactive with surfaces and the distance between the lamp and the injector tip is long enough to ensure that all OH radicals are lost on the injector wall and only HO_2 is exiting the injector. This system was used in previous laboratory determinations of HO_2 uptakes.[51–53,58,61,66–68]

To produce organic peroxy radicals (RO_2), specific VOCs can be added before the photolysis cell. The concentration of the VOC is adjusted to quantitatively convert 99% of the OH radicals into RO_2 through reaction (R44) in less than 2 ms. In the case of isoprene, the concentration set in the injector is about 1 ppm.

$$VOC + OH\ (+O_2) \rightarrow RO_2 \qquad (R44)$$

The peroxy radical concentration has to be sufficiently high ($>10^8$ cm^{-3}) to see a relative change by the detection system during the uptake experiment. However, the concentration has also to be low enough ($<5.10^9$ cm^{-3}) to avoid the contribution of gas-phase peroxy radical self-reactions to the observed radical decay.

I.4 Measurements of peroxy radicals - PERCA system

There are only a few methods capable of measuring low concentrations of gas-phase peroxy radicals, including the matrix isolation electron spin resonance technique[152] (MIESR), the laser-induced fluorescence technique after chemical conversion of peroxy radicals into OH[153] (LIF-FAGE), and chemical amplification techniques converting peroxy radicals into either H_2SO_4 with a detection based on chemical ionization mass spectrometry (CIMS)[154,155] or NO_2 with a detection using a suitable analyzer (PERCA, ECHAMP).[156–158]

Table 9 presents the detection limit and the integration times of the analyzers cited previously. The measured compounds are also specified.

Table 9: Specifications of different analytical tools for the quantification of peroxy radicals.

Instrument	Detection limit (ppt)	Integration time (min)	Note
LIF-FAGE	~ 0.1 [152,153]	~ 1 [152]	$HO_2 + \varepsilon \times RO_2$
CIMS	~ 0.5 [154,155]	~ 1 [154,155]	$HO_2 + RO_2$
MIESR	~ 2 [152]	~ 30 [152]	Offline method
PERCA, ECHAMP	~ 0.5 [156]	~ 1 [156]	$HO_2 + RO_2$

LIF-FAGE : Laser Induced Fluorescence – Fluorescence Assay by Gas Expansion; CIMS : Chemical Ionization Mass Spectrometry; MIESR : Matrix Isolation Electron Spin Resonance; PERCA : Peroxy Radical Chemical Amplification and ECHAMP : Ethane-based Chemical Amplification. ε account for a few percentage of the compounds.

The measurement technique chosen for this work is the Peroxy Radical Chemical Amplifier (PERCA) developed in the SAGE department as part of Marius Duncianu's postdoctoral work and Ahmad Lahib's Ph.D work (paper in review). Among these instruments, the MIESR is not suitable for the uptake measurement as the detection limit is quite high and the integration time really long. The LIF-FAGE is the most accurate one but is not able to measure the total concentration of RO_2. So, the PERCA and CIMS seem to be the most suitable instruments to measure HO_2 and RO_2 uptake.

The PERCA technique is based on converting peroxy radicals into stable NO_2 molecules through propagation chain reactions involving HO_2 and OH. This is done by sampling air from the AFT inside the PERCA reactor and by adding large concentrations of CO (10 %) and NO (6 ppm) to the sampled flow:

$$HO_2 + NO \rightarrow OH + NO_2 \quad \text{(R45)}$$

$$OH + CO \rightarrow H + CO_2 \quad \text{(R46)}$$

$$H + O_2 + M \rightarrow HO_2 + M \quad \text{(R47)}$$

The following termination steps also occur in the PERCA reactor:

$$HO_2 + NO + M \rightarrow HNO_3 + M \quad \text{(R48)}$$

$$HO_2 + \text{wall} \rightarrow \text{loss} \quad \text{(R49)}$$

$$OH + NO + M \rightarrow HONO + M \quad \text{(R50)}$$

$$RO_2 + NO \rightarrow RO + NO_2 \quad \text{(R51)}$$

$$RO + O_2 \rightarrow R_{-H}O + HO_2 \quad \text{(R52)}$$

When one HO_2 radical (or RO_2 radical after conversion to HO_2 by reaction with NO) is sampled by the PERCA instrument, this chemistry leads to the formation of one molecule of NO_2 each time the HO_2 radical is converted into OH (R4) and cycles back to HO_2 (R5-R6). Therefore, the concentration of NO_2 produced is equal to the initial concentration of peroxy radicals multiplied by the number of times the cycle is repeated (called the chain length, CL). CL depends on the ratio of the propagation rate over the termination rate and is calibrated in the laboratory. It is strongly dependent on humidity and can exhibit a value ranging between 30 (high humidity) and 200 (low humidity).[156]

When the PERCA instrument samples an unknown mixture of peroxy radicals, measuring the NO_2 concentration that is produced allows calculating the peroxy radical concentration using the calibrated chain length.

$$[HO_2 + RO_2] = \frac{[NO_2]^{amp}}{CL(RH)} \quad 19$$

with $[RO_2]$ the peroxy radical concentration, $[NO_2]^{amp}$ the nitrogen dioxide concentration produced by the amplification chemistry and CL(RH) the RH-dependent chain length.

The chain length for both PERCA and ECHAMPS has been investigating during the development of the apparatus for the relative humidity range 10–85%. The chain length decrease (Figure 34) with relative humidity due an enhancement of the wall losses and a potential impact of the $HO_2.H_2O$ complex on the chemistry.

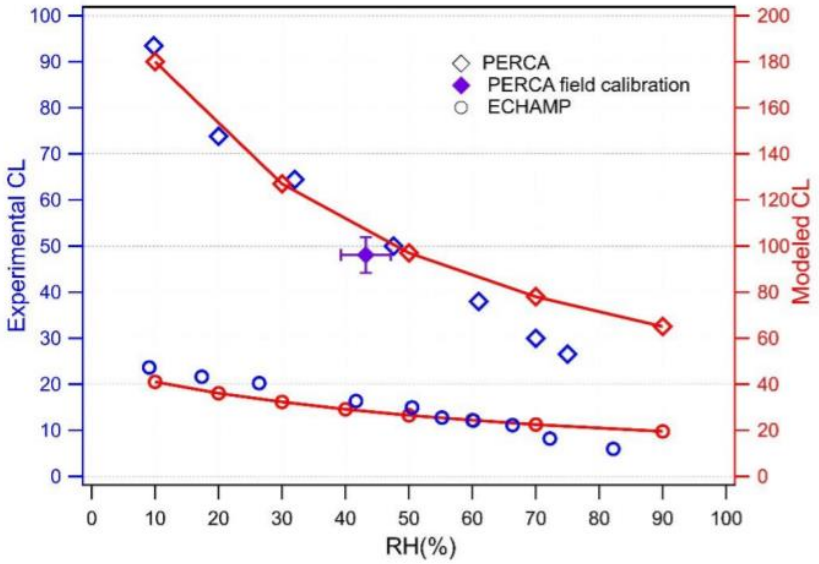

Figure 34: Dependence of experimental (blue, left y-axis) and modeled (red, right y-axis) CL on RH for the ECHAMP and PERCA approaches (T = 23±2°C). The filled diamond represents calibration experiments performed in the field. Error bars are 3σ standard errors. Figure taken from Duncianu et al.

A schematic of the PERCA instrument developed in the SAGE department is shown in Figure 35. The air is sampled in two reaction chambers referred to as "RO_X" (amplification) or "O_X" (Background) reactors. In the "RO_X" reactor, CO is added upstream and N_2 downstream (Figure 5), which leads to the measurement of the sum of ambient NO_2, NO_2 resulting from ambient O_3 titration ($O_3+NO \rightarrow NO_2$), and NO_2 from amplification reactions R1-R3. In the "O_X" reactor, CO is added downstream and N_2 upstream, which leads to the measurement of the sum of ambient NO_2 and titrated O_3. The amount of NO_2 produced by the amplification chemistry, $[NO_2]^{amp}$, is determined by the difference in NO_2 between the two reactors and used in equation 19 to derive the sampled concentration of peroxy radicals.

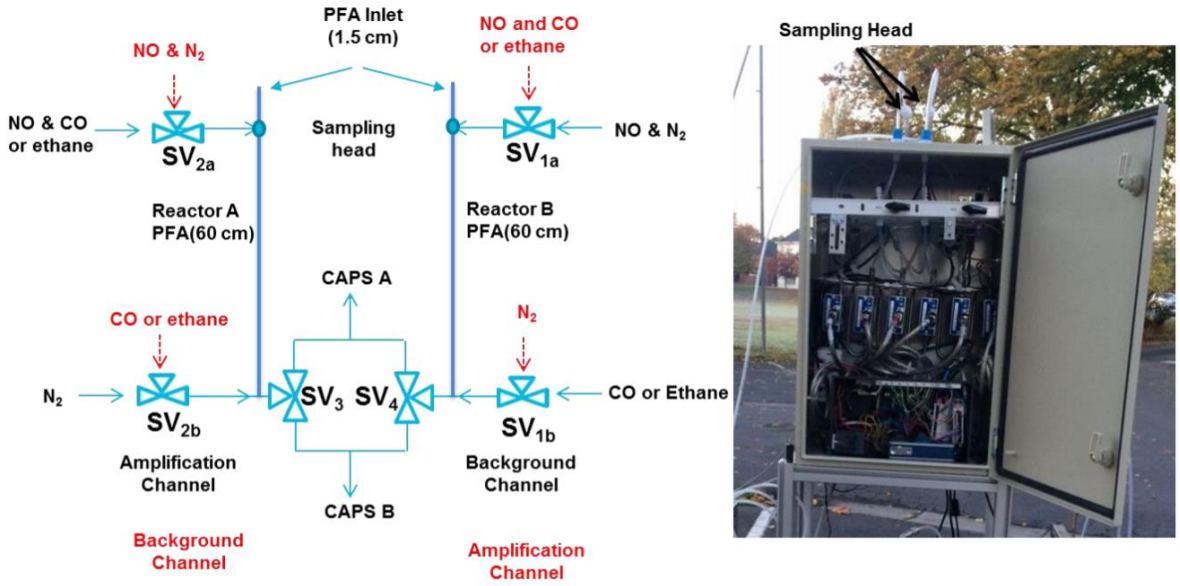

Figure 35: Schematic (left) and picture (right) of the PERCA setup described in Duncianu et al. (2019 in review)[156]. SV accounts for Solenoid Valve, CAPS for Cavity Attenuated Phase Shift spectroscopy and PFA for Perfluoroalkoxy.

I.5 Aerosol measurement - Scanning Mobilizer Particle Sizer

The aerosol distribution (number concentration per size bin) is monitored by a Scanning Mobility Particle Sizer (SMPS)[147] as shown in Figure 6. At the entrance of the SMPS an impactor is set in order to impact bigger particles that will not be measured by the SMPS. This impactor may be set at the entrance of the aerosol flow tube in order to remove these particles from the kinetics. Inside the SMPS, the aerosol goes through a neutralizer (radioactive source made of ^{85}Kr) which will standardize the aerosol charge distribution as a function of the particle diameter by means of radioactive radiations. For the SMPS used in this work, the 3080L Classifier model have been mainly used in combination with the 3788 water Condensation Particle Counter (CPC) model. However, when it was not available the Classifier 3082 was used instead in combination with the 3750 butanol CPC model. Their characteristic are introduced in the Table 10.

Table 10: Characteristics of both classifiers used.

	Classifier 3080L	Classifier 3082
Aerosol flow	0.1 to 2 LPM	0.2 to 5 LPM
Sheath flow	2 to 15 LPM	2 to 30 LPM
Particle size range	Adjustable from 10 to 1000 nm	Adjustable from 10 to 1000 nm
Charger/Neutralizer	^{85}Kr	X-ray
CPC	Model 3788 (water)	Model 3750 (butanol)

The aerosols then pass through a Differential Mobility Analyzer (DMA) column which consists of a center rod and an outer grounded tube. The high voltage applied to the center rod causes the mobility of the aerosols from the outer grounded tube to the center rod. The deviation of the aerosols at a given voltage depends on its charge distribution and its size. It is therefore possible to select the size of the aerosol passing through a slit at the exit of the DMA by varying the voltage of the center rod. The sheath flow within the DMA allows the adjustment of the particle size range measured. Indeed, when the flow is increased, the particles move faster thus they have less time to diffuse toward the aerosol outlet. That leads to a measurement of smaller particles. According to the manufacturer this sheath flow should be at least ten times higher than the aerosol flow.

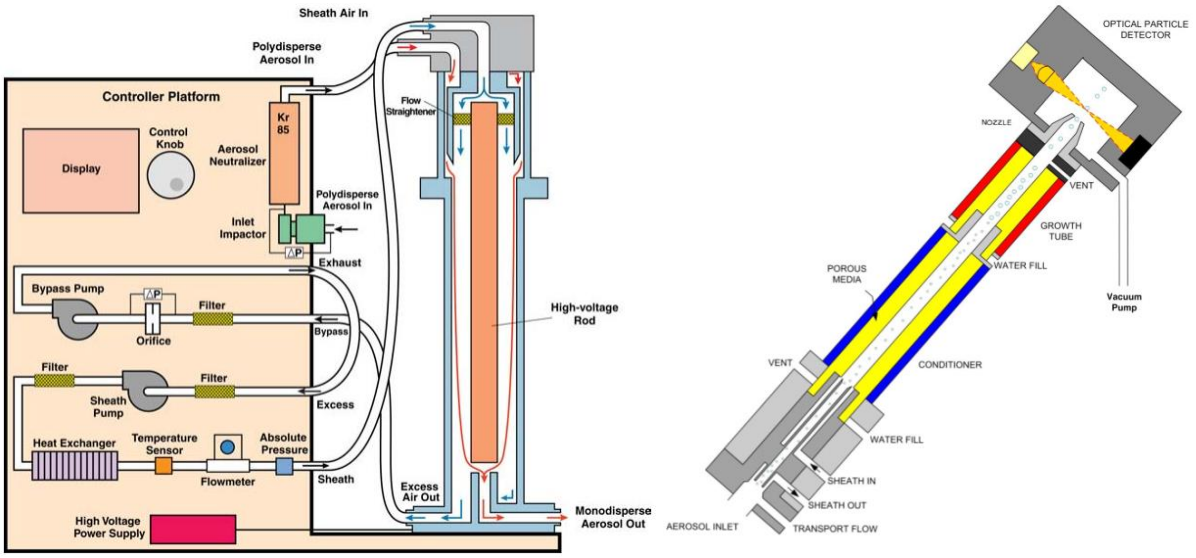

Figure 36: Schematics of the DMA (left) and CPC (right).

The selected particles then enter the Condensation Particle Counter (CPC, Figure 6) through the aerosol inlet. They go through the conditioner and growth tube where water or butanol will condense onto the particles. The condensation induces a growth of the particles and allows a detection of the smaller ones by the optical detection system. The characteristics of the CPC are introduced in Table 11.

Table 11: Characteristics of both condensation particle counters used.

	Water CPC 3788	Butanol CPC 3750
Max concentration	4.10^6 particles/cm^3	10^5 particles/cm^3
Concentration accuracy	±10% to 4.10^5 particles/cm^3	±5% at $<10^5$ particles/cm^3
Detection range	2.5 nm to >3 µm	7 nm to >3 µm
False Background count (12-hour average)	<0.02 particles/cm^3	<0.001 particles/cm^3
Flow range	0.6 or 1.5 LPM	1 LPM
Pumping system	Internal pump	External pump

I.6 Uptake measurement procedure

The uptake measurement procedure is presented below for HO_2 uptake experiments. In order to determine the uptake coefficient experimentally, both the loss rates of HO_2 with and without aerosols have to be measured. When measurements are performed without aerosols, two reactions occur inside the AFT:

$$HO_2 + HO_2 \rightarrow H_2O_2 + O_2 \quad \text{(R53)}$$

$$HO_2 + \text{wall} \rightarrow \text{losses} \quad \text{(R54)}$$

These two unwanted sinks of HO_2 will limit the quantification of small aerosol uptakes. The recombination reaction (R53) rate is a quadratic function of HO_2 while the wall loss (R54) is a first order function. Thus, we can efficiently reduce the effect of reaction (R53) and facilitate the treatment of the kinetic equations by decreasing the concentration of HO_2. Indeed, if $[HO_2]$ is sufficiently low ($<5.10^9$ cm^{-3}), (R53) can be neglected and the time-dependent concentration of HO_2 in the AFT is given by Equation 20:

$$[HO_2]_t = [HO_2]_0 \exp[-k_{wall} t] \quad 20$$

With $[HO_2]_0$ the initial concentration and k_{wall} the wall loss rate constant.

When aerosols are introduced inside the AFT, the uptake reaction occurs besides (R53) and (R54):

$$HO_2 + \text{Aerosol} \rightarrow \text{losses} \quad \text{(R55)}$$

The time-resolved concentration of HO_2 in the AFT is then given by Eq. 21.

$$[HO_2]_t = [HO_2]_0 \exp[-(k_{wall} + k_{aerosol})t] \quad 21$$

Thus, the HO_2 concentration is measured at different injector positions at fixed surface aerosol concentration. The rate constant k is then calculated by fitting the neperian logarithm of the measured HO_2 concentrations as function of the time. The total rate constant ($k = k_{wall} + k_{aerosol}$) is measured for different aerosol surface concentrations. Finally, $k_{aerosol}$ is computed by subtraction the wall loss rate constant k_{wall} to the observed rate constant k.

As previously discussed in chapter 1 section II.1, $k_{aerosol}$ and the uptake coefficient γ are linked together as shown in equation 22. Plotting $k_{aerosol}$ as a function of the aerosol surface concentration and fitting this data with a linear regression leads to the determination of the uptake coefficient knowing the mean thermal velocity $\bar{c}$.

$$k = \frac{\gamma \bar{c} S}{4} \quad 22$$

As we are under laminar flow conditions, once the rate constant is obtained, it has to be corrected by the Brown formalism.[145] Indeed, the AFT wall induces some effects (radial gradient of velocity) on the velocity distribution as it is discussed in section I.1.

II Molecular level calculations

At the molecular level, the aerosol modeling can be done by molecular dynamics (MD) to explore the trajectories of molecules or by Quantum Mechanics (QM) to treat gas phase reactivity. A hybrid method (e.g. QM/MM : Quantum Mechanics/Molecular Mechanics) has also been used. This section summarizes the foundations of these methods.

II.1 Molecular dynamics

II.1.1 Principle

Classical Molecular Dynamics (MD) consists in the resolution of Newton's second law (equation 23) for each atom i at every time step:

$$\sum_i \vec{F}_i = m_i \vec{a}_i \qquad 23$$

with $\vec{F_I}$ being the force acting on a particle i of mass m_i and $\vec{a_i}$ the acceleration of particle i.

The acceleration can be easily computed by equation 24:

$$\vec{a}_i = \frac{-1}{m_i} \vec{\nabla} V_i \qquad 24$$

where V_i is the potential from which the force is derived.

To solve equation 23, the idea is to do a simulation on both a temporal and a space grid. Usually integrators based on Taylor expansions are used. The first example of integrator that we can use, is the Velocity Verlet integrator[159] (equations 25 and 26). This integrator computes the position and the velocity at each timestep Δt:

$$r(t+\Delta t) = r(t) + \Delta t v(t) + \frac{\Delta t^2}{2m} F(t) \qquad 25$$

$$v(t+\Delta t) = v(t) + \frac{\Delta t}{2m} [F(t) + F(t+\Delta t)] \qquad 26$$

Another example of integrator is the "leap frog" integrator (equations 27 and 28) where the velocity is computed at one half time step later than the position (see Figure 37).

$$v\left(t+\frac{1}{2}\Delta t\right) = v\left(t-\frac{1}{2}\Delta t\right) + \frac{\Delta t}{m} F(t) \qquad 27$$

$$r(t+\Delta t) = r(t) + \Delta t\, v\left(t+\frac{1}{2}\Delta t\right) \qquad 28$$

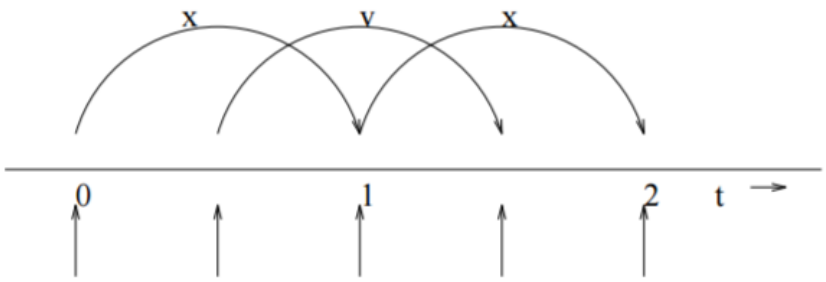

Figure 37: Scheme of the leap-frog integrator with x the position and v the velocity.[160]

The leapfrog integrator has a minimized numerical imprecision but the velocity at the first half step is not known accurately. Velocity Verlet is very stable despite its simplicity. In this work, the velocity Verlet integrator has been chosen.

The potential used to compute the force (in atomic units, a.u.; see Appendix C) is a sum of bonded terms such as bonds, bending angles, proper angles and improper dihedrals (respectively terms 29, 30, 31 and 32; Figure 38 and Figure 39) and non-bonded terms, i.e. electrostatic and dispersion-repulsion interactions (term 33). The dispersion-repulsion term used in this study is expressed with a Lennard Jones form:

$$V = \sum_{\text{bonds}} K_r\left(r - r_{eq}\right)^2 \quad (29)$$

$$+ \sum_{\text{angles}} K_\theta\left(\theta - \theta_{eq}\right)^2 \quad (30)$$

$$+ \sum_{\text{dihedrals}} \sum_{n} \frac{V_n}{2} * [1 + \cos(n\phi - \gamma)] \quad (31)$$

$$+ \sum_{\text{Impropers}} K_\chi\left(\chi - \chi_{eq}\right)^2 \quad (32)$$

$$+ \sum_{i<j} \frac{q_i q_j}{\varepsilon r_{ij}} f_{ij} + 4\varepsilon_{LJ}\left[\left(\frac{r_0}{r_{ij}}\right)^{12} - \left(\frac{r_0}{r_{ij}}\right)^{6}\right] f_{ij} \quad (33)$$

Table 12: Terms of equations 29 - 33.

K_r	Bond force constant	χ	Improper angle
r	Bond length	χ_{eq}	Improper angle at equilibrium
r_{eq}	Bond length at equilibrium	q_i q_j	Partial charges of atoms i or j
K_θ	Angle force constant	ε	Permitivity
θ	Angle	r_{ij}	Distance between atoms i and j
θ_{eq}	Angle at equilibrium	f_{ij}	Fudge factor
V_n	Dihedral force constant	ε_{LJ}	Lennard Jones parameters
n	Multiplicity	σ_{ij}	
ϕ	Dihedral angle		
γ	Phase angle		

The 1-4 interactions (non-bonded interactions between two atoms separated by three bonds) are scaled by a fudge factor f_{ij}. This factor was first introduced in 1975 by Momany *et al.*[161] Indeed, for 1-4 interactions, quantum effects such as overlap, exchange and coulombic contributions have to be taken into account. Monamy *et al*. have fitted this parameter (equal to 1/1.2 for GAFF and ½ for OPLS, see below) on the basis of *ab initio* calculations of repulsive force constants and when available, with experimental data of the dihedral rotational barriers. Then, to improve the force field, the parameter was fitted at the same time as the torsional potential.[162,163]

In the case of intermolecular interaction, the factor f_{ij} is set to 1.

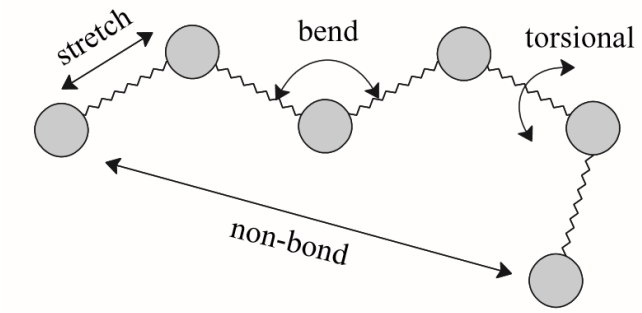

Figure 38: Illustration of the fundamental force field terms.[164]

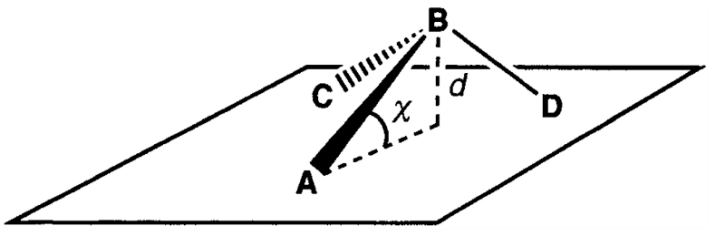

Figure 39: Definition of the improper angle.[164]

To mimic experiments usually performed at given temperature T and pressure P conditions, temperature and pressure can be defined using a thermostat and a barostat, respectively. One example of thermostat is the Berendsen thermostat (equation 34) with λ the velocity scaling factor, T the temperature of the system, T_0 the set point temperature and τ_T the "coupling time" of the thermostat.[165] The velocities are then multiplied by λ.

$$\lambda = \left[1 + \frac{\Delta t}{\tau_T}\left(\frac{T}{T_0} - 1\right)\right]^{1/2} \quad 34$$

One example of barostat is the Berendsen pressure coupling (equation 35),[166] corresponding to the computation of the scaling factor μ with Δt the timestep, τ_p the coupling time constant, β the isothermal compressibility:

$$\mu = \left(1 + \frac{\Delta t}{\tau_p}\beta[P(t) - P_0]\right)^{1/3} \quad 35$$

The length of the system (length of the box) is then multiplied by μ (dimensionless).

The studied system is inserted in a box of a few nanometers size. In order to avoid edge effects, we use periodic boundary conditions and duplicate the simulation cell along the three directions (x, y, z). When a molecule reaches the top or the bottom of the box, this molecule is reinserted on the opposite side to ensure a constant number of atoms (Figure 40).

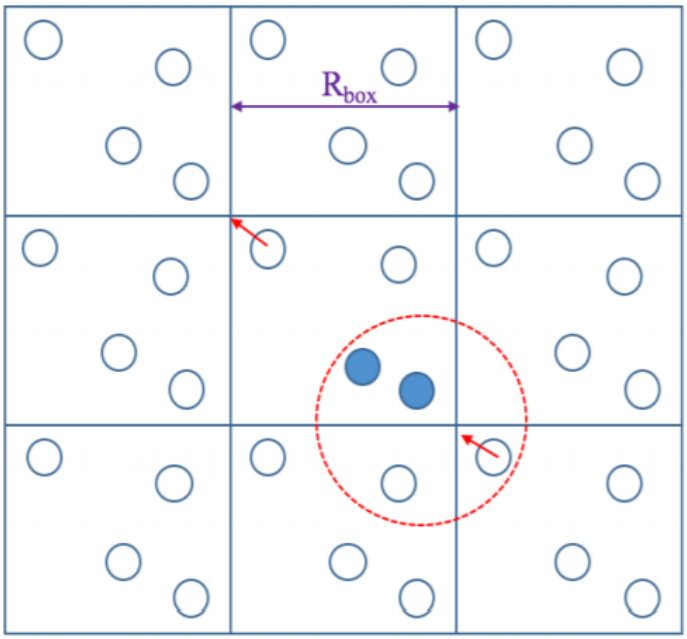

Figure 40: Illustration of the boxes and the application of periodic boundary conditions. All the interaction are computed within the radius of the Rc (represented by the red dotted circle). Figure taken from Fotsing[167].

In order to reduce the computational cost, it is possible to cut the electrostatic and Van der Waals interactions. Indeed, as the interaction decreases proportionally to r^6 and r for Van der Waals and electrostatic interactions, respectively, it is possible to define a cutoff radius for each interaction. Every interaction pair that has a distance above the cutoff radius will be neglected. In the case of the Van der Waals interaction, this approximation leads only to a small error for a reasonable cutoff distance (~1 nm). However, in the case of the electrostatic interaction, the error can be non-negligible.

It is still possible to compute long range interactions using some approximations. Indeed it is possible to add a long range correction for Van der Waals and Coulomb interactions using the dispersion correction and the Particle Mesh Ewald correction.[168] In this work, this Particle Mesh Ewald method has been used, because it is more satisfactory in the case where the system outside the cutoff distance is non homogeneous.

Then, the algorithm – which can be implemented in any molecular dynamics software (such as GROMACS,[160] CHARMM,[169] AMBER[170]) – consists in the following:

1) Input initial conditions (potential parameters V, positions **r**…)
2) Compute forces on all atoms
3) Compute scaling factors for the thermostat and barostat (depends on the frequency of the coupling with the thermostat or barostat)
4) Update configuration
5) If required, store the coordinates, velocities and energies
6) Repeat steps 2 to 5 until the desired duration is reached

Then, the results and properties have to be analyzed and computed (see below).

The main advantage of molecular dynamics is the possibility to apply it on large systems (several hundreds of molecules). Indeed, compared to quantum methods, the computation takes

significantly less time. The main drawbacks of classical MD, based on semi-empirical force-fields, are that (i) quantum effects such as chemical reactions or tunneling effects of the hydrogen cannot be dealt with; (ii) the simulation is always performed at the ground electronic state or one single electronic state and it cannot treat charge transfers or photodissociation processes; (iii) despite its efficiency, it is not possible to compute particles larger than 15 nm within a "reasonable time". Global time and length scales of classical MD are presented in Figure 41 (until some new improvements have been proposed).

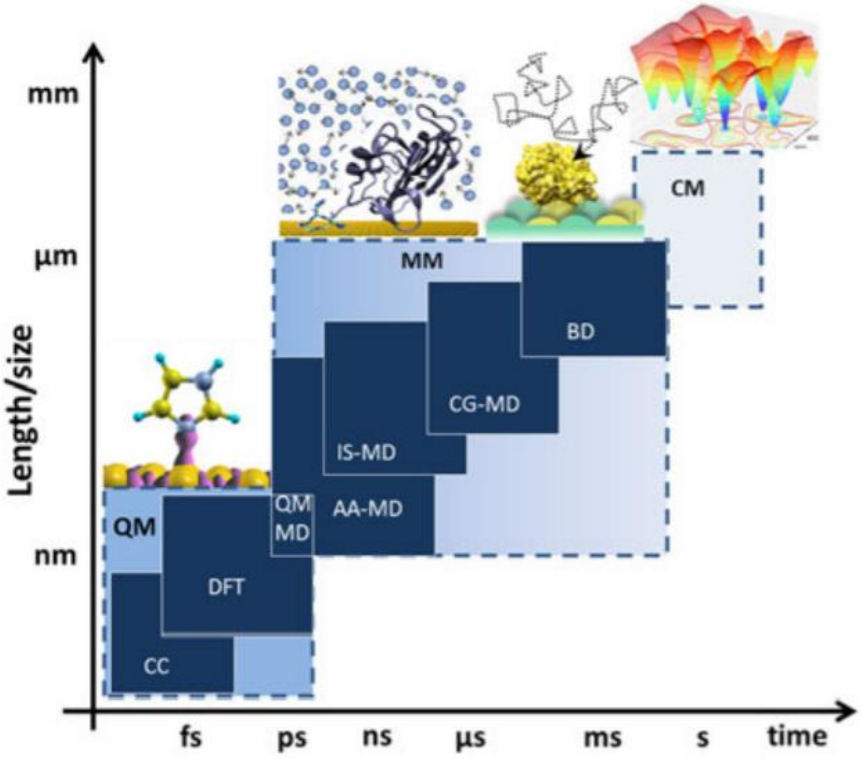

Figure 41: Typical time and length scales of different simulation techniques: quantum mechanics (QM), including coupled cluster (CC) and Density Functional Theory (DFT) methods (see below); molecular mechanics (MM) including all-atom molecular dynamics (AA-MD) simulations, implicit solvent and coarse grained MD (IS-MD and CG-MD), and Brownian dynamics (BD) technique; and continuum mechanics (CM). The ranges of time and length are approximate. Figure taken from OzboyacuI et al. [171]

II.1.2 Force fields

In order to compute the terms 29 to 33, we have to use a set of parameters corresponding to the equilibrium geometry of the molecule. Some of these parameters correspond to values at the equilibrium geometry (interatomic distance r_0, bond angle θ_0, etc.) and to the corresponding force constant k. The partial charges q and Lennard Jones parameters σ and ε have also to be defined.

These parameters can be found in standard force fields (AMBER,[172,173] OPLS,[163] CHARMM,[174] etc.) where they have been generally tuned with respect to experimental data or *ab initio* computations when experimental data were not available.

In this study, we used the General Amber Force Field (GAFF[173]). It was first designed to be as compatible as possible with most of the pharmaceutical compounds and the traditional AMBER

force field that was initially developed for proteins and nucleic acids.[173] GAFF performance was tested in three cases:

- Comparison of GAFF minimized structure with 74 crystallographic structures;
- Comparison of 22 nucleic acid pairs (after gas phase minimization) with MP2/6-31G* (see section II.2) results;
- Comparison of the relative energies of 71 conformational pairs with experimental data.

Noticeably in the case of water, and despite its apparent simplicity, force fields are difficult to model and specific force fields have been created to reproduce some of its properties, such as SPC/E,[175] TIP3P,[176] TIP4P,[176] and TIP5P.[177] Table 13 shows the different parameters and properties that have been tested in each model. Note that none of these models was able to reproduce all the considered properties; thus they are based on a selected set of the water properties.

Table 13: Comparison of some of the common models used for water [175–178]

	SPC/E	TIP3P	TIP4P	TIP5P
Number of sites	3	3	4	5
d O-H (Å)	1	0.9572	0.9572	0.9572
Θ H-O-H	109.47°	104.52°	104.52°	104.52°
qH (electronic charge unit)	0.4238	0.417	0.520	0.241
qO (electronic charge unit)	-0.8476	-0.834	-1.04	-0.214
d O-L (Å)			0.15	0.7
Θ L-O-L				109.47
A (x10^{-3} kcal.Å^{12}/mol)	629.4	582.0	600	544.5
B (kcal.Å^{6}/mol)	625.5	595.0	610	554.3
μ	2.35D	2.35D	2.18D	2.29D
Based on	Radial distribution curves and characteristic of liquid water (diffusivity and density)	Vaporization enthalpy and liquid density in ambient condition	Vaporization enthalpy and liquid density in ambient condition	Vaporization enthalpy, liquid density in ambient condition and maximum density at 277K

In order to confirm if the chosen force field can reproduce the system, a validation step has to be done. These tests can be done by doing comparisons with some experimental properties (crystalline structure, melting point, densities, etc.).

II.2 Quantum chemistry

While molecular dynamics is an empirical method that does not describe explicitly the electrons, another way to perform molecular modeling involves *ab initio* computations (i.e. solving the Schrödinger equation), which in principle provides the exact properties of a molecular system. However, this kind of computation is slow, requires a lot of computer resources and therefore does not allow the treatment of large systems.

II.2.1 Schrödinger equation and Born-Oppenheimer approximation

Quantum chemistry consists in the resolution of the time-independent Schrödinger equation (equation 36):

$$H\Psi = E\Psi \quad (36)$$

where Ψ is the total wave function, E the energy of the system and H the Hamiltonian operator of the system (in atomic units, a.u.), which for a molecule is the sum of operators accounting for the kinetic energy of electrons (T_e, term 37) and nuclei (T_N, term 38), and those for the potential energy of the coulombic interaction nuclei-electrons (V_{Ne}, term 39), electrons-electrons (V_{ee}, term 40) and nuclei-nuclei (V_{NN}, term 41).

$$H = -\sum_i \frac{1}{2}\nabla_i^2 \quad (37)$$

$$-\sum_i \frac{1}{2M_k}\nabla_k^2 \quad (38)$$

$$-\sum_i \sum_k \frac{Z_k}{r_{ik}} \quad (39)$$

$$+\sum_{i<j} \frac{1}{r_{ij}} \quad (40)$$

$$+\sum_{k<l} \frac{Z_k Z_l}{r_{kl}} \quad (41)$$

Z_k being the atomic number of the nucleus k, M_k its mass, and the r's the respective distances between the particles (electrons i, j and nuclei k, l).

However, this equation is really complex to solve and its analytical treatment is no longer possible. Indeed, H. Poincaré proved that N body problem does not have an exact solution if N is higher than 2.[179] One approximation that can be applied is the Born-Oppenheimer approximation, which neglects the coupling between the nuclear and electronic velocities.[164] Indeed, because of their mass ratio (m_N/m_e=1820 in case of H, the lightest atom) the nucleus does not move from an electronic point of view. This approximation allows to split the Schrödinger equation in an electronic part (equation 42) and a nuclear part (equation 43).

$$H_e\Psi_e(\vec{R},\vec{r}) = E_e(\vec{R})\Psi_e(\vec{R},\vec{r}) \quad (42)$$

$$\left(T_N + E_e(\vec{R})\right)\Psi_N(\vec{R}) = E_{tot}\Psi_N(\vec{R}) \quad (43)$$

where $\vec{R}$ are now the parameters of the positions of the nuclei, $\vec{r}$ the position variables of the electrons and:

$$H_e = T_e + V_{Ne} + V_{ee} + V_{NN} \quad (44)$$

Still some problems persist to compute exact solutions, because of the V_{ee} term as the dynamics of many-electron systems is very complex and has no exact solution for more than 2 particles.

So, other approximations have to be done and lead to different computational methods described in the following section II.2.2.

II.2.2 Computational methods

There is a full set of existing computational methods (Hartree-Fock, density functional theory, DFT, coupled cluster theory, CC etc.). Here, a focus has been made on methods that have been used for this work.[164]

II.2.2.1 The Hartree-Fock method

In 1928, Hartree suggested an approximate solution (mean field approximation) of the Schrödinger equation of the electronic part by considering the Hamiltonian as a sum of monoelectronic Hamiltonians (equation 45):

$$H^e \cong H_0 = \sum_{i=1}^{n} h_i = \sum_{i=1}^{n} \left\{ \frac{-\Delta_i}{2} + \sum_{A=1}^{N} \frac{-Z_A}{|R_A - r_i|} + \sum_{j \neq i}^{n} \frac{1}{r_{ij}} \right\} \quad 45$$

From now on, n is the total number of electrons. Later, Fock included the Pauli principle by writing the monoelectronic Hamiltonian as a Fock operator (equation 46).

$$f(j) = h^c(j) + \sum_{i=1}^{n} [\mathbb{J}_i(j) - \mathbb{K}_i(j)] \quad 46$$

with h^c the core Hamiltonian (equation 47), $\mathbb{J}$ the Coulombian operator (equation 48) and $\mathbb{K}$ the exchange operator (equation 49).

$$h^c(j) = -\frac{\Delta_j}{2} + \sum_{A=1}^{N} \frac{-Z_A}{|R_A - r_j|} \quad 47$$

$$\mathbb{J}_j(1) = \left\langle \varphi_j(2) \left| \frac{1}{r_{12}} \right| \varphi_j(2) \right\rangle \quad 48$$

$$\mathbb{K}_j(1)\varphi_i(1) = \left\langle \varphi_j(2) \left| \frac{1}{r_{12}} \right| \varphi_i(2) \right\rangle \varphi_j(1) > \quad 49$$

Using the Equation 46 notation, Equation 42 becomes:

$$f\varphi_i = \varepsilon_i \varphi_i \quad 50$$

The Hartree-Fock energy of the system can be computed using equation 51:

$$E_{HF} = \sum_{i=1}^{n} \varepsilon_i - \frac{1}{2} \sum_{i=1}^{n} \sum_{j=1}^{n} \left(\left\langle \varphi_i(1)\varphi_j(2) \left| \frac{1}{r_{ij}} \right| \varphi_i(1)\varphi_j(2) \right\rangle - \left\langle \varphi_i(1)\varphi_j(2) \left| \frac{1}{r_{ij}} \right| \varphi_j(1)\varphi_i(2) \right\rangle \right) \quad 51$$

For each electron, there is an associated wave function φ_i (spin-orbital) and the global wave function can be written as a Slater determinant (equation 53) to fulfill Pauli principle.

$$H_i\varphi_i=\varepsilon_i\varphi_i \quad (52)$$

$$\Psi_0=|\varphi_1\varphi_2...\varphi_n| \quad (53)$$

But to solve equation 52, the Molecular Orbital (MO) φ_i of the system has to be known for each electron i. The Coulomb operator and the exchange operator need therefore to be calculated but they are dependent of the φ_i which are not known. To get rid of this revolving door cycle, an iterative method called the self-consistent field (SCF) is used. To initiate the calculation, we compute the φ_i's based on a linear combination of non-orthogonal atomic orbitals (LCAO) χ_m (equation 54) taken from a database[180] (see chapter 2 section II.2.2.2).

$$f|\varphi_i\rangle=f\sum_{m=1}^{M}C_{im}|\chi_m\rangle=\varepsilon_i\sum_{m=1}^{M}C_{im}|\chi_m\rangle \quad (54)$$

where χ_m is the atomic orbital and M the atomic basis set size.

So, by multiplying equation 54 by $\langle\chi_p|$, Roothaan[181] obtained a matrix equation:

$$\hat{F}\hat{C}=\hat{S}\hat{C}\hat{E} \quad (55)$$

with $\hat{C}$ the matrix of LCAO coefficients, E the energy matrix, S the non-orthogonal atomic orbital overlap matrix and F the Hartree-Fock matrix expressed in the atomic basis set:

$$f_{pq}=\langle\chi_p|f|\chi_q\rangle=h^c_{pq}+\sum_{r=1}^{M}\sum_{s=1}^{M}P_{rs}[\langle pq|rs\rangle-\langle ps|rq\rangle] \quad (56)$$

and

$$P_{rs}=\sum_{a=1}^{n}C_{ra}C^*_{sa}\ \text{(density matrix)} \quad (57)$$

$$h^c_{pq}=\langle\chi_p|h^c|\chi_q\rangle\ \text{(mono-electronic integral)} \quad (58)$$

$$\langle pq|rs\rangle=\left\langle\chi_p\chi_q\left|\frac{1}{r_{12}}\right|\chi_r\chi_s\right\rangle\ \text{(bi-electronic integral)} \quad (59)$$

As the terms in equations 58 and 59 are fixed, they are computed once the basis set is chosen at the beginning of the calculation. Then, the initial φ_i^0 and the density matrix P^0 are calculated. The C^0 matrix is deduced. The F^0 matrix is computed and the equation $F^0C^1 = SC^1E^0$ is solved (diagonalization of F^0). The results are the E^0 and C^1 matrices that allow the new density matrix P^1 and the new φ_i^1 deduction. If there is a large change between C^0 and C^1, another cycle of calculations begins with C^1. The iteration stops when the convergence criteria (energy and electron density) are respected, i.e. C^0 close to C^1. To get better results, a large basis set is needed. However, the computational time is proportional to the basis set size at the power 4, so a compromise has to be found, balancing cost and accuracy.

Nevertheless, there are limitations to the Hartree-Fock method even when large orbital basis sets are used. It is also not possible to describe the excited electronic states and processes such as dissociation. Indeed, in the Hartree-Fock theory, the probability to find two electrons of identical spins at the same position is not equal to zero (the Coulomb hole is not taken into

account properly). There is a missing term called correlation, whose energy E_c is defined as follows:

$$E_c = E_{exact} - E_{HF} \quad (60)$$

To take this correlation energy into account, some Post Hartree-Fock[182] methods have been developed.[164]

II.2.2.2 Orbital basis sets

Two types of functions can be used to represent the molecular orbitals (MO's) φ_i. The most physically meaningful type is the Slater orbital (exponential) but its computational cost is quite high. However, we can approach a Slater-type orbital (STO) by using a (small) combination $\mathbb{C}$ (called contraction) of Gaussian-type orbitals (GTO, equation 61).

$$\mathbb{C} = \sum_{\lambda=1}^{n_c} d_\lambda G_\lambda \quad (61)$$

where G_λ is a Gaussian called primitive and d_λ the so-called contraction coefficient. The quality of a basis set depends on the number of available primitives, on the value and method used to optimize the parameters and on the number of contractions used.

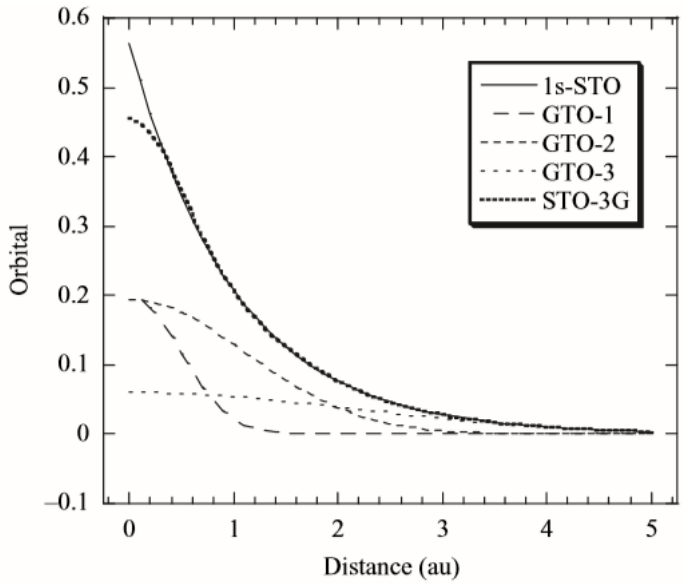

Figure 42: A 1s-STO orbital modelled by a linear combination of three GTOs (STO-3G).[164]

Many types of orbital basis sets have been developed.[183,184] The first type is the minimal basis set where each atomic orbital is represented by only one combination of Gaussians. The second type is the multiple zeta basis set where each orbital is represented by two or more Slater orbitals. A specific class of multiple zeta orbitals is the Pople's basis sets. In this type of basis set, the core orbitals are only a simple zeta contrary to the valence orbitals which are double zeta or more. One example of a Pople's basis set is the 6-311G where the core orbitals are described by a sum of six Gaussians and the valence orbitals are described by three Gaussians, one of them being a sum of three Gaussians itself. A second class of multiple zeta basis set is the Dunning correlation consistent basis set family (cc-pV(x)Z with (x) = D, T, Q, 5, 6, 7 or 8

for double up to octuple zeta). For the description of Van der Waals interactions, it is necessary to add diffuse orbitals in the Dunning basis sets, for which the extension 'aug' is added before the basis set name (e.g. aug-cc-pVTZ). In Pople's basis sets, we add a "+" to indicate a diffuse orbital on non-hydrogen atoms (6-31+G) and another one for diffuse orbitals on hydrogens (6-31++G).

Sometimes, it can also be necessary to add some polarization orbitals to get a correct geometry (see Figure 43). These orbitals are added to the valence orbital and possess a higher angular momentum (p orbital for H, d or f orbital for heavier atoms). In Pople's basis sets, they are noted by a first "*" for an orbital of polarization on H and a second one for bigger atoms (e.g. 6-311G**).

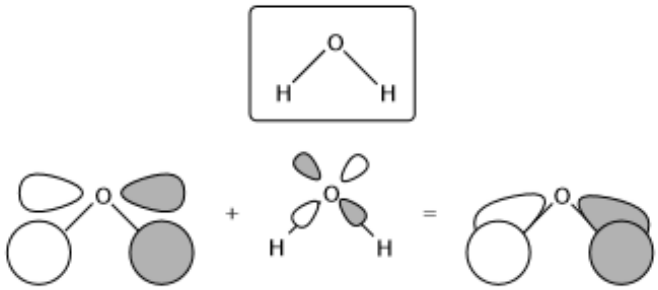

Figure 43: The molecular orbital (MO) formed by the interaction between the antisymmetric combination of H 1s orbital and the oxygen p_x orbital. Bonding interactions are enhanced by mixing a small amount of O d_{xz} character into the MO.[185]

II.2.2.3 Møller-Plesset perturbation theory

In contrast to the Hartree-Fock method, which is a variational method (i.e. which minimizes the total energy of the molecule by varying the weight of each AO in each occupied MO), the Møller-Plesset method is a perturbation method which consists in splitting the Hamiltonian in two parts, a reference (H_0) and a "small" perturbation (H'), with a scaling factor λ.

$$H = H_0 + \lambda H' \quad (62)$$

with $H_0 >> H'$. The perturbed Schrödinger equation is written as follows:

$$H\Psi = W\Psi \quad (63)$$

As λ increases from zero to a finite value, the new energy W and the new wave function can be written as a Taylor expansion.

$$W = \lambda^{(0)}W_0 + \lambda^{(1)}W_1 + \lambda^{(2)}W_2 + \lambda^{(3)}W_3 + \ldots \quad (64)$$

$$\Psi = \lambda^{(0)}\Psi_0 + \lambda^{(1)}\Psi_1 + \lambda^{(2)}\Psi_2 + \lambda^{(3)}\Psi_3 + \ldots \quad (65)$$

where $\Psi_1, \Psi_2, \ldots$ and $W_1, W_2, \ldots$ are 1st order, 2nd order, etc. corrections. λ is eventually set equal to 1. The Schrödinger equation then becomes equation 66:

$$(H_0 + \lambda H')\left(\lambda^{(0)}\Psi_0 + \lambda^{(1)}\Psi_1 + \lambda^{(2)}\Psi_2 + \ldots\right) = \left(\lambda^{(0)}W_0 + \lambda^{(1)}W_1 + \lambda^{(2)}W_2 + \ldots\right)\left(\lambda^{(0)}\Psi_0 + \lambda^{(1)}\Psi_1 + \lambda^{(2)}\Psi_2 + \ldots\right) \quad (66)$$

So, by collecting terms of the same order of λ, we get:

$$\lambda^{(0)}: H_0\Psi_0 = W_0\Psi_0$$

$$\lambda^{(1)}: H_0\Psi_1 + H'\Psi_0 = W_0\Psi_1 + W_1\Psi_0$$

$$\lambda^{(2)}: H_0\Psi_2 + H'\Psi_1 = W_0\Psi_2 + W_1\Psi_1 + W_2\Psi_0 \qquad 67$$

$$\lambda^{(n)}: H_0\Psi_n + \Psi_{n-1} = \sum_{i=0}^{n} W_i\Psi_{n-i}$$

So, at the zeroth-order we retrieve the unperturbed Schrödinger equation. In the case of Møller-Plesset partition, the unperturbed Hamiltonian is taken as the Fock operator (H_0=F) :

$$H_0 = \sum_{i=1}^{n}\left(h_i + \sum_{j=1}^{n}\left(J_j - K_j\right)\right) = \sum_{i=1}^{n} h_i + 2\langle V_{ee}\rangle \qquad 68$$

$$H' = V_{ee} - 2\langle V_{ee}\rangle$$

The zeroth order wave function and energy correspond to the Hartree-Fock determinant and the sum of MO energies, respectively. The first-order energy correction is the average of perturbation operator over the zeroth-order wave function. Thus, the first-order energy is exactly the Hartree Fock HF energy:

$$W_1 = E(MP0) + E(MP1) = E(HF) \qquad 69$$

In Møller-Plesset (MP) theory, we will take at least the second-order correction. The MP2 energy is given by equation 70:

$$W_2 = E(MP2) = \sum_{i<j}^{occ}\sum_{a<b}^{vir} \frac{\left(\langle\varphi_i\varphi_j|\varphi_a\varphi_b\rangle - \langle\varphi_i\varphi_j|\varphi_b\varphi_a\rangle\right)}{\varepsilon_i + \varepsilon_j - \varepsilon_a - \varepsilon_b} \qquad 70$$

In principle, we can increase the degree of perturbation to refine the value (MP4, MP5, MP6, etc.). However, there are some drawbacks to use higher orders. Indeed, by increasing the order of perturbation, the energy will converge more slowly towards the exact value and, depending on the orbital basis set, may diverge from certain orders of perturbation (see Figure 44). The computational time increases considerably for orders higher than 4. Therefore, in practice we only use the second order method MP2.

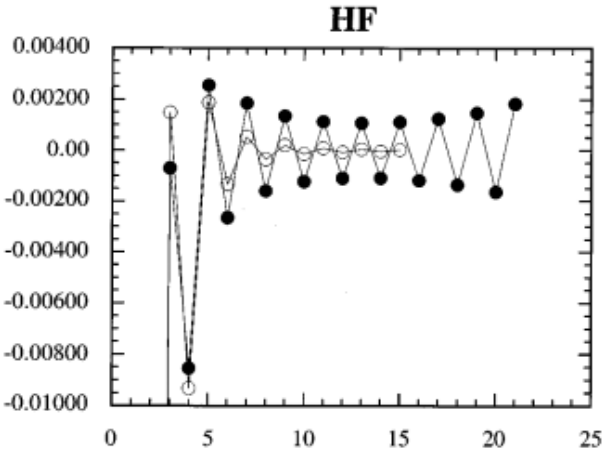

Figure 44: Correlation contributions for a HF molecule in the cc-pVTZ-(f/d) (white) and aug-cc-pVDZ (black) basis sets.[186]

II.2.2.4 Coupled cluster method

In order to compute the correlation energy of ground states, we first have to define a new operator T (Equation 71)

$$T = T_1 + T_2 + T_3 + \cdots + T_N = \sum_{i=1}^{\infty} T_n \quad 71$$

Where T_1 is the operator promoting one electron into a virtual (unoccupied) orbital, T_2 the operator promoting two electrons into two virtual orbitals, etc. This operator allows to rewrite the full configuration wavefunction $|\Phi_{FCI}\rangle$ with equation 72 and knowing that the exponential can be written as a Taylor expansion (Equation 73).

$$|\Phi_{FCI}\rangle = e^{T}|\Phi_0\rangle \quad 72$$

$$e^{T} = 1 + T + \frac{T^2}{2!} + \frac{T^3}{3!} + \cdots + \frac{T^N}{N!} = \sum_{i=0}^{\infty} \frac{T^i}{i!} \quad 73$$

Where T is defined by equation 71. It is possible (and in fact necessary because of the cost) to limit the sum to a few terms in order to take into account only a few excited electrons. For example, one can compute the Coupled Cluster Doubles (CCD, equation 74), Coupled Cluster Singles and Doubles (CCSD, equation 75) or the Coupled Cluster Single, Doubles and Triples (CCSDT , equation 76).

$$CCD = e^{T_2}|\Phi_0\rangle \quad 74$$

$$CCSD = e^{T_1+T_2}|\Phi_0\rangle \quad 75$$

$$CCSDT = e^{T_1+T_2+T_3}|\Phi_0\rangle \quad 76$$

To compute the coupled cluster energy E_{CC}, the Schrödinger equation (Equation 77) has to be solved:

$$He^{T}|\Phi_0\rangle = E_{CC}e^{T}|\Phi_0\rangle \quad 77$$

One can use the variational method to do so but another method consists in multiplying each side of the equation by e^{-T}. The resulting equation (78) has then to be multiplied by Φ_0^* to obtain the energy (Equation 79):

$$e^{-T}He^{T}|\Phi_0\rangle = E_{CC}|\Phi_0\rangle \quad 78$$

$$E_{CC} = \langle\Phi_0|e^{-T}He^{T}|\Phi_0\rangle \quad 79$$

The CCSD and CCSDT methods can provide accurate observables depending on the system that is computed. However, their computational cost is about N_{basis}^6 and N_{basis}^8, respectively, so these methods become difficult to use. But it is still possible to get an approximate value of the triple excitation term using a perturbative method (CCSD(T) method) and thus to decrease the computational cost by one order of magnitude.[164,187]

II.2.2.5 Density Functional Theory (DFT)

Instead of using the wave function, the Density Functional Theory uses the total electronic density ρ(r), which is an observable in principle. In the 1960s, Hohenberg and Kohn[188] have proved two theorems:

- All the properties of the ground state of a molecule are only determined by the exact electronical density ρ_0.
- The density ρ_0 follows the variational principle, similarly to the wave function. But ρ_0 cannot be exactly calculated.

Kohn and Sham proposed an approximate solution in 1965 by writing the Born-Oppenheimer Hamiltonian as equation 80. They considered the difference between the real system and a fictitious system of non-interacting electrons. They split the equation in terms that are easy to compute (T_{ni}, V_{Ne}, and V_{ee}) and two terms for which ΔT (for the kinetic part) and ΔV_{ee} are not exactly known.

$$H[\rho(r)]=T_{ni}[\rho(r)]+V_{Ne}[\rho(r)]+V_{ee}[\rho(r)]+\Delta T[\rho(r)]+\Delta V_{ee}[\rho(r)] \quad 80$$

with T_{ni} the kinetic energy of the electrons without interaction, ΔT the kinetic energy difference between the real and fictitious (non-interacting) systems, and ΔV_{ee} all the inter-electronical interaction corrections. So, by taking:

$$\rho(r)=\sum_{i=1}^{n}\langle\theta_i|\theta_i\rangle \quad 81$$

with θ_i being the Kohn-Sham molecular orbitals, we get the following expression of energy:

$$E[\rho(r)]=\sum_{i=1}^{n}\left[\left\langle\theta_i\left|\frac{-\Delta_i}{2}\right|\theta_i\right\rangle-\left\langle\theta_i\left|\sum_{A=1}^{N}\frac{Z_A}{|R_A-r|}\right|\theta_i\right\rangle+\left\langle\theta_i\left|\int\frac{\rho(r')}{|r_i-r'|}dr'\right|\theta_i\right\rangle\right]+E_{xc}[\rho(r)] \quad 82$$

where the so-called exchange correlation energy $E_{xc}[\rho(r)]$ is approached by an approximate functional due to the fact that there is no exact solution available.

Functionals have been classified by John Perdew as a Jacob's ladder (biblical reference).[189] The Earth is the Hartree-Fock model and the Heaven is the chemical accuracy. Between them, there

are five steps ("rungs") which have an increased accuracy when we get closer to the top of the ladder. The first step is the local density approximation (LDA) type of functional. The LDA idea is to consider the exchange correlation potential as the potential of a uniform electron gas (jellium). In the case of an open shell molecule, the spin is considered (ρ_α and ρ_β) which leads to local spin density approximation (LSDA) functional. The next step is the generalized gradient approximation (GGA). The GGA idea is to consider that the electronic density is not uniform. A local density approach and its gradient $\nabla\rho(r)$ are thus used. The meta-GGA functional consists in adding the second order gradients $\Delta\rho(r)$ to the GGA. The fourth step is the hybrid functional. In this type of functionals, a mixture of GGA and LDA is used. A part of Hartree-Fock exchange energy is also added. One of the most popular functional of this type is the B3LYP (Becke, 3 parameters, Lee, Yang, Parr):

$$E_{xc}^{B3LYP}=(1-a_0-a_x)E_x^{LDA}+a_0E_x^{HF}+a_xE_x^{B88}+(1-a_c)E_c^{VWN}+a_cE_c^{LYP} \quad 83$$

where a_0 (0.2), a_x (0.72) and a_c (0.81) are three empirical parameters optimized to reproduce some chemical properties. The last step of the Jacob's ladder is the generalized random phase approximation. In this type of functionals, not only occupied orbitals are taken into account but also unoccupied ones.

DFT has a high cost effectiveness, but its semi-empirical character (cf. exchange-correlation term) introduces some defaults. The self-interaction correction (interaction of one electron with itself) is not taken into account correctly, which can induce an error in the calculations. For large molecules, DFT is often the only choice when considering the computational cost. However, it is still too expensive for very large systems such as model aerosol particles. Furthermore, there is a large set of functionals available nowadays and it may quite difficult to select the most suitable.[190–192] For systems too large even for DFT, a possible solution is therefore to use hybrid methods combining both classical and quantum approaches.

II.2.3 The ONIOM method

The ONIOM (Own N-layered Integrated molecular Orbital Molecular Mechanics) method is an example of a hybrid method combining quantum mechanics (QM) and molecular mechanics (MM) also called QM/MM method. The idea is to treat a reactive site of the system by quantum mechanics and the rest of the system by molecular mechanics. The QM part can be treated by methods seen previously (HF, MP2, DFT, CCSDT, etc.) and the MM part by a classical force field like AMBER. As the ONIOM method is a subtractive method, the energy corresponds to the sum of the energy of all the systems treated by molecular mechanics E_{MM}(QM+MM) plus the energy of the isolated subsystem treated by quantum mechanics E_{QM}(QM) minus the energy of the isolated subsystem treated by molecular dynamics E_{MM}(QM) (see Figure 45 and equation 84):

$$E_{QM/MM}=E_{MM}(QM+MM)+E_{QM}(QM)-E_{MM}(QM) \quad 84$$

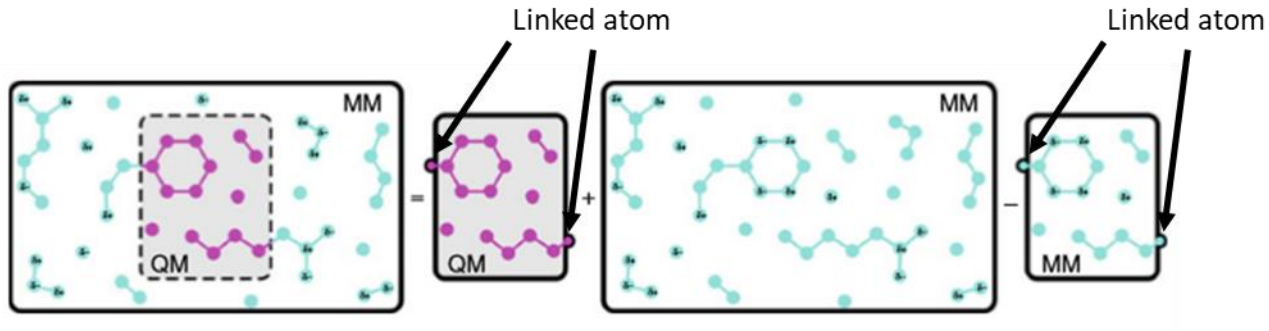

Figure 45: Substractive QM/MM coupling as implemented in ONIOM.[193]

For proteins or large molecules, the problem is to find where the QM part can be cut. When a covalent bond is cut, a link atom may be added in order to keep a good treatment of the bond. In our model of aerosols, the QM/MM boundary is between non-bonded atoms, so there is no need for a link atom. To take into account interface effects, we can use either mechanical embedding (ME), which includes the pair potential between QM atoms and MM atoms in the MM part, or electrostatic embedding (EE), which includes the partial charges of MM atoms in the Hamiltonian of the QM part (polarization of the QM region by the MM part).[164,194]

II.2.4 Conclusion on the quantum mechanics methods

The different methods have different computational costs and are more or less accurate. Table 14 summarizes the methods introduced previously.

Table 14: Summary of the different methods used in quantum mechanics

Method	Cost	Comment
HF	N_{basis}^4	Basis of the *ab initio* methods Does not take into account the electronic correlation
MP2	N_{basis}^5	Perturbative method
MP4	N_{basis}^7	Perturbative method
CCSD	N_{basis}^6	Method that adds singled and doubled excitations
CCSD(T)	N_{basis}^7	Method that adds singled and doubled excitations The tripled excitation is treated by a perturbative method
CCSDT	N_{basis}^8	Method that adds singled, doubled, and tripled excitations
DFT	N_{basis}^4	Semi-empirical method based on electronic density
ONIOM	Depends on the QM part	Method that treats part of the system with quantum mechanics and the rest with molecular mechanics Allows the treatment of large systems

According to Jensen (2013),[164] considering a medium-sized basis set, the order of accuracy often observed is as follows:

$$HF << MP2 < CCSD < MP4 < CCSD(T) < CCSDT$$

The accuracy of the DFT strongly depends on the functional chosen to treat the system. In any case, the accuracy depends also on the size of the basis set. Typically, at least a triple-zeta basis set should be employed, if possible. But, contrary to pure *ab initio* methods, an increase of the basis set size in DFT does not necessarily guarantee an improvement of the quality of the results.

In order to get high accuracy with a reasonable computational cost, many literature[133,195] studies first use a low-cost method to get a good geometry of the system and then correct the energy using a high accuracy method in a so-called single point energy calculation (computation of the energy at the geometry given as input). Some studies have shown that geometries obtained at the MP2 level are quite close to the much more expensive CCSD(T).[164,196]

II.3 Treatment of reactivity

II.3.1 Transition State Theory

In order to compute the theoretical rate coefficient of a chemical reaction, one can use the transition state theory, TST. The first step is to find the geometry of the transition state (TS). The potential energy surface (Figure 46) has to be scanned in order to find the first-order saddle point (maximum on the reaction coordinate and minimum on the other coordinates). This point connects reactants to products and is generally characterized by a single "imaginary" frequency, because the curvature of the surface at the TS is reversed compared to the equilibrium geometry. Once this TS is found, the energy of the reaction barrier or activation energy E_a can be computed using Equation 85:

$$E_a = E_{TS} - \sum E_{Reactant} \qquad 85$$

with E_{TS} the energy of the TS and $E_{reactant}$ the energy of the reactants.

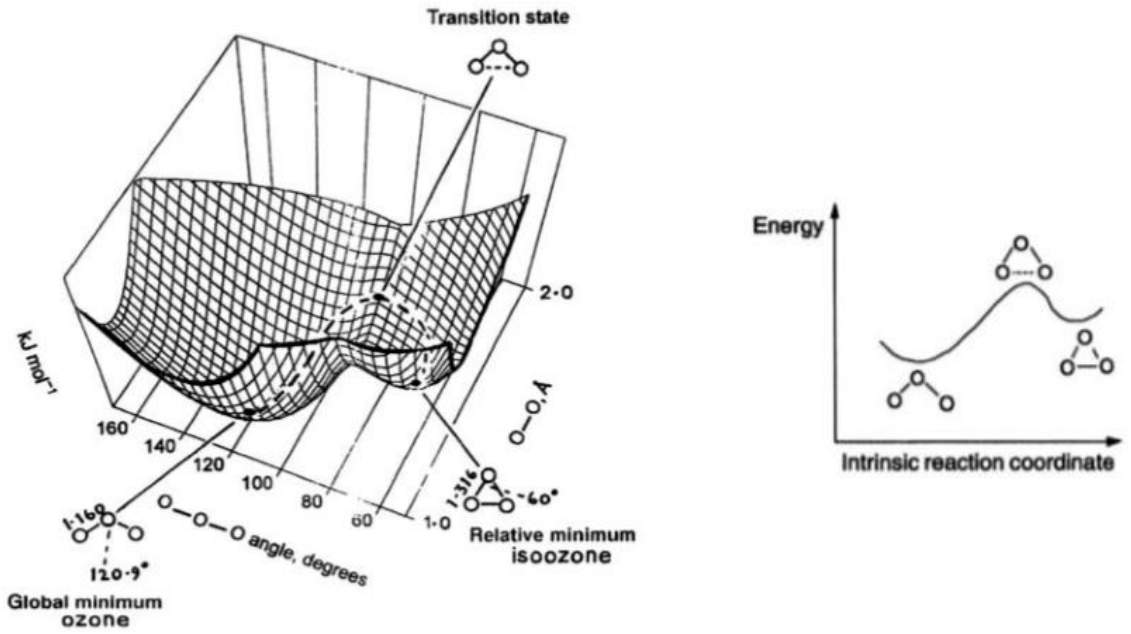

Figure 46: Schematic of a reaction path (case of isomerization of ozone).[164]

In order for the reaction to take place, the reactants have to collide first. The collision rate can be described (in a purely classical picture) by equation 86:

$$Z_{12} = \pi b_{max}^2 v_r n_1^* n_2^* \qquad 86$$

where b_{max} is the sum of the radius of the two reactants, v_r is the relative velocity of the reactants, n_1^* and n_2^* the number of molecules per unit of volume for reactants 1 and 2, respectively. Since a reaction occurs only when the energy is sufficiently high to exceed the barrier, Equation 86 has to be multiplied by the Boltzmann factor, $\exp(-E_a/kT)$, leading to the expression of the classical reaction rate (Equation 87) and the definition of the rate coefficient k(T). [164,197]

$$v = \pi b_{max}^2 v_r \exp\left(\frac{-E_a}{kT}\right) n_1^* n_2^* = k(T) n_1^* n_2^* \qquad 87$$

II.3.2 Activated complex theory

However, equation 87 overestimates the rate coefficient because the reactants may not be well oriented during the collision. According to the activated complex theory, one may write the rate coefficient as a function of the partition function of the reactants and the activated complex (corresponding to the TS). Then k(T) in equation 87 can be expressed by equations 88 or 89 in the case of a unimolecular rate coefficient or a pre-reactive Van der Waals complex.

$$k(T) = \frac{k_b T}{h} \frac{q^{TS}}{q^a q^b} \exp\left(\frac{-E_a}{kT}\right) \qquad 88$$

$$k(T) = \frac{k_b T}{h} \frac{q^{TS}}{q^a} \exp\left(\frac{-E_a}{kT}\right) \qquad 89$$

with k_b the Boltzmann constant, q^{TS} the partition function per unit of volume of the transition state, q^a the partition function per unit of volume of the reactant A and q^b the partition function

per unit of volume of the reactant B. The partition function can be interpreted as a number of possible states for the system at a given energy. The partition function depends on the translation, the rotation, the vibration degrees of freedom and the energy levels of the molecule. The partition function per unit of volume can be computed using equation 90:

$$q = \frac{z}{V} = \frac{z_t z_r z_v z_e}{V} \quad 90$$

where V is the volume, z the total partition function, z_t the translational partition function, z_r the rotational partition function, z_v the vibrational partition function and z_e the electronic partition function. The expression of each particle function is shown in Table 15.[197]

Table 15: Partition functions for molecular degrees of freedom.[197]

Type of Motion	Partition Function	Order of Magnitude
Translational, three-dimensional, per unit volume	$z_t/V = (2\pi mkT)^{3/2}/h^3$	10^{24} cm^{-3}
Rotational, linear molecule	$z_r = 8\pi^2 IkT/h^2\sigma$	10^2
Rotational, nonlinear molecule	$z_r = [\pi^{1/2}(8\pi^2 kT)^{3/2}/h^3\sigma] \times (I_A I_B I_C)^{1/2}$	10^3
Vibrational, each degree of freedom, measured from the lowest (zero point) vibrational level	$z_v = [1 - \exp(-h\nu/kT)]^{-1}$	1 (high ν) 10 (low ν)
Electronic	$z_e = \Sigma\, g_i \exp(-\epsilon_i^e/kT)$	1

Notes: I is the moment of inertia; ν is the vibrational frequency; ϵ_i^e are the electronic energy levels, g_i is the degeneracy, and σ is a symmetry number (e.g., $\sigma = 2$ for a homonuclear diatomic molecule).

Finally, a last effect has to be taken into account. This effect is the tunneling (*Figure 47*). Indeed, as the proton can tunnel through the activation barrier, a correction in the rate coefficient is mandatory. Liu et al.[198] have developed a correction factor κ_{WKB} (Equations 92 and 93) based on the Wentzel-Kramer-Brillouin approximation.[199] So the corrected rate coefficient is given by Equation 91.

$$k_{tunneling}(T) = \kappa_{WKB} k(T) \quad 91$$

$$\kappa_{WKB} = \left(1 + e^{2\theta(E)/\hbar}\right)^{-1} \quad 92$$

$$\theta(E) = \int_{r_a}^{r_b} \sqrt{2m(V(r) - E)}\, dr \quad 93$$

where $\theta(E)$ is the barrier penetration integral, m the mass of the tunnelling particle, r_a and r_b the two classical turning points of the path and E the energy of the path between the two points.

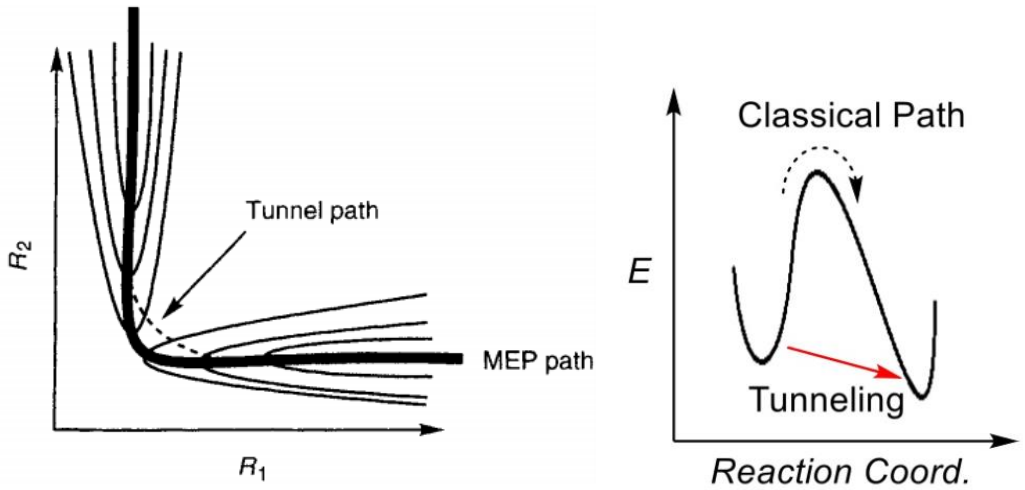

Figure 47: Contour plot illustration of the tunneling path[164,200]

Another approximation is by using the Eckart potential function in order to get the correction function Γ* (equation 94) which is defined as the ratio of the quantum mechanical to the classical mechanical barrier crossing rate.

$$\Gamma^* = e^{\frac{V_1}{k_b T}} \int_{E_a}^{\infty} K e^{-\frac{E}{k_b T}} \frac{dE}{dT} \qquad 94$$

where V_1 is the height of the potential barrier, and K is the transmission probability for tunnelling. K depends on E and three other parameters function of the shape of the barrier.[201]

II.4 Analysis methods

Several tools have been developed to analyze the results provided by molecular dynamics and quantum mechanics calculations. This section presents the tools that have been used in this work.

II.4.1 Binding energy

To get an information on the cohesion of the system, the binding energies can be computed. This energy corresponds to the sum of the Coulombic and Van der Waals interactions (equation 95) between one molecule and the others (intermolecular).

$$E_b = \sum_{i=1}^{N} \sum_{j>i} \frac{q_i q_j}{\varepsilon r_{ij}} f_{ij} + 4\varepsilon \left[\left(\frac{r_0}{r} \right)^{12} - \left(\frac{r_0}{r} \right)^{6} \right] f_{ij} \qquad 95$$

with E_b the binding energy. A distribution can be extracted from the various configurations sampled along the molecular dynamics trajectory.

In the case of quantum mechanics, the binding energy is simply found by subtracting the energy of each monomer $E_{monomer}$ of a cluster to the global energy of the cluster $E_{cluster}$ (Equation 96). It should however be noticed that for small basis sets, the so-called "basis set superposition error" should be taken into account.[164]

$$E_b = E_{cluster} - \sum E_{monomer} \quad 96$$

II.4.2 Radial distribution function

Radial distribution functions g(r) provide an information about the structure of a system. This function is computed according to equation 97:

$$g(r) = \frac{\frac{1}{N}\sum_i \langle \sum_{i' \neq i} \delta(r - \|\overrightarrow{r_{i'}} - \overrightarrow{r_i}\|) \rangle}{\rho_0 4\pi r^2} = \frac{\rho(r)}{\rho_0} \quad 97$$

with g(r) the radial distribution function, r the radius, ρ(r) the density at radius r, ρ_0 the mean density, $\|\overrightarrow{r_{i'}} - \overrightarrow{r_i}\|$ the distance between atoms i and i' (Figure 48) (by definition $\delta(r - \|\overrightarrow{r_{i'}} - \overrightarrow{r_i}\|)$ is equal to 1 if r is equal to $\|\overrightarrow{r_{i'}} - \overrightarrow{r_i}\|$ otherwise it is equal to 0), N the number of atoms.

The coordination number can also be computed by equation 98:

$$CN = \int_{r_i}^{r_e} 4\pi r^2 \rho_0 g(r) \quad 98$$

with CN the coordination number, r_i the internal radius and r_e the external radius.

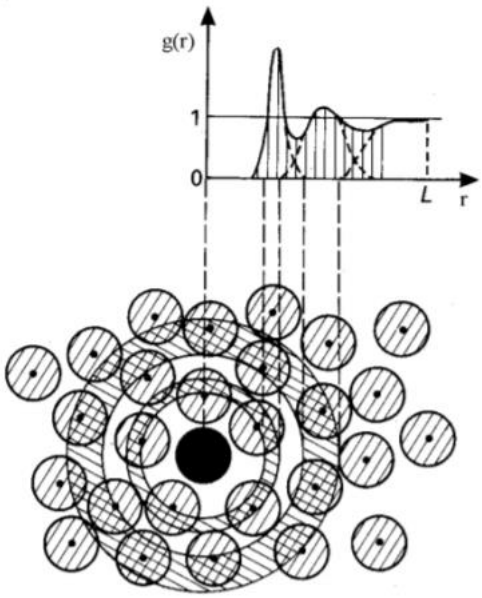

Figure 48: Construction of a radial distribution function[202]

II.4.3 Connolly surface

The surface of a particle can also be analyzed by means of a Connolly surface or solvent accessible surface.[203] This method consists in probing the surface by rolling a Van der Waals sphere on it (see Figure 49). The atomic radius of the probe atom on the surface that we want to analyze is generally fixed to the Van der Waals radius of the molecule that is stuck on the

surface. The analysis of the surface distribution per type of atoms can also be performed by this method.

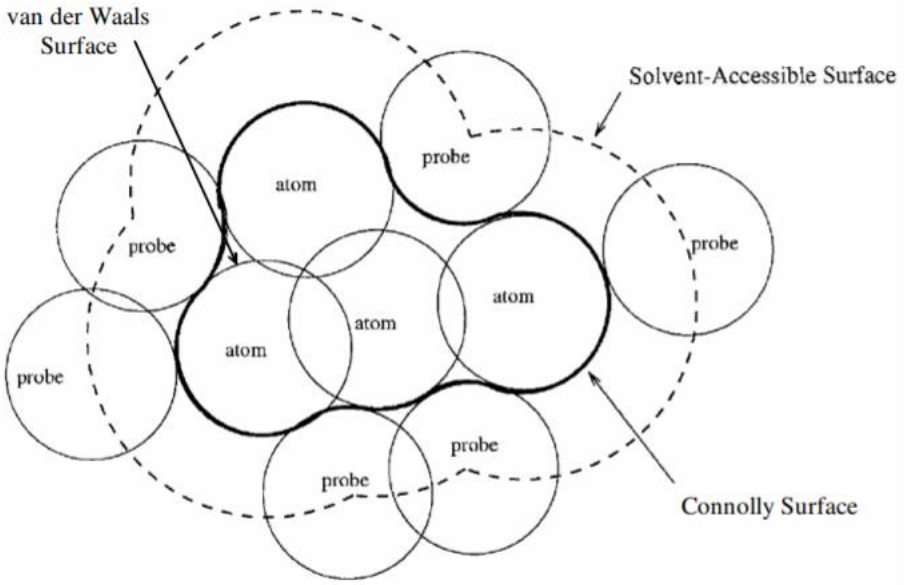

Figure 49: Schematic for the probing of a Connolly surface or solvent accessible surface.[204]

II.4.4 Autocorrelation function

One way to analyze the dynamics of hydrogen bonds within the particles is to look at the corresponding autocorrelation function as introduced by Luzar and Chandler.[205] Denoting h(t) equal to unity in the case of two molecules forming a hydrogen bond and zero otherwise, we can compute the autocorrelation function using equation 99:

$$c(t) = \frac{\langle h(0)h(t)\rangle}{\langle h\rangle} \qquad 99$$

with h(0) the operator of the hydrogen bond at time equal to zero, h(t) the operator of the hydrogen bond at time t, and ⟨h⟩ the average of h(t). The autocorrelation function represents the probability for the hydrogen bond to be intact at time t. This function tends to zero at an infinite time.

According to how fast the function decreases, we can estimate the state of the system. For short simulations, if the autocorrelation function decreases rapidly, we are in the case of a liquid-like state. But if the autocorrelation function remains high, it means that we are in glassy-like state and the system evolves too slowly to determine a significant change, meaning an autocorrelation function close to zero.[205–207]

CHAPTER 3: CHARACTERIZATION OF THE AEROSOL FLOW TUBE AND DEVELOPMENT OF A METHODOLOGY FOR HO_2 UPTAKE MEASUREMENTS

The aerosol flow-tube (AFT) built in this work has been described in Chapter 2:. In the following sections, we present experiments carried out to characterize (1) the generation of organic aerosols and peroxy radicals in the AFT, (2) their wall loss rates, and (3) the contact time between radicals and aerosols. We then describe the methodology developed to conduct uptake experiments and to derive uptake coefficients of HO_2 onto glutaric acid aerosols.

I Characterization of the AFT

I.1 Parameterization of the radical-aerosol contact time

For the AFT setup described in chapter 2, the contact time between aerosols and radicals is varied by changing the position of the central injector, which injects the radicals inside the aerosol flow. In order to determine the relationship between the contact time and the injector position, we carried out experiments using the setup shown in Figure 50. A Proton Transfer Reaction-Time of Flight Mass Spectrometer (PTR-ToFMS) was used to quantify the residence time of a pulse of toluene in the AFT after its injection through the injector. The setup required to synchronize the PTR-ToFMS acquisition with the pulse injection using a solenoid valve controlled by the instrument. The pulse was then detected at the AFT outlet. The time elapsed between injection and detection corresponds to a sum of residence times in the injector and AFT (radical-aerosol contact time). During an experiment, the injector was moved to different positions to parameterize the contact time as a function of the injector position. The flow rate in the injector was set at 1.3 Standard Liter Per Minute (SLPM) (based on the experiment of George et al.[58]) for all experiments, whereas different total air flow rates ranging from 4 to 10 SLPM were used in the AFT.

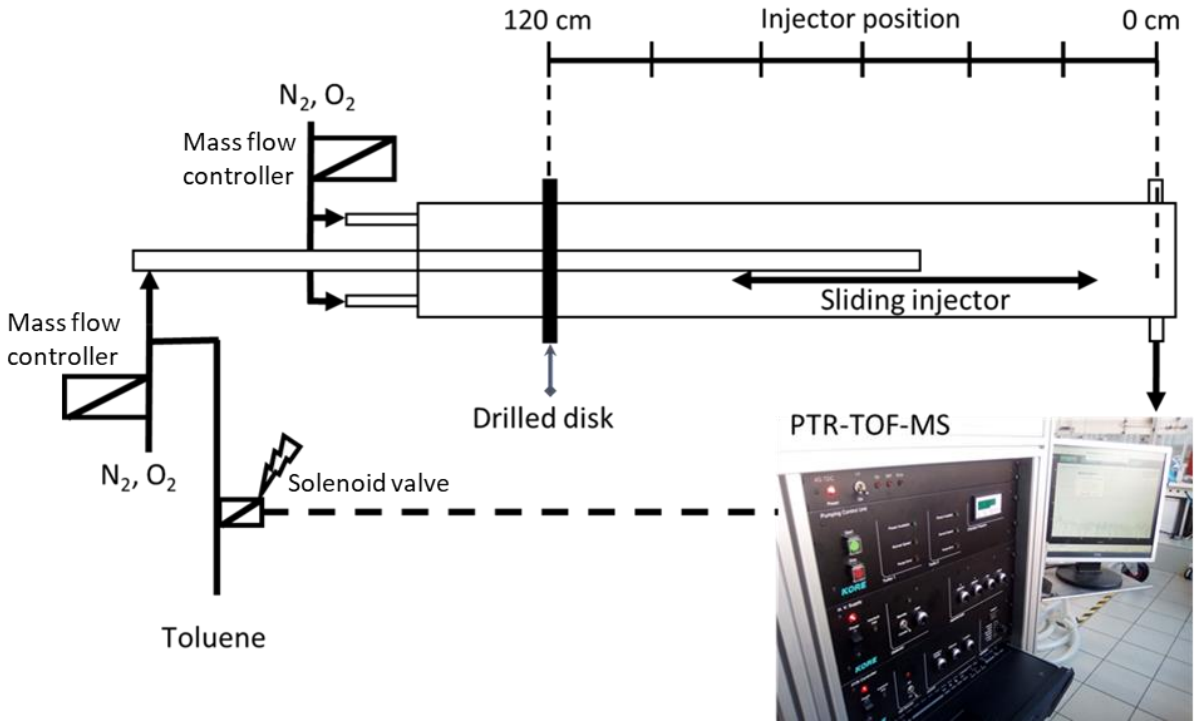

Figure 50: Experimental setup used to parameterize the radical-aerosol contact time as a function of the injector position..

To quantify the elapsed time between the toluene injection and its detection, we determined an averaged pulse detection time as gas-phase diffusion leads to a significant axial dispersion of the toluene molecules (Figure 51). In this study, the pulse detection time t_{fin} was determined in order to get half of the measured signal on each side of t_{fin}. Concerning the injection time, t_{ini} was set as half the time of the injection duration (Figure 51). The pulse residence time inside the (i) injector (+ PTR-ToFMS sampling line) and (ii) AFT can be derived from equation 100.

$$t_{measured} = t_{fin} - t_{ini} = x_{pos} f + t_0 \quad (100)$$

where $t_{measured}$ is the time which has elapsed between the pulse injection (t_{ini}) and its detection (t_{fin}), x_{pos} the position of the injector, t_0 the pulse residence time in the injector (and the PTR-ToFMS sampling line) and f the position-time conversion factor (s/cm) in the AFT. A linear fit between measured times and positions provides the conversion factor (f) and the residence time inside the injector (t_0).

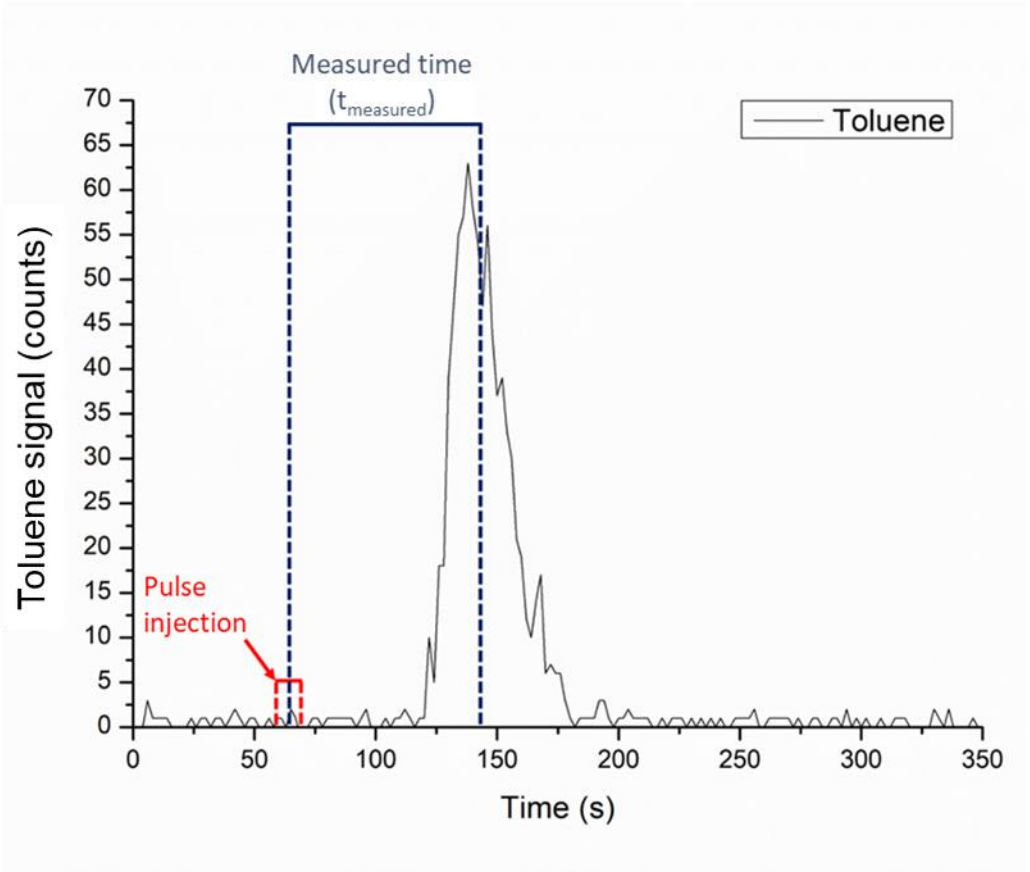

Figure 51: Residence time of a toluene pulse inside the injector and the AFT measured by PTR-ToFMS for a total flow rate of 6 SLPM.

Figure 52 shows the measured residence time ($t_{measured}$) after subtraction of the t_0 offset as a function of the injector position (x_{pos}) for different total air flow rates inside the AFT (4, 6, 8 and 10 SLPM). Each dataset can be fitted by a linear regression leading to conversion factors of 0.447 ± 0.005 (1σ), 0.247 ± 0.004, 0.155 ± 0.004 and 0.193 ± 0.005 s cm^{-1} for 4, 6, 8 and 10 SLPM, respectively. The average residence time (t_0) inside the injector and sample line was found to be 50.5 ± 0.9 (1σ) s.

Figure 53 compares the measured residence time with a calculated value assuming plug-flow conditions in the AFT. It is interesting to note that the measured contact times are within 5 to 20% of the calculated values, the dashed line being the 1:1 line. The AFT flow rate exhibiting contact times that are the closest to the one expected under plug-flow conditions is 6 SLPM. As a consequence, this flow rate was selected to perform uptake experiments, which in turn allows varying the contact time in the range 10-30 s. For uptake experiments, the flow rate in the injector was kept at 1.3 SLPM, similar to the flow conditions used above, while the aerosol flow rate was set to 4.7 SLPM. The latter is the sum of the flow coming from the aerosol generation system (approx. 1 SLPM) and the air flow coming from the dilution system (approx. 3.7 SLPM). Relative Humidity (RH) was adjusted in the dilution flow to control RH in the AFT.

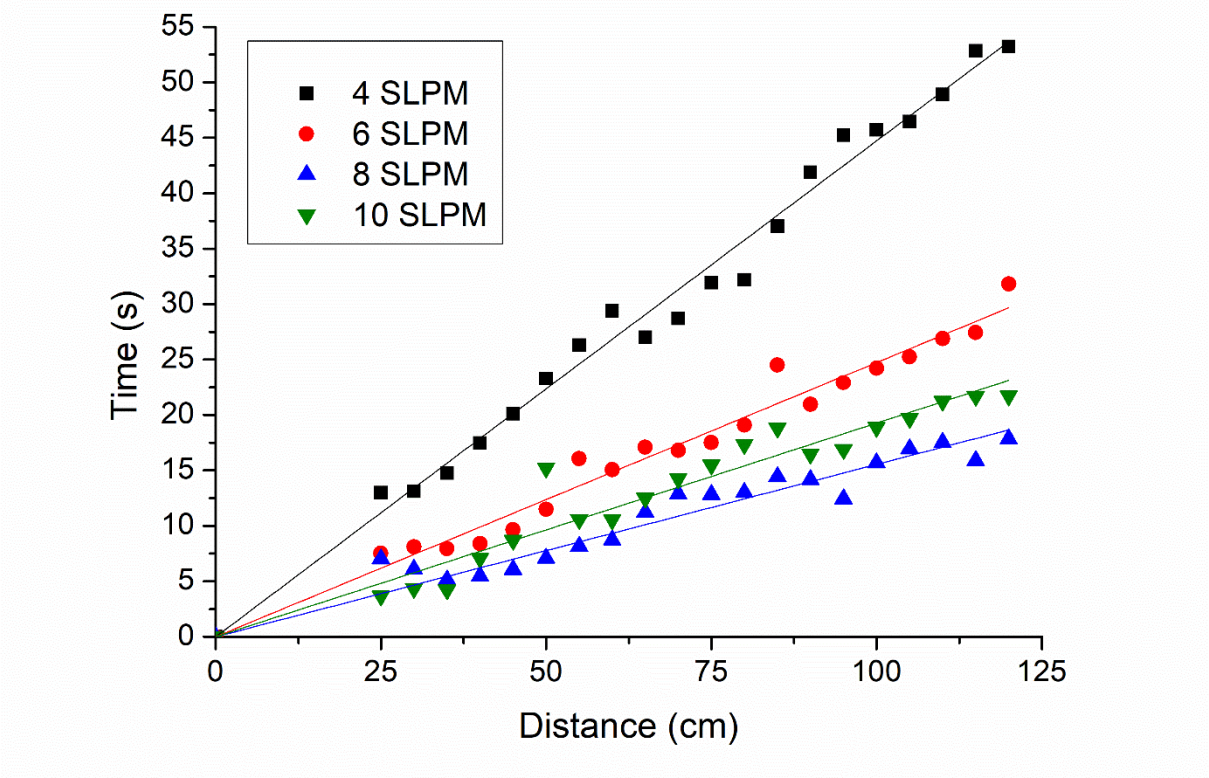

Figure 52: Plot of the contact time vs the injector position for various total flow rates in the AFT.

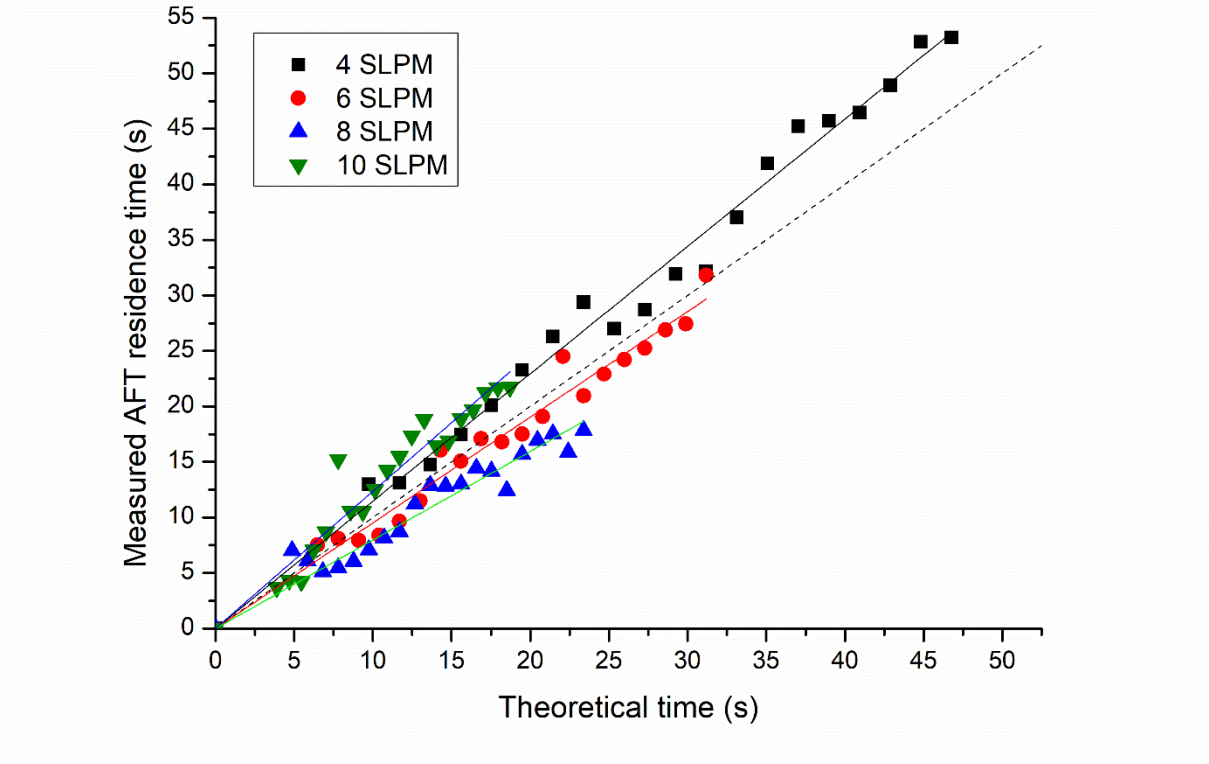

Figure 53: Scatter plot of measured AFT residence times vs. calculated residence times (assuming plug-flow conditions). The dashed line corresponds to the 1:1 line.

The experiments described above also showed significant differences in the pulse intensity over the reactor length as displayed in Figure 54. This figure shows that the pulse intensity is constant between 120 and 60 cm but starts increasing from 60 to 45 cm and then decreases from 45 to 20 cm. This effect is likely due to an incomplete mixing of the toluene pulse exiting the injector with the AFT air flow. Indeed, a mixing time of 21 s can be calculated for these experiments assuming plug-flow conditions (according to equation 18 with $D_{toluene}$ = 0.08 cm² s^{-1} from Erbil et al.[208]). The measured time corresponding to this mixing process (determined as the maximum peak) is about 11 s at a total AFT flow rate of 6 LPM. The difference between the experimental and calculated mixing times may be due to turbulences at the tip of the injector, which also promote mixing in addition to molecular diffusion. As discussed in chapter 2 section I.1, the mixing time should be lower for HO_2 since the diffusion coefficient for this species is faster than for toluene by a factor of ~3. These experiments helped to identify an area in the AFT (0-45 cm) where we cannot perform uptake measurements as the injector flow is not well mixed with the aerosol flow (mixing time of about 11 s).

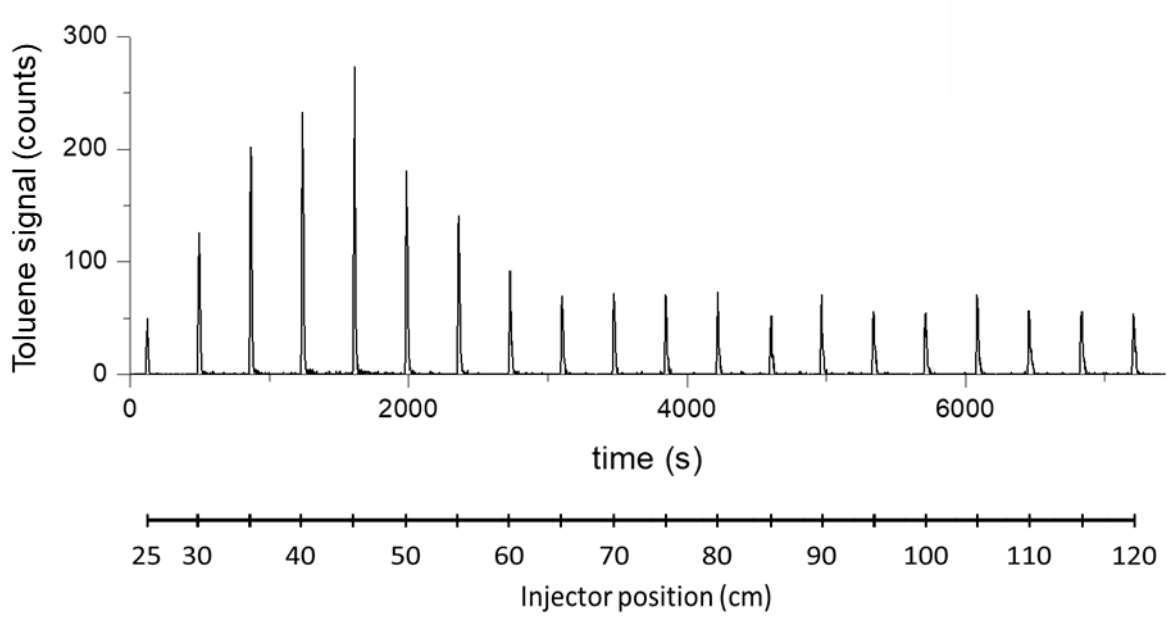

Figure 54: Peak distribution of toluene pulses over different positions of the injector for an AFT flow rate of 6 SLPM. The time indicated on the x-axis is the measurement time from the PTR-ToFMS and is not related to the residence time in the AFT.

I.2 Characterization of the two aerosol generation setups

Two different aerosol generation systems (based on nebulization or nucleation) have been assembled and tested in order to assess their suitability for uptake experiments. Both the aerosol concentrations and size distributions were characterized, and the generation stability was evaluated.

I.2.1 Nebulization setup

This generation system was composed of an atomizer (TSI model 3076), a dryer containing silica gel (TSI model 3062) and a set of HEPA filters (Figure 55). The solution was prepared by diluting glutaric acid (99%, Sigma Aldrich) in pure water (UPLC_MS water). Synthetic air (5.0) was used as carrier gas for the atomizer at a flow rate of 1 SLPM.

The atomizer produces wet aerosols by spraying the solution and the dryer allows reducing the amount of water in the aerosol (chapter 2 see section I.2). The HEPA filters are used to either completely remove the aerosol (blank) or to dilute the aerosol concentration. In Figure 54, a dilution stage composed of two lines, one equipped with a HEPA filter, allows adjusting the amount of aerosols generated while keeping the total flow rate the same. This filter system has been used to perform uptake measurements at different aerosol concentrations (chapter 3 section II.1).

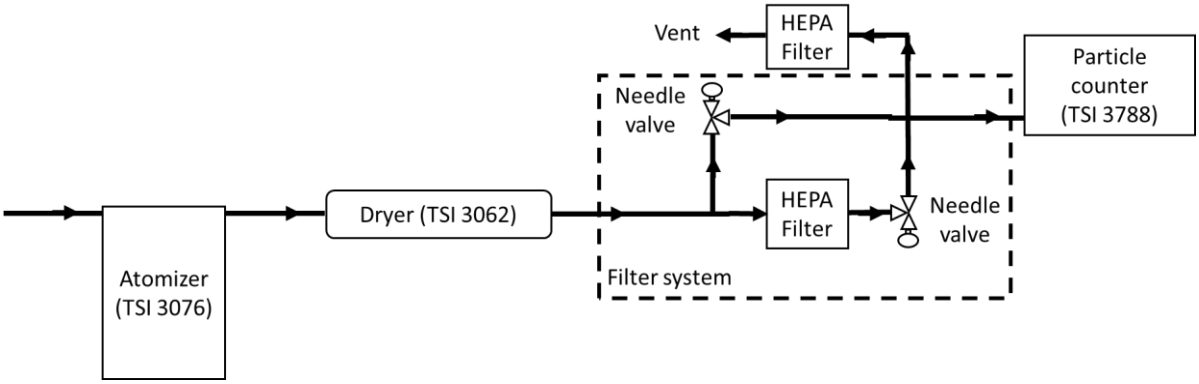

Figure 55: Experimental setup for generating aerosols by nebulization of a liquid solution

A particle counter (electrical classifier series 3080 + Nano water condensation particle counter (CPC) 3088, both from TSI) was used to sample the size distribution (SMPS mode) or the concentration of a specific size bin selected by the electrical classifier (CPC Mode). Indeed, for an uptake measurement, we can choose to either send the whole size distribution inside the AFT or one particular size bin at a time to study the effect of particle size on uptake coefficients. The latter can be done by placing a DMA at the entrance of the AFT to only select one size bin. Thus, the CPC mode provides the concentration of a selected size bin while the SMPS mode provides the concentration of the whole size distribution.

The classifier (DMA) sheath flow was set to 6 or 10 SLPM to be at least ten times larger than the sample flow rate of 0.6 LPM (recommended by the manufacturer). This sheath flow impacts the particle size range that can be measured as well as the width of the size bin that is selected, with a higher sheath flow allowing to shift the measurement window toward smaller particles and narrowing the bin width. The measurable particle size ranges from 11–385 nm for a sheath flow of 6 SLPM to a size range of 7–279 nm for a sheath flow of 10 SLPM.

As mentioned above, several tests were performed to (i) quantify the aerosol surface concentration that can be generated during an uptake experiment and to (ii) insure that the aerosol concentration is stable over the duration of a measurement step as defined in section II.1 (typically half an hour). The characterization experiments were performed under different operating conditions of glutaric acid concentration (2.5×10^{-3} to 2.5×10^{-2} M) and pressure at the entrance of the atomizer (1 to 1.6 bar).

I.2.1.1 Characterization of the aerosol concentration and size distribution

The first experiments were carried out to quantify the aerosol concentration produced by the generator and to assess its stability over time for various size bins in CPC mode. A glutaric acid solution of 5×10^{-3} M was used in the atomizer at various inlet pressures of 1.0, 1.2 and 1.6 bar. The glutaric acid concentration was chosen based on manufacturer recommendations for the TSI nebulizer (5×10^{-3} mol/L). If higher concentrations were used, multi-charged aerosols may be formed, which in turn could bias the quantification. Indeed, large aerosols can be detected as lower-size aerosols if multiple charges are present at their surface (mass over charge m/z ratio decreases while m is not changing).

Figure 56 shows the aerosol concentration averaged over 15 min after equilibration of the generation system. A maximum concentration ranging between 8.5×10^3 and 18.4×10^3 cm^{-3} corresponding to a maximum surface concentration of 0.8×10^8 and 1.9×10^8 nm^2/cm^3 respectively was observed for the 100 nm size bin when the entrance pressure was varied between 1 and 1.6 bar, the highest pressure leading to the highest concentration.

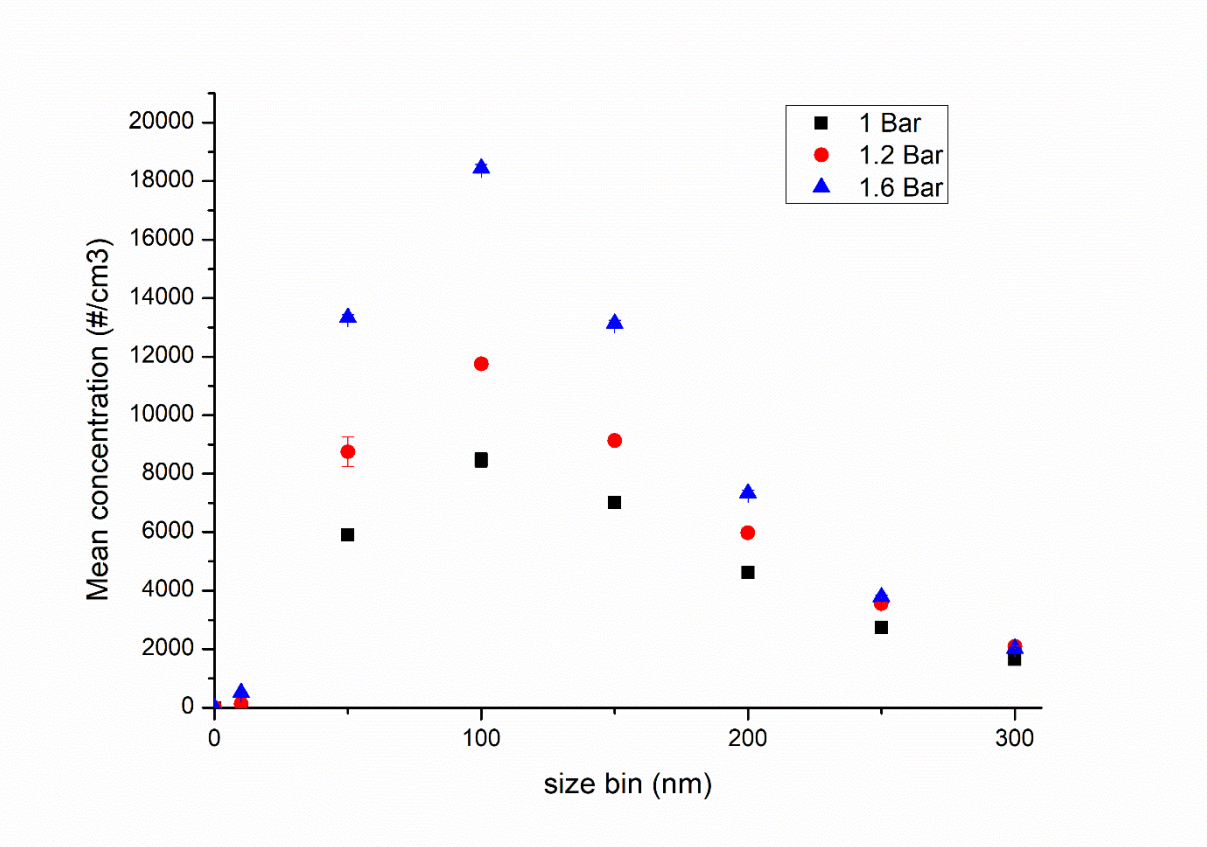

Figure 56: Concentration of aerosols generated by nebulization of a 5×10^{-3} M glutaric acid solution at 3 entrance pressures in the atomizer. Error bar are 3σ

The concentration was found to be very stable over 15 minutes as shown by the error bars (RSD lower than 5%) in Figure 56, which is suitable for uptake experiments lasting around 20 minutes. However, the surface concentration generated with this system (CPC mode) is about one to two orders of magnitude lower than that observed in experiments carried out by George et al. 2013.[58] Based on the low uptake coefficient of HO_2 reported for glutaric acid aerosols (see chapter 1 section II.2.2), the surface concentration generated in these experiments is too low to

observe a significant concentration decay of HO_2 on the timescale of an uptake experiment (10-30 s).

While it would be tempting to increase the entrance pressure in the atomizer to increase the surface concentration, it could also create multiple charges on aerosols, and as a consequence, a bias in the measured distribution. The recommended pressure is about 1 bar.

Due to the too-low aerosol concentration generated at a specific size bin, the CPC mode will not be used for uptake experiments in this work. However, it may be usable with an aerosol whose nature produces higher surface concentrations or with an aerosol exhibiting a higher uptake coefficient.

I.2.2 Dependence of the aerosol size distribution on the glutaric acid concentration in solution

As the CPC mode is not suitable for uptake measurements of HO_2 onto glutaric acid aerosols, similar tests were performed using the SMPS mode to assess the total aerosol concentration that could be provided to the AFT if the whole aerosol distribution was used. The classifier sheath flow was set at 10 SLPM and the glutaric acid concentration at 5×10^{-3} M.

As shown in Figure 57, higher aerosol concentrations have been observed compared to Figure 56 due to a larger size bin than in CPC mode. For instance, the concentration generated for the 100 nm bin is 5 times larger in SMPS mode than in CPC mode. Considering the whole aerosol distribution introduced in the AFT, the increase in concentration is about a factor of 500 for the SMPS mode, which translates in an increase of surface concentration by a factor of 54. The pressure tends to increase the concentration of particles over the whole mode by a factor of 1.9 and 2.3 for the 1.4 bar and 1.6 bar pressures, respectively

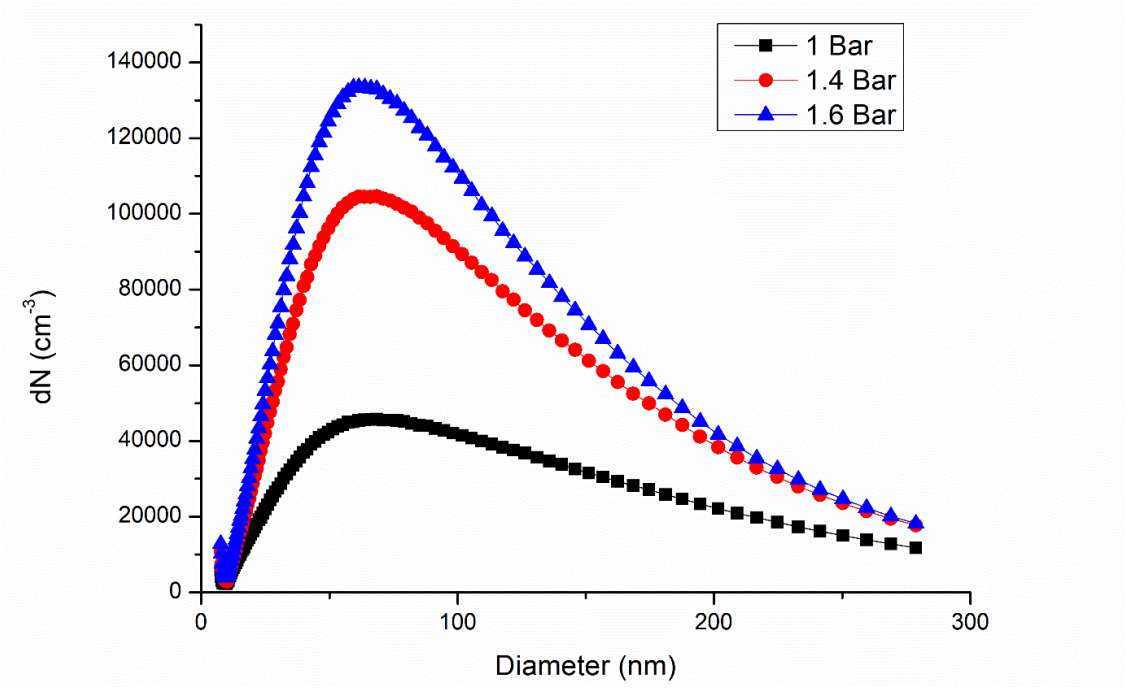

Figure 57: Glutaric acid aerosols size distribution in SMPS mode at various entrance pressures in the atomizer. Glutaric acid concentration of 5×10^{-3} M.

A stability test carried out at 5 × 10^{-3} M of glutaric acid and an entrance pressure of 1 Bar is shown in Figures 58 and 59 to check the generation stability over two hours. The results are shown in Figure 58 for the whole distribution and in Figure 59 for a few selected size bins (85.1, 140.7 and 232.9 nm). Error bars in Figure 58 are 1σ standard deviation. These results indicate that the concentration varies within 6% at the modal diameter of 85-90 nm.

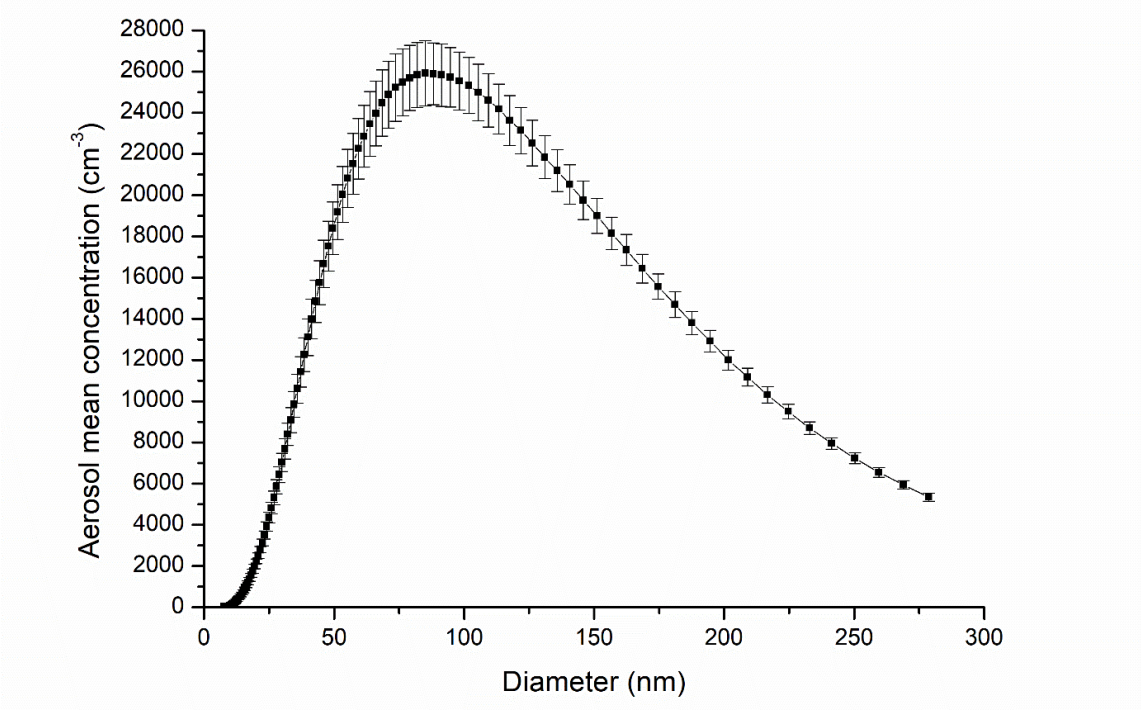

Figure 58: Size distribution of glutaric acid aerosols formed by atomization of a 5 × 10^{-3} M glutaric acid solution. Error bars are 1σ standard deviation over two hours of experiment.

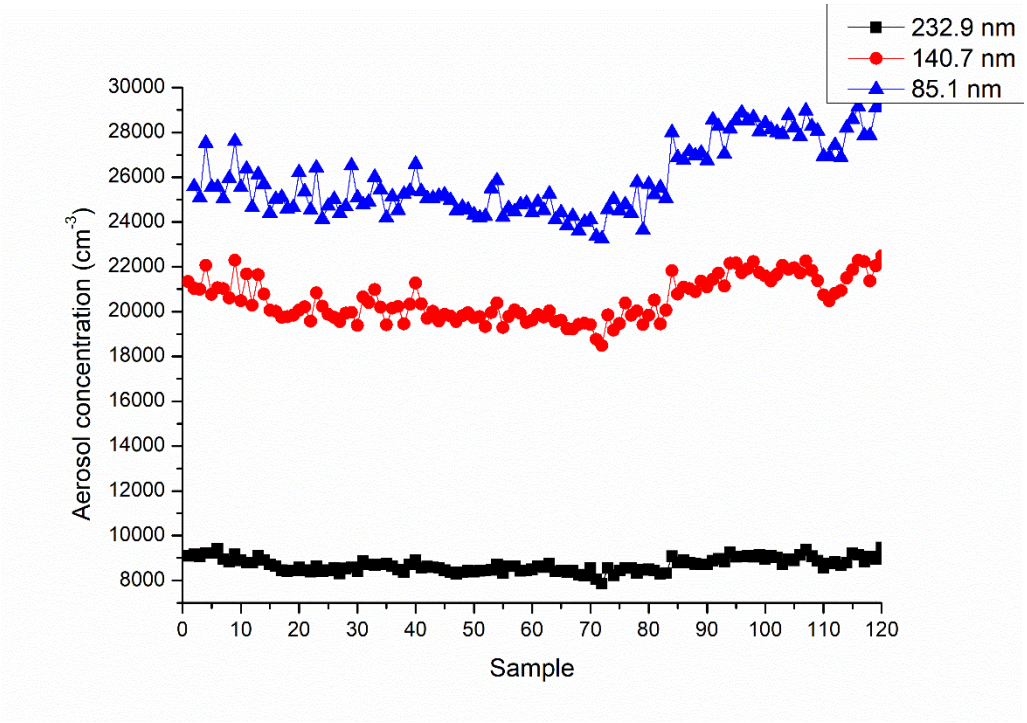

Figure 59: Stability of glutaric acid aerosols formed by atomization of a 5 × 10^{-3} M glutaric acid solution over two hours of experiment for three size bins in SMPS mode.

The influence of the acid concentration level has also been studied at a pressure of 1 bar. Three concentrations have been used:

- a concentration of 5.0×10^{-3} M as above, recommended by the manufacturer (reference)
- a concentration 5 times larger than the reference one: 2.5×10^{-2} M
- a concentration 5 times lower than the reference one: 1.0×10^{-3} M

The results are shown in Figure 60. Error bars are 3σ observed over a duration of 2 hours. This figure shows that aerosol concentrations vary only within 3% (on average considering 3σ error) for the three glutaric acid solutions, which confirms the good stability overtime. This figure also shows that the glutaric acid concentration has a large impact on the generated aerosol concentration, with an increase by approximately a factor of 4.5 when the acid concentration is increased by a factor of 25 (from 1×10^{-3} to 2.5×10^{-3} M). In addition, the mode diameter is also observed to increase with the solution concentration, with a shift from approximately 60 nm at 1×10^{-3} M to 85-90 nm at 2.5×10^{-3} M.

However, increasing the glutaric acid concentration above a certain threshold (as already mentioned the manufacturer recommends 5×10^{-3} M) may lead to electrostatic effects as observed when the entrance pressure is increased, which may in turn induce a bias in the measurements due to the presence of multiple charges on aerosols. To determine whether this shift appears, an experiment with a particle counter based on a different detection method (other than electric mobility classification) would be useful to compare both size distributions.

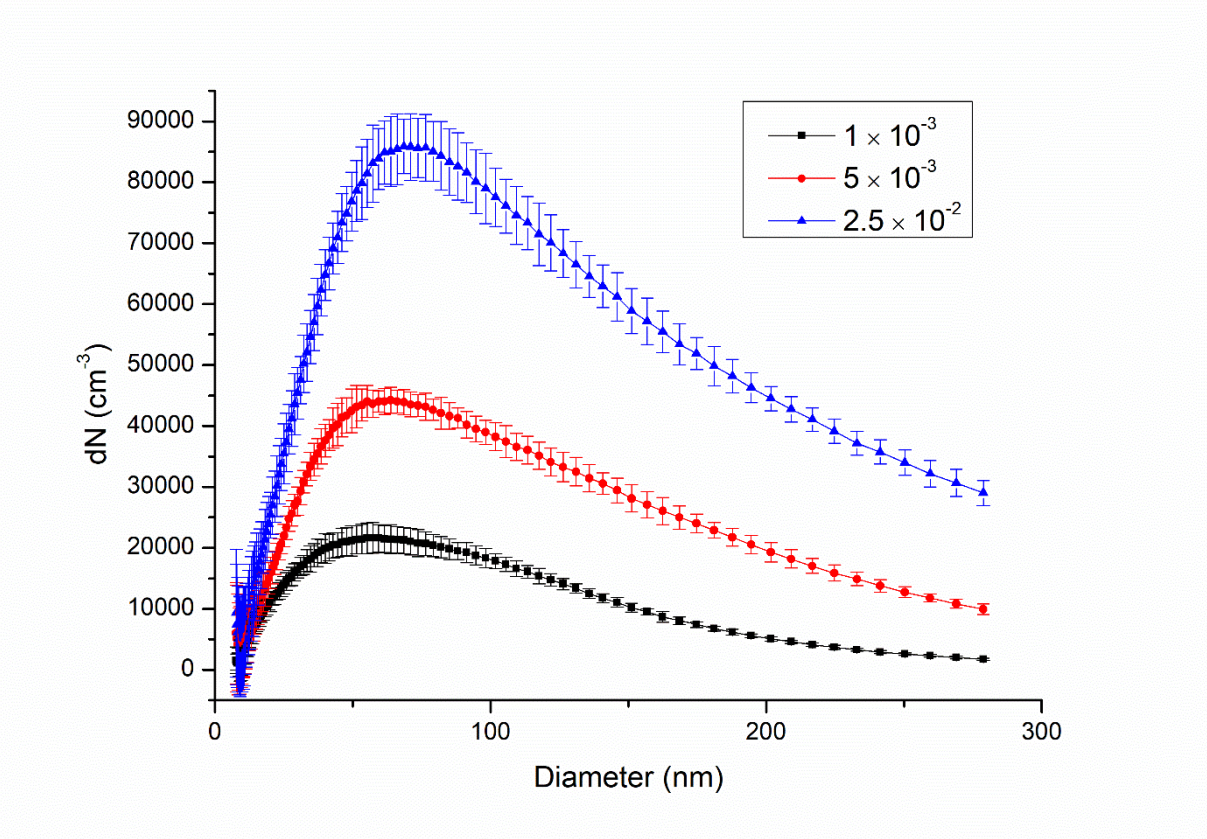

Figure 60: Aerosol size distribution for various glutaric acid concentrations (mol L^{-1}) in solution for an entrance pressure of 1 bar in the atomizer. Error bars are 3σ.

In order to measure the HO_2 mass accommodation coefficient during uptake experiments, the glutaric acid aerosols can be doped with copper to catalyze the HO_2 consumption onto the aerosol surface (see chapter 1 section II.2.2), which in turn will increase the uptake rate of HO_2 until the accommodation rate is reached. Some experiments were performed to ensure the feasibility to work with such solutions; however since no uptake experiments could be performed with copper-doped glutaric acid aerosols due to lack of time, the results are only presented in Appendix D.

I.2.3 Nucleation setup

The nucleation setup built in this study is based on the work of Mendez et al.[148] The principle consists of heating pure glutaric acid to increase its vapor pressure and as a consequence its gas phase concentration. Then a small flow of dry zero air carries the organic vapors through a cooling system which induces their nucleation into particles.

Figure 61 shows a schematic of the setup consisting of a small Pyrex reactor, a cooling system and a buffer volume. The air flow rate flushing the reactor was set at 0.5 SLPM based on Mendez et al.[148] A flow of tap water (room temperature) was passed through the jacket of the cooling unit. The flow was initially set to come towards the reactor (referred to as backward flow in the following) in order to develop a negative gradient of temperature. However an inverted flow (referred to as forward flow) was also tested to check the effect of a positive temperature gradient on the nucleation process. The purpose of the buffer volume is to let the remaining glutaric acid vapors to condense onto particles. In addition, a cartridge of activated charcoal can be set at the output of the buffer volume to remove the excess of glutaric acid vapors before introducing the aerosols in the AFT. This cartridge was however not used in the experiments described below.

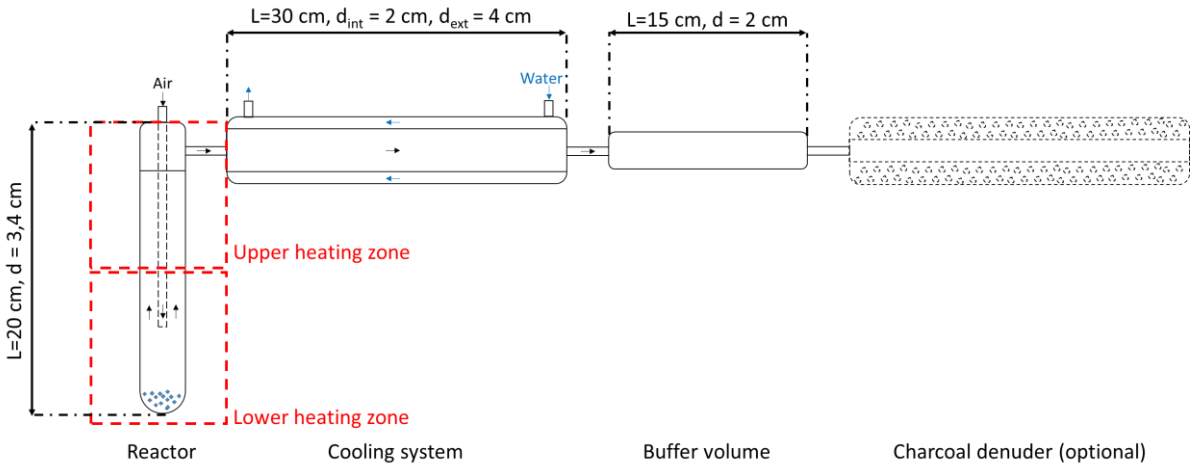

Figure 61: schematic of the nucleation setup for aerosol generation.

Two independent heating systems have been set, one on the lower part of the reactor, which allows heating the glutaric acid powder, and the other one on the upper part, which avoids the condensation of glutaric acid vapors on the reactor wall and tubing. The upper heating system is important to avoid clogging the tube located between the reactor and the cooling system (referred to as transfer line in the following).

Characterizing this nucleation system consisted in the determination of the best set of temperatures (both heated zones) that provides the highest concentration/surface of particles. However, as the particle size distribution will be cut by an impactor at the entrance of the AFT (in order to have a size range detected by the SMPS; see chapter 2 section I.5), the diameter of the particles has to be small enough, considering what the best conditions would be to generate a size distribution in the SMPS measurement range (between 10 and 385 nm at a classifier sheath flow of 6 LPM). Indeed these operating conditions would avoid technical problems linked to the efficiency of the impactor where particles larger than the cut off radius can still go through the impactor due to rebounce effects.

As the fusion temperature of glutaric acid is approximately 98°C and since this compound can decompose at temperatures higher than 302°C, we have investigated a range of temperatures comprised between 98 and 150 °C for the upper reactor section. For the lower section, the maximum temperature that can be reached with the heating element is about 140°C and the lower limit has been extended down to 88°C for this study, so the tested temperature was ranging from 88-140 °C.

The aerosol characterization has been carried out in SMPS mode and two types of diameter have been computed. The first diameter has been computed as the arithmetic mean $\bar{x}$ of the measured diameters using Equation 101 and the second as the geometric mean $\overline{x_g}$ using Equation 102. For the latter, Equation 103 provides the geometric standard deviation σ_g. The use of both diameter allows a better characterization of the size distribution mode.

$$\bar{x} = \frac{\sum_i \left(c_i D_{p,i}\right)}{C_{tot}} \quad 101$$

$$\overline{x_g} = \mathrm{Exp}\left[\frac{\sum_i \left(c_i \ln D_{p,i}\right)}{C_{tot}}\right] \quad 102$$

$$\sigma_g = Exp\left[\sqrt{\frac{\sum_i \left(c(\ln D_{p,i} - \ln \overline{x_g})^2\right)}{C_{tot}}}\right] \quad 103$$

where c_i is the concentration within a size bin i, $D_{p,i}$ the midpoint diameter of the size bin i, and C_{tot} the total concentration (sum of all size bins).

Results of the conducted experiments are shown in Figure 62. As can be observed in panels a and d, an increase of temperature in the upper section (T_{up}) leads to an increase of particle concentrations for all the temperatures that were tested for the lower section (T_{low}). This is likely due to a lower rate of condensation of organic vapors on the upper part of the reactor and inside the transfer line. Indeed, the concentration increases from 4.5×10^3 to 740×10^3 cm^{-3} at T_{low} = 123°C and from 64.6×10^3 to 812×10^3 cm^{-3} at T_{low} = 139°C. We only observe a global increase in aerosol concentration and the shape of the size distribution is not impacted.

Panel a, Figure 62 also clearly shows that the aerosol concentration increases with T_{low} due to a higher vapor pressure of glutaric acid in the reactor. For the lowest temperature of 88°C no particles are produced since glutaric acid is still solid under this conditions.

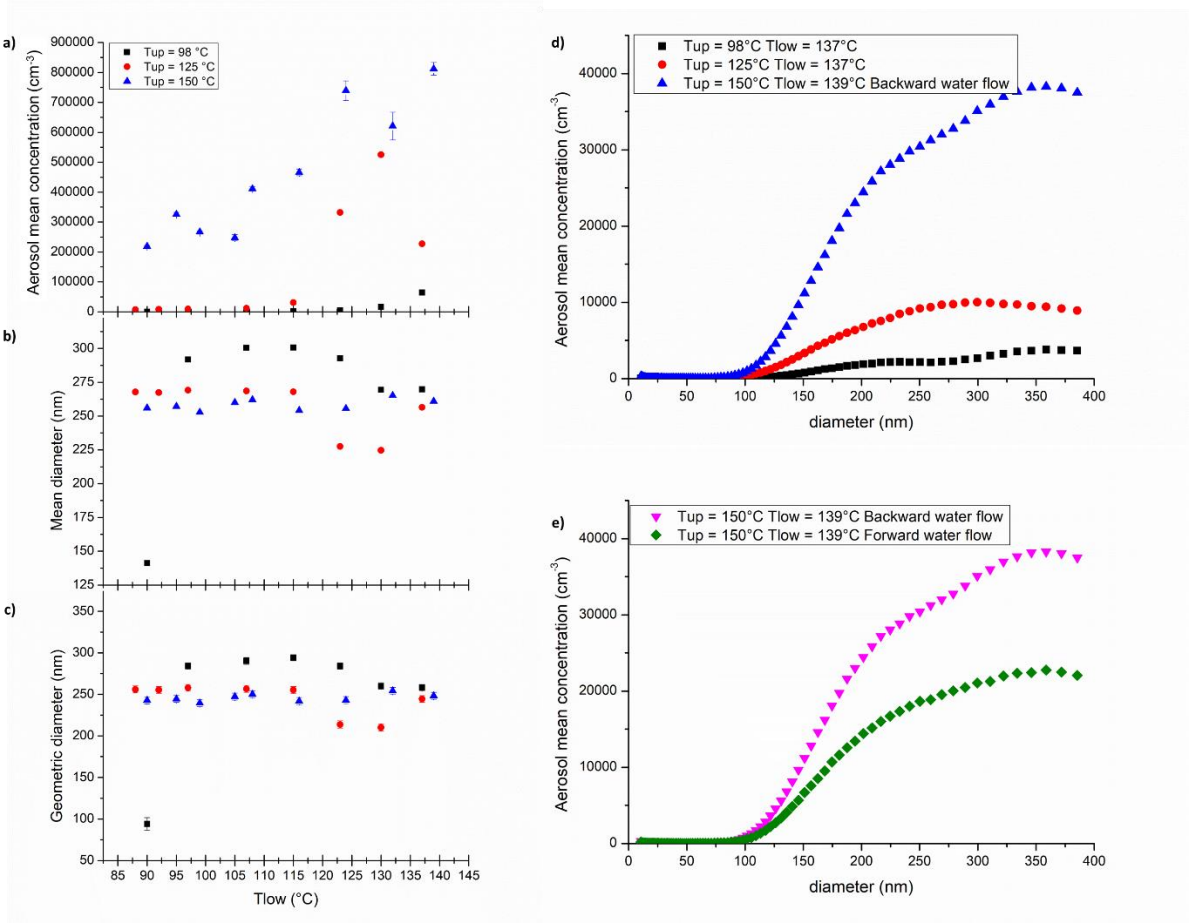

Figure 62: a) Total concentration of glutaric acid aerosols generated by nucleation vs. upper (T_{up}) and lower (T_{low}) reactor temperatures, b) particle mean diameter, c) particle geometric diameter, d) examples of size distributions produced for different set of temperatures, e) Comparison of size distributions observed using a backward (magenta) and a forward (green) water flow for the cooling system. Error bars are 3σ.

Panels b and c in Figure 62 show that both diameters are not impacted by the increase of temperature in both sections of the reactor, indicating that the size of the particles cannot be controlled within our range of operating conditions. This is confirmed by results shown in panel d where the aerosol concentration is observed to increase with the upper temperature but without a shift in size. The mean and geometric diameters are around 260 and 250 nm, respectively for the measured size range. Compared to the nebulization setup, the particles produced are larger by a factor of approximately 3.3. The sheath flow of 6 SLPM in the SMPS allows only the measurement of particles within the size range 10 to 385 nm, thus approximately half of the size distribution is outside the size range measured by the SMPS.

Panel e from Figure 62 shows the impact of using a positive temperature gradient in the cooling system (forward water flow). The positive gradient tends to reduce the particle concentration without shifting the mode of the aerosol population. This effect can possibly be explained by a higher condensation rate of organics on the wall at the entrance of the cooling system. In order to reach the largest concentration in aerosols a backward water flow is thus needed.

Finally, the optimal set of temperatures for this nucleation system is T_{low} = 139°C and T_{up} = 150°C since it allows generating the highest concentration of particles (812×10^3 cm^{-3}) with a mean diameter of 261 nm. This would translate into a maximum surface concentration

of 4.7×10^{-4} cm^2 cm^{-3} if a similar impactor than the one set on the SMPS was used to cut the aerosol distribution at the entrance of the AFT.

I.2.4 Conclusions on aerosol generation

Experiments performed with the nebulization setup have shown that stable surface concentrations can be produced within a range of 0.8×10^7 nm^2 cm^{-3} in CPC mode (with size selection at the entrance of the AFT) to 6.9×10^9 nm^2 cm^{-3} in SMPS mode (when the whole aerosol distribution is introduced into the AFT; Figure 63). In SMPS mode, the aerosol concentration is high enough to generate a significant uptake rate of HO_2 since Lakey et al.[51] were able to measure uptakes on glutaric acid aerosols at concentrations close to 10^9 nm^2/cm^3. On the contrary, the CPC mode method produces an aerosol concentration that is too low for these experiments. Increasing the aerosol concentration in CPC mode by adjusting parameters such as the entrance pressure or the concentration of glutaric acid in solution may lead to the formation of multiply-charged aerosols, which in turn would lead to artefacts in the measurements of the aerosol distribution and surface concentration. We have demonstrated that the nebulizer is also suitable for the formation of copper-doped aerosol which allows the measurement of HO_2 mass accommodation measurement for further studies.

The nucleation setup allows generating aerosols that are dryer than those formed by nebulization. The highest concentration reached in the size range measurable by SMPS is lower by a factor of 1.5 compared to the nebulization setup but is comparable when the surface concentration is considered. However, half of the distribution mode is outside the SMPS measurement range and thus cannot be quantified. Using the impactor at the entrance of the AFT should allow removing most of the aerosols from the unmeasured range but the rebounce effect could still lead to measurement artefacts in surface concentrations. Indeed, Figure 63 shows that for the nucleation setup, the largest particles will have a strong impact on the total surface concentration in the AFT. We therefore decided to use the nebulization system for the HO_2 uptake experiments with glutaric acid aerosols. The nucleation system could be eventually used in future experiments with other types of aerosols.

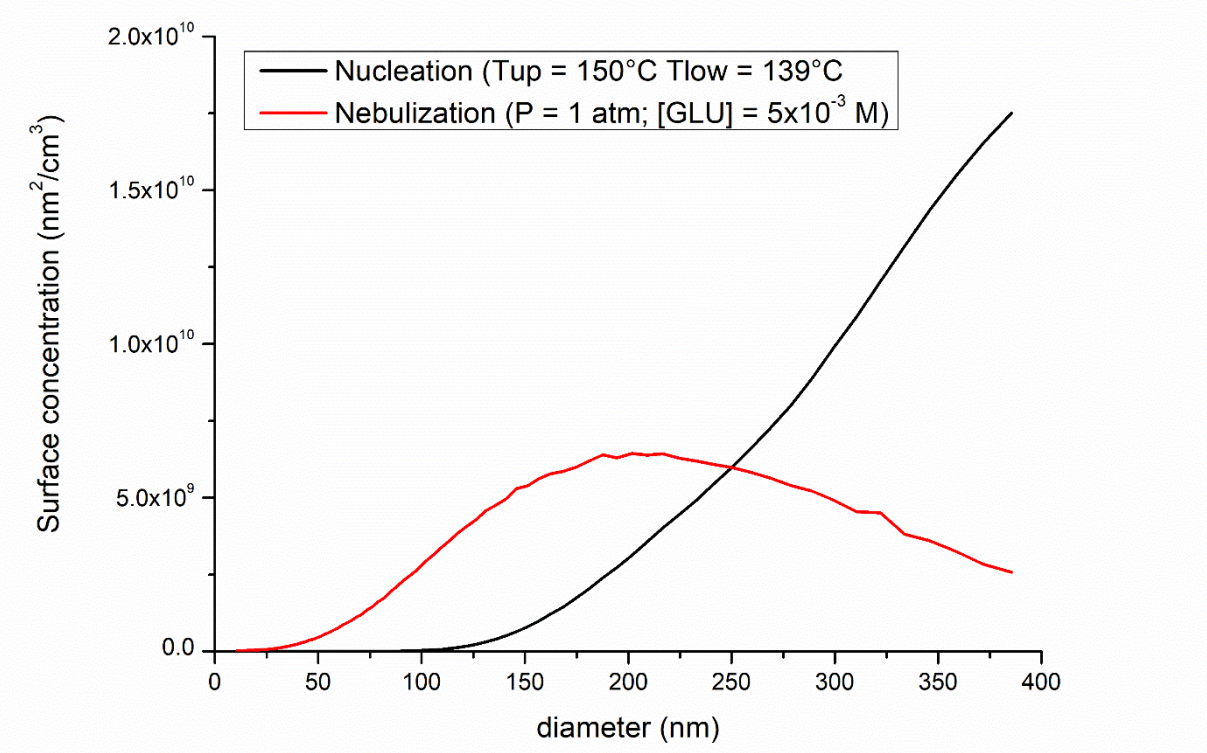

Figure 63: Comparison of surface distributions generated by the nebulization and nucleation setups for glutaric acid aerosols

I.3 Characterization of aerosol wall losses in the AFT

Once the particles have been generated and introduced into the aerosol flow tube, some losses may occur on the wall of the reactor. These losses will have an impact on the mean surface concentration in contact with radicals inside the AFT, which has to be known and quantified with good accuracy based on SMPS measurements made at the AFT outlet to derive an uptake coefficient (see chapter 1 section II.1 and Figure 28, chapter 2 section I.1).

The setup shown in Figure 64 was used to characterize aerosol wall losses. Aerosols were generated by the nebulizer (see chapter 2 section I.2) and introduced into the AFT on the left side of the reactor. The SMPS sampled the particles using the injector as an inlet for different injector positions starting from 120 cm (near the drilled disk) up to 0 cm (where the SMPS and PERCA instruments sample during an uptake experiment). The SMPS impactor was set at the AFT inlet port in order to remove the largest particles that are not measured by the SMPS and to avoid clogging.

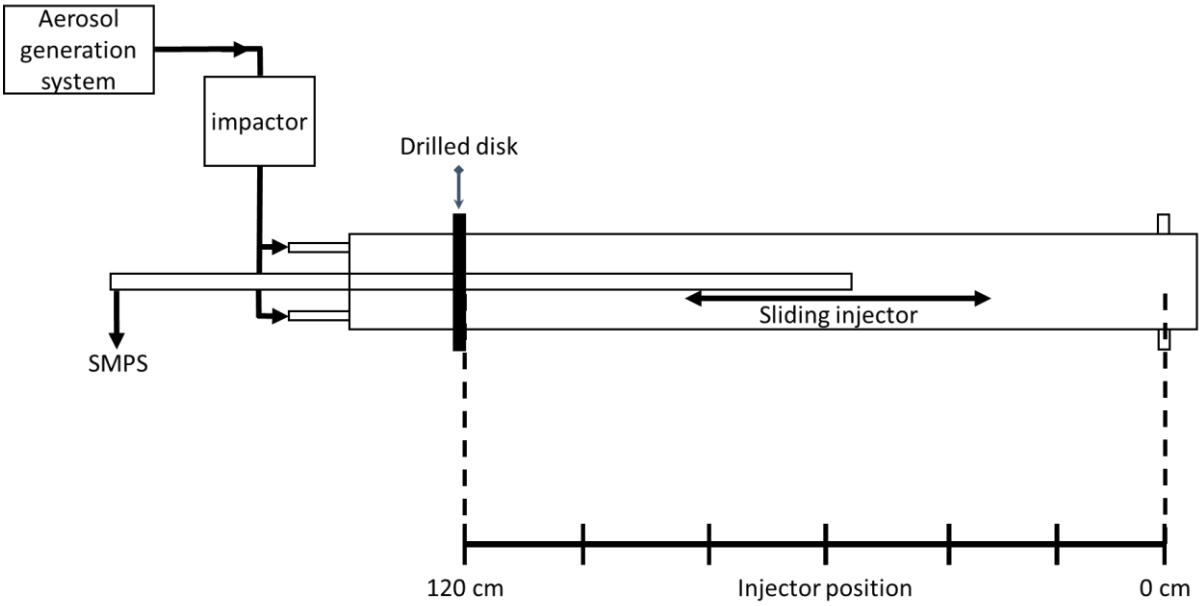

Figure 64: AFT setup used for the determination of aerosol wall losses.

To describe the aerosol wall losses, preliminary tests were performed using the CPC mode (total concentration measurement) at 6 SLPM with a concentration range of 1.5×10^{3} - 3×10^{5} cm^{-3}. During these preliminary tests, the sampling was done between 0 and 120 cm. Then additional tests were carried out in SMPS mode using the same AFT flow rate and range of aerosol concentrations to characterize the losses of particles according to their size. For the latter, the aerosol sampling was done in the AFT area where the uptake measurements are performed.

Figure 65 shows three decays of total aerosol concentrations for experiments performed at an AFT flow rate of 6 SLPM, atmospheric pressure and different initial concentrations of aerosols. A close inspection of the decays recorded at the two lowest aerosol concentrations evidences two loss regimes: (i) a first regime where the decay seems to be mainly due to a first-order kinetic process (straight line) between 0 and ~100 cm, which is likely due to wall losses, and (ii) a second regime where the decay seems to include additional loss processes (enhanced wall loss, coagulation) due to a more turbulent flow between the drilled disk and the 100 cm position. As the aerosol decay in this area is not only due to wall losses, this region will be avoided for the measurement of uptakes. According to this result and the observation that a mixing time of 11 s (equivalent to 45 cm when a total flow rate of 6 SLPM is used in the AFT, see section I.1) is required when the radicals are injected in the AFT, a monitoring area suitable for uptake experiments has been found between 50 and 90 cm (yellow area), corresponding to a contact time of approximately 12 to 22 s.

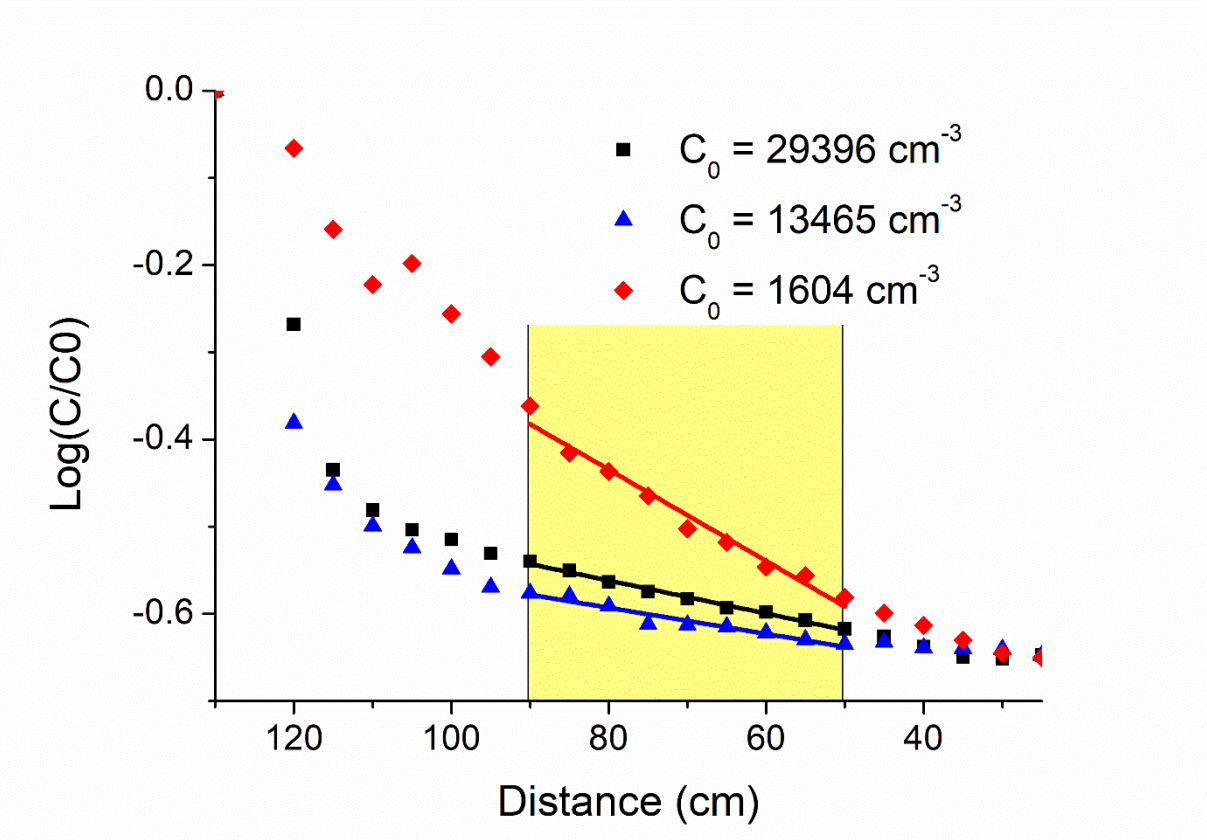

Figure 65: Decays of aerosol number concentration (whole distribution) in the AFT. The yellow area represents the area suitable for uptake experiment.

It is clear from Figure 65 that the decay in the 50-90 cm AFT area is faster for the lowest aerosol concentration. In order to correct aerosol surface concentrations measured during an uptake experiment (SMPS connected at the outlet of the AFT), the wall loss rate associated to each size bin recorded by the SMPS has to be known. These wall loss rates have been computed considering a first order decay for each size bin between 50 and 90 cm (area in the AFT used for uptake measurements). The results are shown in Figure 66 for a total flow rate of 6 SLPM. The first order loss rate was measured by fitting the data to equation 104:

$$\mathrm{Ln}(S_{\text{size bin}}) = \mathrm{Ln}(S_{0,\text{size bin}}) - k_{\text{size bin}} t \qquad 104$$

where t is the time, $S_{\text{size bin}}$ the aerosol surface concentration of the size bin of interest at time t, $S_{0,\text{size bin}}$ the initial aerosol surface concentration of the size bin of interest and $k_{\text{size bin}}$ the first order loss rate for this size bin.

This figure shows that the aerosol loss rate decreases linearly as the particle size increases, which is expected since larger particles diffuse more slowly than smaller ones. The empirical parameters a and b from equation 105 determined for each surface concentration are shown in Table 16.

$$k_{\text{size bin}} = a * D_{\text{size bin}} + b \qquad 105$$

with $D_{\text{size bin}}$ the midpoint diameter of the size bin.

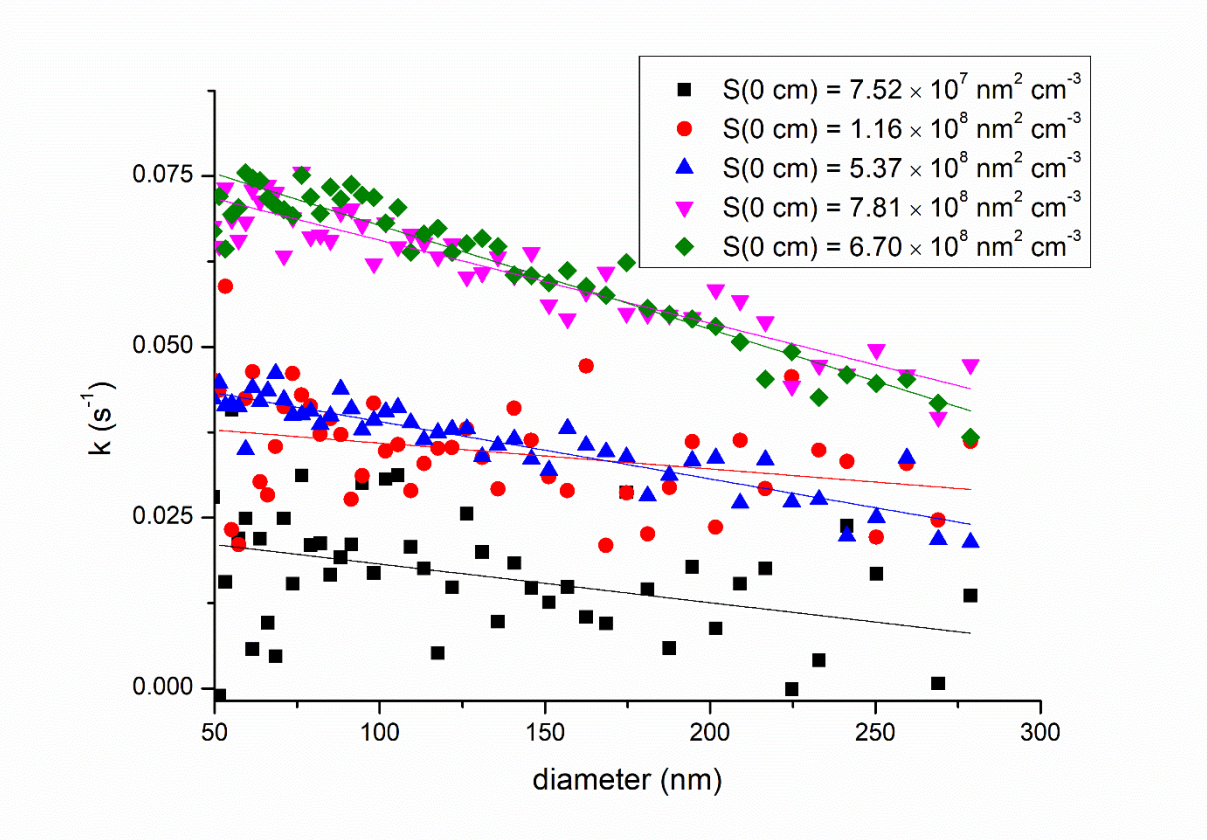

Figure 66: : Plot of aerosol first-order wall loss rates vs. aerosol size bins.

Table 16: parameters of Equation 105 determined for different total aerosol surface concentrations.

S(0 cm) (10^8 nm²/cm³)	0.76	1.2	5.4	6.7	7.8
a (10^{-5} s^{-1} nm^{-1})	-5.7	-3.8	-8.4	-1.2	-15
b (s^{-1})	0.0239	0.0397	0.0475	0.0778	0.083
σ_a (10^{-5} s^{-1} nm^{-1})	0.87	2.1	2.1	0.61	10
σ_b (s^{-1})	0.0012	0.0027	0.0028	0.0008	0.0141

However those parameters, as well as the total aerosol wall loss rate constant (Figure 65), depend on the aerosol surface concentration. The parameters determined in Table 16 have been plotted as a function of the total surface concentration at the 0-cm position in Figure 67. This figure shows a reasonable linear trend between both a and b and S(0 cm). It was therefore possible to fit this dependence with a linear regression model to derive new parameters (a_1, a_2, b_1, b_2) allowing to calculate a and b from the measured S(0 cm) as shown in Equations 106 and 107:

$$a = a_1 \times S(0\ cm) + a_2 \quad (106)$$

$$b = b_1 \times S(0\ cm) + b_2 \quad (107)$$

The parameters found for Equation 106 are a_1 = -1.37 × 10^{-13} s^{-1} nm^{-3} cm^3 and a_2 = -3.10 × 10^{-5} s^{-1} nm^{-1} while the parameters found for Equation 107 are b_1 = 7.29 × 10^{-11} s^{-1} nm^{-2} cm^3 and b_2 = 2.37 × 10^{-11} s^{-1}.

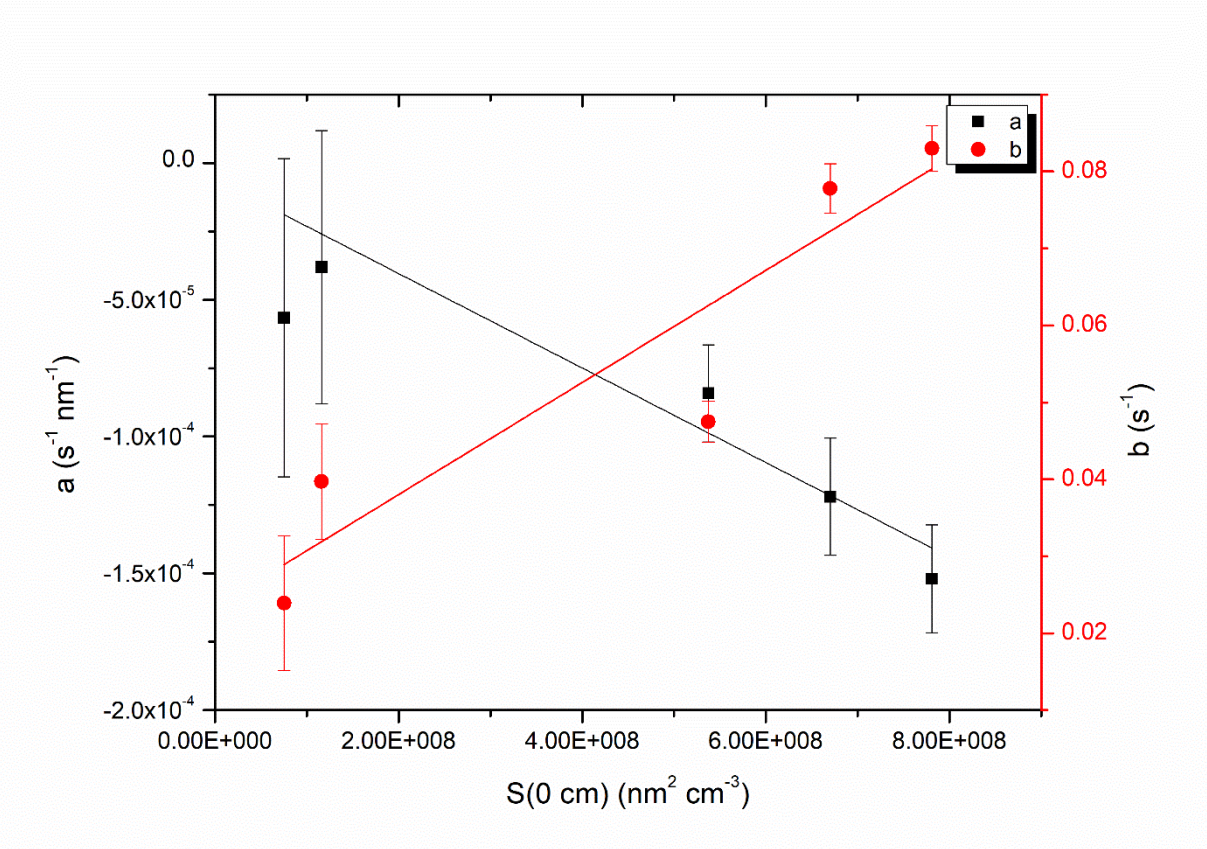

Figure 67: Plot of parameters a and b from Equation 105 vs. the total surface concentration at position 0 cm. The error bar are 1σ.

The above characterization allows a precise determination of the aerosol surface concentration at a given position knowing the surface concentration at the 0 cm position. Once the parameters of Equation 105 have been computed using Equations 106 and 107, the first-order rate constant for the size bin of interest can be calculated. Then the surface concentration at a given position x-cm is derived from Equation 108.

$$S_{size\ bin}(x\ \ cm) = S_{size\ bin}(0\ cm)e^{k_{size\ bin}t(x\ cm)} \quad 108$$

where $S_{size\ bin}(x\ cm\ )$ is the surface concentration of an individual size bin at the x-cm position, $S_{size\ bin}(0\ cm)$ the surface concentration measured at 0-cm for the size bin of interest, $k_{size\ bin}$ the first order wall loss rate of this size bin and $t_{(x\ cm)}$ the contact time between the x-cm and 0-cm positions.

I.4 Characterization of the HO_2 radical source

Several setups were tested to generate a concentration of HO_2 inside the AFT that is high enough to allow precise measurements with the PERCA instrument (limit of detection of 0.5 ppt) but low enough to avoid an impact of the gas-phase HO_2 self-reaction on the HO_2 decay during uptake experiments, which in turn would complicate data analysis (see chapter 2 section

I.6). Special attention has been taken to characterize how the generated HO_2 concentration was varying with humidity in the injector.

As described in chapter 2 section I.3, the HO_2 is produced by the photolysis of water and should provide a concentration in the range of 10^8 -5.10^9 cm^{-3}.

Concerning the generation setup, a first attempt consisted in flowing humid nitrogen around the quartz envelope of the mercury lamp which was inserted at the entrance of the 150-cm long Pyrex injector. However, this setup failed in generating enough radicals in the AFT due to their rapid loss on the injector surface. Thus, in order to reduce HO_2 wall losses, the injector inner surface was coated with halocarbon wax and the mercury lamp was set outside the injector to prevent the photolysis of halocarbon wax which could result in the release of halogen atoms. Consequently, a quartz cell flushed with humid nitrogen was added at the bottom of the injector (Figure 68). The mercury lamp was secured outside the cell whose quartz material allowed the lamp radiation to go through. This setup was found to produce a higher concentrations of HO_2 inside the AFT.

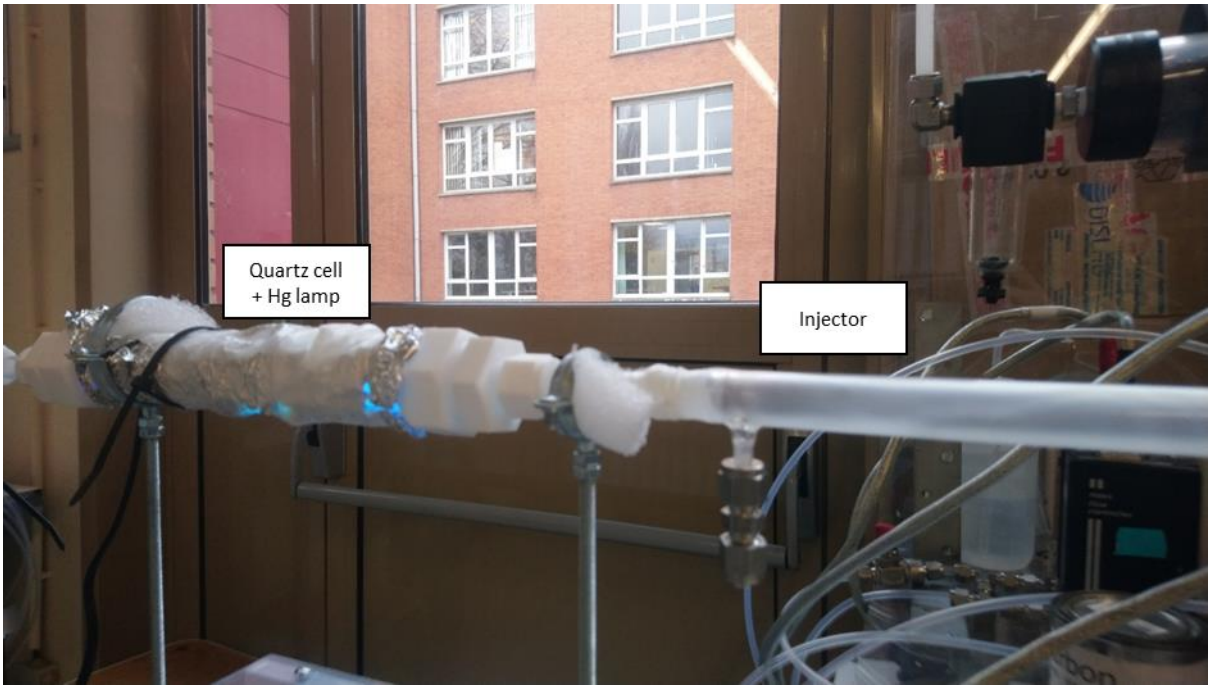

Figure 68: Picture of the quartz cell connected at the upstream end of the injector. The mercury lamp was placed outside the cell and covered with aluminum foil to protect the user from UV radiations.

The characterization tests consisted in measuring the HO_2 concentration generated in the AFT as a function of the relative humidity set in the quartz cell. The water mixing ratio was measured at the entrance of the quartz cell using a LICOR 840A probe. The water mixing ratio was controlled using a system composed of two mass flow controllers (MFC, MKS 2000 sccm), one of them being connected to a water bubbler in order to mix adjustable flow rates of dry and humid (100% RH) nitrogen. This setup was capable of generating humid nitrogen with a water mixing ratio ranging from 0-1.6% (ambient temperature of 20 ± 2°C) at a total flow rate of 1.3 SLPM.

Figure 69 shows the HO_2 concentration measured in the AFT by the PERCA instrument when the injector was set at the 50-cm position. The PERCA instrument was sampling from the AFT

outlet as planned for uptake experiments. Humidity in the injector was varied from dry conditions up to 1.5%. Figure 69 shows that an increase in concentration is observed when a small amount of water (up to 0.05%) is added in the N_2 flow. Then a plateau is reached at approximately 5.3×10^8 cm^{-3} for water mixing ratios ranging from 0.05 to 0.4% before HO_2 decreases as the water content keeps increasing. This experimental observation contrasts with the expected increase in HO_2 that should result from the photolysis of a larger amount of water molecules in the quartz cell. The decrease observed in these tests is likely due to a concomitant increase of the HO_2 wall loss rate inside the injector when the amount of water molecules adsorbed on the halocarbon wax increases, the wall loss rate increasing faster than the HO_2 production rate.

The operating condition selected for uptake experiments is a water mixing ratio of about 0.2-0.5% in the quartz cell. This amount of water allows the formation of the highest concentration of HO_2 which is still kept low enough in order to avoid significant HO_2 self-reaction (see chapter 3 section I.5). Furthermore, as the HO_2 concentration reached a plateau, a small shift in humidity in the quartz cell will have a negligible impact on the HO_2 concentration generated in the AFT, ensuring stability during the uptake experiments.

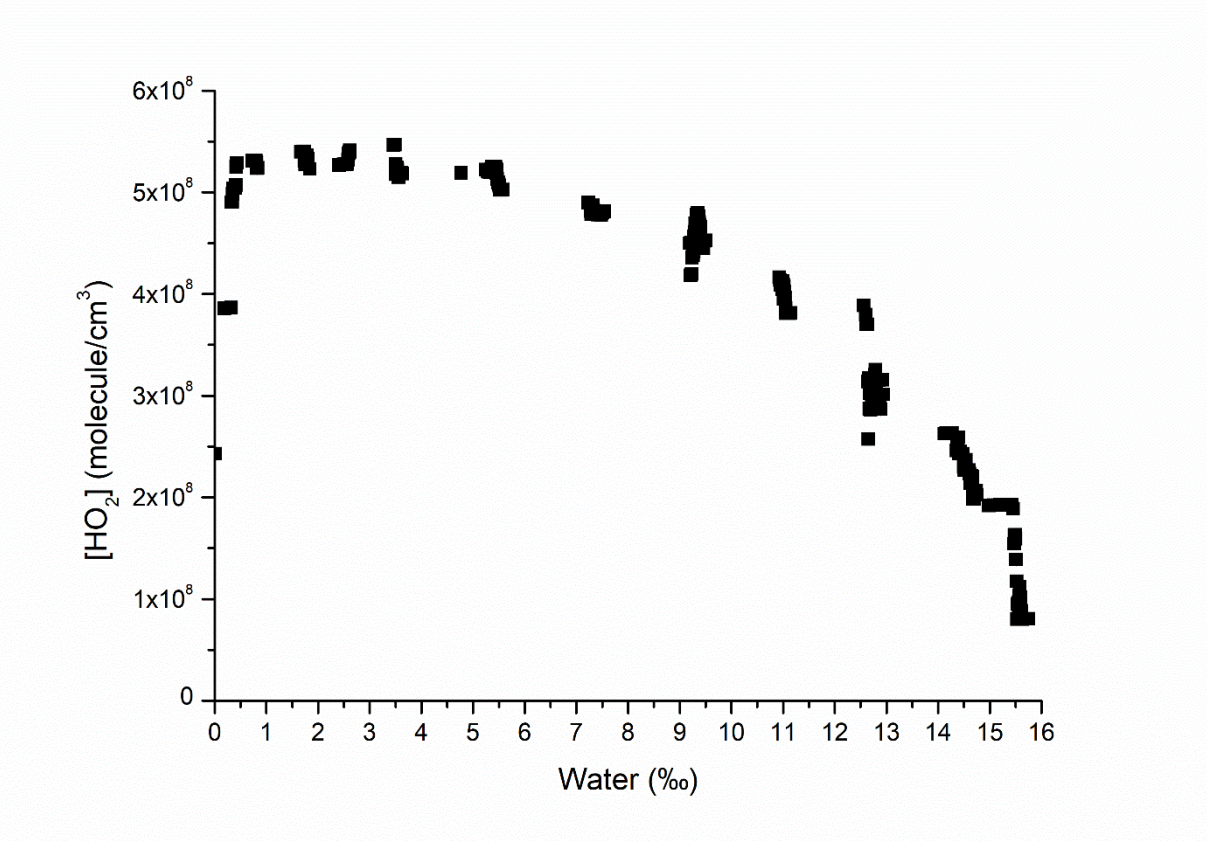

Figure 69: Concentration of HO_2 measured in the AFT vs. water mixing ratio in the injector.

I.5 Characterization of HO_2 wall losses in the AFT and gas-phase losses from HO_2+HO_2

Once the characterization of the HO_2 radical generation system was completed, the HO_2 wall loss rate inside the AFT was measured at different relative humidities. Two series of tests were conducted to characterize the HO_2 loss rate on the raw Pyrex material and a coating of

halocarbon wax (Figure 70). The flow rate was set at 1.3 SLPM within the injector with a water mixing ration of 0.15% and a total flow rate of 6 SLPM was set in the AFT. The range of humidity generated in the reactor was 0 – 65 %RH. The HO_2 decays have been measured in the 30 – 90 cm area of the AFT.

Figure 70: Picture of the AFT whose inner surface has been coated with halocarbon wax.

Figure 71 shows the logarithm of the measured HO_2 concentration as a function of the contact time at three different RH values (0, 33, 65%) for both the non-coated and coated walls. As can be seen in this figure, the HO_2 decays can be fitted by a linear function, indicating a first-order kinetic process. The rate constants k determined according to the linear equation 109 (t being the time, $[HO_2]$ the HO_2 concentration at time t, $[HO_2]_0$ the HO_2 initial concentration) are reported in Table 17.

$$\mathrm{Ln}([HO_2]) = \mathrm{Ln}([HO_2]_0) - kt \qquad 109$$

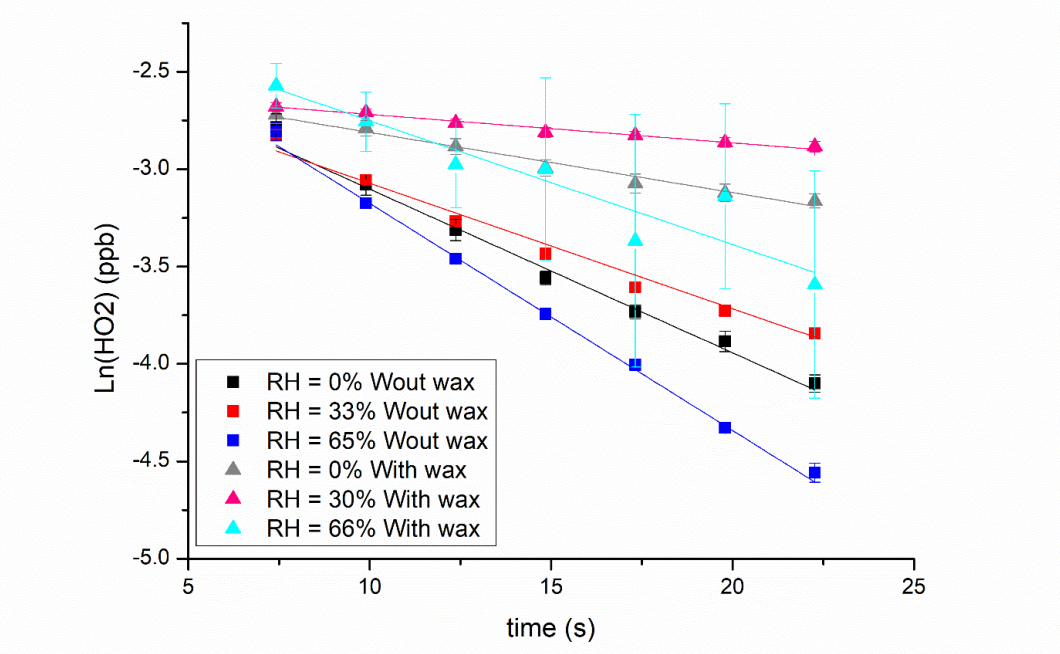

Figure 71: Characterization of HO_2 wall losses in the AFT – Temporal decays of HO_2 (markers: experimental data; lines: linear least-square fits) for the determination of first-order loss rates at different values of relative humidity: 0% (black and gray); 30-33% (red and magenta); 65-66% (dark and light blue). Decays for uncoated walls are displayed with square markers while decays for wax coated walls are displayed with triangle.

Table 17: HO_2 wall loss rates as function of humidity and wall coating.

RH (%)	0	30-33	65-66
k (without wax) (10^{-2} s^{-1})	8.4	6.4	11.7
k (with wax) (10^{-2} s^{-1})	3.1	1.5	6.4

As expected the wall loss rate is lower by approximately a factor of 2 when the AFT wall is coated with halocarbon wax. For both types of surfaces, we can observe a decrease of the wall loss rate when humidity is varied from dry conditions to 30% RH followed by an increase from 30 to 65% RH. This may be due to the fact that at 30% RH a partial cover of the wall with water molecules (monolayer) leads to a decrease of the number of reactive sites for HO_2. However, above 30% RH, the humidity reaches the point where there is more than one monolayer of water molecules condensed on the reactor wall,[209] which could result in a higher loss of HO_2 due to its good solubility.

The above determinations of wall loss rates are based on the assumption that the gas-phase loss of HO_2 in the AFT is negligible. This assumption will also be made during uptake experiments to consider that the HO_2 decay is only due to losses on the inner surface of the AFT and on aerosols. In order to check the validity of this assumption, we investigated the potential contribution of the gas-phase self-reaction of HO_2 shown below:

$$HO_2 + HO_2 + M \rightarrow H_2O_2 + O_2 + M \qquad (R56)$$

According to Atkinson *et al.* (2004),[210] the HO_2 self-reaction rate constant is equal to 1.25×10^{-12} cm^3 $molecule^{-1}$ s^{-1} in air. The presence of water tends to increase the rate constant by a factor f that can be computed by the following equation:

$$f = 1 + 1.4 \times 10^{-21}[H_2O]\exp\left(\frac{2200}{T}\right) \quad (110)$$

where T is the temperature in Kelvin and $[H_2O]$ the water concentration in molecule cm^{-3}. At 20°C, the HO_2 self-reaction rate constant is increased by a factor of 1.52 and 2.13 at 30 and 65% of relative humidity respectively.

Table 18 reports the contribution of the HO_2 self-reaction to the total HO_2 loss in the AFT for different relative humidities, different HO_2 concentrations and different aerosol uptake values. The reported values were derived from simulations performed with Kintecus.[211] The contribution reported was computed using the HO_2 concentration loosed at the first time step of the decay.

We can see that at the HO_2 concentration generated in the AFT (5×10^8 molecule cm^{-3}), the highest contribution of the self-reaction to the total loss of HO_2 is 6% at 30% RH. This contribution decreases when the aerosol uptake is taken into account. The low contribution of the self-reaction to the total loss of HO_2 allows assuming that it will be negligible for uptake measurements.

Table 18: HO_2 self-reaction contribution to the overall loss rate at different relative humidities in the AFT.

RH	0%	30%	65%
kself (10^{-12} $cm^3 molecule^{-1} s^{-1}$)[a]	1.25	1.89	2.65
kwall (10^{-2} s^{-1})[b]	3.09	1.46	6.35
$[HO_2]_0$ (10^8 molecules/cm3)	**Contribution of the self-reaction (%)**		
$[HO_2]_0$ = 1	0.40	1.28	0.20
$[HO_2]_0$ = 5	1.98	6.09	0.97
$[HO_2]_0$ = 7.5	2.94	8.86	1.45
$[HO_2]_0$ = 10	3.88	11.48	1.92
$[HO_2]_0$ = 25	9.17	24.48	4.68
γ at $[HO_2]_0 = 5 \times 10^8$ molecules/cm^3	**Contribution of the self-reaction (%)**		
0.05	0.76	1.44	0.55
0.01	1.50	3.71	0.84
0.005	1.71	4.61	0.90
0.003	1.81	5.10	0.93

a. Atkinson et al. 2004[210]. b. This work.

II Uptake measurements

II.1 Development of a measurement procedure

The procedure followed for uptake measurements was the following:

- A first step was necessary for conditioning the wall of the flow tube (RH and deposited aerosols). The humid air flow passed through the AFT (adjusted at the RH of interest for an uptake experiment) as well as the humid N_2 passed through the injector were set ON for at least one hour before the uptake measurement. Then aerosols were added in the air flow at the concentration needed to conduct an experiment half an hour before the beginning of the HO_2 decay measurements (deposition of particles on the wall).
- A second step consisted in measuring the HO_2 wall loss rate, using the bypass filter (Figure 55, chapter 3 section I.2.1) to remove aerosols from the air flow. The methodology used to measure the HO_2 wall loss rate was described in section I.5. The injector was moved at five different positions (every ten centimeters from 50 to 90 cm, corresponding to 12-22 s of contact time) going both backward and forward the 0-cm position where aerosols and HO_2 are measured. Each HO_2 measurement was performed with an integration time of one minute to get a sufficient precision. Once the injector was moved from a position to another, one minute was left before recording the next HO_2 measurement to achieve stable conditions at each point in the AFT.
- A third step consisted in re-introducing the aerosols in the AFT and measuring HO_2 using same methodology as the second step.
- A fourth and last step consisted in measuring the HO_2 wall loss again, similarly to the second step. In this way, each measurement of an HO_2 decay in the presence of aerosols was surrounded by two HO_2 wall loss measurements (no aerosol in the AFT). This procedure allows to account for the small variation in wall losses that may be due to the adsorption/desorption of aerosols on the inner surface of the AFT during the uptake experiment.
- Steps 2-4 were repeated at different aerosol concentrations to derive the HO_2 uptake as described in chapter 2 section I.6.

II.1.1 Measurement of the HO_2 decay

As described in chapter 2 section I.4, peroxy radical measurements with PERCA are achieved using two sampling reactors: one reactor in a chemical amplification mode and the other one in a background mode. Each reactor is connected to a different CAPS analyzer for the measurement of NO_2 at a time resolution of 1 s. Since peroxy radical concentrations are inferred from the subtraction between NO_2 concentrations recorded under amplification and background conditions, an offset between the two CAPS analyzers would lead to a bias in the retrieval of peroxy radical concentrations. For this reason, the sampling reactor run in the chemical amplification mode was switched in background mode several times during the uptake experiment in order to check for a potential offset between the two analyzers. The measurement of the offset was made three times during a rate constant measurement (steps 2-4 described in II.1): (i) one at the beginning of the measurement sequence, (ii) one between the backward and forward measurements and (iii) a last one at the end of the sequence.

An example is shown in Figure 72 for the case a decay of HO_2 in presence of aerosol (Surface concentration of 1.36×10^{-4} cm^2 cm^{-3}) at 29.7% RH.

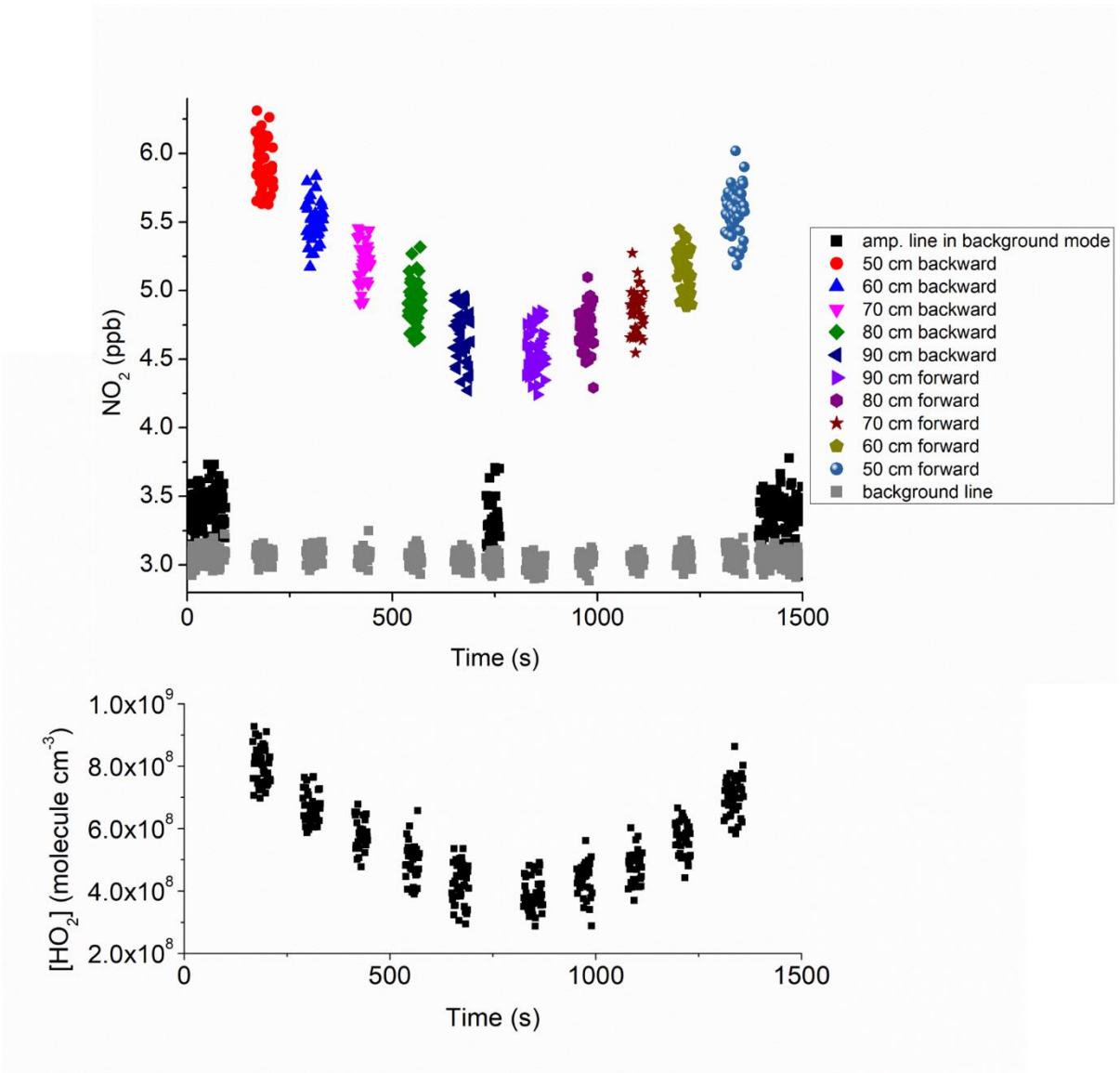

Figure 72: PERCA measurements of HO_2 during an uptake experiment for glutaric acid aerosols at 29.7% RH. NO_2 concentrations measured under amplification and background conditions by the two CAPS monitors during an uptake experiment. Concentrations lower than 4 ppb were measured by the background channel and concentrations higher than 4 ppb by the amplification channel, with the exception of the black symbols (upper panel) displaying the period when both the two channels ran under background conditions (see text).

The mean concentration of NO_2 produced from chemical amplification of the peroxy radicals is derived for each injector position from the difference between the amplification and background channels (Eq. 111). The offset determined when running the two channels in background mode is also subtracted. This offset is interpolated for each injector position assuming that the change in the measured offset was due to a linear drift of the monitors. Finally, the NO_2 concentration is converted in HO_2 concentration using the calibrated chain length (equation 111).

$$[HO_2] = \frac{[NO_2]_{amp} - [NO_2]_{back} - \Delta[NO_2]_{back}}{CL(RH)} \quad (111)$$

With $[HO_2]$ the HO_2 concentration, $[NO_2]_{amp}$ the NO_2 concentration in the amplification mode, $[NO_2]_{back}$ the NO_2 concentration in the background mode, $\Delta[NO_2]_{back}$ the difference between the background of both lines and CL(RH) the relative humidity-dependent chain length.

The bottom panel in Figure 72 displays the conversion of the measured NO_2 concentrations in HO_2 concentrations. The HO_2 concentration varies from 4×10^8 to 8×10^8 molecule cm^{-3} over the range of 12 – 22 s.

II.1.2 Determination of the HO_2 loss rate due to aerosol uptake

In order to derive the first-order loss rate of HO_2 due to either the sum of wall losses and aerosol uptake or wall losses only (absence of aerosols during the experiment), the logarithm of HO_2 over the contact time is fitted by a linear equation (first-order kinetics, see Chapter 2: section I.6) (Figure 73). These first-order loss rates are derived from the slopes of the regression lines.

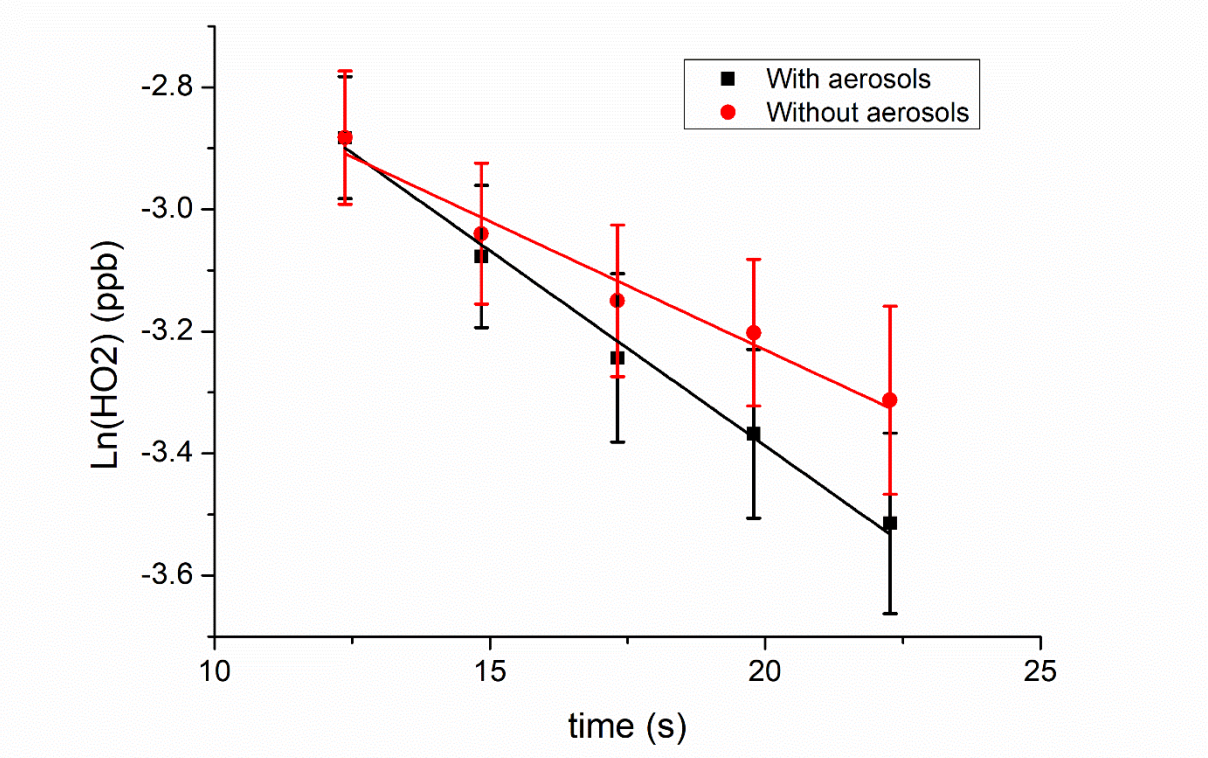

Figure 73: Determination of HO_2 loss rates without (wall losses) and with (wall losses+aerosol uptake) aerosols in the AFT for glutaric acid aerosols at 29.7% RH and a total surface concentration of 3.9 cm^2 cm^{-3} - Line: linear least-square fit of the logarithm of HO_2 concentrations vs. contact time. Error bars represent 1σ standard deviation.

In order to derive the HO_2 loss rate due to the aerosol uptake, we have to subtract the wall loss rate from the total loss rate measured in the presence of aerosols taking into account the impact of the diffusion. For the latter, Brown[145] has developed an algorithm allowing to correct the measured rate of uptake based on parameters such as diffusion and radius of the reactor. This Brown correction leads to an increase of 40% of the value of the rate constant which is

comparable with previous study where the increase is within the range of 10 – 40% depending on the wall loss rate constant.[51,58]

The measurement of the wall loss rate constant and total loss rate constant is then repeated with different concentrations as shown in the Table 19. The wall loss rate taken into account for each uptake measurement is an average value from the two measurements performed before and after (steps 2 and 4 in section II.1) the total loss rate measurement (step 3 in section II.1 shown in Figure 73).

Table 19: Values measured and determined during the uptake measurement at 29.7% RH.

Exp.	k_{obs} (10^{-2} s^{-1})	mean k_{wall} (10^{-2} s^{-1})	S (10^{-4} cm^2 cm^{-3})	$k_{obs,corr}$ (10^{-2} s^{-1})	$k_{wall,corr}$ (10^{-2} s^{-1})	$k_{aerosol}$ (10^{-2} s^{-1})	S_{corr} (10^{-4} cm^2 cm^{-3})
1	4.4 ± 0.8	4.4 ± 1	0.2 ± 0.1	3.2 ± 0.6	2.4 ± 0.5	0.8 ± 0.8	0.4 ± 0.1
2	5.5 ± 1	4.3 ± 1.1	0.8 ± 0.3	4.4 ± 0.8	2.5 ± 0.6	1.9 ± 1	2.1 ± 0.6
3	6.1 ± 1.5	4.9 ± 1.5	1 ± 0.2	5 ± 1.2	2.8 ± 0.9	2.2 ± 1.5	2.6 ± 0.7
4	6.4 ± 1.6	4.2 ± 1.6	1.3 ± 0.3	5.5 ± 1.4	2.4 ± 0.9	3.1 ± 1.7	3.9 ± 1
5	5.8 ± 2	3.1 ± 1.1	2 ± 0.4	5.2 ± 1.8	1.9 ± 0.7	3.5 ± 1.9	6.1 ± 1.6

One main challenge consist in the measurement of low uptake coefficient. In the case of this study, a good assumption of the lower detection limit can be estimated by looking at the variation of the wall loss rate constant during an uptake measurement. In average, the variation between two measurements of the wall loss rate constant is equal to 9×10^{-3} s^{-1} corresponding to an uptake of 4×10^{-3}. This uptake coefficient may be assumed as the lower detection limit in the case of this setup.

The application of the aerosol surface concentration correction (as described previously in chapter 3 section I.3) tends to increase the surface concentration by a factor of ~2 as shown in the Table 19.

However, the radial distribution profile of aerosols can be different at each injector position and more characterization tests have to be carried out to fully describe how the aerosol concentration varies within the aerosol flow tube. It is estimated that an additional error of approximately 30% corresponding to the variation of radial aerosol concentration profile has to be taken into account to derive the total uncertainty on the measured uptake coefficients. The radial profile of the aerosol concentration has been estimated by probing the aerosol surface concentration at the 0 cm position along the radius of the AFT.

II.1.3 Determination of the HO_2 uptake coefficient

The uptake coefficient can be derived from a series of measurements (first-order loss rates due to aerosol uptake) performed at various aerosol concentrations. A linear least-square fitting of these first-order HO_2 loss rates vs. aerosol surface concentrations (Figure 74) provides a slope that is directly proportional to the uptake coefficient (chapter 2 section I.6):

$$Slope = \frac{\bar{c}}{4}\gamma \qquad 112$$

with $\bar{c}$ the mean thermal velocity and γ the uptake coefficient. The uncertainties have been obtained using error propagation and the algorithm of C. A. Cantrell for the linear least-square fitting.[212]

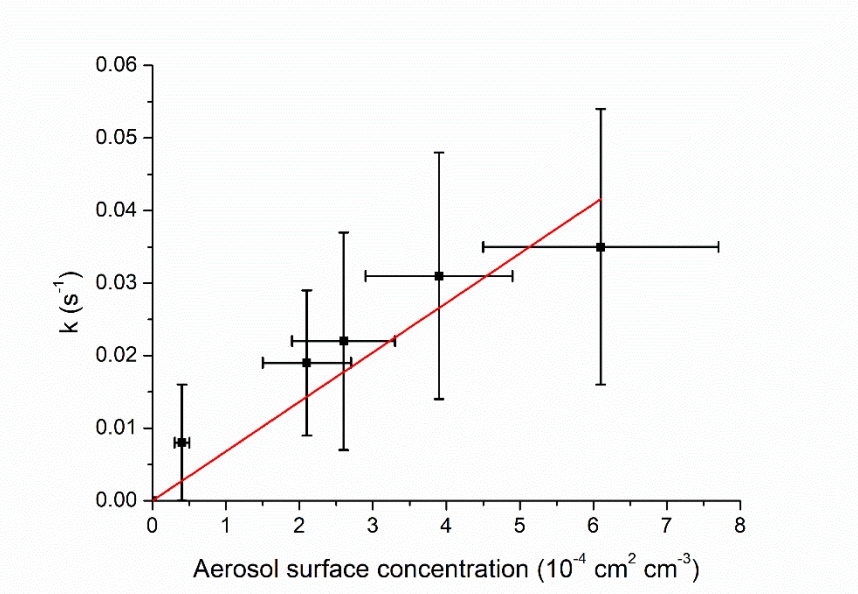

Figure 74: Determination of the HO_2 uptake coefficient for glutaric acid aerosols at 29.7% RH. Line: linear least-square fit of the HO_2 first-order loss rate due to aerosol uptake vs. aerosol surface concentration. Error bars represent 1σ standard deviation.

The diffusion of HO_2 in gas phase is the first limiting process thus, the uptake can be easily corrected. Indeed, according to the theory of Fuchs and Suttugin,[85] it is possible to remove the impact of gas diffusion on the measured uptake coefficient. Using equations 113, one can compute a corrected uptake coefficient:

$$\gamma_{HO_2} = \frac{\gamma}{\left(1 - \gamma\lambda(r)\right)} \qquad 113$$

with γ_{HO_2} the uptake coefficient without gas diffusion limitations and λ(r) a parameter depending on the Knudsen number that can be computed using equation 114.

$$\lambda(r) = \frac{0.75 * Kn + 0.283}{1 + Kn} \qquad 114$$

When the full aerosol distribution is introduced in the AFT, one can compute an average Knudsen number $\overline{Kn}$ using equation 115.

$$\overline{Kn} = \frac{\sum Kn(r_i)\, S(r_i)}{\sum S(r_i)} \quad (115)$$

with $S(r_i)$ the aerosol surface concentration of the size bin r_i, and $Kn(r_i)$ the Knudsen number of the size bin r_i.

The Fuchs and Sutugin corrections leads to the increase of the uptake (and its uncertainty) by less than 1%. Same increases have been observed in the literature[51,53,58].

II.2 Measurements of HO_2 uptakes on glutaric acid aerosols and dependence on RH

The HO_2 uptake coefficient has been measured for various relative humidity values. The conditions of operation used are introduced in Table 20.

Table 20: Operating conditions used during uptake measurements

AFT	
Temperature (°C)	20
Range of humidity (% RH)	15 - 33.6
Total flow rate (SLPM)	6
Range of measurement (s)	12 - 22
Injector	
flow rate (SLPM)	1.3
Water ratio (‰)	1.5
Nebulization	
Glutaric acid concentration (M)	5×10^{-3}
Inlet pressure (Bar)	1

The measured values of uptake coefficients can be found in Table 21. At 15% RH, the uptake coefficient was found below the detection limit of the setup while it reached 1.0×10^{-2} at a relative humidity of 30%.

Table 21: HO_2 uptake coefficient measured on glutaric acid aerosols. Uncertainties have been computed using error propagations.

Relative humidity (%RH)	γ_{eff}
15.0	< LD
29.7	0.010 ± 0.003
30.5	0.016 ± 0.007
33.6	0.016 ± 0.008

The measured uptake coefficients at 30% RH are higher than the values measured by Lakey et al.[51] (<0.004 – 0.006) and lower than the values measured by Taketani et al.[54] (0.07 – 0.15) (see Table 2). The differences between the values measured during this work and those measured

by Lakey et al. may be due to the impact of iron and copper on the uptake as explained in chapter 1 section II.2.2.

ICP analysis carried out by Laurent Alleman and Bruno Malet within the SAGE department were performed on the solutions used in the nebulizer in order to measure the contamination by metals such as iron and copper. The concentration measured was then used in order to determine an estimation of the concentration in the aerosol generated. Copper and iron concentrations founds in aerosol phase were 2.5×10^{-6} mol L^{-1} and 5.1×10^{-7} mol L^{-1}, respectively. The copper concentration is approximately one order of magnitude higher than the concentrations reported by Lakey et al. ($0.7 – 1.3 \times 10^{-7}$ mol L^{-1}). According to the Figure 18, and by considering that the uptake of HO_2 on glutaric acid follows the same trends as the uptake of HO_2 on ammonium sulfate, the uptake coefficient should start to increase rapidly when a copper concentration of $10^{-6} – 10^{-5}$ M is reached. Taketani et al. do not report the copper and iron concentrations in the solutions used to generate aerosols and the higher values measured by these authors may be due to large concentrations of these metals in the generated concentrations. According to Figure 18 the concentration of copper that they should have is about 10^{-4} M.

More studies are needed in order to determine the exact impact of copper concentration on the HO_2 uptake on glutaric acid aerosols.

To summarize, the Aerosol Flow Tube as well as the aerosol and HO_2 generation systems have been built and coupled to the detection systems used for the measurement of particles (SMPS) and peroxy radicals (PERCA). Then characterization has been performed on the setup.

Secondly, a procedure for the uptake measurement has been developed, the detection limit have been quantified and some HO_2 uptake measurement has been performed for different relative humidity. The values found are comprised between the values performed earlier by the two other groups. However, it is assumed that higher copper concentration may have increased the uptake values.

In the future, the measurement of RO_2 uptake will be performed as the PERCA system is able to measure both HO_2 and RO_2. The trends of copper concentration on HO_2 uptake onto glutaric acid particle will be determined (i) to validate the assumption made for the comparison of our values with the values found in literature (ii) to determine the mass accommodation coefficient experimentally.

CHAPTER 4: MOLECULAR MODELLING OF THE HO_2 UPTAKE

I Benchmarking of the force field

To test if the chosen force field gives a good description of the system, some preliminary tests have been made. This benchmark is an important step of the work as it will influence the whole molecular dynamics study. Dimers of two organic acids (glutaric acid, $C_5H_8O_4$, and valeric acid, $C_5H_{10}O_2$) as well as of glutaric acid with water have been used for the benchmark. The choice of valeric acid was motivated to compare the pure aerosol structure made from a monoacid containing the same number of carbon atoms as glutaric acid, in order to determine the impact of the second acidic function on the structure of the aerosol.

The Amber GAFF force field[213] was selected among all the possible force fields that we can find in the literature as it can describe organic molecules reasonably. It has also been chosen since it is implemented in both GROMACS[214] and Gaussian[215] (QM/MM). The list of the parameters can be found in Appendix E. Concerning water, the SPC/E model,[175] known to describe reasonably clusters and liquid water, was used.

The benchmark has been made on various systems (organic acid monomer, organic acid homodimer, crystalline structure and organic acid – water heterodimer), by comparing the properties determined by molecular dynamics and quantum mechanics (structural parameters: optimized geometry, minimum energy conformation, etc.) and/or experimental data (densities, ect.) when available.

I.1 Monomer of glutaric acid

The glutaric acid molecule conformation has been first analyzed at different temperatures (10, 50, 150 and 300 K). The topology files were generated using the Antechamber Acpype program.[216] An energy minimization followed by a NVT molecular dynamics (10 ns with a 2 fs time step, analysis on the last 5 ns) was performed. During the dynamics, only the bond lengths were constrained.

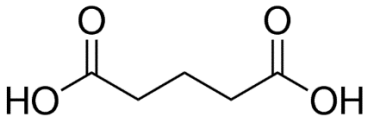

Figure 75: Scheme representing the glutaric acid molecule.

During the simulations at 10 and 50 K, the glutaric acid kept its C_{2v} symmetry. This means that the energy provided to the molecule (thermal energy) was not enough to go over the energy barrier of dihedral rotations as will be discussed later.

We nonetheless observed (Table 22) that the simulated Coulomb 1-4 contribution (-305.4 kJ mol^{-1}) to the potential (-199.2 kJ mol^{-1}) is really important compared to all the other types of energy (which do not exceed 32 kJ mol^{-1} in absolute value). This energy has a great influence on the potential energy and thus on total energy and therefore we had to verify that this energy is correctly estimated.

A comparison was made with the OPLS/AA force field. As a first attempt, Restrained Electrostatic Potential Fit (RESP[217]) charges were calculated at the HF/6-31G** level to determine partial charges. Then, an energy minimization was performed followed by a NVT trajectory at 300 K (10 ns with a time step of 2 fs). The obtained energies are listed in Table 22. The analysis of the different types of energy was done using the GROMACS energy analysis program, where:

- "angle" is the angular term of the energy (term 30 defined in chapter 2 section II.1.1) (intramolecular);
- "proper dih." is the energy due to the improper dihedrals term 32 (GROMACS treats improper dihedrals as proper dihedrals and the proper dihedrals as Ryckaert Belleman (equation 32) dihedrals in the case of AMBER) (intramolecular);
- "Ryckaert Bell.", the energy due to the proper dihedral term 31 (intramolecular);
- "LJ 1-4" and "Coulomb 1-4", the energies due to the Lennard-Jones and the Coulomb terms 33 between two atoms separated by three bonds ($f_{ij} \neq 1$);
- "LJ (SR)" and "Coulomb (SR)" the short-range part of the energies due to the Lennard-Jones and the Coulomb terms 33 between two atoms separated by more than three bonds or atoms of two different molecules ($f_{ij} = 1$);
- "Coul. Recip." the long-range part (developed in the reciprocal space) of the Coulomb interactions.
- The sum of these terms gives the potential energy (as bonds are constrained during dynamics, the bond energy is equal to 0). Adding the kinetic energy (Kinetic En.), we obtain the total energy;

Table 22: Details of the energy contributions (kJ mol^{-1}) for a glutaric acid monomer at 300 K with the OPLS/AA FF compared to GAFF.

	OPLS/AA		GAFF	
	Energy	RMSD	Energy	RMSD
Angle	35.7	9.8	32	9.9
Ryckaert Bell.	3.9	6.9	1.4	1.1
LJ 1-4	9.1	2.4	9.9	2.5
Coulomb 1-4	-153.1	4.5	-305.4	13.1
LJ (SR)	-2.7	2.3	-1.6	2.9
Coulomb (SR)	-2.3	2.5	26	8.3
Coul. Recip.	3.9	0.6	7.9	2.2
Potential	-105.4	9.8	-199.2	11.4
Kinetic En.	40	9.9	39.9	10
Total Energy	-65.5	13.9	-159.3	15.2

With the OPLS/AA force field,[163] the Coulomb 1-4 energy is twice lower than with the AMBER GAFF force field but it still represents a major part of the potential energy. The source of this difference is due to the fudge factor (f_{ij} in equation 33) applied in the Coulomb 1-4 energy which is equal to 0.50 for OPLS/AA and 1/1.2=0.8333 for AMBER GAFF.

To further understand the origin of the 1-4 interactions, a program in FORTRAN language has been written to compute this energy explicitly. The 1-4 Coulomb energy has been calculated by pair (Table 23) for one glutaric acid (labelled atoms represented in Figure 76) with the AMBER GAFF force field.

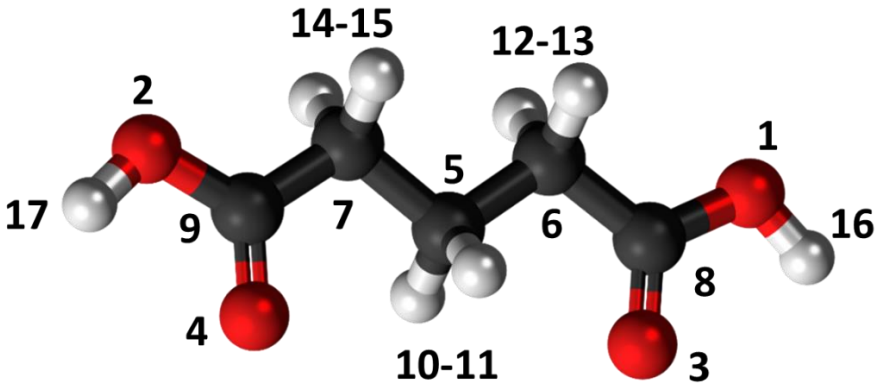

Figure 76: Glutaric acid with labeled atoms

Table 23: 1-4 Coulomb energy (kJ mol^{-1}) for each interaction pair.

Pair	1-4 Coulomb energy	Pair	1-4 Coulomb energy
1-5	13.7	7-13	-4.9
1-12	-19.4	7-17	-27.1
1-13	-15.5	8-10	21.7
2-5	14.6	8-11	21.7
2-14	-14.0	9-10	18.1
2-15	-18.0	9-11	22.6
3-5	12.7	10-12	2.1
3-12	-11.6	10-13	2.6
3-13	-14.1	10-14	3.0
4-5	11.6	10-15	2.6
4-14	-14.1	11-12	2.5
4-15	-11.8	11-13	2.1
4-17	-117.0	11-14	2.4
6-9	-38.6	11-15	2.2
6-14	-4.1	16-3	-78.9
6-15	-5.6	16-6	-39.2
7-8	-32.4	Total	-315.0
7-12	-4.9	mean MD	-305.4

We can observe that the interactions 16-3 and 4-17 between the acid hydrogen (H17 or H16) and the carbonyl oxygen (O4 or O3) of the acid are large in absolute value. The importance of the different pair contributions is related to the charges carried by the atoms as will be seen later.

Moreover, at high temperature, the radial distribution function characterizing the distance between the two acid carbons has allowed to identify three conformers (Figure 77 and Figure

78). These conformers correspond to a different bending of the chain. Conformer 1 corresponds to the trans-conformation while conformer 3 is characterized by a bent conformation with strong intramolecular H-bonds. Conformer 2 has an intermediate geometry.

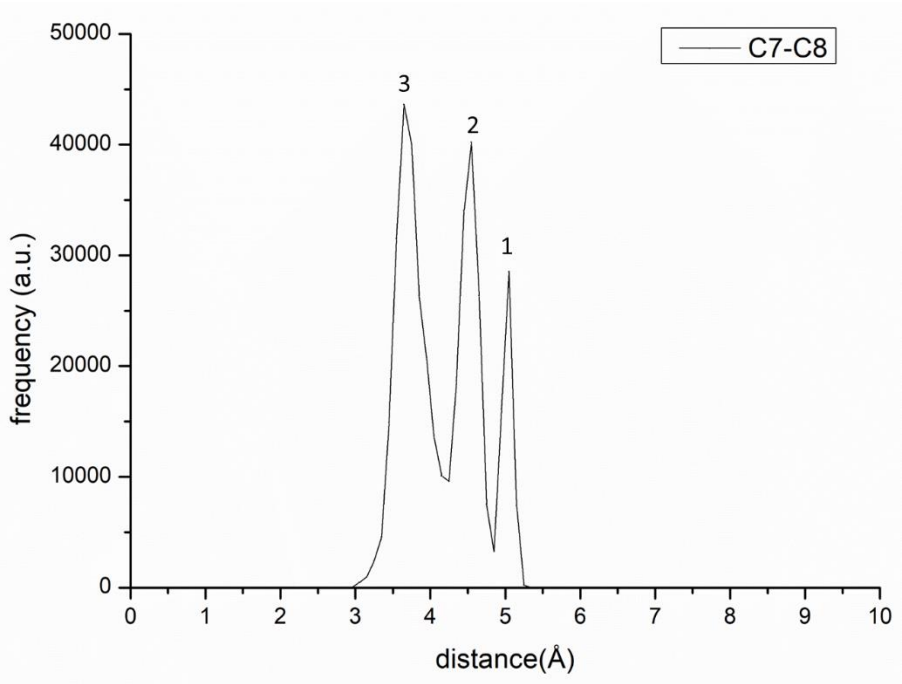

Figure 77: Radial distribution of the distance separating the two acid carbons (C7-C8) averaged over the last 5 ns of a 10 ns molecular dynamics simulation of the monomer with AMBER GAFF at 300 K

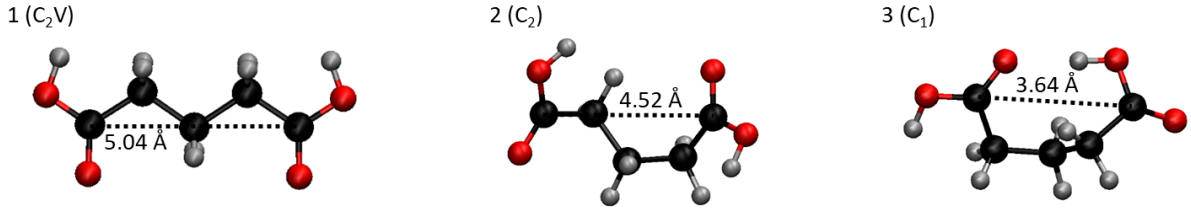

Figure 78: Molecular representation of the three conformers identified for the glutaric acid monomer and the corresponding C7-C8 distances.

The geometries of the three conformers were taken as starting points for *ab initio* calculations (energy minimization) with two methods (MP2/6-31+G** and HF/6-31G**) and molecular dynamics (energy minimization). The energies (ZPE corrected) were then compared (Table 24).

The RESP charges were computed for the three conformers at the MP2/6-31+G** level (Figure 79). One can observe that the charges do not vary a lot with the conformation. The latter result provides confidence to the charges used in our simulations and thus, RESP charges calculated for conformer 1 have been chosen for subsequent calculations.

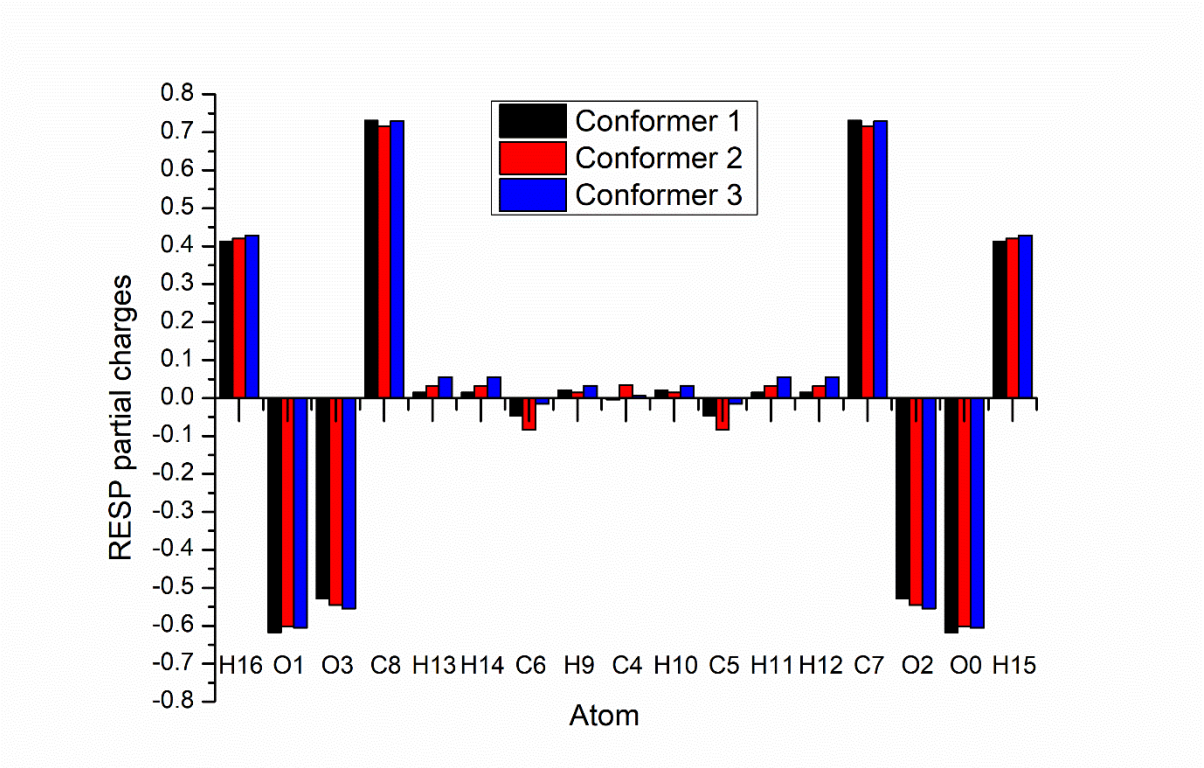

Figure 79: Variation of the RESP charges for the three conformers as a function of the atom. (Values are in Appendix F)

Regarding the energetics, the MP2 method having a higher level of accuracy, the results of this method will be taken for the benchmark. Energy differences were calculated by taking the symmetric conformer (conformer 1) as the reference. The energies obtained by molecular dynamics follow qualitatively the same trend as the quantum ones.

Table 24: Comparison of the energy differences (kJ mol^{-1}) computed by Energy Minimization (EM) with molecular dynamics (GAFF) and with different quantum methods and basis sets (with ZPE energies). Conformer 1 is taken as the reference.

	1 (C_{2V})	2 (C_2)	3 (C_1)
B3LYP			
6-311++G(2d,2p)	0.00	-0.15	-2.32
aug-cc-pVDZ	0.00	-0.19	-2.56
aug-cc-pVTZ	0.00	-0.07	-2.31
M06-2X			
6-311++G(2d,2p)	0.00	-1.05	-3.97
aug-cc-pVDZ	0.00	-1.24	-4.20
aug-cc-pVTZ	0.00	-0.94	-3.97
PW91			
6-311++G(2d,2p)	0.00	-0.23	-3.00
aug-cc-pVDZ	0.00	-0.28	-3.28
aug-cc-pVTZ	0.00	-0.09	-2.96
MP2			
6-311++G(2d,2p)	0.00	-0.95	-3.32
aug-cc-pVDZ	0.00	-1.09	-3.63
aug-cc-pVTZ	0.00	-0.94	-3.66
Molecular Dynamic			
Amber GAFF	0.00	-1.07	-2.48

Table 24 shows that there is no significant basis set dependency. We can also observe that the functional that gives energies closest to the MP2 values (considered as the most precise method used) is M06-2X. Indeed, the M06-2X functional gives values very close to the MP2 with the aug-cc-pVTZ basis set for every conformer. This functional may be used instead of the MP2 method to save computational time.

The influence of the fudge factor on the Coulomb 1-4 interaction was tested (MD, Amber GAFF) by varying its magnitude from 0.5 to 1. The occurrence probabilities were computed for each of the three conformers from a MD run of 10 ns duration. We determined that a fudge factor ranging between 0.8 and 1 is in accordance with the relative stability obtained from quantum calculations as seen in Table 24. Indeed, we assumed that the lower the energy of the conformer, the more stable and thus the more probable the conformer should be. As a consequence, MD calculations with a fudge factor > 0.8 indicate that the conformers can be classified from the most to the least stable as: conformer 3 > conformer 2 > conformer 1. In the following, a fudge factor equal to 0.833, as generally done with Amber, will be used for the Coulomb 1-4 interaction.

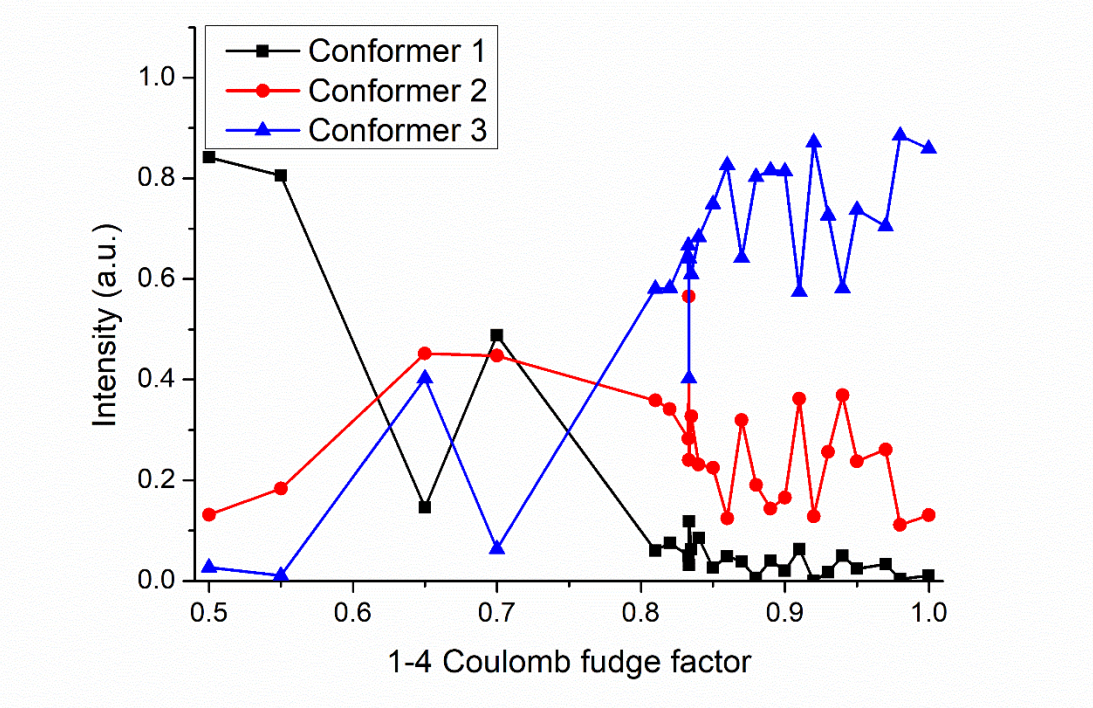

Figure 80: Variation of the probability of occurrence of the three conformers as a function of the fudge factor on the Coulomb 1-4 interaction.

A further test of the fudge factor was performed: the potential energy curve was computed by scanning the potential along the HOCO dihedral angle (19 points from 180° to 360° with a 10° step) at the MP2/aug-cc-pVDZ and B3LYP/6-311++G** levels of theory. Then the energy difference between the two minima (ΔE 1-2) and the energy difference between the lowest energy minima and the transition state (ΔE TS-2) were calculated.

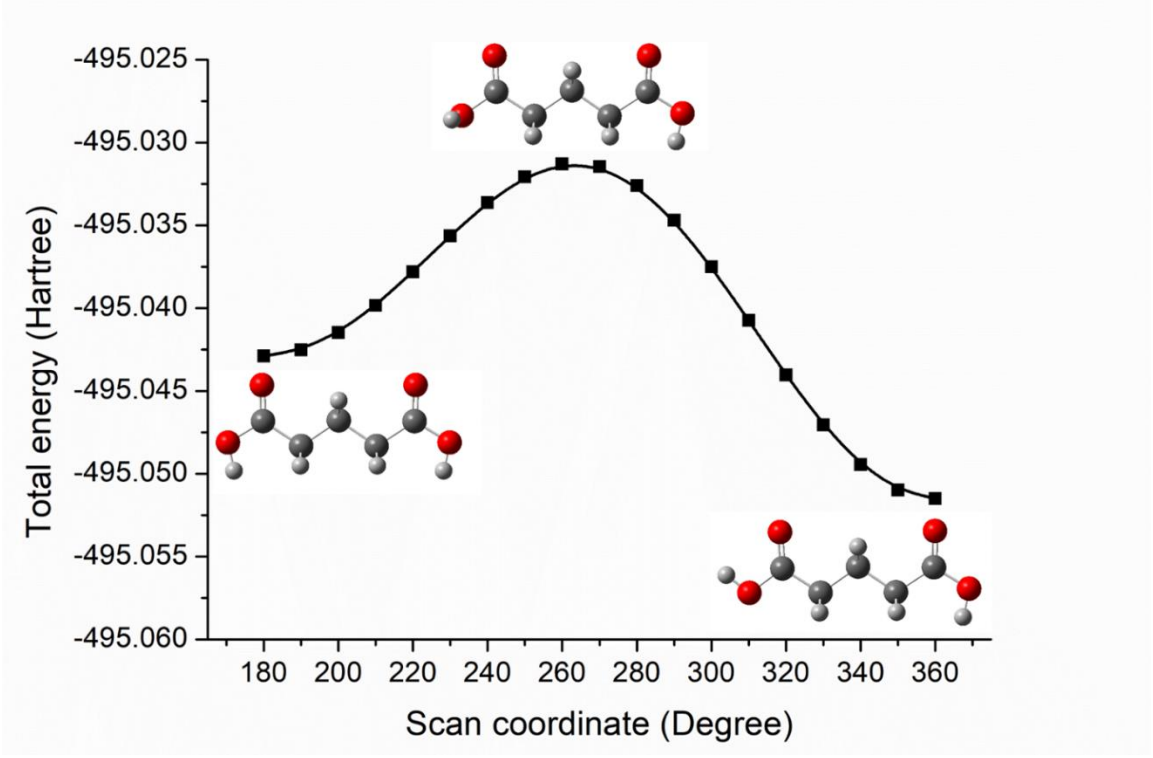

Figure 81: Scan of the potential energy along the HOCO dihedral angle at MP2/aug-cc-pVDZ.

Then the geometries of the two minima and the transition state were inserted in GROMACS and a single point energy calculation was performed to get the value of the energy of each geometry. Finally the same energy differences were calculated in molecular dynamics and compared with *ab initio* computations.

Table 25: Comparison of the energy differences (kJ mol^{-1}) along the scan of the potential energy from QM calculations (MP2/aug-cc-pVDZ with ZPE) and MD calculations (GAFF with fudge factor equal to 0.833).

Geometry	ΔE (TS-2)		ΔE (1-2)	
	QM	MD	QM	MD
B3LYP	55.1	63.1	26.2	18.9
MP2	55.1	54.6	23.6	12.8

We can observe that the energy differences obtained with molecular dynamics correspond to the quantum mechanics values qualitatively, further confirming that the fudge factor of 0.8333 is reasonable to describe the molecule folding.

I.2 Glutaric acid-glutaric acid interactions

Before generating large clusters, clusters of two (Figure 82) and four glutaric acids (not shown) have been formed at 300 K using molecular dynamics. The interaction energy (Figure 83) and acid – acid radial distribution functions analysis (Figure 84) were performed over the 5 ns trajectory. The mean binding energy is -39.24 kJ mol^{-1} for $(GLU)_2$ and -98.23 kJ mol^{-1} for the $(GLU)_4$. In $(GLU)_2$, given that the typical energy for one H-bond is 20-25 kJ mol^{-1},[117,218] between 1 and 2 intermolecular H-bonds are formed while in $(GLU)_4$ between 4 and 5 H-bonds are formed.

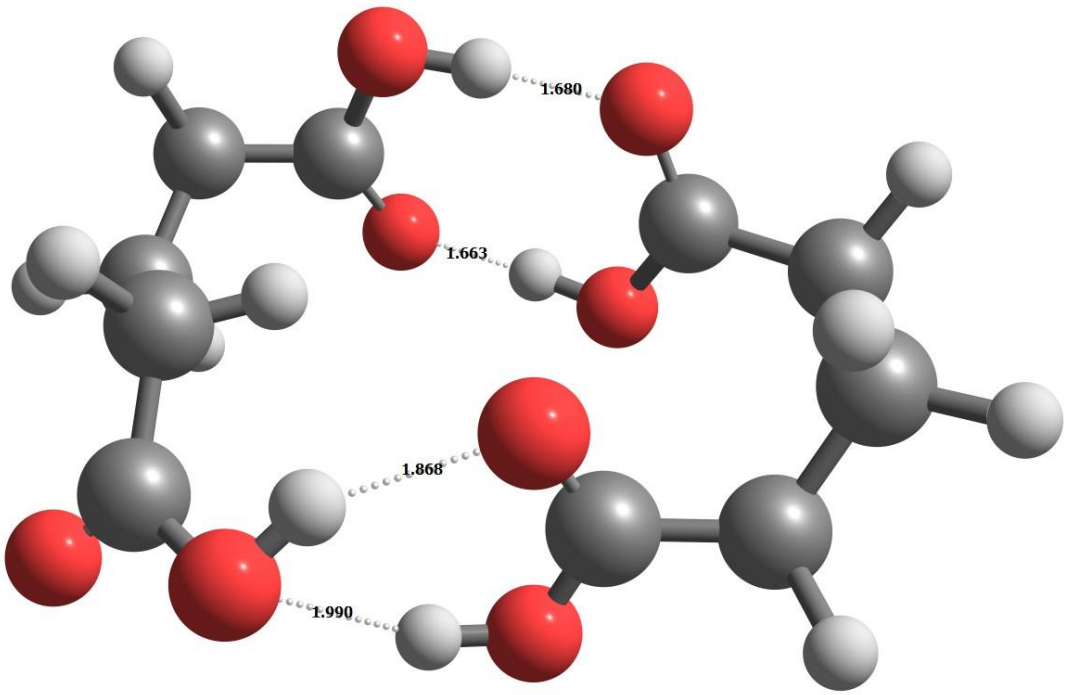

Figure 82: Dimers of glutaric acids $(GLU)_2$, dashed lines represent intermolecular H-bonds (in Å).

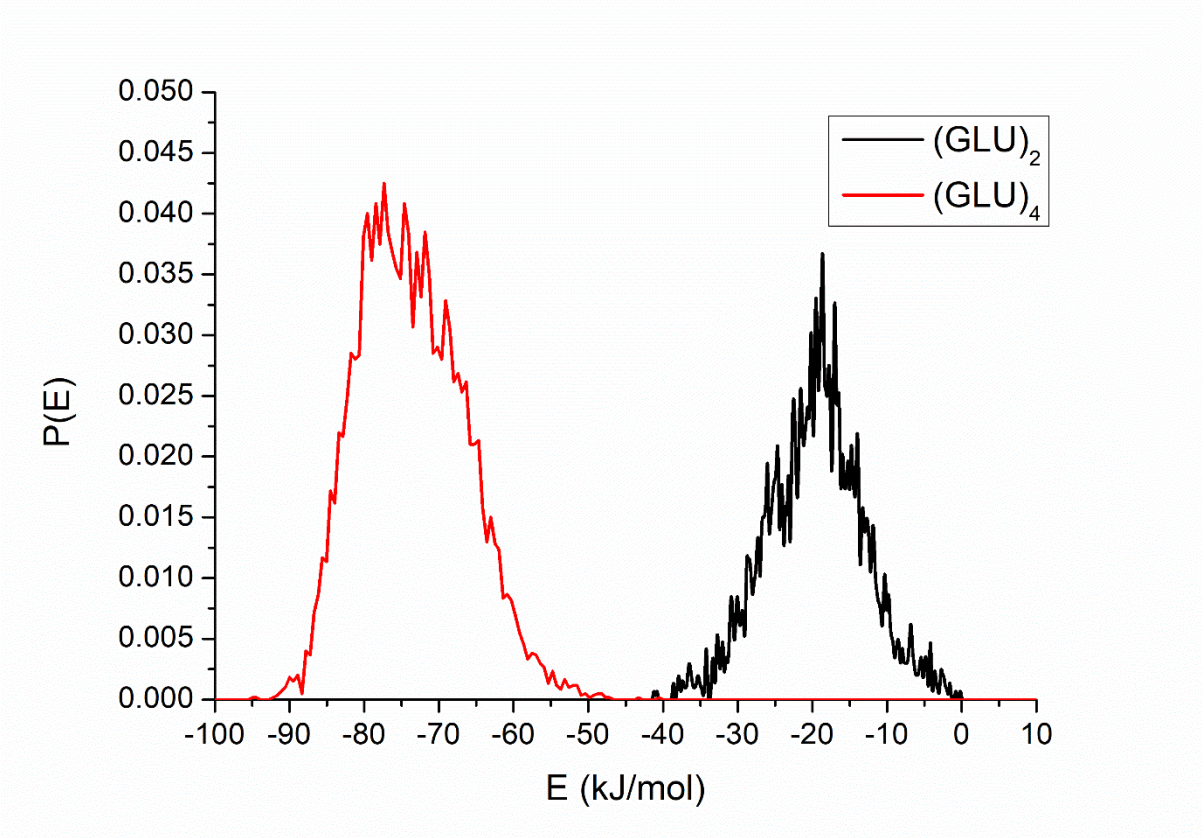

Figure 83: Binding energy distributions for $(GLU)_2$ and $(GLU)_4$

A comparison between the energy and the geometry of the $(GLU)_2$ dimer computed by molecular dynamics and MP2/6-311++G(2d,2p) (using ZPE corrections) has been made. The force field derived data agree fairly with the *ab initio* data for the geometries. Indeed *ab initio* hydrogen bond lengths are 0.166 nm, 0.168 nm, 0.187 nm and 0.199 nm while in MD, the bond length are 0.175 nm, 0.179 nm, 0.190 nm and 0.208 nm, respectively. Concerning the energies (Table 26), the differences are more important but within an acceptable range. It may be noticed that there are no basis set superposition error (BSSE) effects included, so the *ab initio* value may be too high.

Table 26: Comparison between the energies of the glutaric acid dimer computed by molecular dynamic and ab initio MP2/6-311++G(2d,2p) method.

	E(MP2/6-311++G(2d,2p)) (a.u.)	E(MD) (kJ/mol)
Glutaric-glutaric dimer	-990.294490	-485.02
Molecule 1	-495.118203	-187.83
Molecule 2	-495.128246	-207.22
ΔE (kJ/mol)	-126.13	-89.97

As we go from $(GLU)_2$ to $(GLU)_4$, the radial distribution functions of the C7-C8 distance (Figure 84) shows that contrary to the monomer, the proportion of conformers is sliding toward

conformer 1. We can conclude that the interaction between molecules tends to open the chain, the molecules rather adopting the linear conformation (conformation 1).

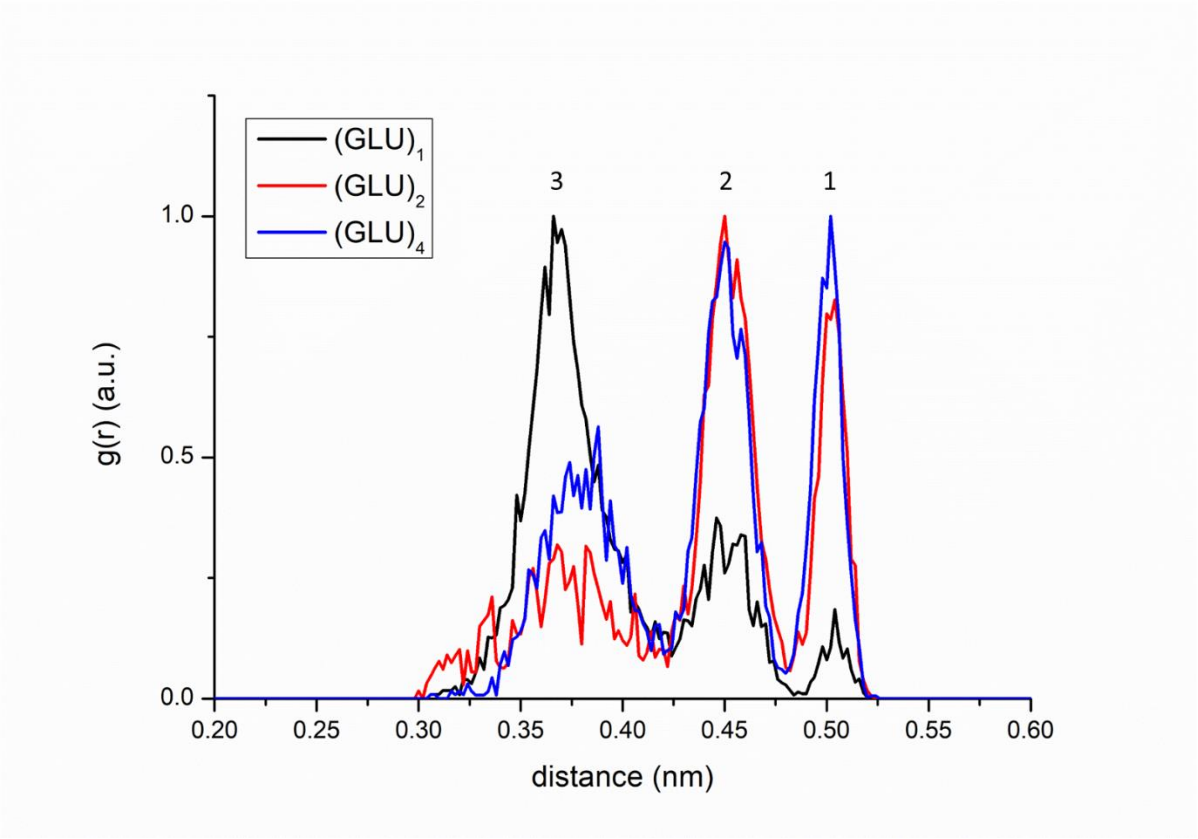

Figure 84: Evolution of the C7-C8 radial distribution function with the number of molecules in the cluster.

Then, computation on a glutaric acid crystal was also performed to test the description of the long-range interactions. The unit cell geometry was taken from Bhattacharya et al.[219] This unit cell was replicated one time in axis *a*, two times in axis *b* and three times in axis *c* which leads to a number of 120 glutaric acid molecules (Figure 85). The MD computation was done in a NPT ensemble with a Berendsen isotropic pressure coupling at 288 K. The lattice parameters computed with our GAFF/RESP force field were close to the previous work carried out by Bhattacharya et al.[219] as shown on Table 27. The calculated density (1.41 g cm^{-3}) compared fairly well to the experimental one (1.43 g cm^{-3} at 288 K).[220]

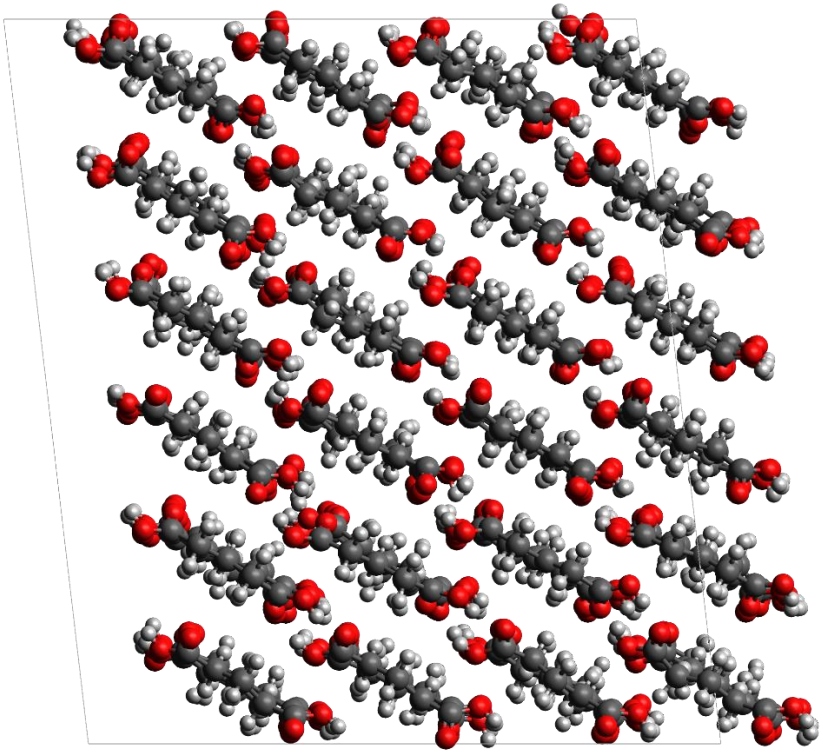

Figure 85: Structure of the glutaric acid crystal (120 molecules).

Table 27: Calculated MD lattice parameters of a glutaric acid crystal (using isotropic pressure and temperature Berendsen couplings) compared to previous works.

	N replica	MD box	Primitive mesh	Exp. [b]	Exp. [b]
GA [a]					
a (nm)	2	25.88	12.94	12.91	12.89
b (nm)	5	24.19	4.84	4.80	4.82
c (nm)	3	29.87	9.96	9.85	9.92
α (°)			90.00	90.00	90.00
β (°)			96.67	97.24	96.67
γ (°)			90.00	90.00	90.00
T (K)			288	260	298

a This work; b Bhattacharya et al.[219]

According to the previous comparisons, it has been finally established that the GAFF force field combined with the MP2/6-31+G** RESP charges can describe properly the glutaric acid system.

I.3 Clusters of glutaric acid and water

Since in both the experiment and the atmosphere, water is always present, it is necessary to test also its impact. Computations were done to study a dimer made of glutaric acid and water (SPC/E force field) at 300 K (Figure 86). As for the pure clusters of glutaric acids, binding energy analysis was also carried out (Figure 87).

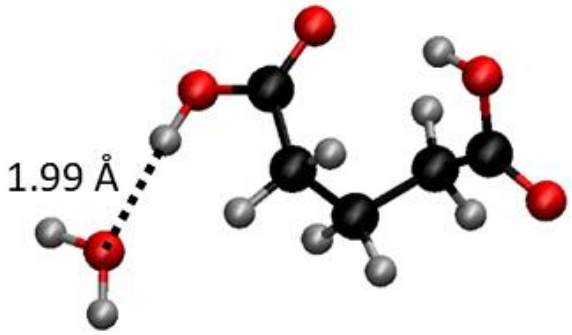

Figure 86: Cluster of one glutaric acid and one water molecules.

An average binding energy of -19.90 kJ mol^{-1} was found which is twice lower than for the cluster of two glutaric acids. It is not surprising since water tends to form only one single H-bond while glutaric acid manages to form 2 H-bonds via its acidic groups. So, the addition of water on dry aerosol of glutaric acid may weaken its bulk cohesion.

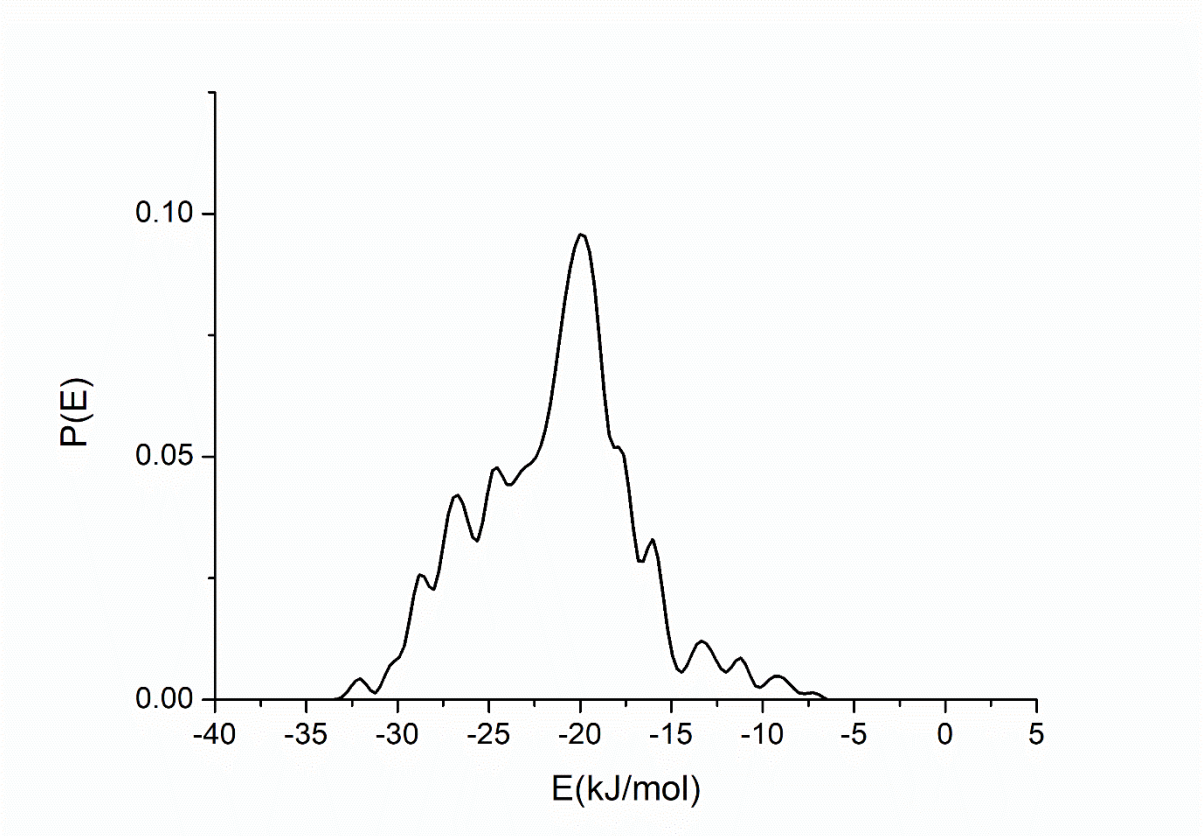

Figure 87: Binding energy distribution of the glutaric acid – water cluster.

The binding energies and the hydrogen bond lengths were also compared with the same methodology as the one used for the glutaric acid dimer. The MP2/6-311++G(2d,2p) binding energy is found at about -28.47 kJ mol^{-1} and the MD energy is about -19.97 kJ mol^{-1}. Both interaction energies are quite close as well as the intermolecular H-bond lengths that were found equal to 0.185 nm and 0.175 nm for *ab initio* and MD computations, respectively. So the SPC/E water model seems to be an appropriate choice for this system.

I.4 Valeric acid

In order to check the influence of the second acid function on the aerosol structure, aerosols of valeric acid were also generated. This molecule was already investigated in the PhLAM group (Thèse C. Fotsing-Kwetche[167]), and AM1/BCC charges were taken from this work. Figure 16 shows the comparison between the binding energies and hydrogen bonds computed by *ab initio* MP2/6-311++G(2d,2p) method and molecular dynamics for the valeric acid dimer. Even if adding water onto the valeric acid aerosols was not planned, the interaction with SPC/E water model has also been studied.

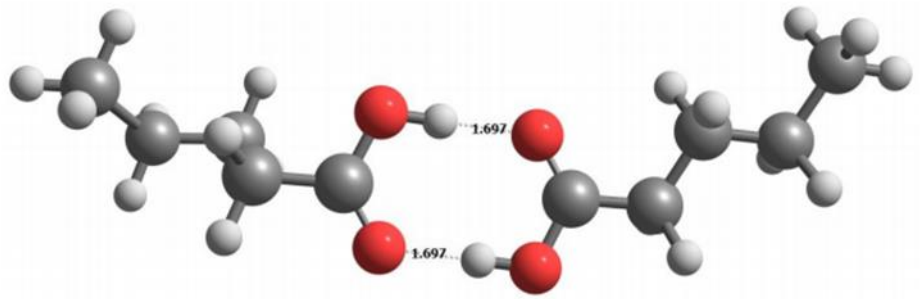

Figure 88: Valeric acid dimer minimum energy configuration obtained from ab initio (MP2/6-311++G(2d,2p)+ZPE). Bond lengths indicated in Angstroms.

The intermolecular hydrogen bond lengths were close whatever method used: two bonds of 0.170 nm were found by *ab initio* computation and bonds of 0.170 nm and 0.169 nm were found by molecular dynamics. Again, the binding energies obtained agree well with each other for both methods (Table 28).

Table 28: Binding energies (kJ mol^{-1}) of the valeric acid dimer and valeric acid – water dimer computed by ab initio method and molecular dynamics.

System	MP2/6-311++G(2d,2p) level	MD
Valeric acid-Valeric acid	-63.02	-58.56
Valeric acid-Water	-33.22	-42.51

A benchmark was also carried out on the valeric acid crystal using the initial geometry provided by Dr Josip Lovrić (Figure 89). The computation was done in the same condition as for the glutaric acid crystal (NPT ensemble, Berendsen isotopic, V – rescale).

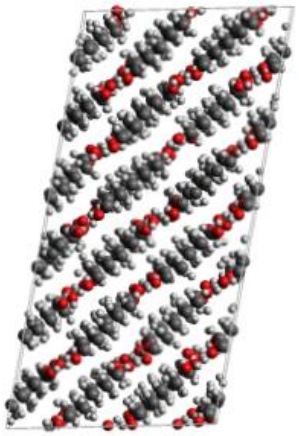

Figure 89: Valeric acid crystal.

The lattice parameters obtained (Table 29) agree with the ones from previous studies.[221,222] The density was found equal to 1.15 g cm^{-3} (210 K) which is close to the experimental density of 1.106 g cm^{-3} (236 K).[221]

Table 29: Calculated MD lattice parameters of valeric acid crystal (using Berendsen isotropic pressure and V-rescale temperature couplings) compared to previous works.

VA [a]	N replica	MD box	Primitive mesh	Exp. [b]	MD. [c]
a (nm)	3	16.60	5.53	5.55	5.55/5.67
b (nm)	3	28.90	9.63	9.66	9.37/9.37
c (nm)	3	33.91	11.3	11.34	11.26/11.27
α (°)			90.00	90.00	90.00
β (°)			101.82	101.82	102.48/100.57
γ (°)			90.00	90.00	90.00
T (K)			210	138	

a J. Lovrić, private communication; b Scheuerman et al.[221]; c Hagler et al.[222]

To conclude, considering previous observations, the GAFF force field combined with AM1/BCC charges seems to describe correctly the valeric acid system and its interaction with water.

II Aerosol formation

II.1 Adjustment of the minimum box size

Firstly, before creating aerosols, test calculations were done to determine the size of the simulation box that should be set to avoid box effect artefacts.

To be sure that the box size has no effect, we consider that the radial distribution function needs to be equal to zero at the edge of the box. Tests were carried out on an aerosol consisting of 100 glutaric acid molecules $(GLU)_{100}$ with different box sizes. Aerosol centre of mass (COM) – glutaric acid COM radial distribution functions are presented in Figure 90.

We can clearly see that the box size has an impact on the structure of the aerosol. At 3.5 nm and 5 nm, the radial distribution functions are not yet equal to zero when the aerosol diameter (2r) reaches the size of the box, which is clearly not the case at 10 nm and 20 nm.

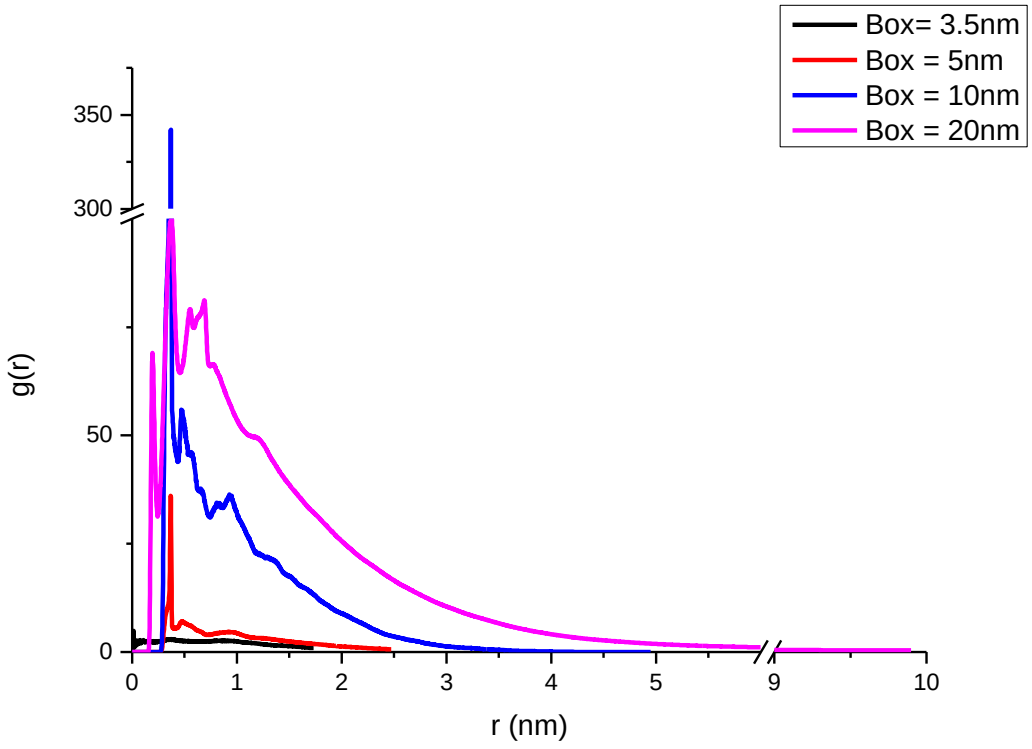

Figure 90: Radial distribution function of a $(GLU)_{100}$ aerosol with different box sizes.

As we can observe on Figure 91.A, a box too small tends to create a flat surface, a nearly infinite slab. A larger box (Figure 91.B) does not influence the shape of the aerosol and there is a sufficient distance between the edge of the box and the aerosol surrounded only by vacuum. So, a box of 20 nm or larger can be set to produce the aerosol.

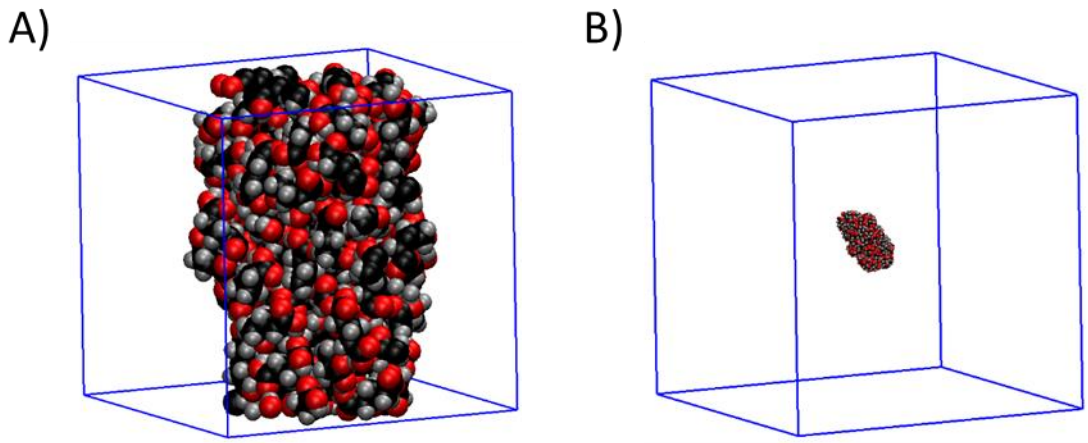

Figure 91: A) $(GLU)_{100}$ in a box of 3.5 nm long after a 10 ns trajectory.; B) $(GLU)_{100}$ in a box of 20 nm long after a 10 ns trajectory (GAFF).

II.2 Methodological approach

II.2.1 Dry aggregate

One can imagine many ways to form aerosols by molecular dynamics simulations. For dry organic acid aerosols, two methods can be used:

- The nucleation method which consists in progressively adding a small amount of molecules, stabilizing the aerosol at each stage. By this method, the particle grows slowly until the desired amount of molecules is reached.
- The "one in all" method which consists in the addition of the desired number of molecules randomly in the box, followed by a run for stabilizing the aerosol.

However, the aerosol may stabilize in a local minimum which may not be the overall minimum. Thus a step of annealing may be added in order to get the system in this minimum once the aerosol is formed. Generally, a first step of 10 ns (with a time step of 2 fs) was used in the NVT ensemble to let the molecules aggregate (Figure 92). The MD runs always proceed after an energy minimization step using the steepest descent algorithm.

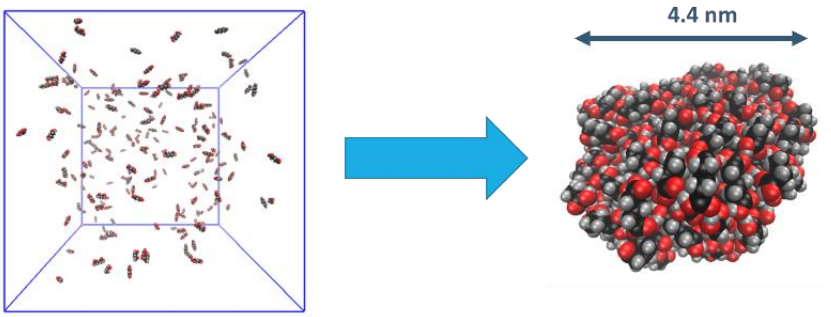

Formation of glutaric acid aerosols at 300 K

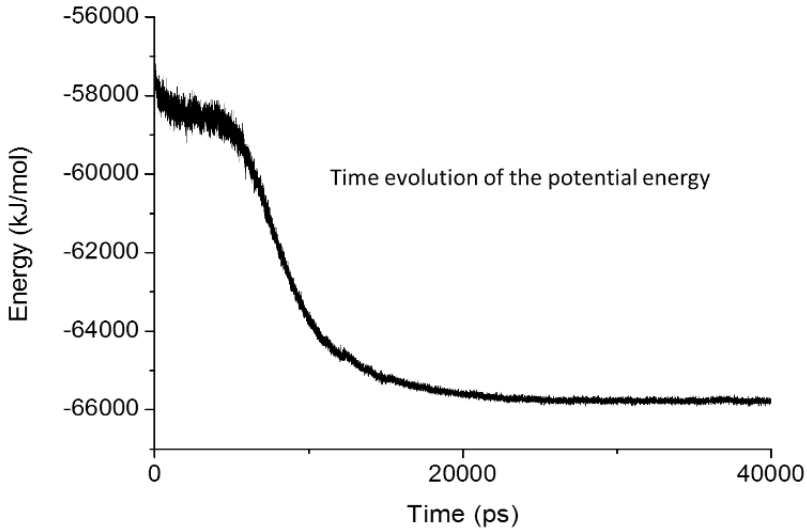

Figure 92: "One in all" method to form an aerosol of glutaric acid (200 molecules). The molecules are placed randomly in the box followed by a MD run in the NVT ensemble (300K) until stabilization of the potential energy (at least 10 ns).

The variation of the total energy is the criterion used to confirm that the particle is equilibrated. More especially, the potential energy should decrease and reach a plateau indicating that the system has reached the equilibrium.

First tests were done on an aerosol of 200 molecules. However, the aerosol generally breaks in two parts after a few steps. The two parts can collide again to form another aerosol, but the aerosol never stabilizes enough and breaks again. This can be followed both from the energy variations and by visualizing the trajectory (see energy profile in Figure 93).

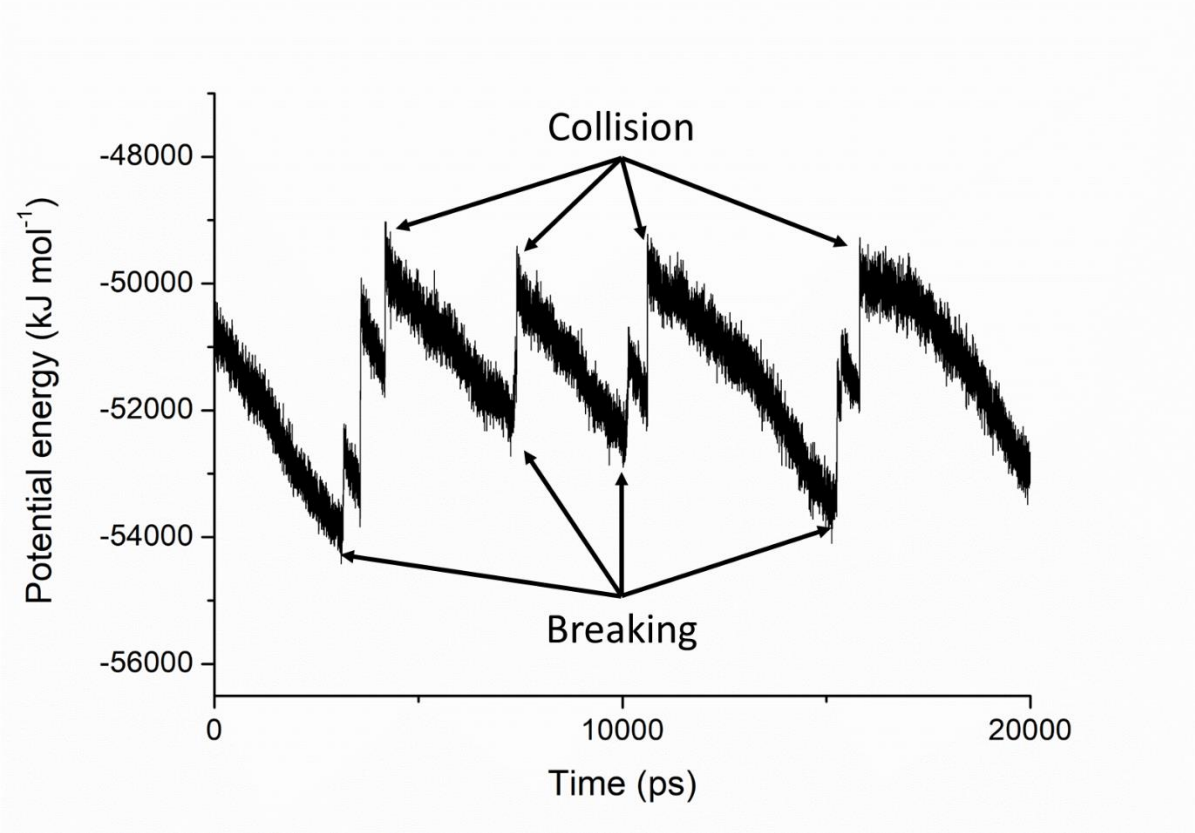

Figure 93: Time evolution of the potential energy showing that the aerosol breaks into two parts or forms again a single particle.

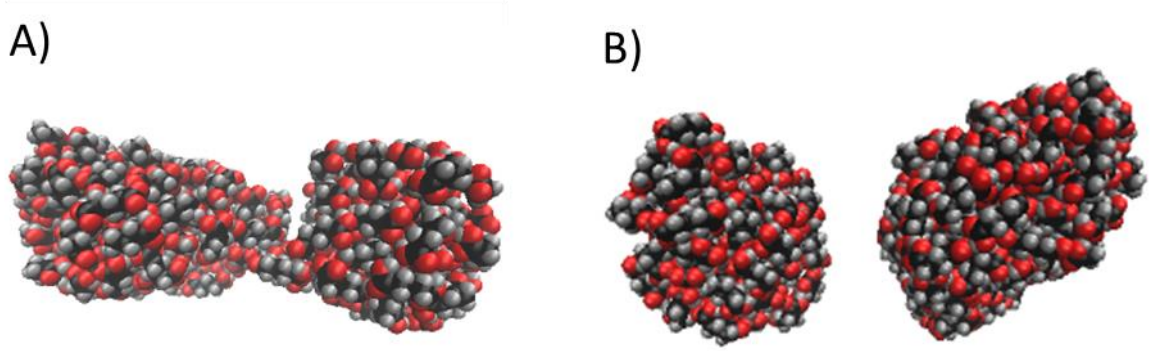

Figure 94: A) $(GLU)_{200}$ during breaking; B) Two aerosol parts of $(GLU)_{200}$ before they collide.

One explanation for this breaking phenomenon is the rotation of the aerosol which induces enhanced centrifugal forces and leads to the separation of the aerosol. This rotation may be an artefact of the computation.

To stabilize this aerosol, rotation was removed at first: the kinetic energy is then used to make the molecule move to a more stable configuration. After a 10 ns trajectory, the rotation is allowed again and the simulation runs until the potential energy is stable during at least 10 ns (see energy profile in Figure 92). Once it is done, analysis is carried out on this sample for 10 ns.

Finally, concerning the dry aerosol generation, the methods selected were the following. Firstly, a step of energy minimization was performed on the system followed by a 10 ns NVT run in order to aggregate the molecules. Then three ways have been selected to stabilize the system:

- The first way was to prolongate the run up to 60 ns without any annealing on angular momentum removal. This procedure will be called Generation Process 1 (GP1).
- The second way was to do a 5 ns long annealing before restarting the computation in the NVT ensemble during 60 ns. This procedure will be called Generation Process 2 (GP2).
- The third way was to do a 5 ns run where the angular momentum was removed. However, in order to use the angular removal algorithm, the periodic boundary conditions have to be removed as well. In order to keep the accuracy and the number N of molecules, the cut-off radius for both Van der Waals and electrostatic interaction was increased to 6 nm in order to be sure that long range interactions are taken into account properly. Moreover, the LINCS algorithm that freezes the bonds has to be removed as well.
  Then an energy minimization step followed by a 60 ns NVT run was done in the same conditions as previously. This procedure will be called Generation Process 3 (GP3).

Using these three generation processes, aggregates of 20, 50, 100, 200 and 500 molecules were generated.

A fourth way was also tested mimicking the nucleation process. In each case a first step of energy minimization was done followed by a 60 ns run in NVT ensemble. The molecules were added 20 by 20 but as the computation was time-consuming, only aggregates up to 100 molecules were generated. This procedure will be called Generation Process 4 (GP4).

All the generation trajectories were followed by a 2 ns production run.

II.2.2 Wet aerosol

In the case of glutaric acid, the influence of water has been studied. Both 1:1 and 1:2 glutaric acid: water ratios have been selected. We know that these ratios can only be representative of low relative humidity conditions and the characterization of aggregates with a higher amount of water[117–119] may be the scope of another study. Addition of water on the particles has been modelled following two methods:

- The nucleation of water by adding the desired amount of water molecules randomly in the box already containing the dry aggregate (Figure 95). The chosen dry aggregates that serve as starting points are those generated with GP3 (angular momentum is removed). This choice has been made since these aggregates proved to be stable as will be discussed later.

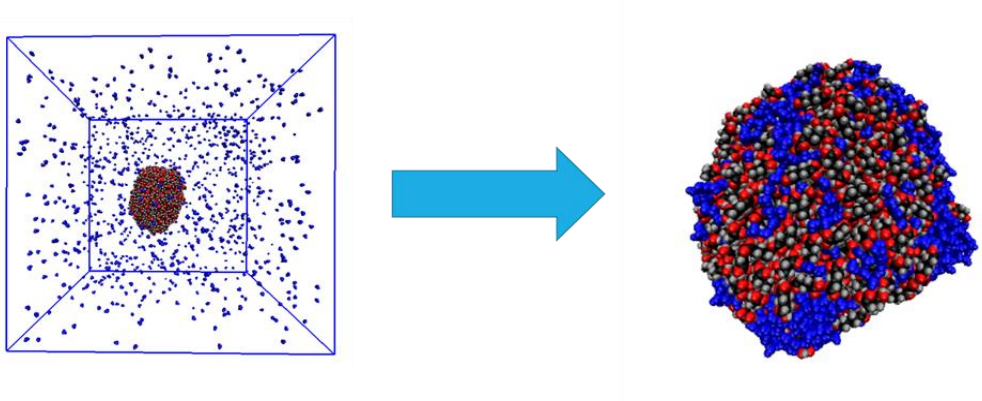

Figure 95: Generation method of wet aggregates by nucleation of water around the dry aggregate.

- The co-condensation of a certain amount of water molecules and glutaric acids that are both placed randomly in the box. Then the generation processes used for dry aggregates were used. In this case, aggregates with the same glutaric acid and water ratios as the nucleation method have been modelled.

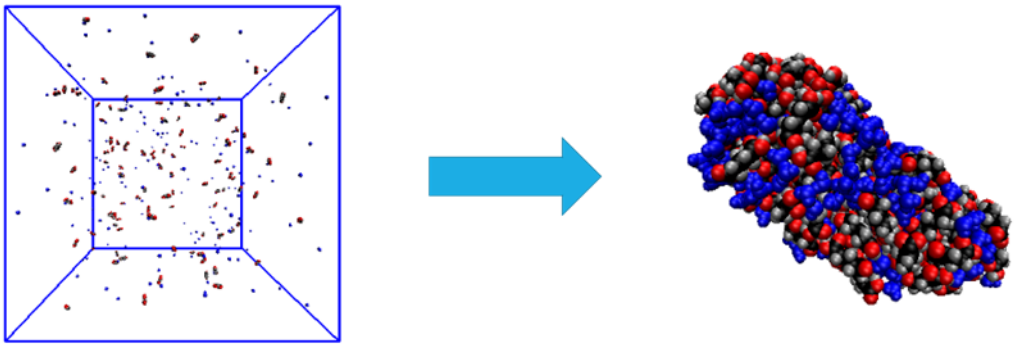

Figure 96: Generation method of wet aggregates by cocondensation of both acid and water molecules.

In both cases, a production run of 2 ns was then performed for the analysis.

II.3 Aerosol characterization

II.3.1 Impact of the methodology on the stability

It has been observed that there is a high variability concerning the stability of the aggregate depending on the system and the generation process as can be seen in Table 30. Indeed, in the case of glutaric acid, we were not able to generate an aggregate of more than 50 molecules using the GP1 and 100 molecules in the case of GP2 (with annealing step). Only generation processes GP3 and GP4 were able to stabilize the particles. GP4 proved to be time consuming for reaching particle sizes comparable to the other generation modes. However, as discussed in the article that will follow, when the particle is too small, the properties may not be representative of the "real" system.

Table 30: Stability of the glutaric and valeric acid aggregates as a function of the number of molecules and the generation process used. '-': cases not tested.

	N	GP1	GP2	GP3	GP4
Glutaric acid	20	stable	stable	stable	stable
	40	-	-	-	stable
	50	stable	stable	stable	stable
	60	-	-	-	stable
	80	-	-	-	stable
	100	unstable	stable	stable	stable
	200	unstable	unstable	stable	-
	500	unstable	unstable	stable	-
Valeric acid	20	stable	stable	stable	stable
	40	-	-	-	stable
	50	stable	stable	stable	stable
	60	-	-	-	stable
	80	-	-	-	stable
	100	stable	stable	unstable	stable
	200	stable	unstable	unstable	-
	500	stable	unstable	unstable	-

Concerning valeric acid, the trend is the opposite of the glutaric acid aerosol. Indeed, GP3 is not able to produce stable aggregates containing more than 50 molecules while GP1 is able to produce larger particles.

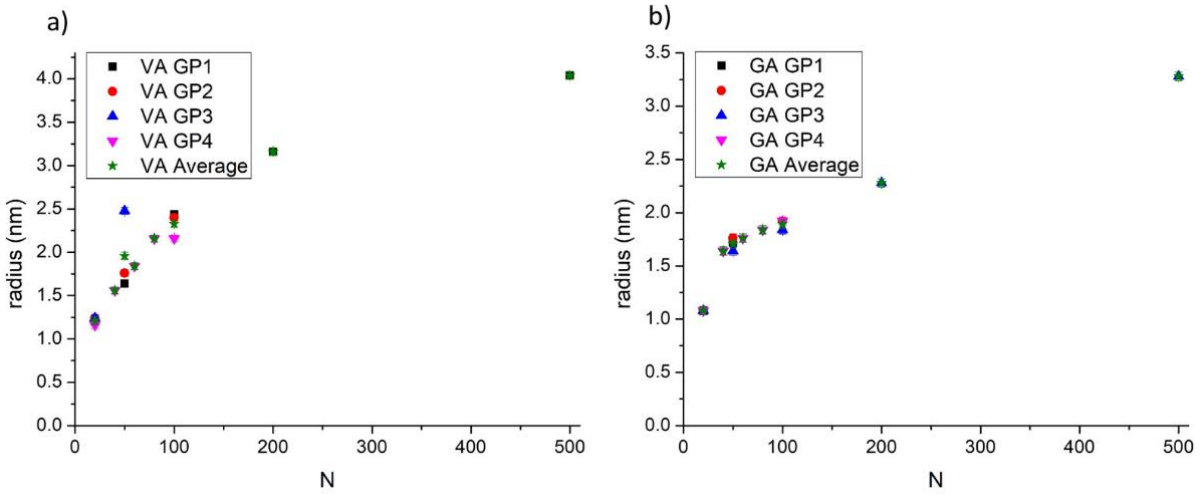

Figure 97: a) Radius of valeric acid aerosols (VA) as a function of the number of molecules N for the different generation processes (GP1: Random generation (Black); GP2: Random generation + annealing (Red); GP3: Random generation + Angular (Blue); GP4: Generation step by step (Pink)). b) Radius of Glutaric acid aerosols (GA) as function of the number of molecules N for the different generation processes. For both figures, the average for a given aerosol size over the generation processes is represented in green.

An interesting result, is that the radius of the particle calculated from the radial distribution of the COM of the acids with respect to the aerosols COM, follows the same trends whatever the generation process, as plotted in Figure 25. The atom surface ratio computed with Connolly

surfaces (see chapter 2 section II.4.3) shown in Figure 98 remains also constant whatever the generation process.

These are important conclusions showing that our results are not depending on the generation method.

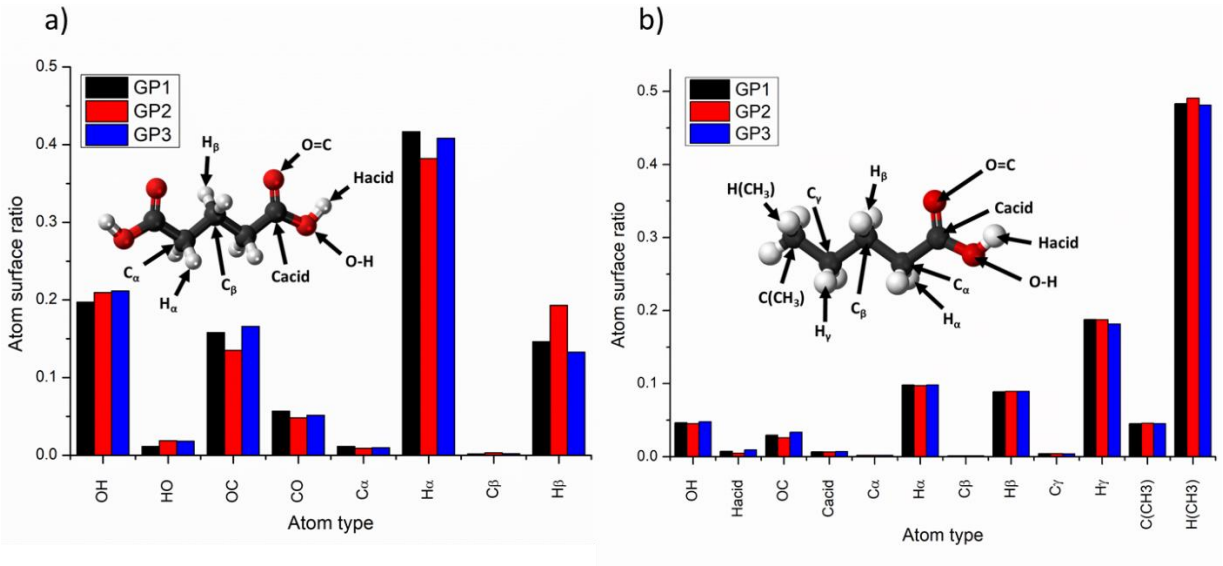

Figure 98: Atom surface repartition of (a) the glutaric acid and (b) the valeric acid aggregates made of 50 molecules as a function of the generation process used.

Concerning the generation of wetted aggregates, the generation by co-condensation leads to unstable aggregates for almost all generation processes and sizes (Table 31) while the condensation of water on dry aggregates formed stable ones except for two cases: (i) the aggregates at both ratios and 200 molecules of glutaric acid, and (ii) the aggregate of 100 glutaric acid and 200 water molecules which may be an artefact from computation. The instability of this generation process (cocondensation) may be due to the fact that the system has not enough time to stabilize before the aerosol breaks due to its rotation. On the contrary, in the case of water addition the aerosol is already stabilized so when water molecules condensate they can stabilize more easily.

Table 31: Stability of the wetted glutaric acid aggregates formed by co-condensation as a function of the number of molecules, the glutaric acid:water ratio and the generation process used. '-': cases not tested..

Ratio GA:H2O	N(GA)	GP1	GP2	GP3	GP4
Ratio 1:1	20	-	-	-	stable
	40	-	-	-	stable
	60	-	-	-	unstable
	80	-	-	-	unstable
	100	unstable	unstable	stable	unstable
	200	unstable	unstable	stable	-
Ratio 1:2	20	-	-	-	stable
	40	-	-	-	stable
	60	-	-	-	stable
	80	-	-	-	unstable
	100	unstable	unstable	stable	unstable
	200	unstable	unstable	unstable	-

However, the characteristics of the particles generated by co-condensation are the same as the aggregates generated by nucleation. Indeed, as shown in Figure 99, the structures determined by the radial distribution function of both generation methods are quite close. Furthermore, on Figure 100, we can observe that the atomic surface ratios do not change neither. To conclude, we have verified that the molecular organization of our model aerosol particles does not depend on the generation process. Therefore, the generation process that has been adopted is the one that gives the most stable aggregates within a reasonable computational time.

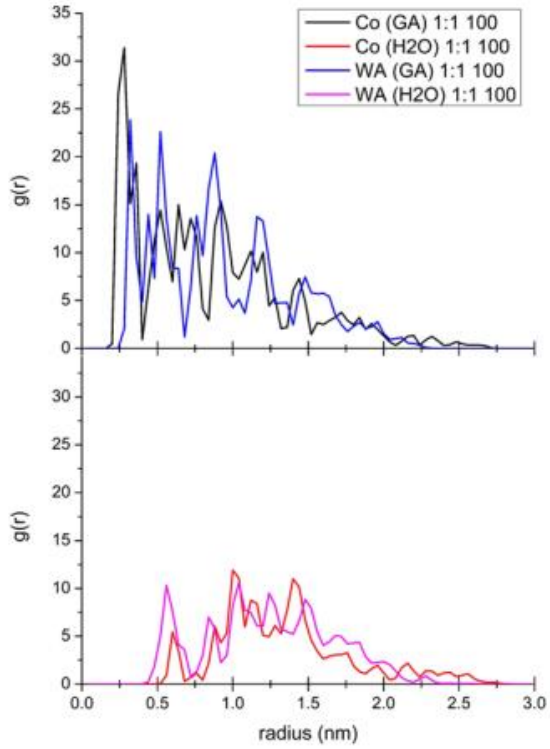

Figure 99: Comparison of the radial distribution functions (RDFs) between the 1:1 ratios of glutaric acid:water aggregates of 100 glutaric acid molecules generated either by co-condensation (Co) method or by nucleation of water on the dry aggregate

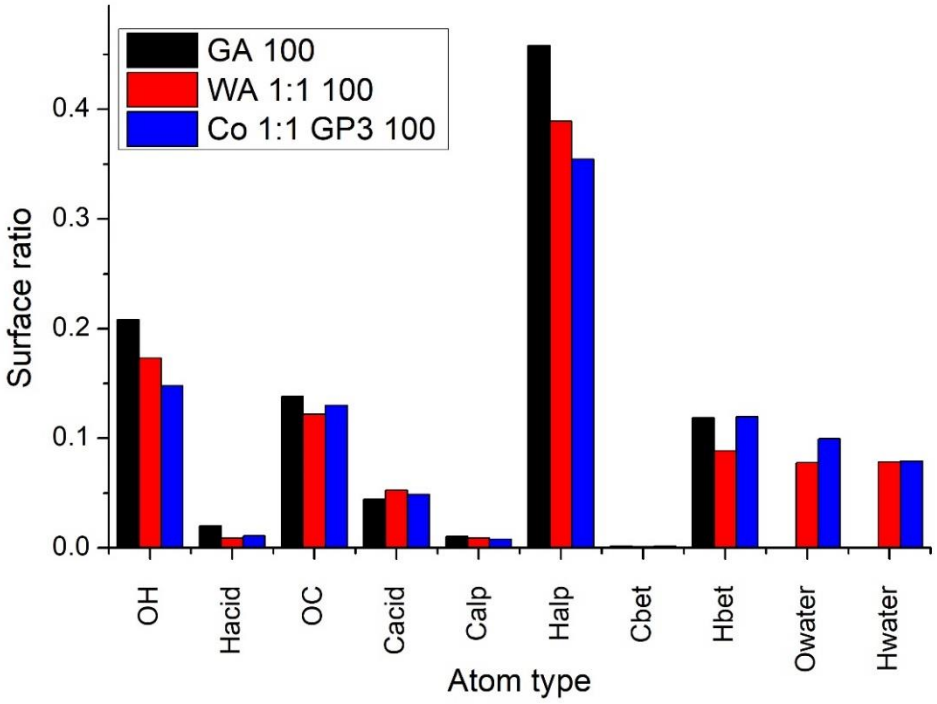

Figure 100: Comparison of the atoms repartition at the surface of the glutaric acid aggregate (GA) of 100 molecules (black), the wetted glutaric acid aggregates with a 1:1 glutaric acid:water ratio generated by nucleation of water on the dry aggregate (WA, in red) and by co-condensation (Co, in blue).

II.3.2 ACS Earth and Space Chemistry paper

The following paper published in ACS Earth and Space Chemistry (DOI: 10.1021/acsearthspacechem.8b00172) introduces the main results regarding the characterization of the aggregates formed (Structure, Connolly surface, hydrogen bonds and binding energies). This paper was selected as an issue front cover (Figure 101).

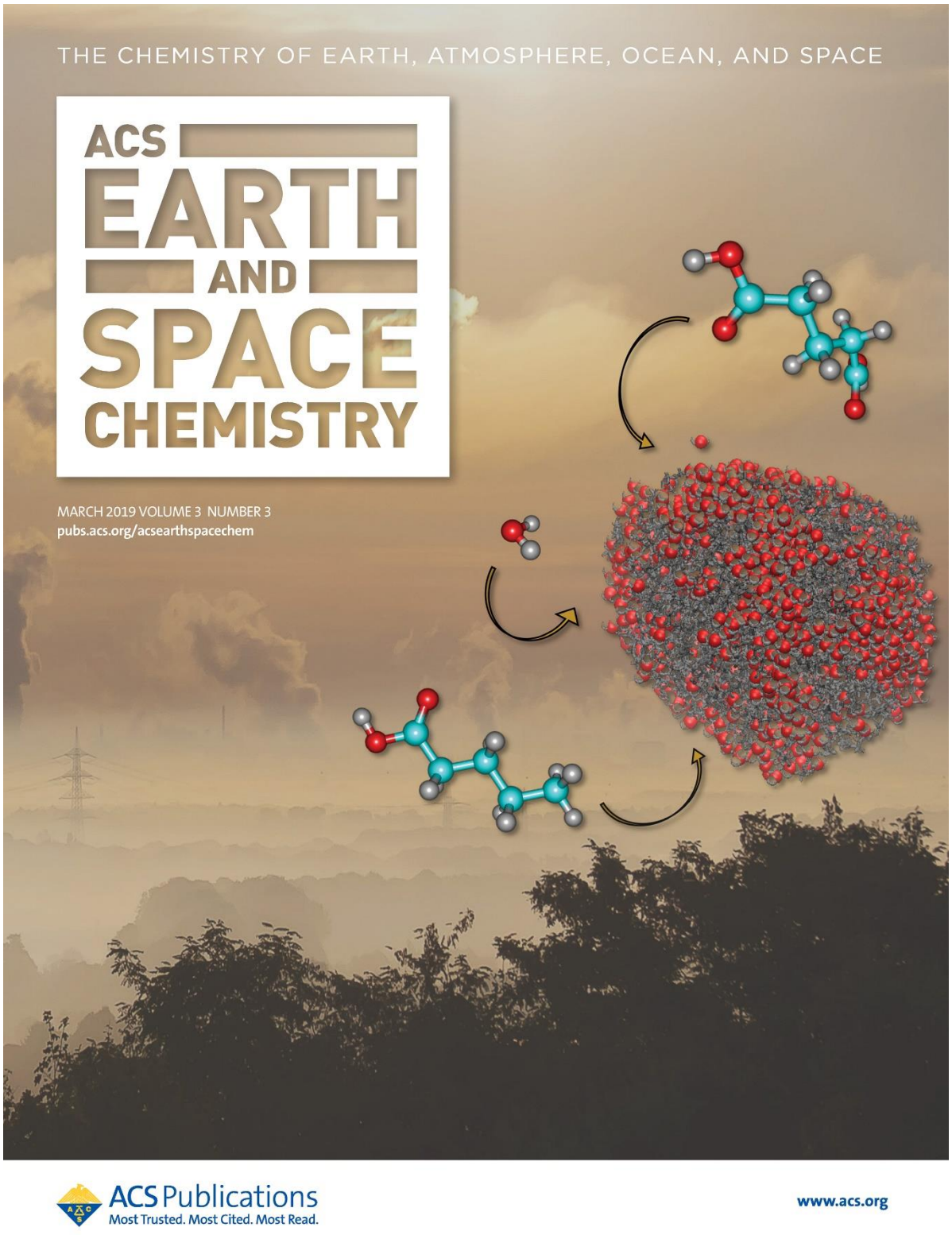

Figure 101: Front cover of the ACS Earth and Space Chemistry issue of March 2019.

ACS EARTH AND SPACE CHEMISTRY

Article

Cite This: ACS Earth Space Chem. 2019, 3, 380−389

http://pubs.acs.org/journal/aesccq

Classical Molecular Dynamics Study of Small-Chain Carboxylic Acid Aerosol Particles

Antoine Roose,[†,‡] Céline Toubin,[†] Sébastien Dusanter,[‡] Véronique Riffault,[‡] and Denis Duflot*[,†]

[†]Université de Lille, CNRS, UMR 8523 - PhLAM - Physique des Lasers Atomes et Molécules, F-59000 Lille, France

[‡]Département Sciences de l'Atmosphère et Génie de l'Environnement (SAGE), IMT Lille Douai, Université de Lille, F-59000 Lille, France

Supporting Information

ABSTRACT: The growth of small valeric (pentanoic) and glutaric (pentanedioic) acid aerosol particles from 20 to 500 molecules has been investigated at room temperature using classical molecular dynamics simulations. As a result of a higher propensity to form hydrogen bonds, glutaric acid aggregates are shown to be denser than their valeric counterpart. The addition of water molecules with water/acid ratios of 1:1 and 2:1 has then been studied in the case of the diacid. At a low water content, water primarily forms small islands on the surface. When the amount of water increases, it penetrates deeper into the aggregate but a significant fraction remains at the surface. A Connolly surface analysis reveals that the surface is mostly covered by hydrogen atoms from CH_2 groups, with acidic hydrogens being saturated and not available at the surface, for both dry and wet particles. These atomic distributions could impact the reactivity of such particles with gas-phase oxidants and the uptake of trace gases.

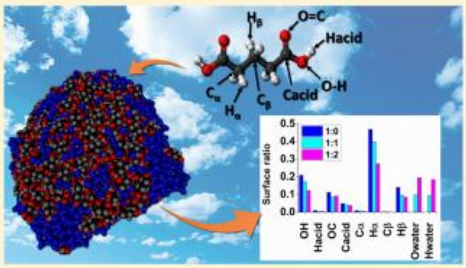

KEYWORDS: *glutaric acid, valeric acid, classical molecular dynamics, aerosol, atmosphere*

INTRODUCTION

It is well-known that atmospheric aerosols contain a significant part of carbonaceous compounds, either elemental (black carbon and fresh soot), organic, or a mixture of both types (brown carbon).[1] They can be primarily emitted from either biomass burning or other anthropogenic sources or formed via the oxidation of gaseous precursors. In addition to their direct effect on the radiative balance of the Earth,[2] they can also act as cloud condensation nuclei (CCN)[3] onto which water will condense to form cloud droplets. In this context, a better understanding of their formation processes and interaction with water is fundamental.

Carboxylic acids are ubiquitous in the atmosphere and constitute one of the most abundant groups of species among organic compounds as oxidation end products.[4,5] These acids have been observed in both the gas and particulate phases, with low-molecular-weight compounds, such as formic and acetic acids, being mainly observed in the gas phase,[6] and higher molecular weight compounds, such as dicarboxylic acids, partitioning predominantly to the particulate phase.[7] Small-chain fatty acids (mono- and dicarboxylic) have for example been detected in various areas,[8,7−10] including valeric acid (VA) and glutaric acid (GA). For example, in the north of France, measurements at an urban background in Douai[9] and an industrialized coastal site in Dunkirk[10] gave concentrations of only a few nanograms per meter cubed on a daily average with no clear seasonal trend.

To better understand the formation of secondary organic aerosols (SOAs) and the impact of environmental conditions, such as relative humidity (RH) and temperature, on their atmospheric fate, simulation tools are paramount. Several molecular dynamics (MD) studies have focused previously on organic aerosols, with some of them specifically on carboxylic acid aerosols. Ma et al.[11] have studied the behavior of inverted micelles of a dicarboxylic acid (C_3−C_9 and branched C_9) layer on a droplet of water at 300 K and observed the formation of two separate phases, except for malonic acid (C_3), which dissolves in water. Water nucleation was also investigated by MD simulations on small dicarboxylic acid aggregates[12,13] as well as formic,[14] acetic, and propionic acid aggregates[15] in the 100−250 K temperature range. These authors have highlighted that pressure does not have a strong influence, in contrast to the temperature and RH. For the highest temperature range ($200 < T < 250$ K), mixed water−acid droplets were formed, while water islands were observed at lower temperatures. More recently, the same kind of study has been performed on mixed formic and acetic acid aggregates.[16] These simulations have shown that the interaction between both acids has no influence

Received: November 6, 2018
Revised: February 11, 2019
Accepted: February 12, 2019
Published: February 12, 2019

DOI: 10.1021/acsearthspacechem.8b00172
ACS Earth Space Chem. 2019, 3, 380−389

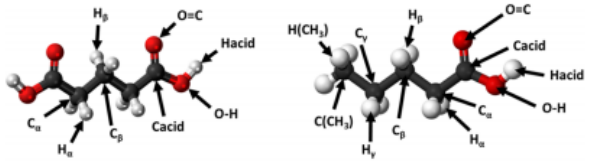

Glutaric acid Valeric acid

Figure 1. Labeling of atoms and functional groups in both molecules.

and the overall behavior is similar to what was found for the pure organic aggregates.

These MD studies could be used to provide a better understanding of observations made in laboratory experiments, such as studies focusing on the uptake of trace gases on atmospheric aerosols. Indeed, some experiments carried out by Taketani et al.[17] and Lakey et al.[18] on dicarboxylic acid particles have highlighted some trends for the hydroperoxy radical (HO_2) uptake, which depends upon RH. Humidity can increase the uptake because it can enhance the diffusivity of gaseous compounds in the bulk.[19] On the contrary, Lakey et al.[18] have also estimated that, for some organic aerosols, such as humic acids, the increase of RH can finally lead to the formation of a micelle, which creates a diffusion barrier and, thus, decreases the uptake. Studying the structure of organic aerosols by MD can lead to the prediction of such effects.

The goal of the present paper is to study the properties of small organic aerosols, formed of GA molecules ($C_5H_8O_4$), and to perform a comparison to its monoacid counterpart, i.e., VA ($C_5H_{10}O_2$). In addition, this study investigates the adsorption of water molecules on the glutaric aerosol surface. Indeed, as a result of the size of the molecules, quantum calculations can only be considered for small clusters[20] and the use of classical MD techniques is mandatory.

■ COMPUTATIONAL DETAILS

Aerosols of pure VA, pure GA, and wetted GA were generated by classical MD simulations with the GROMACS program package (version 5.0.7).[21]

The geometries of isolated VA and GA molecules (Figure 1) were both optimized quantum mechanically at the M06-2X/6-311++G** and MP2/6-31+G** levels,[22−24] respectively, using the Gaussian 09 quantum package.[25] Topology files were generated with the Antechamber program[26] using the parameters from the AMBER GAFF force field[27] (see the Supporting Information). RESP charges[28−30] for GA have been computed at the MP2/6-31+G** level, while for VA, AM1-BCC charges were used.[31] Water was described with the SPC/E model.[32]

The simulations have been performed in the *NVT* canonical ensemble after an energy minimization with the steepest descent algorithm. The temperature was kept fixed at 300 K with the velocity rescale algorithm and a coupling time of 0.1 ps.[33] The cubic box was set to a width of 30 nm. Dry aerosols were formed from the aggregation of 20, 50, 100, 200, and 500 molecules of carboxylic acids, randomly placed inside the box. The *NVT* simulation was performed with a time step of 2 fs until stabilization of the total energy. The total simulation time was 60 ns for dry aggregates and 40 ns for wet aggregates, except for the 500 wet case, where the simulations were prolonged for 50 ns. All calculated properties appear to be converged after 30 ns. Finally, 2 ns of production was used for the analysis. Molecules were kept rigid thanks to the LINCS algorithm,[34] where only the angles are free to move, except for water, constrained in the SPC/E geometry. The intermolecular interactions (Coulomb and Lennard−Jones) have been cut beyond 1.2 nm. To take into account the long-range electrostatic interaction, the particle mesh Ewald (PME) method has been used,[35] with a Fourier spacing of 0.12 nm.

Once the aggregate is formed, its angular momentum starts to increase because there is no collision. To remove this artificial motion that leads to the breaking of the aggregate, the center of mass rotation was disabled for 10 ns, with the periodicity of the box and the constraint on the bonds (LINCS algorithm) also being removed during this period. The time step used was decreased from 2 to 0.5 fs. The long-range intermolecular interaction has also been removed, and the cutoff radii for the Lennard−Jones and Coulombic interactions were set to 6 nm to take into account all of the interatomic interactions. Once the aggregate becomes stabilized, the rotation is reactivated and the run is prolonged.

Wetted aggregates have been generated for 1:1 and 1:2 GA/water ratios. The corresponding amount of water molecules was added randomly on the previously obtained dry GA aggregates. It should be noted that only neutral molecules were considered in the present work, even though deprotonated molecules could also be found in atmospheric particles.[36]

Finally, a Connolly surface analysis[37] has been performed using a probing sphere of 0.2 nm with a precision of 500 dots per sphere using the method described by Eisenhaber et al.[38] Note that the Connolly surface corresponds to the contact between the sampling sphere and the van der Waals surface of the aerosol. This provides an estimate of the atomic distribution at the surface of the particle as well as its surface and volume (see Table 1).

■ RESULTS AND DISCUSSION

Geometries of Gas-Phase Acids. Before turning to the analysis of the particle phase, it is worth mentioning an important difference between GA and VA geometries in the gas phase (see Figure 1). Indeed, while isolated VA has a unique geometry of C_s symmetry, GA has three possible conformers (see the Supporting Information). The less stable conformer corresponds to a C_s symmetry similar to VA. The second conformer is stabilized by an intramolecular hydrogen bond between C═O oxygen and the opposite H_α hydrogen atom. At the MP2/6-31+G** level, this conformer is 1.64 kcal mol^{-1} lower in energy. Finally, the third conformation has a hydrogen bond between C═O oxygen and the opposite O−H hydrogen, making it more stable by 4.81 kcal mol^{-1} (MP2/6-31+G*). With a higher level of theory (MP2/aug-cc-pVTZ), the relative energies are not modified significantly (−0.94 and

DOI: 10.1021/acsearthspacechem.8b00172
ACS Earth Space Chem. 2019, 3, 380−389

Table 1. List of the Particle Surfaces and Volumes Given by the Connolly Surface Analysis and Corresponding Calculated Densities

N	surface (nm^2)	volume (nm^3)	density (g/cm^3)
		GA	
20	19.8	6.3	0.70
50	33.8	13.6	0.81
100	50.1	24.6	0.89
200	76.2	45.3	0.97
500	136.5	106.0	1.04
		VA	
20	23.0	6.8	0.50
50	41.7	14.9	0.57
100	63.9	27.4	0.62
200	109.0	49.0	0.66
500	173.0	116.2	0.73
		1:1 GA/Water	
20	32.9	8.4	0.60
50	40.1	16.0	0.78
100	58.6	28.7	0.87
500	151.8	121.7	1.02
		1:2 GA/Water	
20	29.2	8.6	0.65
50	47.8	18.5	0.76
500	171.0	137.3	1.02

−3.66 kcal mol^{-1}, respectively), as also happens for other dicarboxylic acids.[20] All conformers appear to have very similar RESP charges. However, in the aerosol phase, the intramolecular hydrogen bonds are broken to the benefit of intermolecular hydrogen bonds. For this reason, the RESP charges calculated for conformer 1 geometry were used in the MD simulations.

As detailed in the Supporting Information, the force-field parameters were validated by comparing the calculated density and lattice parameters of the bulk crystals to available experimental values.[39−41] The geometry and energy (see below) of the hydrogen bonds were also compared to experimental values as well as *ab initio* results obtained at the MP2/6-311++G(2d,2p) level with zero-point energy (ZPE) corrections.

Structure of VA and GA Aggregates. The snapshots of dry GA and VA aerosols, shown in panels a and b of Figure 2, do not exhibit noticeable differences, thus requiring the calculation of several observables to quantitatively differentiate the two acid aggregation properties.

Radial distribution functions (RDFs), $g(r)$, were obtained by computing the distance between the mass center of the molecule or a functional group and the mass center of the whole aggregate, fixed at r = 0 nm. RDFs have been calculated for the COOH group of both acids, the $(CH_2)_\beta$ carbon chain of GA, and the CH_3 tail of VA with respect to the aggregate mass center. Note that, for clarity, RDFs shown in Figure 3 are

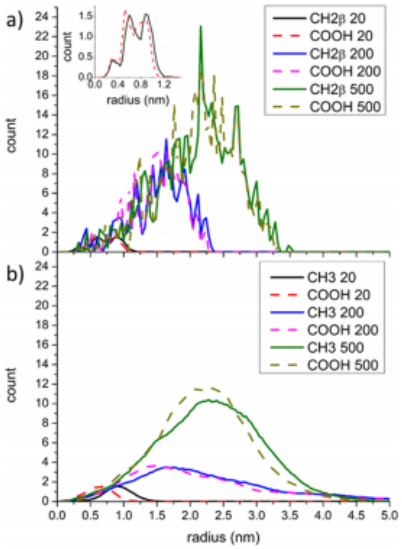

Figure 3. Mean number of specific atom groups as a function of the distance to the (a) GA and (b) VA aerosol centers of mass. The solid and dashed curves represent the distribution functions of the centers of mass of $CH_{2\beta}$ (GA) or CH_3 (VA) and COOH, respectively.

not normalized. For all studied sizes from 20 to 500 GA molecules, the two distributions exhibit well-correlated peaks, with the atoms being uniformly distributed in the volume of the aggregate. For VA, the behavior of $g(r)$ is rather similar. For smaller sizes (N = 20 and 50), the COOH functions are located close to the center of the aggregate. This is due to the creation of intermolecular hydrogen bonds between the COOH groups at the center. When the size increases, the COOH groups are still located in the particle bulk, while the CH_3 groups are becoming more abundant toward the surface.

The GA RDFs exhibit sharper oscillations than the VA RDFs as a result of the formation of hydrogen bonds on both sides of the chains, which provide additional structural features. This effect has also been observed for the orientation of the

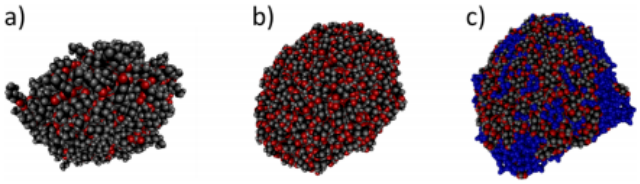

Figure 2. Snapshots of dry (a) VA and (b) GA aggregates containing 500 molecules and (c) 1:2 acid/water aggregate composed of 500 GA molecules.

DOI: 10.1021/acsearthspacechem.8b00172
ACS Earth Space Chem. 2019, 3, 380−389

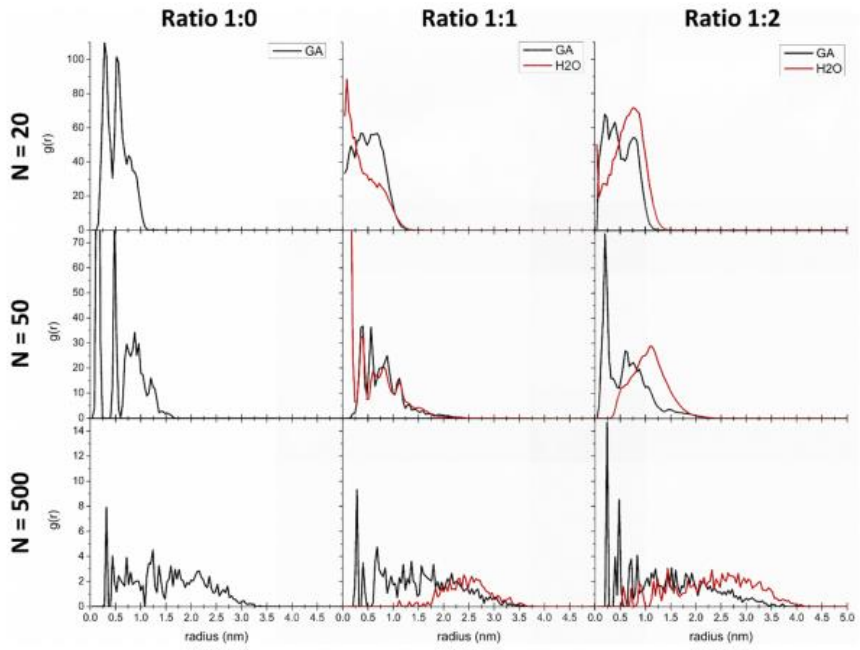

Figure 4. RDFs of (left) dry GA and (middle) 1:1 and (right) 1:2 ratios of GA/water aggregates. The black curve corresponds to the GA center of mass, and the red curve corresponds to the water center of mass.

chains (see the angle distributions presented as Supporting Information).

It is interesting to see how the organization of the chains in the aggregate is affected by the subsequent addition of water. In Figure 2c, a snapshot of the aggregate with 500 GA molecules and 1000 water molecules is shown as an example. In Figure 4, the RDFs of GA and water mass centers for both 1:1 and 1:2 ratios are compared to the RDF of the glutaric center of mass without water at the corresponding size. For the 1:1 ratio and N = 20, the water molecules are located at the center of the cluster, with the acid being repelled outside. At this size, water manages to diffuse between the acid molecules that are less strongly bonded than at larger sizes, as shown later. As the size becomes significant (N = 500) for the 1:1 ratio, most of the water molecules are at the upper edge (r > 2 nm). This is in line with the results of Radola et al.[15] for a N = 120 1:1 propionic acid/water cluster simulated at 250 K; at this water content, the acid aerosol is preserved at the center. It is possible that, for higher acid/water ratios, the acid would create a shell around a water droplet, as found in the propionic acid/water case studied by Radola et al.[15]

When the ratio is increased to 1:2 (Figure 4), the situation is somewhat different because, for small aggregates, the water molecules lie preferentially at the surface of the aggregate, whereas for N = 500, water molecules can also be found in the core of the particle. The larger number of molecules present at the surface tends to create a pseudo-pressure that pushes the water molecules toward the interior. It should be noted that simulations have been extended to 90 ns for both ratios and the largest sizes, N = 200 and 500, to make sure that the distributions are not dependent upon the sampling time, because the diffusion process requires a longer simulation time to be captured.[13] The diffusion of water through an organic core has also been observed by Zhang et al.[42] for a size of N = 120 acetic acid molecules and a 1:3 acid/water ratio at 260 K. For larger acid/water ratios (1:6 or 1:10) and fewer propionic acid molecules (N = 120), Radola et al.[15] showed that, at 250 K, water forms a liquid droplet at the center of the particle, with the acid molecules being repelled toward the edge of the particle. This behavior is consistent with our own results obtained with lower water coverage, longer chains, and larger aggregates, at room temperature.

Using these functions, it is possible to estimate the radius of the formed aggregate. For a homogeneous particle, this radius should be proportional to a power of the number of molecules N: $r(N) = r_0 N^{\alpha}$. Ideally, α should be equal to $^1/_3$ if we assume that the aggregate has a spherical shape. Figure 5 depicts the radius of dry GA and VA particles as a function of N together with a fit of the above function. The radius was obtained by taking the distance corresponding to 5% of the maximum value of the non-normalized RDF. The radii deduced for dry aggregates of both acids appear to closely follow this law, because α = 0.306 and 0.379 for GA and VA, respectively. Interestingly, r_0(GA) = 0.48 nm and r_0(VA) = 0.38 nm, which roughly correspond to half of the length of each isolated molecule (0.37 nm for GA and 0.39 nm for VA). Thus, both acid aggregates appear to behave more or less like spherical objects whose diameters are the length of the monomer.

DOI: 10.1021/acsearthspacechem.8b00172
ACS Earth Space Chem. 2019, 3, 380−389

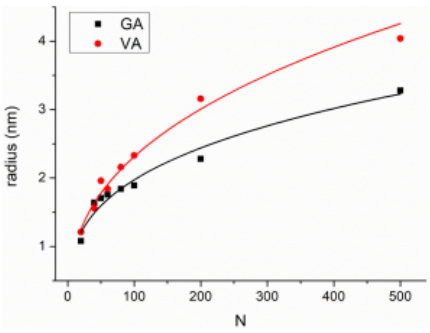

Figure 5. Comparison of the mean radius of the formed (black) GA or (red) VA particles as a function of the number N of molecules. The curves correspond to a $r(N) = r_0N^{\alpha}$ fit.

The density can be calculated from the number of molecules (N = 500) divided by the volume deduced from the Connolly surface (see Table 1). For GA, it is 1.04 g/cm^3, which is about 40% lower than the value measured at 298 K (1.41 g/cm^3[43]) for a solid bulk. For VA, the density is calculated to be 0.73 g/cm^3, which is about 20% less than the measured value of 0.93 g/cm^3.[44] Consistently, the model particles are much less dense than their corresponding bulk counterparts.

From the radii and estimated densities, we observe that VA aerosols are slightly less compact than the GA aerosols. This can be rationalized by the fact that one GA molecule has two acidic tails, instead of one acidic tail for VA. This allows for the formation of a larger number of hydrogen bonds per molecule on average and, thus, a more condensed aerosol.

Upon the addition of water on GA, the radius increases only slightly: for N = 500, by about 6% for the 1:1 acid/water ratio and 24% for the 1:2 acid/water ratio compared to the dry counterpart. The density for both wet aerosols is only slightly lower than that for the dry case (1.02 g/cm^3). Thus, the increase of mass due to water is compensated by the augmentation of the radius and, hence, the volume, indicating an inhomogeneous distribution of the molecules in the aggregate as observed on the RDFs (Figure 5).

Connolly Surfaces. Characterizing the surface in terms of the density of atoms gives some indication on the heterogeneous reactions that may occur depending upon the nature of the gaseous species impinging the particle. Figure 6 displays the surface repartition of the GA atoms for increasing aggregate sizes. Growing from 20 to 500 molecules only make the results vary by a few percentages, suggesting that the surface of relatively small particles could be representative of larger particles. Most of the surface is occupied by hydrogen atoms from the carbon chain (H_α and H_β), followed by both oxygen atoms from the acid functions. Acid functions represent about 40% of the surface, which explains why water is easily adsorbed on the aerosol. However, very few acidic hydrogen atoms are present at the surface, because they are involved in strong intermolecular bonds favoring the cohesion of the aerosol. The same trends occur for VA (not shown here) but with the hydrogen atoms from the methyl group being predominant (almost 50% of the total surface).

On Figure 7, the same distributions obtained for both 1:1 and 1:2 GA/water ratios are compared to the dry case for a

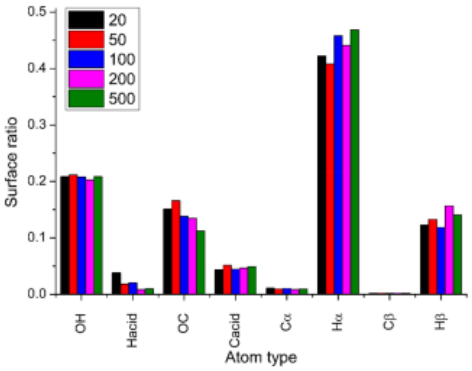

Figure 6. Atom distribution at the surface of dry GA particles for sizes varying between 20 and 500 molecules. The labels are described in Figure 1.

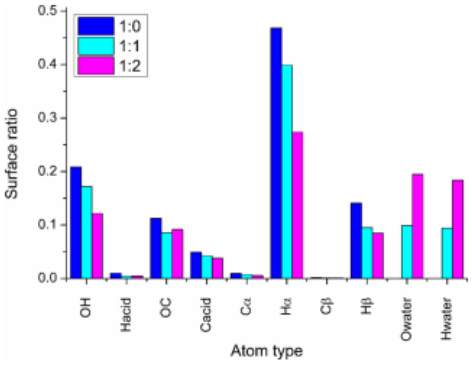

Figure 7. Comparison of the atom surface distribution of dry GA and both 1:1 and 1:2 ratios of GA/water aggregates containing 500 GA molecules.

500 molecule size. For the 1:1 ratio, about 20% of the surface is covered by water, while this proportion increases to about 40% for the 1:2 ratio. This is in agreement with the observation that water molecules tend to stay at the surface, according to the RDF depicted in Figure 4. Reciprocally, the amount of GA atoms remaining at the surface decreases. However, the relative proportion of each GA atom type does not change significantly with respect to the dry case. This further confirms that water molecules, even if adsorbed at the surface, do not induce any substantial change in the molecular organization. Finally, using the Connolly method, the water surface to bulk ratio is found to be 45% for the 1:1 case and 49% for the 1:2 case.

Hydrogen Bonds. The hydrogen bond length and O−O−H angle distribution for increasing sizes of GA and VA aggregates are shown in Figure 8. It should be recalled that, within our classical description, a strong hydrogen bond is characterized by a H−O bond of the order of 0.28−0.29 nm and a O···O−H angle close to 0°. For both molecules, the bond lengths are centered at the same value (~0.269 nm, Figure 8a for GA; 0.285 nm, Figure 8c for VA). These values

DOI: 10.1021/acsearthspacechem.8b00172
ACS Earth Space Chem. 2019, 3, 380−389

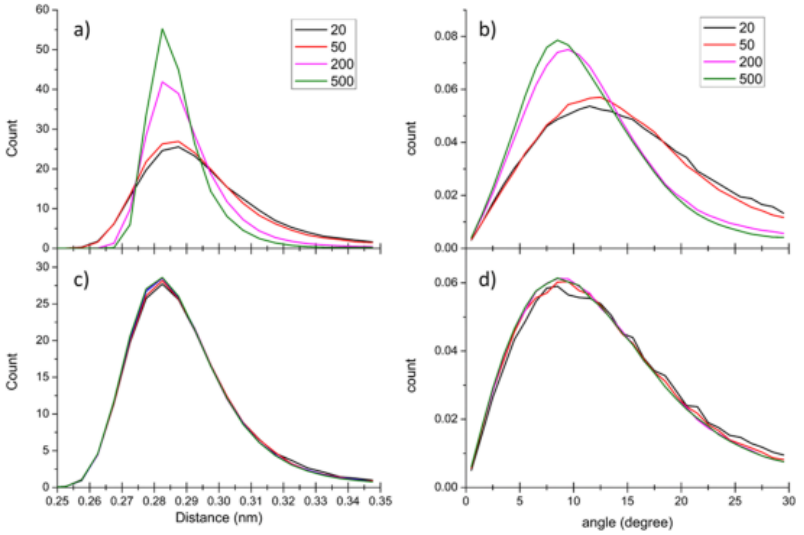

Figure 8. (a and c) Hydrogen bond distance distribution and (b and d) O···O−H angle distribution of dry (a and b) GA and (c and d) VA aerosols for sizes varying between 20 and 500 molecules.

are close to the experimental values.[39,40] As expected, the number of hydrogen bonds is about twice larger for GA than for VA. For VA, the distribution does not depend upon the size, while for GA, it becomes thinner as the number of molecules increases: the full width at half maximum (fwhm) decreases from ∼0.03 nm for N = 20 to ∼0.02 nm for N = 500. Similarly, it remains essentially constant around 10° for the angles (panels b and d of Figure 8), with the exception of a small shift when the GA aerosol size increases, meaning that the three atoms are almost perfectly colinear (Figure 8b). This angle is close to ∼12° found experimentally for both acids in the crystalline phase.[45,46] These results indicate that the core of the aggregate does not evolve during the growth for VA, whereas in the case of GA, the growth of the particle is associated with a significant strengthening of the hydrogen bonds. When water is added on GA (see the Supporting Information), the results remain essentially the same, for both acid/water ratios, supporting the previously stated assessment that water does not significantly change the molecular organization of the particle.

Complementary to the geometrical parameters, the dynamics of hydrogen bond formation/breaking inside the simulated aggregate can be characterized through the calculation of the time evolution of the hydrogen bond autocorrelation functions $a(t)$.[47] This is depicted in Figure 9 for small and large dry GA and VA aggregates. For both acids, the decay is faster for the small aggregate, indicating that the hydrogen bond lifetime is shorter. In comparison of the two acids, GA exhibits a slower decay than VA for each size and $a(t)$ is close to 1 and remains constant over time for N = 500. These trends are the signature of the difference of nature between the two acids: GA behaves like a solid, with the molecules being more tightly bonded, while VA behaves like a liquid. When water is added to GA,

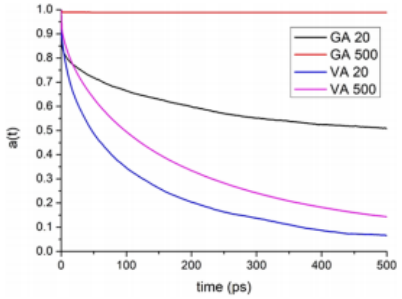

Figure 9. Autocorrelation function over hydrogen bonds between dry GA and VA aggregates of 20 and 500 molecules.

$a(t)$ remains the same and close to 1 for N = 500; therefore, the nature of the wetted aggregate is not significantly altered.

Binding Energies. With the water SPC/E model, a typical energy for a hydrogen bond formation is about 20 kJ/mol (e.g., see ref 48). For the acid−acid interaction, Darvas et al.[13] have implicitly assumed the same value for malonic−malonic acid and water−malonic acid interactions. The present simulations give a value of 90 kJ/mol for GA−GA, corresponding to four bonds, so that a typical value would be about 22.5 kJ/mol (see the Supporting Information). This is slightly below a previous MD value obtained on the crystal (27.4 kJ/mol in ref 49) but underestimated when compared to more refined results. Indeed, at the MP2/6-311++G(2d,2p)+ZPE level, we obtain for the gas-phase GA−GA dimer a value of 139 kJ/mol, corresponding to 34.7 kJ/mol per bond. This is close to the formic acid dimer, for which the best *ab initio* result (at MP2/VQZ2PP//TZ2P with counterpoise correction) is 31 kJ/

DOI: 10.1021/acsearthspacechem.8b00172
ACS Earth Space Chem. 2019, 3, 380−389

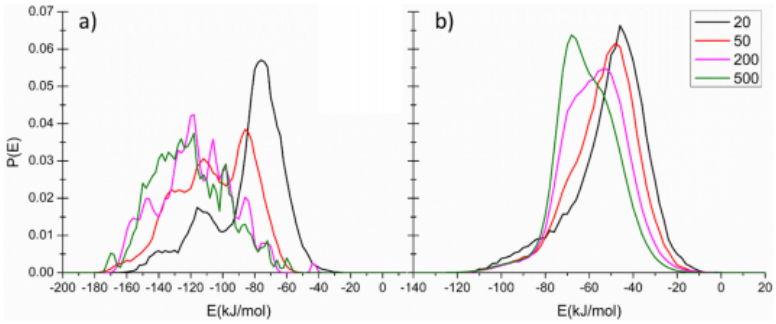

Figure 10. Binding energy distribution of dry (a) GA and (b) VA particles for 20−500 molecules.

mol.[50] In another work by Petit et al.[51] on C_6−C_{12} diacid crystals using density functional theory (DFT), an upper estimate of 42 kJ/mol per bond was obtained. As shown in the Supporting Information, the four bonds are not identical in their geometry, so that the energy of each of them is not strictly speaking the same. For the VA−VA dimer, the geometry of the dimer is simple because the two COOH groups form two very similar bonds (see the Supporting Information). The calculated MD energy of 29.3 kJ/mol (per bond) is very close to the MP2/6-311++G(2d,2p)+ZPE energy (31.5 kJ/mol) and just above classical simulations on the crystal (27.9 kJ/mol in ref 49). Finally, for the GA−water interaction, we use the "unfolded" isomer of the acid, more representative of what happens in the aggregate. The MD energy of the hydrogen bond is 42.7 kJ/mol, much larger than the *ab initio* result (28.5 kJ/mol). The same situation occurs for the VA−water case, because the MD value is 42.5 kJ/mol, while the *ab initio* result is 33.2 kJ/mol. Clearly, a more detailed study at the quantum level is needed, including basis set superposition error in particular, especially for the GA−GA and GA−water cases, but this is beyond the scope of the present study.

For consistency, the MD values will be used to obtain an estimation of the average number of hydrogen bonds per molecule in the analysis of the binding energy distributions of the aggregates. Such global distributions for dry GA and VA are depicted in Figure 10. For the smallest (N = 20; Figure 10b) VA cluster, the maximum is found around −40 kJ/mol, indicating between 1 or 2 hydrogen bonds. When the size increases, the maximum is shifted toward lower values, culminating to about −70 kJ/mol, i.e., between 2 and 3 bonds. The widths of the distributions are approximately the same. For GA (Figure 10a), the behavior is somewhat different qualitatively and quantitatively. For N = 20, there are well-defined peaks at about −80, −120, and −140 kJ/mol, characteristic of about 4, 5, and 6 bonds, respectively. The peak corresponding to the lowest number of bonds is by far the most intense. Increasing the size of the aggregate to 50 then 100 lowers the intensity of this first peak to the benefit of the second and third peaks. For even larger sizes, the peaks become less well-defined and the −80 kJ/mol peak disappears. For N = 500, the maximum probabilities now correspond to −120 and −140 kJ/mol and to a less extent −100 kJ/mol. This means that the number of hydrogen bonds is now about 6 ± 1. As expected from the dicarboxylic nature of GA, this number is roughly twice that found for VA and is consistent with the more compact nature of GA aggregates with respect to VA inferred from the density and hydrogen bond geometrical distributions.

When water is added, a more refined analysis is needed as a result of the three different types of interactions. Moreover, it is possible to distinguish between an acid molecule surrounded by water (GA−water) and a water molecule interacting with the surrounded acid molecules (water−GA). The binding energy distributions for 1:1 and 1:2 GA/water are displayed in Figure 11. The acid−acid binding distribution is compared to the dry case (Figure 11a). Upon the addition of water, the distribution is shifted toward higher energies, with the maximum being displaced from −120 kJ/mol in the dry case to −100 kJ/mol. This can be rationalized by the fact that some of the GA−GA bonds present in the dry aggregate have been broken in favor of interactions with water. This is clearly seen on the GA−water interaction (Figure 11b) that is characterized for both ratios by a broad distribution ranging between −100 and 0 kJ/mol. Dependent upon the configuration of the molecules in the aggregate and using the MD energy of 42.7 kJ/mol, the number of hydrogen bonds formed between one GA and water would then vary between 2 and 0. From the water point of view, the binding energy distributions are presented in Figure 11c, which gives the probability for a water molecule to be bonded to a GA molecule. For the 1:1 case, the maximum is indeed located around −40 kJ/mol, corresponding to 1 bond. At a ratio of 1:2, the distribution shape is slightly changed, with a larger proportion of water molecules that are not interacting with the carboxylic acids but that are instead interacting with other water molecules, as seen on the water−water binding energy distribution (Figure 11d), whose maximum is shifted toward lower energies as the number of water molecules increases. The binding energy analysis is representative of the formation of water islands at the surface of the organic aggregate.

These findings may be compared to two previous studies on similar systems, both with classical MD. First, Radola et al.[15] studied the formation of acetic and propionic acid aggregates for 1:1 to 1:6 water/acid ratios. The number of molecules was set to 120, but similar results were obtained with 240 molecules. Because of the use of the TIP5P potential for water,[52] the maximum temperature is 250 K and the typical water−water binding energy is about −25 kJ/mol. The results of the 1:1 propionic acid/water cluster at 250 K may be

DOI: 10.1021/acsearthspacechem.8b00172
ACS Earth Space Chem. 2019, 3, 380−389

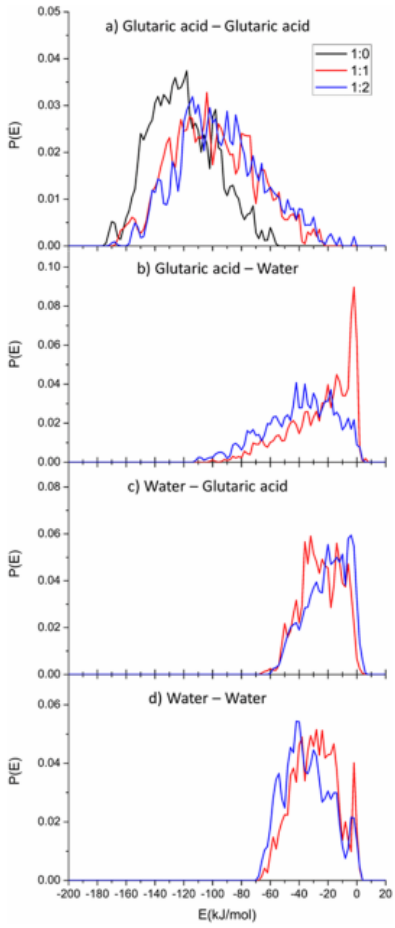

Figure 11. Comparison of binding energy distributions of dry (black) GA particles and (red) 1:1 and (blue) 1:2 GA/water particles for the (a) GA−GA, (b) GA−water, (c) water−GA, and (d) water−water interactions.

compared to the present 1:2 GA/water aggregate at 300 K. The three propionic−propionic, propionic−water, and water−water interactions show three well-defined peaks centered at −25, −25, and −75 kJ/mol. It should be kept in mind that these authors assumed the same value of −25 kJ/mol for all types of hydrogen bonds. Thus, at low water contents and high temperature, the results are similar to those for GA, with water islands scattered at the surface of the aggregate. However, because propionic acid is a monocarboxylic acid, the number of bonds is lower than that for GA. In another work,[13] Darvas et al. also used the same methods to study water adsorption on malonic acid aggregates, a smaller dicarboxylic acid ($C_3H_4O_4$). The use of 212 malonic acid molecules and 300 water molecules provides a ratio close to the present 1:2 GA/water ratio. As seen by comparison of Figure 5 of ref 13 to the present Figure 11, similar trends are observed: a broad distribution from malonic−malonic binding energy centered around −125 kJ/mol, three well-defined peaks at 0, −75, and −125 kJ/mol for malonic−water, and four peaks characteristic of 0−4 hydrogen bonds for water−water interactions. The competition between the acid−acid and acid−water interactions has also been observed for palmitic acid adsorbed on NaCl at various humidities.[53] For long-chain acids, lateral intermolecular interactions are also playing a role in the organization of the molecules and not only the bonding through the COOH groups.

CONCLUSION

MD simulations have been performed to model the formation of sub-micrometer organic aerosols of carboxylic acids, a monoacid (VA) and a diacid (GA), under dry or humid conditions at two acid/water ratios and ambient temperature. Two sets of comparisons have been addressed: first, GA aggregation properties have been compared to those of VA, and second, the alteration of the GA particle upon the addition of water has been studied.

The ability of GA to form hydrogen bonds on both sides of the chain triggers some significant differences in terms of structure, density, and binding energies with respect to VA. The aerosols composed of the diacid molecules are more compact than the monoacid molecules as a result of stronger intermolecular interactions. This is mostly due to the formation of a larger number of intermolecular hydrogen bonds that persist for a long time, even at room temperature.

When water is added on the particle, for a 1:1 acid/water ratio, it may be found in the core of small particles ($N < 100$); however, as the aggregate becomes larger, water tends to accumulate on the surface, forming aqueous islands on the organic particles. At higher humidity (1:2 ratio) and larger sizes ($100 < N < 500$), water molecules at the surface become pushed toward the center, forming an inhomogeneous particle containing water in the bulk and at the surface. This organization is driven by diffusion, and we can wonder if water will be able to completely diffuse toward the bulk, repelling the diacids toward the edge of the particle. Our simulations, even though extended to 90 ns, were not able to reach this state.

Interestingly, the atom distribution at the surface does not depend upon the size of the particle and is not significantly altered upon the addition of water, indicating that some substantial reorganization may only occur locally. This result provides confidence in the description of sub-micrometer particles with a limited number of molecules, although larger than 50 to obtain a significant surface/volume ratio. Descriptions of the organic aerosol surface and bulk at the molecular level can be of interest for laboratory experimentalists investigating the uptake or reactivity of trace gases on aerosol surfaces. Contrasting macroscopic measurements of elementary parameters (e.g., uptake coefficients of trace gases) obtained when environmental parameters are varied (e.g., RH and temperature) with changes in the aerosol surface composition simulated at the molecular level could help interpret experimental observations in more detail.

To study the uptake process of a radical or molecule at the particle surface and the potential reactions that could occur at the surface or within the bulk, approaches combining quantum chemistry and molecular mechanics have to be employed

DOI: 10.1021/acsearthspacechem.8b00172
ACS Earth Space Chem. 2019, 3, 380−389

(QM/MM). While these methods are becoming more and more efficient, the design of the system has, however, to satisfy the constraint of feasibility of the calculations and relevance of the chemical mechanisms. As such, our results give some indications on the atoms available at the surface and the representative particles that could be used for further investigation, including reactive processes.

■ ASSOCIATED CONTENT

Supporting Information

The Supporting Information is available free of charge on the ACS Publications website at DOI: 10.1021/acsearthspacechem.8b00172.

Force-field parameters, GA conformer distribution, crystal data, orientation distributions, and additional information on hydrogen bonding and surface contents for other acid/water ratios (PDF)

■ AUTHOR INFORMATION

Corresponding Author

*Telephone: +33-320434980. E-mail: denis.duflot@univ-lille.fr.

ORCID

Céline Toubin: 0000-0002-7379-8178
Sébastien Dusanter: 0000-0001-5162-3660
Véronique Riffault: 0000-0001-5572-0871
Denis Duflot: 0000-0002-8307-5344

Notes

The authors declare no competing financial interest.

■ ACKNOWLEDGMENTS

This work was performed using high-performance computing (HPC) resources from GENCI-TGCC (Grant 2018-A0010806820) and the Centre de Ressources Informatiques (CRI) of the University of Lille. The authors acknowledge support from the Chemical and Physical Properties of the Atmosphere (CaPPA) project, funded by the Agence Nationale de la Recherche (ANR) through the Programme d'Investissement d'Avenir (PIA) under Contract ANR-10-LABX-005 and contribution from the CPER research project CLIMIBIO. The authors also thank the French Ministère de l'Enseignement Supérieur et de la Recherche, the Hauts de France Region, and the European Funds for Regional Economic Development for their financial support. The authors thank Dr. J. Lovrić for helpful discussions.

■ REFERENCES

(1) Lazaridis, M. Organic Aerosols. In *Environmental Chemistry of Aerosols*; Colbeck, I, Ed.; Wiley-Blackwell: Hoboken, NJ, 2008; Chapter 4, pp 91−115; DOI: 10.1002/9781444305388.ch4.

(2) Paulot, F.; Paynter, D.; Ginoux, P.; Naik, V.; Horowitz, L. W. Changes in the aerosol direct radiative forcing from 2001 to 2015: Observational constraints and regional mechanisms. *Atmos. Chem. Phys.* **2018**, *18*, 13265−13281.

(3) Lohmann, U.; Feichter, J. Global indirect aerosol effects: A review. *Atmos. Chem. Phys.* **2005**, *5*, 715−737.

(4) Boreddy, S. K. R.; Kawamura, K.; Tachibana, E. Long-term (2001−2013) observations of water-soluble dicarboxylic acids and related compounds over the western North Pacific: Trends, seasonality and source apportionment. *Sci. Rep.* **2017**, *7*, 8518.

(5) Rozaini, M. Z. H. The Chemistry of Dicarboxylic Acids in the Atmospheric Aerosols. In *Atmospheric Aerosols—Regional Characteristics—Chemistry and Physics* Abdul-Razzak, H., Ed.; IntechOpen Limited: London, U.K., 2012; DOI: 10.5772/50127.

(6) Paulot, F.; Wunch, D.; Crounse, J. D.; Toon, G. C.; Millet, D. B.; DeCarlo, P. F.; Vigouroux, C.; Deutscher, N. M.; González Abad, G.; Notholt, J.; Warneke, T.; Hannigan, J. W.; Warneke, C.; de Gouw, J. A.; Dunlea, E. J.; De Mazière, M.; Griffith, D. W. T.; Bernath, P.; Jimenez, J. L.; Wennberg, P. O. Importance of secondary sources in the atmospheric budgets of formic and acetic acids. *Atmos. Chem. Phys.* **2011**, *11*, 1989−2013.

(7) Kawamura, K.; Bikkina, S. A review of dicarboxylic acids and related compounds in atmospheric aerosols: Molecular distributions, sources and transformation. *Atmos. Res.* **2016**, *170*, 140−160.

(8) Falkovich, A. H.; Graber, E. R.; Schkolnik, G.; Rudich, Y.; Maenhaut, W.; Artaxo, P. Low molecular weight organic acids in aerosol particles from Rondônia, Brazil, during the biomass-burning, transition and wet periods. *Atmos. Chem. Phys.* **2005**, *5*, 781−797.

(9) Mirivel, G.; Riffault, V.; Galloo, J.-C. Analysis of phthalic, isophthalic and long-chain (C_4−C_{12}) dicarboxylic acids in atmospheric aerosols by UPLC/ESI/ToF-MS. *Anal. Methods* **2011**, *3*, 1172.

(10) Crenn, V.; Fronval, I.; Petitprez, D.; Riffault, V. Fine particles sampled at an urban background site and an industrialized coastal site in Northern France — Part 1: Seasonal variations and chemical characterization. *Sci. Total Environ.* **2017**, *578*, 203−218.

(11) Ma, X.; Chakraborty, P.; Henz, B. J.; Zachariah, M. R. Molecular dynamic simulation of dicarboxylic acid coated aqueous aerosol: Structure and processing of water vapor. *Phys. Chem. Chem. Phys.* **2011**, *13*, 9374−9384.

(12) Darvas, M.; Picaud, S.; Jedlovszky, P. Water adsorption around oxalic acid aggregates: A molecular dynamics simulation of water nucleation on organic aerosols. *Phys. Chem. Chem. Phys.* **2011**, *13*, 19830−19839.

(13) Darvas, M.; Picaud, S.; Jedlovszky, P. Molecular dynamics simulations of the water adsorption around malonic acid aerosol models. *Phys. Chem. Chem. Phys.* **2013**, *15*, 10942−10951.

(14) Vardanega, D.; Picaud, S. Water and formic acid aggregates: A molecular dynamics study. *J. Chem. Phys.* **2014**, *141*, 104701.

(15) Radola, B.; Picaud, S.; Vardanega, D.; Jedlovszky, P. Molecular Dynamics Simulations of the Interaction between Water Molecules and Aggregates of Acetic or Propionic Acid Molecules. *J. Phys. Chem. B* **2015**, *119*, 15662−15674.

(16) Radola, B.; Picaud, S.; Vardanega, D.; Jedlovszky, P. Analysis of Mixed Formic and Acetic Acid Aggregates Interacting With Water: A Molecular Dynamics Simulation Study. *J. Phys. Chem. C* **2017**, *121*, 13863−13875.

(17) Taketani, F.; Kanaya, Y.; Akimoto, H. Kinetic Studies of Heterogeneous Reaction of HO_2 Radical by Dicarboxylic Acid Particles. *Int. J. Chem. Kinet.* **2013**, *45*, 560−565.

(18) Lakey, P. S. J.; George, I. J.; Whalley, L. K.; Baeza-Romero, M. T.; Heard, D. E. Measurements of the HO_2 Uptake Coefficients onto Single Component Organic Aerosols. *Environ. Sci. Technol.* **2015**, *49*, 4878−4885.

(19) Lakey, P. S. J.; Berkemeier, T.; Krapf, M.; Dommen, J.; Steimer, S. S.; Whalley, L. K.; Ingham, T.; Baeza-Romero, M. T.; Pöschl, U.; Shiraiwa, M.; Ammann, M.; Heard, D. E. The effect of viscosity and diffusion on the HO_2 uptake by sucrose and secondary organic aerosol particles. *Atmos. Chem. Phys.* **2016**, *16*, 13035−13047.

(20) Xu, W.; Zhang, R. Theoretical Investigation of Interaction of Dicarboxylic Acids with Common Aerosol Nucleation Precursors. *J. Phys. Chem. A* **2012**, *116*, 4539−4550.

(21) Abraham, M. J.; Murtola, T.; Schulz, R.; Páll, S.; Smith, J. C.; Hess, B.; Lindahl, E. GROMACS: High performance molecular simulations through multi-level parallelism from laptops to supercomputers. *SoftwareX* **2015**, *1*−*2*, 19−25.

(22) Zhao, Y.; Truhlar, D. G. The M06 suite of density functionals for main group thermochemistry, thermochemical kinetics, noncovalent interactions, excited states, and transition elements: Two new functionals and systematic testing of four M06-class functionals and 12 other functionals. *Theor. Chem. Acc.* **2008**, *120*, 215−241.

DOI: 10.1021/acsearthspacechem.8b00172
ACS Earth Space Chem. 2019, 3, 380−389

(23) Krishnan, R.; Binkley, J. S.; Seeger, R.; Pople, J. A. Self-consistent molecular orbital methods. XX. A basis set for correlated wave functions. *J. Chem. Phys.* **1980**, *72*, 650−654.
(24) Clark, T.; Chandrasekhar, J.; Spitznagel, G. W.; Schleyer, P. V. R. Efficient diffuse function-augmented basis sets for anion calculations. III. The 3-21+G basis set for first-row elements, Li−F. *J. Comput. Chem.* **1983**, *4*, 294−301.
(25) Frisch, M. J.; Trucks, G. W.; Schlegel, H. B.; Scuseria, G. E.; Robb, M. A.; Cheeseman, J. R.; Scalmani, G.; Barone, V.; Petersson, G. A.; Nakatsuji, H.; Li, X.; Caricato, M.; Marenich, A.; Bloino, J.; Janesko, B. G.; Gomperts, R.; Mennucci, B.; Hratchian, H. P.; Ortiz, J. V.; Izmaylov, A. F.; Sonnenberg, J. L.; Williams-Young, D.; Ding, F.; Lipparini, F.; Egidi, F.; Goings, J.; Peng, B.; Petrone, A.; Henderson, T.; Ranasinghe, D.; Zakrzewski, V. G.; Gao, J.; Rega, N.; Zheng, G.; Liang, W.; Hada, M.; Ehara, M.; Toyota, K.; Fukuda, R.; Hasegawa, J.; Ishida, M.; Nakajima, T.; Honda, Y.; Kitao, O.; Nakai, H.; Vreven, T.; Throssell, K.; Montgomery, J. A., Jr.; Peralta, J. E.; Ogliaro, F.; Bearpark, M.; Heyd, J. J.; Brothers, E.; Kudin, K. N.; Staroverov, V. N.; Keith, T.; Kobayashi, R.; Normand, J.; Raghavachari, K.; Rendell, A.; Burant, J. C.; Iyengar, S. S.; Tomasi, J.; Cossi, M.; Millam, J. M.; Klene, M.; Adamo, C.; Cammi, R.; Ochterski, J. W.; Martin, R. L.; Morokuma, K.; Farkas, Ö.; Foresman, J. B.; Fox, D. J. *Gaussian 16, Revision B.01*; Gaussian, Inc.: Wallingford, CT, 2016.
(26) Sousa da Silva, A. W.; Vranken, W. F. ACPYPE—AnteChamber PYthon Parser interfacE. *BMC Res. Notes* **2012**, *5*, 367.
(27) Wang, J.; Wolf, R. M.; Caldwell, J. W.; Kollman, P. A.; Case, D. A. Development and testing of a general amber force field. *J. Comput. Chem.* **2004**, *25*, 1157−1174.
(28) Bayly, C. I.; Cieplak, P.; Cornell, W.; Kollman, P. A. A well-behaved electrostatic potential based method using charge restraints for deriving atomic charges: The RESP model. *J. Phys. Chem.* **1993**, *97*, 10269−10280.
(29) Cieplak, P.; Cornell, W. D.; Bayly, C.; Kollman, P. A. Application of the multimolecule and multiconformational RESP methodology to biopolymers: Charge derivation for DNA, RNA, and proteins. *J. Comput. Chem.* **1995**, *16*, 1357−1377.
(30) Cornell, W. D.; Cieplak, P.; Bayly, C. I.; Kollman, P. A. Application of RESP charges to calculate conformational energies, hydrogen bond energies, and free energies of solvation. *J. Am. Chem. Soc.* **1993**, *115*, 9620−9631.
(31) Jakalian, A.; Jack, D. B.; Bayly, C. I. Fast, efficient generation of high-quality atomic charges. AM1-BCC model: II. Parameterization and validation. *J. Comput. Chem.* **2002**, *23*, 1623−1641.
(32) Berendsen, H. J. C.; Grigera, J. R.; Straatsma, T. P. The missing term in effective pair potentials. *J. Phys. Chem.* **1987**, *91*, 6269−6271.
(33) Bussi, G.; Donadio, D.; Parrinello, M. Canonical sampling through velocity rescaling. *J. Chem. Phys.* **2007**, *126*, No. 014101.
(34) Hess, B.; Bekker, H.; Berendsen, H. J. C.; Fraaije, J. G. E. M. LINCS: A linear constraint solver for molecular simulations. *J. Comput. Chem.* **1997**, *18*, 1463−1472.
(35) Darden, T.; York, D.; Pedersen, L. Particle mesh Ewald: An *N*·log(*N*) method for Ewald sums in large systems. *J. Chem. Phys.* **1993**, *98*, 10089−10092.
(36) Cochran, R. E.; Jayarathne, T.; Stone, E. A.; Grassian, V. H. Selectivity Across the Interface: A Test of Surface Activity in the Composition of Organic-Enriched Aerosols from Bubble Bursting. *J. Phys. Chem. Lett.* **2016**, *7*, 1692−1696.
(37) Connolly, M. Analytical molecular surface calculation. *J. Appl. Crystallogr.* **1983**, *16*, 548−558.
(38) Eisenhaber, F.; Lijnzaad, P.; Argos, P.; Sander, C.; Scharf, M. The double cubic lattice method: Efficient approaches to numerical integration of surface area and volume and to dot surface contouring of molecular assemblies. *J. Comput. Chem.* **1995**, *16*, 273−284.
(39) Scheuerman, R. F.; Sass, R. L. The crystal structure of valeric acid. *Acta Crystallogr.* **1962**, *15*, 1244−1247.
(40) Morrison, J. D.; Robertson, J. M. 212. The crystal and molecular structure of certain dicarboxylic acids. Part VII. *β*-Glutaric acid. *J. Chem. Soc.* **1949**, *0*, 1001−1008.
(41) Bhattacharya, S.; Saraswatula, V. G.; Saha, B. K. Thermal Expansion in Alkane Diacids—Another Property Showing Alternation in an Odd−Even Series. *Cryst. Growth Des.* **2013**, *13*, 3651−3656.
(42) Zhang, C.; Wang, Y.; Wang, H. Interaction between water and acetic acid-sodium halide aerosol: A molecular dynamics study. *Powder Technol.* **2017**, *314*, 9−19.
(43) Thalladi, V. R.; Nüsse, M.; Boese, R. The Melting Point Alternation in *α,ω*-Alkanedicarboxylic Acids. *J. Am. Chem. Soc.* **2000**, *122*, 9227−9236.
(44) Schill, G. P.; Tolbert, M. A. Depositional Ice Nucleation on Monocarboxylic Acids: Effect of the O:C Ratio. *J. Phys. Chem. A* **2012**, *116*, 6817−6822.
(45) Lifson, S.; Hagler, A. T.; Dauber, P. Consistent force field studies of intermolecular forces in hydrogen-bonded crystals. 1. Carboxylic acids, amides, and the C:O···H− hydrogen bonds. *J. Am. Chem. Soc.* **1979**, *101*, 5111−5121.
(46) Hagler, A. T.; Lifson, S.; Dauber, P. Consistent force field studies of intermolecular forces in hydrogen-bonded crystals. 2. A benchmark for the objective comparison of alternative force fields. *J. Am. Chem. Soc.* **1979**, *101*, 5122−5130.
(47) Rapaport, D. C. Hydrogen bonds in water. *Mol. Phys.* **1983**, *50*, 1151−1162.
(48) Zielkiewicz, J. Structural properties of water: Comparison of the SPC, SPCE, TIP4P, and TIP5P models of water. *J. Chem. Phys.* **2005**, *123*, 104501.
(49) Hagler, A. T.; Dauber, P.; Lifson, S. Consistent force field studies of intermolecular forces in hydrogen-bonded crystals. 3. The C:O···H−O hydrogen bond and the analysis of the energetics and packing of carboxylic acids. *J. Am. Chem. Soc.* **1979**, *101*, 5131−5141.
(50) Neuheuser, T.; Hess, B. A.; Reutel, C.; Weber, E. Ab Initio Calculations of Supramolecular Recognition Modes. Cyclic versus Noncyclic Hydrogen Bonding in the Formic Acid/Formamide System. *J. Phys. Chem.* **1994**, *98*, 6459−6467.
(51) Petit, L.; Lapalu, L.; Sautet, P. Self-Assembly of Diacid Molecules: A Theoretical Approach of Molecular Interactions. *J. Phys. Chem. C* **2009**, *113*, 17566−17571.
(52) Mahoney, M. W.; Jorgensen, W. L. A five-site model for liquid water and the reproduction of the density anomaly by rigid, nonpolarizable potential functions. *J. Chem. Phys.* **2000**, *112*, 8910−8922.
(53) Lovrić, J.; Duflot, D.; Monnerville, M.; Toubin, C.; Briquez, S. Water-Induced Organization of Palmitic Acid at the Surface of a Model Sea Salt Particle: A Molecular Dynamics Study. *J. Phys. Chem. A* **2016**, *120*, 10141−10149.

DOI: 10.1021/acsearthspacechem.8b00172
ACS Earth Space Chem. 2019, 3, 380−389

II.3.3 Experimental considerations

Even if molecular dynamics can give a molecular point of view of the system, it is still important to keep in mind that the size of the generated aerosol is quite small compared to those found in the environment or generated experimentally. Indeed, in our case the biggest aerosol that has been generated was about 7 nm in diameter which, if we compare with the experimental size

distribution, corresponds to the smallest aerosol that we can detect in our aerosol flow tube (detection limit is about 6 nm). Furthermore, the aerosol surface concentration of those aerosols will not dominate the uptake process. It is still possible to generate aerosols with a bigger diameter but the computational cost will increase to years in order to reach the mean diameter of the size distribution generated in the AFT. Fortunately, as explained in the paper introduction, the characteristics of the aggregates started to converge from a certain size indicating that we can extrapolate the observations with a higher confidence. Another difference worth keeping in mind is that the timescales are not comparable. MD trajectories are run for a few nanoseconds while the timescales of the experimental growth of the aerosol and HO_2 uptake is of the order of the millisecond.[223]

Another issue remains also in comparing the relative humidity in real or experimental conditions to the theoretical ratio of organic acid:water molecules. Indeed, it could be difficult to find good observables (surface coverage, growth radius, etc.) which allows the conversion. In our case the only data available in the literature concern the growth radius of glutaric acid particles. Pope et al.[224] have found mass growth factors of 0.98 (efflorescence) and 1.04 (deliquescence) for RH = 30%; a growth factor of 0.98 (efflorescence) and 1.23 (deliquescence) for RH = 60%, and a growth factor of 0.96 (efflorescence) and 1.73 (deliquescence) for RH = 85%. In our case, the mass growth factor (defined as the ratio of the mass of wetted particles mass over that of the dry particles) is calculated at 1.14 for the 1:1ratio and at 1.27 for the 1:2 ratio, thus following the same trend as the mass growth factors determined for deliquescence processes, and values corresponding to RH around 60%. However, the comparison may be not so obvious as we cannot take into account the effect of charged species that could appear during the efflorescence/deliquescence processes. Furthermore we can have a size effect due to our really small particles.

Another thing to take into consideration is the fact that in our case the system is neutral. It may not be representative of the real system as aerosols are generally charged, especially when freshly formed.[225] However the simulation of charged particles is not straightforward since polarization cannot be neglected due to the excess charges and polarizable force-fields are really more expensive in terms of computational time, which could be a limiting step for the generation process and stabilization that requires few tens of nanoseconds for aerosols containing more than 200 molecules.

III HO_2 mass accommodation coefficient computation

III.1 All in one approach

In order to compute the HO_2 mass accommodation coefficient α, 20 HO_2 molecules were added in the box containing the aggregate (Figure 102). The computation was done on the dry aggregate from 100 to 500 glutaric acid molecules (as smaller aggregates may not be representative of the real system as shown before) and on all ratios of the wetted aggregate with 500 glutaric acid molecules. The parameters used for HO_2 are taken from Chalmet and Ruiz Lopez[142] and Vácha et al.[141] A 20 ns trajectory was then run with a time step of 2 fs.

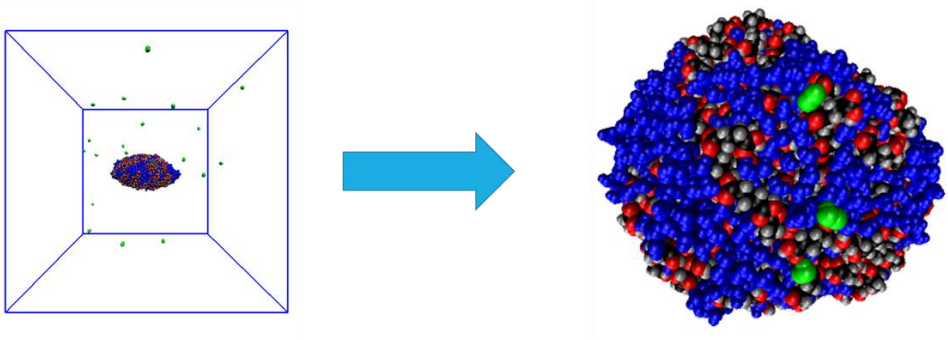

Figure 102: Computational method used for the mass accommodation coefficient of HO_2 (green spheres) on a wetted aggregate, water molecules being represented in blue.

It has been assumed than if no molecule is found around 0.35 nm from the HO_2 radicals, they would be considered in the gas phase. The disappearance of HO_2 from the gas phase follows roughly an exponential decay converging toward an equilibrium state (Figure 103). This decay is consistent with the reactions (R57) and (R58) that govern the mass accommodation coefficient:

$$HO_2 + S_{Aerosol} \xrightarrow{k_{ads}} HO_2\text{-}S \quad \text{(R57)}$$

$$HO_2\text{-}S \xrightarrow{k_{des}} HO_2 + S_{Aerosol} \quad \text{(R58)}$$

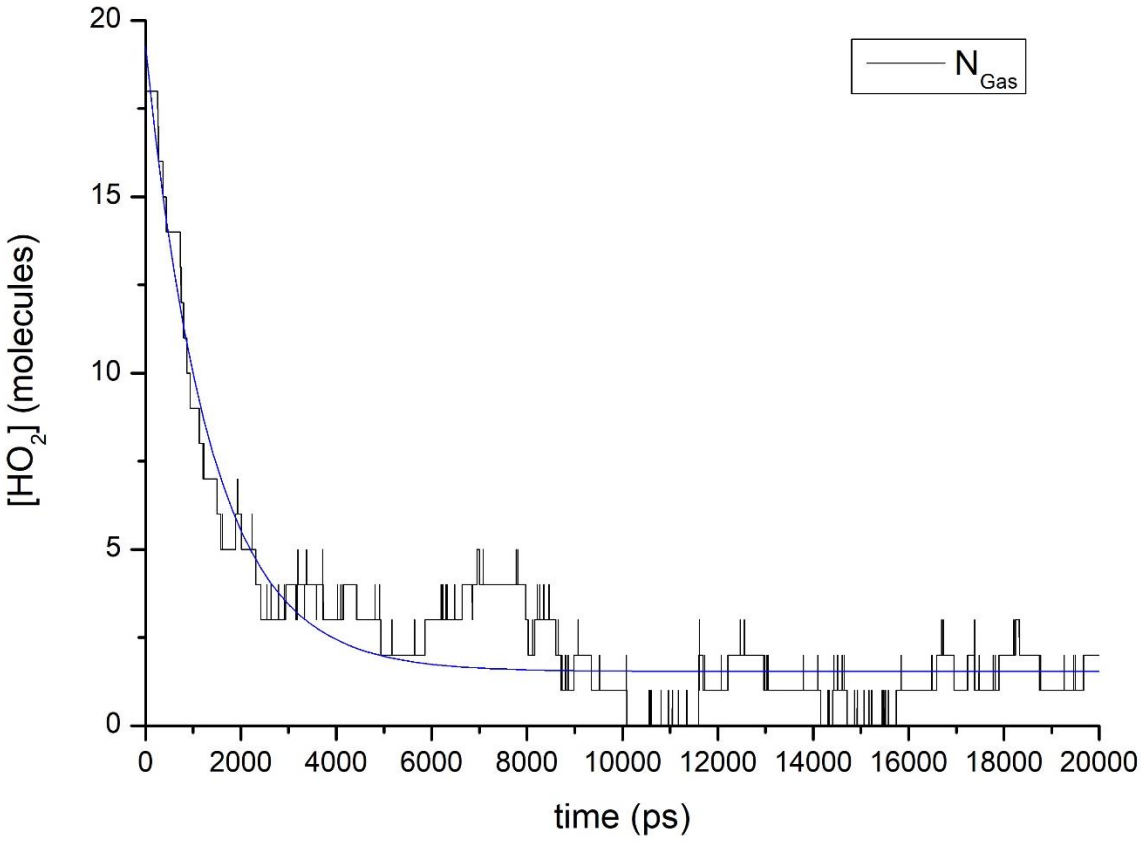

Figure 103: Time evolution of the number of gas phase HO_2 molecules.

We are then able to compute the mass accommodation coefficient using equation 116.[72]

$$\alpha = \frac{N_{gas,0} - N_{gas,eq}}{N_{gas,0}} \quad (116)$$

with $N_{gas,0}$ and $N_{gas,eq}$ the numbers of HO_2 radicals in the gas phase at time t=0 and at equilibrium, respectively.

The mass accommodation coefficients computed for dry aggregates were ~0.99, ~1.00 and ~0.99 for the $(GLU)_{100}$, $(GLU)_{200}$ and $(GLU)_{500}$ aggregates, respectively. For wetted aggregates, the mass accommodation was also found to be close to unity. It is interesting to note that if we compare with the study of Morita et al.[226] (computation of HO_2 mass accommodation on a slab of water; α close to unity), the HO_2 mass accommodation on the glutaric acid particles does not depend on the amount of water and is always close to unity as well.

Connolly analysis at regular time intervals has been performed in order to determine the concentration of HO_2 in the bulk phase or at the aerosol surface. In order to delimitate the concentration in the bulk and gas phases, we have considered that when less than 5% of the HO_2 surface is measured, the HO_2 is in the bulk phase; and when more than 80% of the surface is measured, the molecule is in the gas phase (these criteria may appear arbitrary but tests have been performed with different values to check that there is no influence on the results). On Figure 104, it is shown that both determinations (radius based (see Figure 102) or Conolly surface based), present the same trends on gas phase HO_2 which in turn gives higher confidence on the use of the Connolly analysis for the determination of the surface and bulk HO_2 concentrations.

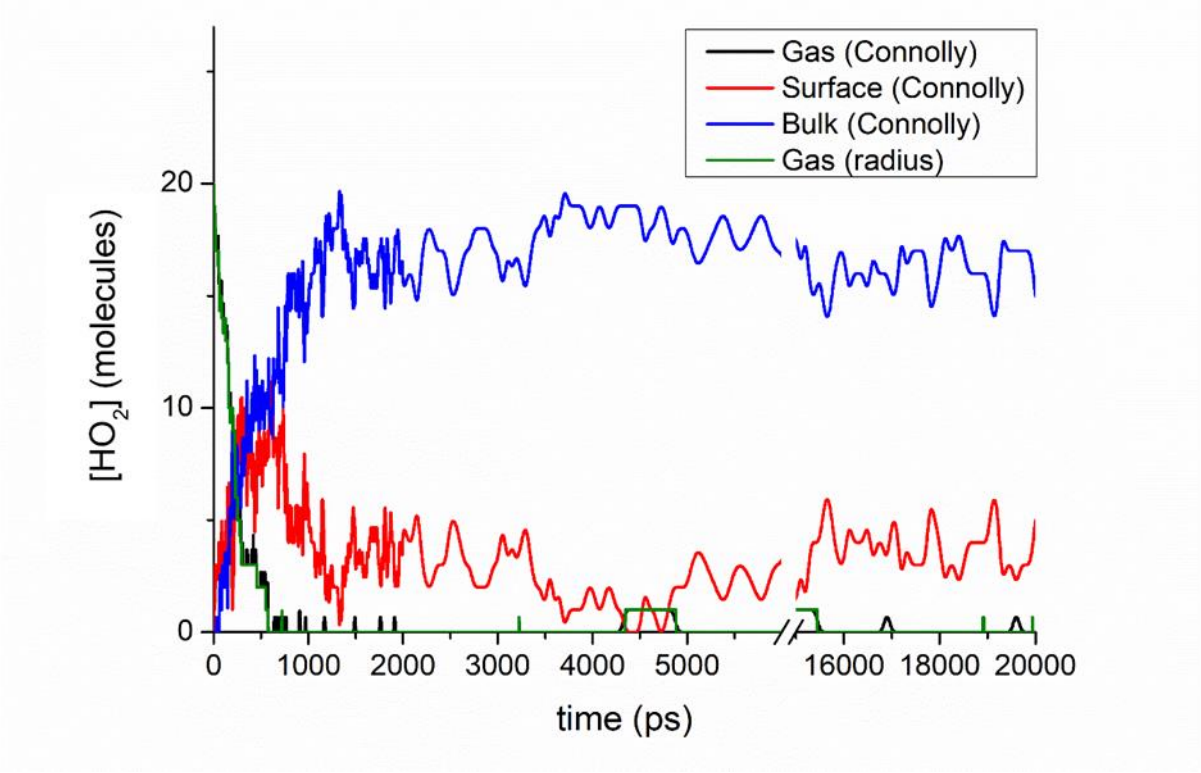

Figure 104: Time evolution of the HO_2 concentration in the gas phase determined by the radius method (green), and the gas phase (black), bulk (blue) and surface (red) concentrations determined by the Connolly method.

Separating the bulk and surface HO_2 concentration then allows the computation of the bulk/surface ratio (Figure 105) which at the equilibrium gives the K parameter of the uptake

coefficient (equation 4). The K parameter found (averaged over the last 5ns) is equal to ~4.8 ± 1.8 giving a sticking coefficient S of ~1.2 ± 0.08.

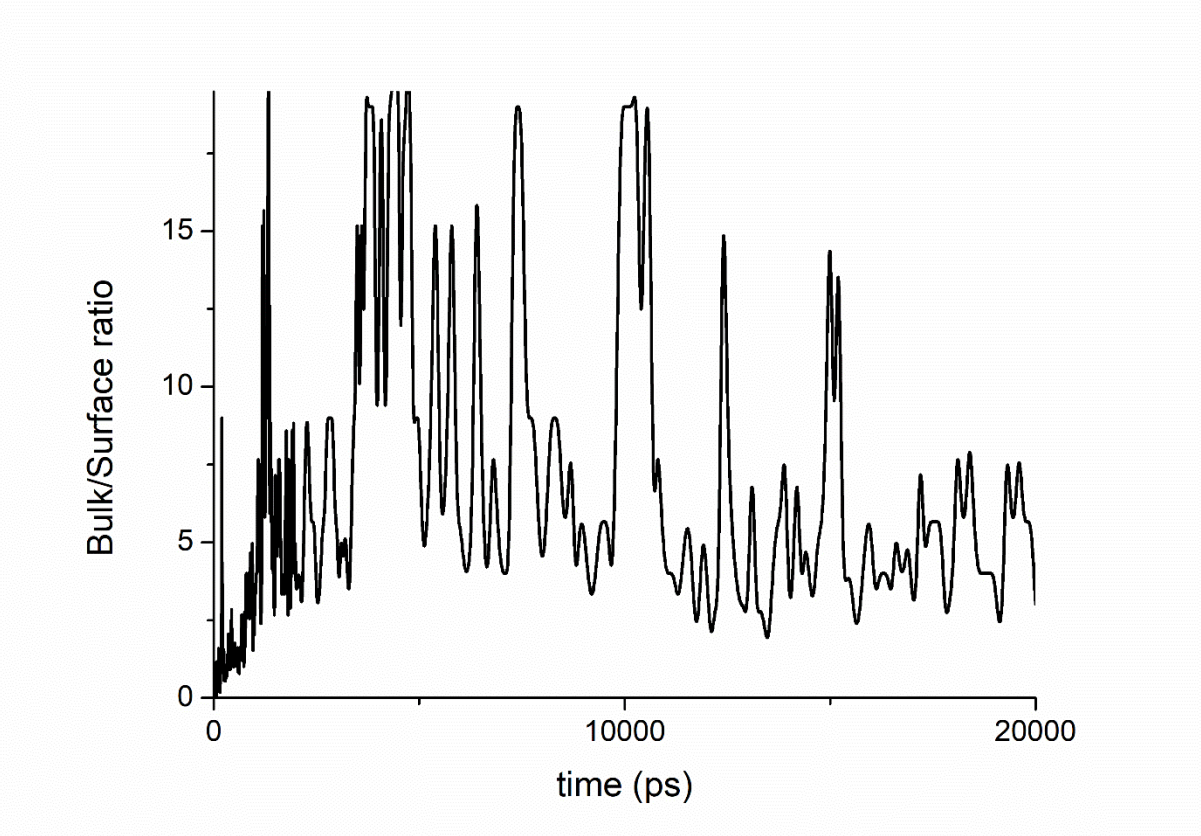

Figure 105: Time evolution of the bulk/surface ratio of HO_2 molecules

Binding energy time evolution analysis on Figure 106, shows that the HO_2 tends to form in average one hydrogen bonds as the mean binding energy is about 30 kJ mol^{-1} per molecule. On a short time range, some HO_2 interact with water molecules and some with glutaric acid. However, as the simulation is prolonged in time, interactions with water tend to decrease while those with glutaric acid tend to increase in absolute values. Thus HO_2 will preferentially interact with glutaric acid molecules on a long time range. This interaction is confirmed with the RDF analysis carried out on the last 2 ns of the run (Figure 107). Indeed, HO_2 radial distribution compared to the center of mass of the aerosol profile is closer to the glutaric acid radial distribution profile than to the one of water. The study of the HO_2 – HO_2 binding energy shows that they do not interact thus this interaction do not product artefact.

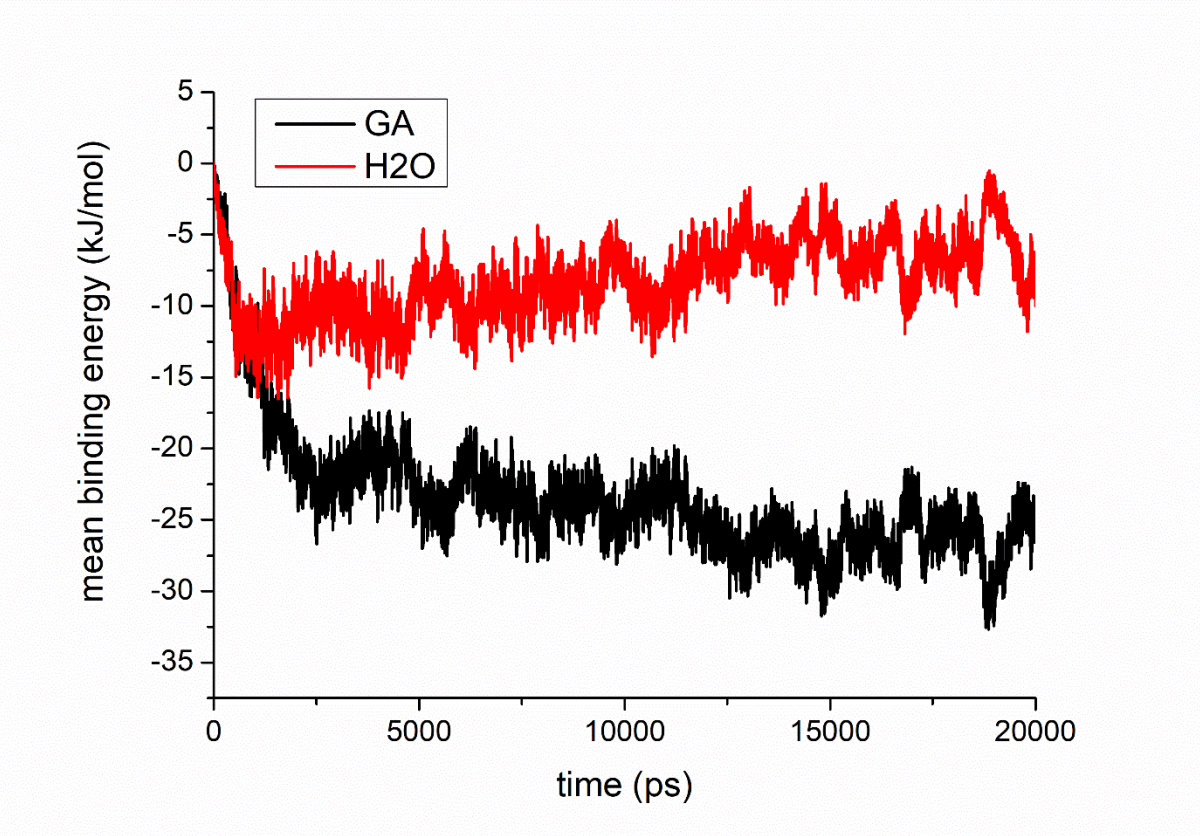

Figure 106: Time evolution of the HO_2-glutaric acid (GA, black) and HO_2-water (H2O, red) binding energy.

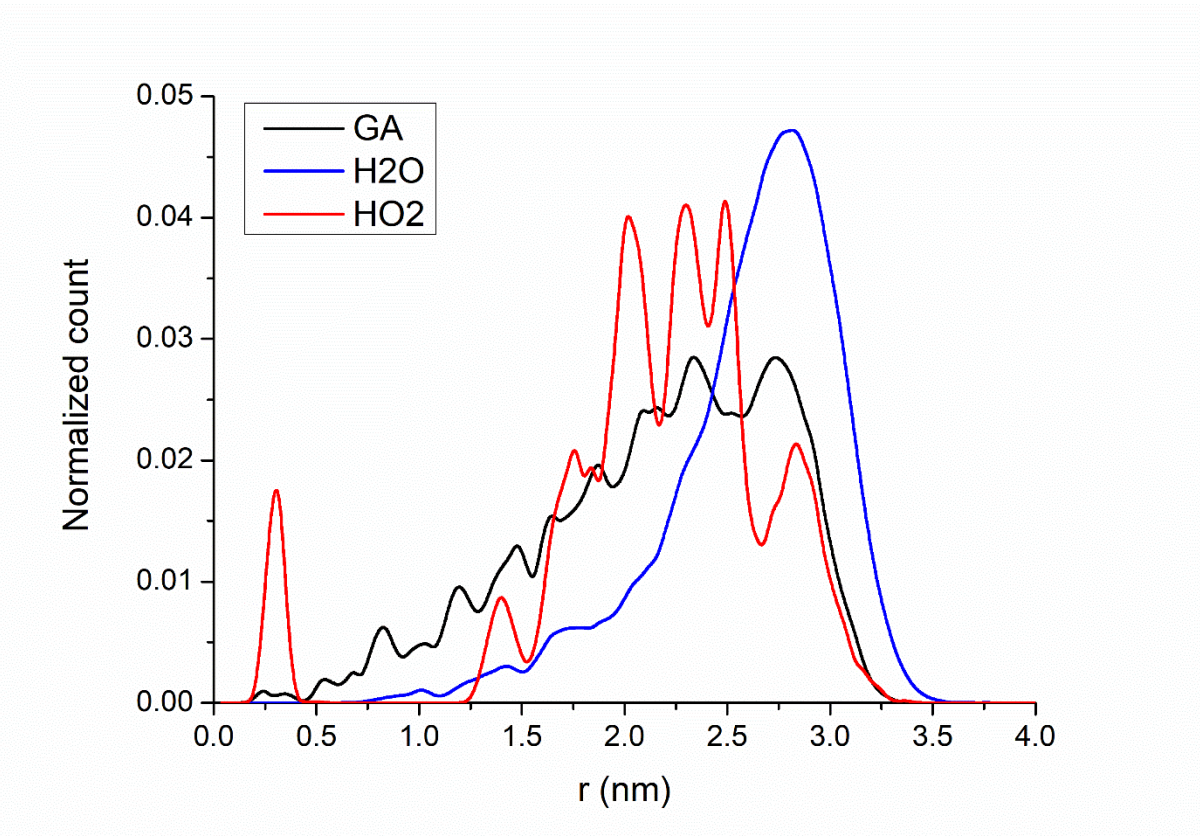

Figure 107: Radial distribution functions of glutaric acid (black), water (blue) and HO_2 (red) with respect to the aerosol center of mass.

However, there is an artefact due to the methodology. Since only one departure configuration has been used for the 20 HO_2 molecules, the sampling is not sufficient. Thus, a smaller number increases the uncertainties on the computation. Finally, even if the ratio of HO_2 with respect to the number of molecules at the aerosol surface is close to the conditions reached in the aerosol flow tube, the small size of the box induces too many collisions compared to the experimental setup. Indeed, the number of collisions modelled in the computation may be more representative of a reaction time close to infinity in the experimental setup. That is the reason why we have used another approach ensuring better statistics.

III.2 Statistical approach

For this approach, the conditions for the molecular dynamics runs were the same as the previous one except that only one HO_2 molecule was introduced randomly in the box. The computation was then run during 500 ps with a timestep of 2 fs. The computation was reproduced more than 2500 times by changing the random generator seed for the position of HO_2 from one trajectory to another.

These statistical trajectories were run only on the wetted aggregates containing 500 glutaric acid and 1000 water molecules due to the excessive computational cost (50000 hours in CPU times in total for the 2500 trajectories). The mass accommodation was computed using the method introduced in the paper of Julin et al.[74] (Equation 117).

$$\alpha = \frac{n_{adsorb} + n_{absorb}}{n_{total}} \qquad 117$$

where n_{adsorb}, n_{absorb} and n_{total} are the number of HO_2 radicals adsorbed, absorbed (molecules in bulk phase) and the total number of collisions, respectively. The mass accommodation obtained in this case was also found to be close to unity noting that at the end of the 500 ps, HO_2 was located in the bulk phase only for 73 trajectories (about 3% of the trajectories). This is not surprising since the trajectory is too short to capture the diffusion into the bulk, the aerosol being compact and molecules strongly bound together.

Concerning HO_2 orientation (Table 32) at the collision event ($t_{collision}$) it appears preferentially oriented to be H-donor (about 77% of the trajectories). However this orientation changes over time since 99% of the trajectories lead to orientation with HO_2 being an H-acceptor at the end of the 500 ps simulation ($t_{500\ ps}$). Concerning the adsorption sites, HO_2 adsorb in equal ratios on the water molecule or on the glutaric acid molecules. This proportion is slightly shifted in favor of the water adsorption sites at the end of the run (t_{500ps}).

Table 32: Proportion of the adsorption site types (water or glutaric acid (GA)) at the moment when the collision happens ($t_{collision}$) and at the end of the simulation (t_{500ps}). The average collision time is about 13.9 ± 5.9 ps.

	HO_2	O-acceptor	H-donor
$t_{Collision}$	GA	15.4%	36.0%
	Water	7.2%	41.3%
$t_{500\ ps}$	GA	0.0%	53.6%
	Water	0.0%	46.4%

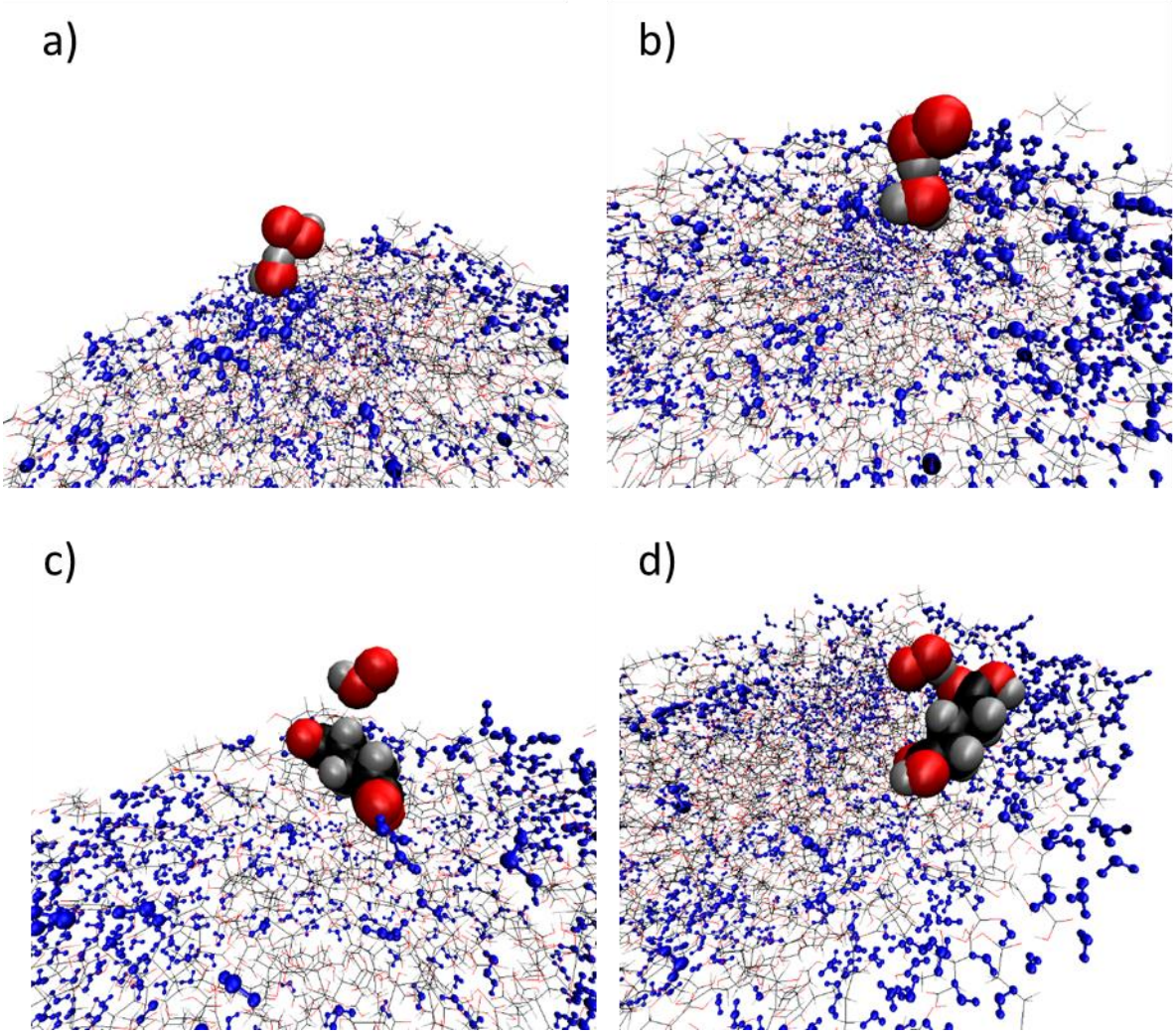

Figure 108: Snapshots of a) O-acceptor HO_2 orientation on a water site, b) H-donor HO_2 orientation on a water site, c) O-acceptor HO_2 conformation on glutaric acid and d) H -donor HO_2 conformation on glutaric acid. The HO_2 and the molecule at the adsorption site are represented by spheres, other water molecules in blue spheres and lines and glutaric acid in lines.

Average radial distribution functions are shown in Figure 109 and shows that HO_2 was rapidly adsorbed on the surface of the particles. Starting from 100 ps, the radial distribution profile becomes constant due to diffusion into the bulk that takes longer times. At 500 ps, the HO_2 radial distribution function shows two peaks, one around 2.5 nm and another around 3.5 nm while glutaric acid distribution is centered around 2.25 nm and water distribution, around 3 nm. The peak at 2.5 nm becomes significant only at 20 ps, therefore it may be reasonable to think that fast diffusion between water molecules happens first followed by a slow diffusion in glutaric acid.

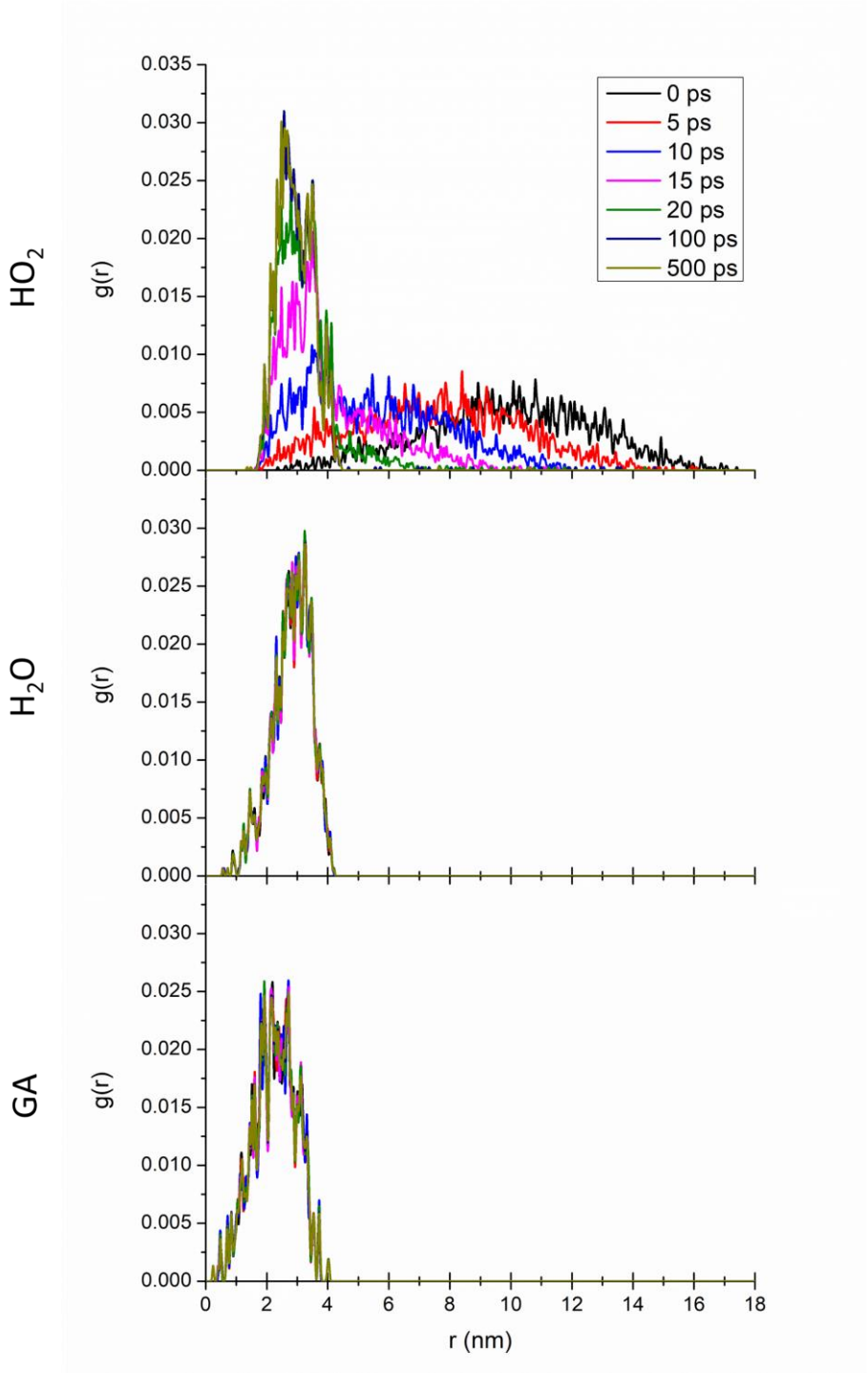

Figure 109: Time evolution of the radial distribution function of HO_2, water and glutaric acid (GA) averaged over all trajectories

Figure 110 displays the time evolution of the mean binding energies between HO_2 and the system (glutaric acid and water), HO_2 and the water molecules as well as HO_2 and the glutaric acid molecules. As may be observed for the HO_2 – system binding energy, the peak at 0 ps is not completely symmetric which means that there is a small bias on the initial conditions. We can observe that the distribution gets thicker with increasing time and shifts toward -25 kJ mol^{-1}, which corresponds to the formation of one hydrogen bond. This phenomenon is due to the fact that HO_2 reorients to optimize its interaction with the neighboring molecules.

Concerning HO_2 – glutaric acid mean interaction energies, one can observe at 500 ps two distinct peaks. The first one around -8 kJ mol^{-1} is due to HO_2 that interacts with water molecules in the vicinity of glutaric acid molecules. The second one corresponds to an adsorption on a glutaric acid molecule around -22 kJ mol^{-1}. The interaction with glutaric acid is stronger by 2 kJ mol^{-1} than the one with water.

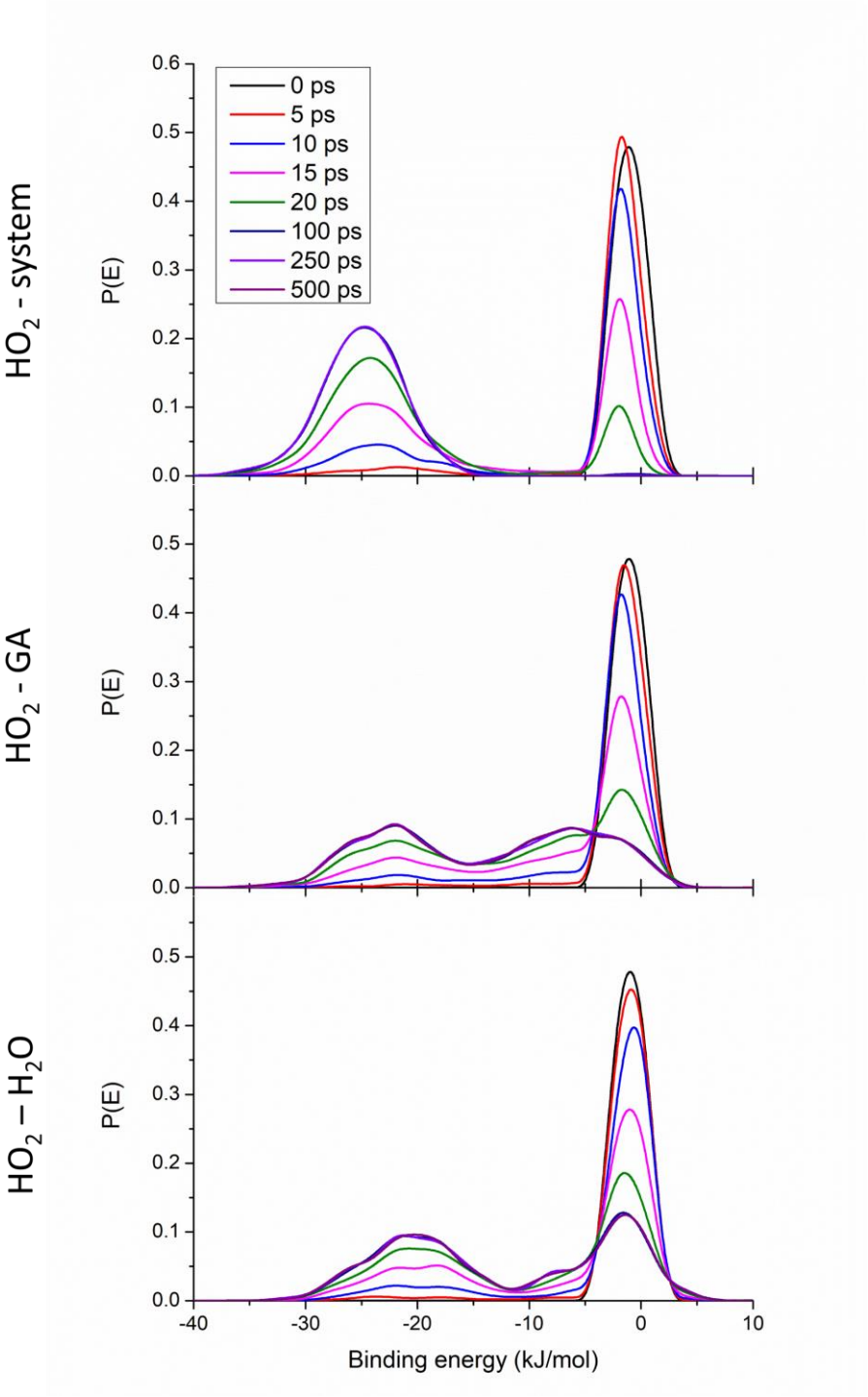

Figure 110: Time evolution of the average interactions HO_2 - system, HO_2 - glutaric acid (GA) and HO_2 – water.

This statistical approach has the advantage to depend less on the starting conditions since HO_2 is always generated in a new position. However, no information is provided on the possible

collision of a second HO_2. We are in the case where only one collision happens which is more relevant of the mass accommodation at time t=0 that is observed in our experimental setup.

Finally, using these two different methodologies, we were able to compute the mass accommodation coefficient that was found close to unity. However the values found do not explain the lower uptake coefficients obtained experimentally. A limitation process may be due to the reactivity or the diffusion in the bulk phase. The reactivity can be studied using quantum mechanics (see chapter 4 section IV) but the HO_2 bulk diffusion needs longer computation time, this process is beyond the scope of the present thesis.

IV Computation of the reactivity

Several reactions between HO_2 and the Glutaric acid–water system may be included in the uptake process. Firstly peroxy radicals may react with water. This reaction has been already studied, as mentioned in Chapter 1:, at the surface of pure water ice but is of interest at the surface of a wetted glutaric acid aerosol where the environment may not be so isotropic. Second, the reactivity of HO_2 with glutaric acid has never been studied theoretically. Thus, before investigating this reactivity at the aerosol surface, it is necessary to investigate it in the gas phase. Finally, the reaction of HO_2 with another HO_2 in the aerosol phase may also be studied since when these two radicals collide in the gas phase, they easily form H_2O_2 while this reaction may be inhibited at the aerosol surface.

IV.1 Gas phase reactivity

The reactivity of HO_2 with glutaric acid in the gas phase has been studied using the Gaussian 16 code[215] at the ωB97X-D/def2-TVZP[227,228] and DSD-PBEP86-D3(BJ)/def2-TVZP[228–230] levels as recommended by Goerigk et al.[192]

Computation of conformers according to Nguyen et al.[231] shows that two are dominant (see Figure 111); conformer A being about 12% of the population compared to conformer B. That leads to the study of two reaction pathways. In each way, due to the symmetry of the conformer, we can determine that only three hydrogens have different environments in path A and only four in path B. However the computations to find one transition state of the reaction way A are still ongoing.

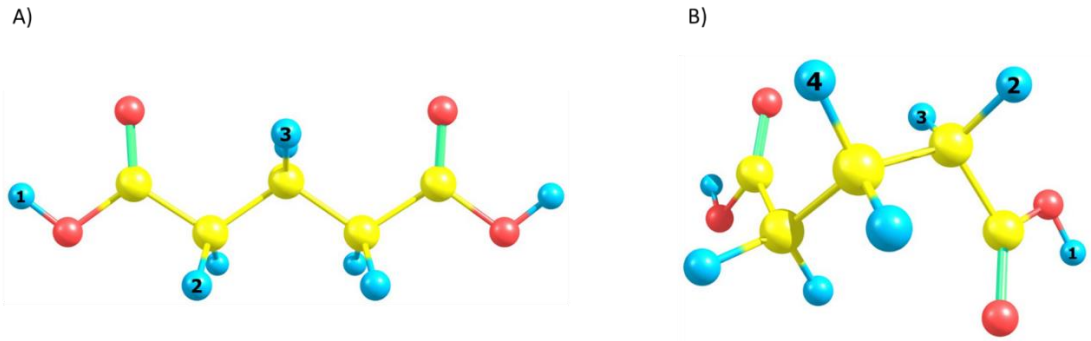

Figure 111: Snapshot of the two most abundant conformers. The hydrogens with different environment (according to the molecule symmetry) are numbered.

The potential energy diagrams (including ZPE) for both functionals are shown in Figure 112 while geometries of the transition states are shown in Figure 113. The geometries of the Van der Waals complexes are shown in Appendix H.

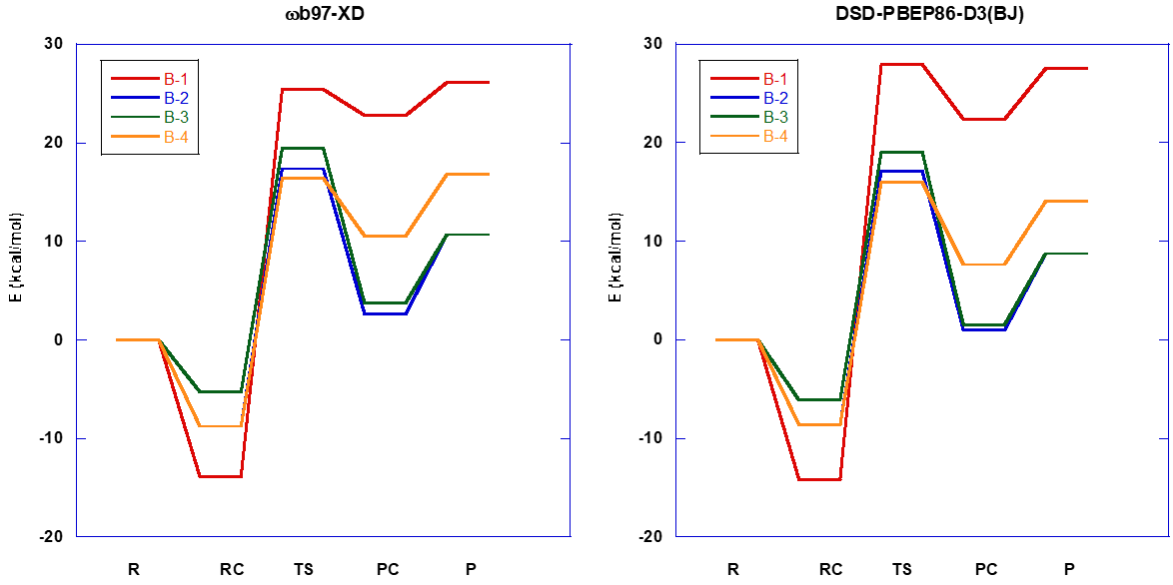

Figure 112: Potential energy diagram of each reaction way found with both functionals. Values are shown in Appendix H.

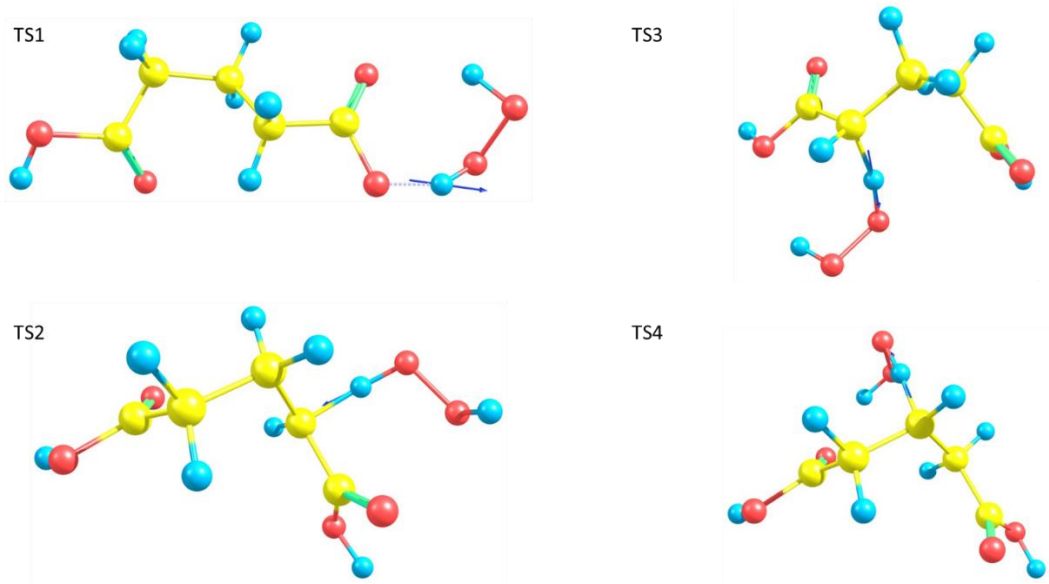

Figure 113: Geometries of the transition states. The arrows represent the mass weighted imaginary mode.

The rate constant has been computed at 298 K using Kisthelp2019[232] (Equation 118):

$$k = \Gamma k_{TST} \quad 118$$

with Γ the Eckart tunnelling effect correction and k_{TST} the rate constant computed with the transition state theory. The total rate constant is then computed as the sum of rate constants of each proton (Equation 119)

$$k_{tot} = 2k_1 + 2k_2 + 2k_3 + 2k_4 \quad 119$$

with k_1, k_2, k_3 and k_4 the rate constant for proton 1, 2, 3 and 4, respectively. The results are summarized in Table 33.

Table 33: Summary of the rate constants computed using the transition state theory for both functionnals

		Γ	k_{TST} (cm^3 $molecule^{-1}$ s^{-1})	k (cm^3 $molecule^{-1}$ s^{-1})
ωB97X-D				
	1	1.72	6.99×10^{-33}	1.22×10^{-32}
	2	379.58	1.05×10^{-27}	2.96×10^{-25}
	3	662.01	3.64×10^{-29}	1.95×10^{-26}
	4	24.61	2.73×10^{-27}	7.07×10^{-26}
	k_{tot}		7.63×10^{-27}	7.73×10^{-25}
DSD-PBEP86-D3(BJ)				
	1	15.16	6.39×10^{-35}	9.69×10^{-34}
	2	472.86	2.01×10^{-26}	9.51×10^{-24}
	3	1048.33	8.27×10^{-28}	8.67×10^{-25}
	4	4.93	5.90×10^{-26}	2.91×10^{-25}
	k_{tot}		1.60×10^{-25}	2.13×10^{-23}

The total rate constants found are different by a factor of 27 between both functionals. However, we can observe the same trends in both cases. Indeed, the proton abstraction of the -COOH group seems to be negligible while the H-abstraction of the $CH_{2,\alpha}$ group seems to be more important. The total rate constant is low in both cases, meaning a negligible loss of HO_2. Indeed, the reactivity with glutaric acid is more than ten orders of magnitude lower than the HO_2 self-reaction ($k = 1.86 \times 10^{-12}$ cm^3 $molecule^{-1}$ s^{-1}).

Assuming the reaction scheme (R59), the rate constant has also been computed by taking into account the equilibrium constant of the reactive complex formation K_{eq} as well (equation 120).

$$R \underset{K_{eq}}{\longleftrightarrow} RC \xrightarrow[k_{TST}]{} TS \rightarrow PC \rightarrow P \qquad \text{(R59)}$$

In this case, the equilibrium constant has to be divided by the concentration [c] of an ideal gas, taken at 101325 Pa and 298 K.

$$k = \frac{K_{eq}}{[c]} \Gamma k_{TST} \qquad 120$$

The rate constants (Table 34) found in this case are slightly higher than the one computed by the transition state theory but are still low. However, the energies have still to be refined by a single-point CCSD(T) computation. This reactivity will be studied in the aerosol phase as well where the barrier may be lower.

Table 34: Summary of the rate constant taking into account the equilibrium constant of the reactive complex formation for both functionals.

		K_{eq}	Γ	k_{TST} (cm^3 $molecule^{-1}$ s^{-1})	k (cm^3 $molecule^{-1}$ s^{-1})
ωB97X-D					
	1	966	1.75	3.52×10^{-16}	2.37×10^{-35}
	2	0.926	283.18	5.49×10^{-8}	7.84×10^{-25}
	3	0.00065	535.21	2.72×10^{-6}	4.76×10^{-26}
	4	0.927	25.85	1.43×10^{-7}	1.33×10^{-25}
	k_{tot}			5.84×10^{-6}	1.93×10^{-24}
DSD-PBEP86-D3(BJ)					
	1	4830	14.44	6.44×10^{-19}	1.82×10^{-33}
	2	2.63	915.47	3.72×10^{-7}	3.64×10^{-23}
	3	0.00556	1795.65	7.24×10^{-6}	2.93×10^{-24}
	4	2.63	80.94	1.09×10^{-6}	9.44×10^{-24}
	k_{tot}			1.74×10^{-5}	9.75×10^{-23}

IV.2 Aerosol surface reactivity

A first attempt has been made on the study of the reactivity of HO_2 and water in the aerosol phase. The HO_2 initial position was either computed starting from a transition state geometry computed in the gas phase, or taken from the molecular dynamics simulation (section III.2). The computation was then done with an ONIOM method at the MP2/aug-cc-pVDZ:Amber level of theory, using the Gaussian 16 code[215]. The Quantum Mechanics (QM) layer was set unfrozen while the Molecular Mechanics (MM) layer has been frozen. If we simply limit the QM layer to HO_2 and a single water molecule, the computation will not converge. So the QM layer has been extended to several molecules that are in the close vicinity of the reactive system. However, even with the increase of the QM layer, the convergence of the computation leads mainly to a Van der Waals complex. An exhaustive list of the tests carried out is presented in Table 35 and Table 36.

Table 35: Computations carried out for the deprotonation of HO_2

Reaction	Method	Force[a]	High Layer	Medium Layer	Unfrozen molecules	Total molecules	Comment
$HO_2 + H_2O \rightarrow O_2^- + H_3O^+$	MP2/aug-cc-pVDZ:: AMBER=Softfirst	calcall	$HO_2 + H_2O$	-	$HO_2 + H_2O$	HO_2 + 500 GLU + 1000 H_2O (11503 atoms)	Converged to proton exchanged TS
	PM6:AMBER=Softfirst	calcall	$HO_2 + H_2O$	-	$HO_2 + H_2O$	HO_2 + 500 GLU + 1000 H_2O (11503 atoms)	No convergence
							Converged on complex (imaginary mode = -9.8380)
				-	all atom	HO_2 + 500 GLU + 1000 H_2O (11503 atoms)	Converged on complex (imaginary mode = -25.8633)
							Converged on complex (imaginary mode = -13.8380)
			$HO_2 + 5\ H_2O$	-	$HO_2 + 5\ H_2O$	HO_2 + 500 GLU + 1000 H_2O (11503 atoms)	Converged on complex (imaginary mode = -22.6922)
			$HO_2 + 10 H_2O$ + GLU	-	$HO_2 + 10\ H_2O$ + GLU	HO_2 + 500 GLU + 1000 H_2O (11503 atoms)	No imaginary frequencies
	B3LYP/6-311++G(2d,2p): AMBER=Softfirst	calcall	$HO_2 + 5\ H_2O$	-	$HO_2 + 5\ H_2O$	HO_2 + 500 GLU + 1000 H_2O (11503 atoms)	Converged on complex (imaginary mode = -34.8978)
	MP2/aug-cc-pVDZ: HF/aug-cc-pVDZ: AMBER=Softfirst	calcall	$HO_2 + 4\ H_2O$ + 2 GLU	4 H_2O + GLU	$HO_2 + 8\ H_2O$ + 3 GLU	HO_2 + 500 GLU + 1000 H_2O (11503 atoms)	No convergence
$H_2O + HO_2\text{-}H_2O \rightarrow H_3O^+ + HO_2\text{-}OH^-$	PM6:AMBER=Softfirst	calcall	$HO_2 + 10\ H_2O$ + GLU	-	$HO_2 + 10\ H_2O$ + GLU	HO_2 + 5 GLU + 45 H_2O (223 atoms)	Converged on complex (imaginary mode = -58.7248)
							Converged on complex (imaginary mode = -97.4330)

[a] Force constant computation (calcall = Hessian computation at every step)

Table 36: Computations carried out for the H-abstraction by HO_2

Reaction	Method	Force[a]	High Layer	Unfrozen molecules	Total molecules	Comment
$HO_2 + H_2O \rightarrow H_2O_2 + OH$	MP2/aug-cc-pVDZ: AMBER=Softfirst	calcall	$HO_2 + H_2O$	$HO_2 + H_2O$	HO_2 + 500 GLU + 1000 H_2O (11503 atoms)	No convergence
			HO_2 + 4 H_2O + 2 GLU	$HO_2 + 4H_2O$ + 2 GLU	HO_2 + 500 GLU + 1000 H_2O (11503 atoms)	Memory crash
	PM6:AMBER=Softfirst	calcall	$HO_2 + H_2O$	$HO_2 + H_2O$	HO_2 + 500 GLU + 1000 H_2O (11503 atoms)	To be checked (multiple imaginary mode). MP2/AVTZ frequency computation ongoing
						To be checked (multiple imaginary mode). MP2/AVTZ frequency computation ongoing

[a] Force constant computation (calcall = Hessian computation at every step)

Table 37: Computation ongoing for the HO_2 deprotonation

Reaction	Method	Force[a]	High Layer	Medium layer	Unfrozen molecules	Total molecules
$H_2O + HO_2\text{-}H_2O \rightarrow H_3O^+ + HO_2\text{-}OH^-$	MP2/aug-cc-pVTZ:PM6	calcfc	HO_2 + 2 H_2O	-	HO_2 + 10 H_2O	HO_2 + 5 GLU + 45 H_2O (223 atoms)
	M062X/aug-cc-pVDZ: HF/aug-cc-pVDZ: AMBER=Softfirst	calcall	HO_2 + 4 H_2O + 2 GLU	4 H_2O + GLU	HO_2 + 8 H_2O + 3 GLU	HO_2 + 500 GLU + 1000 H_2O (11503 atoms)

[a] Force constant computation (calcall = Hessian computation at every step; calcfc = Force constant computed at the first point)

Concerning the HO_2 deprotonation by water, only one computation has led to a transition state with a single imaginary frequency (characteristic of the transition states) equal to around -1852 cm^{-1}. However, this transition state corresponds to a proton exchange between the HO_2 and the water molecule as shown on Figure 114.

Figure 114: Picture of the transition state (middle) corresponding to a proton exchange.

Concerning the H-abstraction by HO_2, two computations converged on a geometry with multiple imaginary modes.

Even if the TS guess is correct (at least one imaginary mode corresponding to the reaction coordinate wanted), the computations have a lot of difficulties to converge on the desired TS. This can be due either to a flat potential energy surface (PES) and/or due to a multidimensional character of the reaction coordinate. One possibility would be to scan the reaction coordinate; however, ONIOM is essentially designed to be performed in Cartesian coordinates and the input file needs to be converted in Z-matrix form, which is not trivial. Furthermore, the sizes of the input and output files are really big and make the visualization of the system difficult.

The study of the reactivity on aerosol phase is far from obvious thus it is still ongoing.

CONCLUSION

The main objective of this Ph.D. work was to improve our understanding of the peroxy radical uptake on organic aerosols using both experimental and theoretical approaches. The first part focused on the building and characterization of an aerosol flow tube for measuring uptake coefficients of peroxy radicals on organic aerosols. The development of this setup has led to the measurement of HO_2 uptake coefficient. The second part was dedicated to the simulation of the processes that happen during the HO_2 uptake at the molecular level on model organic aerosols.

I Conclusion and perspectives of the experimental part

I.1 Conclusions

The aerosol flow tube was built based on previous work described in the literature and coupled to a PERCA system designed in the SAGE department (Marius Duncianu's postdoctroral work and Ahmad Lahib's Ph.D. work; paper in review). This type of setup has already shown its efficiency to measure uptake coefficients but it was for the first time coupled to a PERCA system which allows the measurement of HO_2 as well as RO_2 radicals.

Most part of the work consisted in the characterization of the setup. Indeed, many characterization steps had to be performed before allowing the measurement of the HO_2 uptake coefficient. First, the flux within the reactor has to be well understood in order to determine the contact time for each injector position. This characterization has also highlighted the minimum distance needed for the mixing of HO_2 and aerosols.

Then the HO_2 generation process has been studied. This system had to satisfy two rules: i) the formation of a HO_2 concentration high enough to detect the shift in concentration ii) a concentration sufficiently low in order to minimize the impact of the HO_2 self-reaction. The HO_2 produced has been measured for different relative humidities set in the photolysis cell and an area where the HO_2 concentration is quite stable among a range of relative humidities was evidenced.

The HO_2 wall losses have been characterized too on Pyrex and on halocarbon wax. It has been observed that halocarbon wax allows a significant decrease of the losses on the wall of the AFT. The impact of relative humidity has been quantified as well and kinetic models have confirmed the contribution of the HO_2 self-reaction to the total losses.

Two generation systems for glutaric acid production have been studied. The first one is the constant atomizer manufactured by TSI Inc. and the second one is a homemade nucleation system. The concentration profiles have been observed for different sets of parameters (pressure, glutaric acid concentration in solution for the atomizer and temperature for the nucleation system). It has been shown that the selection of a specific size of aerosol does not provide surface concentration high enough to be able to perform uptake measurement. As the whole size distribution is sent through the reactor, it has also been assessed that the nucleation system may produce a lot of artefact measurements. Indeed, only half of the size distribution is

covered by the SMPS and even if the remaining half should be stopped by an impactor, it has to be taken into account that the efficiency of the impactor may not allow a sufficiently sharp cut-off.

The surface loss has been characterized as well in order to correct for its impact during uptake measurement. The aerosol loss rate constant decreases increasing particle. That is due to the fact that smaller particles diffuse faster towards the wall. However, this part has to be characterized more precisely by doing a complete mapping of the aerosol concentration over the AFT. Indeed, the radial aerosol concentration trends have not been fully characterized.

The effective HO_2 uptake has been computed after adding the Brown correction[145] (diffusion correction), the surface correction determined by the characterization and after removing the gas phase diffusion limitation (according to Fuchs and Sutugin[85]). The values found was higher than those from by Lakey et al.[51] and lower than those from Taketani et al.[54] However, the concentration of copper measured in our aerosol may explain the differences with Lakey et al. while it is not possible to rationalize the difference with Taketani et al. since the latter ones do not report any copper concentration measurements.

I.2 Perspectives

As discussed previously, the values of HO_2 uptake determined with our setup have shown some discrepancies with measurements carried out by two other groups. The copper impurities may be involved in these discrepancies. It could be interesting to determine exactly the impact of copper on the HO_2 uptake on glutaric acid in the future, by adding various amounts of copper and measuring how the uptake is modified by the copper concentrations.

The impact of the pH can also be determined. Indeed, it is well known that the aerosol can attack the stainless steel tube of the setup if its pH is too acid. The pH may also have an impact on the reactivity within the aerosol bulk or at the surface as HO_2 can be deprotonated easily in basic solution.

One big step that will follow this work will be the measurement of isoprene-based RO_2 uptake coefficient at different relative humidities. Indeed, as the system is able to measure both concentrations of HO_2 and RO_2, it is possible to investigate these compounds. The measurement of RO_2 uptake will be an important improvement as there is no value found in the literature up to now, and isoprene-based RO_2 may be a good candidate to explain the discrepancies between atmospheric models and field measurements carried out in forested area.

The aerosol flow tube may eventually be coupled to an aerosol mass spectrometer (to measure the aerosol composition and its oxidation state) and/or a proton transfer reaction time of flight mass spectrometer (to measure the gas phase composition) in order to characterize if there is any reactive product formed during the uptake. The study of the reactivity may also add really interesting information as it may help to describe what happens during the reactive process (reactivity on the surface and in the bulk). The reactivity may be also directly compared to the reactivity computed through quantum mechanics computations.

Even if the PERCA system is able to measure RO_2, is not possible to differentiate the RO_2 from the HO_2 concentration, which leads to additional data treatment (deconvolution). However, is possible to couple a CIMS with proton transfer[233] in order to measure specifically the RO_2

concentration. Indeed this instrument has the advantage to be able to measure the RO_2 in the gas phase even the smallest one (CH_3O_2).

Finally, other atmospherically-relevant aerosol particles (pure or mixed ones) could be investigated, using one of the two generation systems that have been developed. Indeed, we can form inorganic or organic particles quite easily with the atomizer if the compounds are sufficiently soluble in water. If is not soluble (fatty acids for example), the nucleation system may be able to produce particles if the vapor pressure of the compound is quite high.

II Conclusions and perspectives of the theoretical part

II.1 Conclusions

Concerning the theoretical part, the benchmark of the AMBER GAFF force field[173] has been performed on glutaric and valeric acid monomers, dimers and crystals. Energy differences between the glutaric acid conformers have been determined by molecular dynamics with this force field and have been compared to computations carried out at the MP2/6-311++G(2d,2p) level. The binding energies of the acid-acid and acid-water (SPC/E model) interactions have been compared to quantum mechanics computation as well. Finally, crystal structures have been compared to the experimental parameters found in the literature.

Then particles of glutaric and valeric acids have been generated with different amounts of molecules. Wetted glutaric acid aggregates have been formed using either through a cocondensation process, or a nucleation process of water on a pre-existing pure glutaric acid core. It has been shown that depending on the generation process used and the nature of the acid, the aerosol formed is not always stable and may break in two parts.

Once the aggregates were formed, different properties of the particles have been characterized by means of RDF, Connolly surface, binding energy or H-bond autocorrelation function analysis. All the results have been published in a paper in ACS Earth and Space Chemistry.[234]

The HO_2 mass accommodation on glutaric acids aggregates have been computed using two methods. In both cases, the mass accommodation coefficient was found to be close to unity without significant influence of relative humidity. As the mass accommodation coefficient does not explain why the experimental uptake value is low, it is assumed that other processes may limit the uptake as diffusion or reactivity. Finally, the interaction between HO_2 and the aggregate has been characterized too.

The study of the reactivity between HO_2 and the wetted particles of glutaric acid has been initiated. As a first step, the reactivity between glutaric acid and HO_2 in the gas phase has been modeled since to the best of our knowledge no data exist in the literature. This study should allow to provide a guess for a transition state geometry on the aerosol surface. The study of the reactivity of HO_2 with water in the gas phase has been previously performed in the literature, thus we began to investigate the reactivity on the aerosol surface, using the QM/MM ONIOM method. Despite many attempts, varying the size of the QM part, the transition state guess geometry, or switching to QM/QM (semi-empirical) level, no reasonable result has been obtained so far.

II.2 Perspectives

The reactivity of HO_2 with water and/or glutaric acid at the interface between the gas and aerosol phases has yet to be investigated in further details, by identifying the source of the convergence failures. This study will allow an estimation of the total rate constant at the interface and thus to determine if surface reactions are limiting processes for the uptake.

From the MD results, it appears that this reactivity has to be studied in the bulk phase as well in order to get the total reactive rate constant in the bulk phase. Indeed, reactivity in the bulk phase may be slightly different from the gas phase and/or at the surface. To this end, it may be necessary to move from ONIOM to other methodologies which have been tailored from the study of large systems at the quantum level. It can be envisaged to use for example:

- *ab initio* molecular dynamics (AIMD),[235]
- the use of reactive force field (ReaxFF) in molecular dynamics,[236–238]
- the Fragment Molecular Orbital (FMO)[239], which can be coupled to Density Functional Tight Binding (DFTB)[240]

However, in order to compute completely the resistance corresponding to the bulk processes, the diffusion coefficient[241] and the Henry constant[242,243] have to be computed too. The behaviour on the aerosol of a complex $HO_2.H_2O$ formed in gas phase may be studied as well.

In principle, the uptake coefficient may be computed using the data provided by molecular modelling, at least for small particles, and then directly compared to the values measured with the aerosol flow tube. Hopefully, that would allow to determine if all the processes are correctly taken into account or if there are still some missing ones.

Furthermore, the model used can still be improved in order to get closer to the experiment. Indeed, it should be recommended to carry out the study with deprotonated acid molecules as the aerosol generated by the atomizer or the nucleation system may not be neutral.

Finally, this methodology should be applied to larger peroxy radicals RO_2 instead of HO_2 (for example CH_3O_2) as each process may differ with the chemical natures of the species or of the aerosol particle.

REFERENCES

1. Seinfeld, J. H. TROPOSPHERIC CHEMISTRY AND COMPOSITION | Aerosols/Particles A2 - Holton, James R. in *Encyclopedia of Atmospheric Sciences* 2349–2354 (Academic Press, 2003).
2. Seinfeld, J. H. & Pandis, S. N. *Atmospheric chemistry and physics: from air pollution to climate change*. (John Wiley & Sons, 2012).
3. Finlayson-Pitts, B. J. & Pitts Jr., J. N. CHAPTER 1 - Overview of the Chemistry of Polluted and Remote Atmospheres. in *Chemistry of the Upper and Lower Atmosphere* 1–14 (Academic Press, 2000). doi:10.1016/B978-012257060-5/50003-4.
4. Boucher, O. *Aérosols atmosphériques: Propriétés et impacts climatiques*. (Springer Science & Business Media, 2012).
5. Kampa, M. & Castanas, E. Human health effects of air pollution. *Proc. 4th Int. Workshop Biomonitoring Atmospheric Pollut. Emphas. Trace Elem.* **151**, 362–367 (2008).
6. Finlayson-Pitts, B. J. & Pitts Jr., J. N. CHAPTER 14 - Global Tropospheric Chemistry and Climate Change. in *Chemistry of the Upper and Lower Atmosphere* 762–843 (Academic Press, 2000). doi:10.1016/B978-012257060-5/50016-2.
7. Mohd Zul Helmi Rozaini. The Chemistry of Dicarboxylic Acids in the Atmospheric Aerosols Y1 - N1 38764 UR. in *Atmospheric Aerosols - Regional Characteristics - Chemistry and Physics* (2012).
8. Ziemann, P. J. & Atkinson, R. Kinetics, products, and mechanisms of secondary organic aerosol formation. *Chem. Soc. Rev.* **41**, 6582–6605 (2012).
9. Hallquist, M. *et al.* The formation, properties and impact of secondary organic aerosol: current and emerging issues. *Atmos Chem Phys* **9**, 5155–5236 (2009).

10. Heo, J., Adams, P. J. & Gao, H. O. Public Health Costs of Primary PM2.5 and Inorganic PM2.5 Precursor Emissions in the United States. *Environ. Sci. Technol.* **50**, 6061–6070 (2016).

11. Stocker, T. F. *et al.* IPCC, 2013: climate change 2013: the physical science basis. Contribution of working group I to the fifth assessment report of the intergovernmental panel on climate change. (2013).

12. McKeen, S. A. *et al.* Photochemical modeling of hydroxyl and its relationship to other species during the Tropospheric OH Photochemistry Experiment. *J. Geophys. Res. Atmospheres* **102**, 6467–6493 (1997).

13. Hens, K. *et al.* Observation and modelling of HOx radicals in a boreal forest. *Atmos Chem Phys* **14**, 8723–8747 (2014).

14. Sillman, S. *et al.* Loss of isoprene and sources of nighttime OH radicals at a rural site in the United States: Results from photochemical models. *J. Geophys. Res. Atmospheres* **107**, ACH 2-1 (2002).

15. Patra, P. K. *et al.* Observational evidence for interhemispheric hydroxyl-radical parity. *Nature* **513**, 219–223 (2014).

16. Tan, D. *et al.* HO x budgets in a deciduous forest: Results from the PROPHET summer 1998 campaign. *J. Geophys. Res. Atmospheres* **106**, 24407–24427 (2001).

17. Griffith, S. M. *et al.* OH and HO2 radical chemistry during PROPHET 2008 and CABINEX 2009 – Part 1: Measurements and model comparison. *Atmos Chem Phys* **13**, 5403–5423 (2013).

18. Kolb, C. E. *et al.* An overview of current issues in the uptake of atmospheric trace gases by aerosols and clouds. *Atmos Chem Phys* **10**, 10561–10605 (2010).

19. Mao, J., Fan, S., Jacob, D. J. & Travis, K. R. Radical loss in the atmosphere from Cu-Fe redox coupling in aerosols. *Atmos Chem Phys* **13**, 509–519 (2013).

20. Miyazaki, K., Parker, A. E., Fittschen, C., Monks, P. S. & Kajii, Y. A new technique for the selective measurement of atmospheric peroxy radical concentrations of HO 2 and RO 2 using a denuding method. in (2009). doi:10.5194/amt-3-1547-2010.

21. Heard, D. E. Atmospheric field measurements of the hydroxyl radical using laser-induced fluorescence spectroscopy. *Annu. Rev. Phys. Chem.* **57**, 191–216 (2006).

22. Dusanter, S. & Stevens, P. S. Recent Advances in the Chemistry of OH and HO2 Radicals in the Atmosphere: Field and Laboratory Measurements. in *Advances in Atmospheric Chemistry* vol. Volume 1 493–579 (World Scientific, 2017).

23. Finlayson-Pitts, B. J. & Pitts Jr., J. N. CHAPTER 6 - Rates and Mechanisms of Gas-Phase Reactions in Irradiated Organic – NOx – Air Mixtures. in *Chemistry of the Upper and Lower Atmosphere* 179–263 (Academic Press, 2000). doi:10.1016/B978-012257060-5/50008-3.

24. Whalley, L. K. *et al.* The chemistry of OH and HO2 radicals in the boundary layer over the tropical Atlantic Ocean. *Atmos Chem Phys* **10**, 1555–1576 (2010).

25. Goliff, W. S., Stockwell, W. R. & Lawson, C. V. The regional atmospheric chemistry mechanism, version 2. *Atmos. Environ.* **68**, 174–185 (2013).

26. Assaf, E. *et al.* The Reaction between CH3O2 and OH Radicals: Product Yields and Atmospheric Implications. *Environ. Sci. Technol.* **51**, 2170–2177 (2017).

27. Assaf, E., Song, B., Tomas, A., Schoemaecker, C. & Fittschen, C. Rate Constant of the Reaction between CH3O2 Radicals and OH Radicals Revisited. *J. Phys. Chem. A* **120**, 8923–8932 (2016).

28. Fittschen, C. The reaction of peroxy radicals with OH radicals. *Chem. Phys. Lett.* **725**, 102–108 (2019).

29. Xue, L. *et al.* Oxidative capacity and radical chemistry in the polluted atmosphere of Hong Kong and Pearl River Delta region: analysis of a severe photochemical smog episode. *Atmos Chem Phys* **16**, 9891–9903 (2016).

30. Stone, D., Whalley, L. K. & Heard, D. E. Tropospheric OH and HO2 radicals: field measurements and model comparisons. *Chem. Soc. Rev.* **41**, 6348–6404 (2012).

31. Heard, D. E. & Pilling, M. J. Measurement of OH and HO2 in the Troposphere. *Chem. Rev.* **103**, 5163–5198 (2003).

32. MCM Website. http://mcm.leeds.ac.uk/MCM/.

33. Stockwell, W. R., Kirchner, F., Kuhn, M. & Seefeld, S. A new mechanism for regional atmospheric chemistry modeling. *J. Geophys. Res. Atmospheres* **102**, 25847–25879 (1997).

34. Mao, J. *et al.* Insights into hydroxyl measurements and atmospheric oxidation in a California forest. *Atmos Chem Phys* **12**, 8009–8020 (2012).

35. Jacob, D. J. Heterogeneous chemistry and tropospheric ozone. *Atmos. Environ.* **34**, 2131–2159 (2000).

36. Macintyre, H. L. & Evans, M. J. Parameterisation and impact of aerosol uptake of HO2 on a global tropospheric model. *Atmos Chem Phys* **11**, 10965–10974 (2011).

37. Cantrell, C. A., Shetter, R. E., Gilpin, T. M. & Calvert, J. G. Peroxy radicals measured during Mauna Loa Observatory Photochemistry Experiment 2: The data and first analysis. *J. Geophys. Res. Atmospheres* **101**, 14643–14652 (1996).

38. Jaeglé, L. *et al.* Photochemistry of HO x in the upper troposphere at northern midlatitudes. *J. Geophys. Res. Atmospheres* **105**, 3877–3892 (2000).

39. Plummer, D. A., McConnell, J. C., Shepson, P. B., Hastie, D. R. & Niki, H. Modeling of ozone formation at a rural site in Southern Ontario. *WMA Int. Spec. Conf. Reg. Photochem. Meas. Model.* **30**, 2195–2217 (1996).

40. Kanaya, Y. *et al.* Implications of iodine chemistry for daytime HO2 levels at Rishiri Island. *Geophys. Res. Lett.* **29**, 45–1 (2002).

41. Bloss, W. J. *et al.* Impact of halogen monoxide chemistry upon boundary layer OH and HO2 concentrations at a coastal site. *Geophys. Res. Lett.* **32**, (2005).

42. Thornton, J. A., Jaeglé, L. & McNeill, V. F. Assessing known pathways for HO2 loss in aqueous atmospheric aerosols: Regional and global impacts on tropospheric oxidants. *J. Geophys. Res. Atmospheres* **113**, (2008).

43. Hanson, D. R., Burkholder, J. B., Howard, C. J. & Ravishankara, A. R. Measurement of hydroxyl and hydroperoxy radical uptake coefficients on water and sulfuric acid surfaces. *J. Phys. Chem.* **96**, 4979–4985 (1992).

44. Cooper, P. L. & Abbatt, J. P. D. Heterogeneous Interactions of OH and HO2 Radicals with Surfaces Characteristic of Atmospheric Particulate Matter. *J. Phys. Chem.* **100**, 2249–2254 (1996).

45. Thornton, J. & Abbatt, J. P. D. Measurements of HO2 uptake to aqueous aerosol: Mass accommodation coefficients and net reactive loss. *J. Geophys. Res. Atmospheres* **110**, (2005).

46. Ammann, M., Poschl, U. & Rudich, Y. Effects of reversible adsorption and Langmuir-Hinshelwood surface reactions on gas uptake by atmospheric particles. *Phys. Chem. Chem. Phys.* **5**, 351–356 (2003).

47. Sénéchal, H. *et al.* A Review of the Effects of Major Atmospheric Pollutants on Pollen Grains, Pollen Content, and Allergenicity. *Sci. World J.* **2015**, (2015).

48. Shantz, N. C., Leaitch, W. R., Phinney, L., Mozurkewich, M. & Toom-Sauntry, D. The effect of organic compounds on the growth rate of cloud droplets in marine and forest settings. *Atmos Chem Phys* **8**, 5869–5887 (2008).

49. Rastak, N. *et al.* Seasonal variation of aerosol water uptake and its impact on the direct radiative effect at Ny-Ålesund, Svalbard. *Atmos Chem Phys* **14**, 7445–7460 (2014).

50. Patterson, J. P. *et al.* Sea Spray Aerosol Structure and Composition Using Cryogenic Transmission Electron Microscopy. *ACS Cent. Sci.* **2**, 40–47 (2016).

51. Lakey, P. S. J., George, I. J., Whalley, L. K., Baeza-Romero, M. T. & Heard, D. E. Measurements of the HO2 Uptake Coefficients onto Single Component Organic Aerosols. *Environ. Sci. Technol.* **49**, 4878–4885 (2015).

52. Lakey, P. S. J. *et al.* The effect of viscosity and diffusion on the HO2 uptake by sucrose and secondary organic aerosol particles. *Atmos Chem Phys* **16**, 13035–13047 (2016).

53. Lakey, P. S. J., George, I. J., Baeza-Romero, M. T., Whalley, L. K. & Heard, D. E. Organics Substantially Reduce HO2 Uptake onto Aerosols Containing Transition Metal ions. *J. Phys. Chem. A* **120**, 1421–1430 (2016).

54. Taketani, F., Kanaya, Y. & Akimoto, H. Kinetic Studies of Heterogeneous Reaction of HO2 Radical by Dicarboxylic Acid Particles. *Int. J. Chem. Kinet.* **45**, 560–565 (2013).

55. Bedjanian, Y., Lelievre, S. & Le Bras, G. Experimental study of the interaction of HO2 radicals with soot surface. *Phys. Chem. Chem. Phys.* **7**, 334–341 (2005).

56. Bedjanian, Y., Romanias, M. N. & El Zein, A. Uptake of HO2 radicals on Arizona Test Dust. *Atmos Chem Phys* **13**, 6461–6471 (2013).

57. Davis, E. J. Interpretation of Uptake Coefficient Data Obtained with Flow Tubes. *J. Phys. Chem. A* **112**, 1922–1932 (2008).

58. George, I. J. *et al.* Measurements of uptake coefficients for heterogeneous loss of HO2 onto submicron inorganic salt aerosols. *Phys. Chem. Chem. Phys.* **15**, 12829–12845 (2013).

59. Gershenzon, Y. M., Grigorieva, V. M., Ivanov, A. V. & Remorov, R. G. O3 and OH Sensitivity to heterogeneous sinks of HO and CH3O2 on aerosol particles. *Faraday Discuss.* **100**, 83–100 (1995).

60. Loukhovitskaya, E., Bedjanian, Y., Morozov, I. & Le Bras, G. Laboratory study of the interaction of HO2 radicals with the NaCl, NaBr, MgCl2.6H2O and sea salt surfaces. *Phys. Chem. Chem. Phys.* **11**, 7896–7905 (2009).

61. Matthews, P. S. J., Baeza-Romero, M. T., Whalley, L. K. & Heard, D. E. Uptake of HO2 radicals onto Arizona test dust particles using an aerosol flow tube. *Atmos Chem Phys* **14**, 7397–7408 (2014).

62. Mozurkewich, M., McMurry, P. H., Gupta, A. & Calvert, J. G. Mass accommodation coefficient for HO2 radicals on aqueous particles. *J. Geophys. Res. Atmospheres* **92**, 4163–4170 (1987).

63. Remorov, R. G., Gershenzon, Yu. M., Molina, L. T. & Molina, M. J. Kinetics and Mechanism of HO2 Uptake on Solid NaCl. *J. Phys. Chem. A* **106**, 4558–4565 (2002).

64. Saathoff, H. *et al.* The loss of NO2, HNO3, NO3/N2O5, and HO2/HOONO2 on soot aerosol: A chamber and modeling study. *Geophys. Res. Lett.* **28**, 1957–1960 (2001).

65. Taketani, F. *et al.* Measurement of overall uptake coefficients for HO 2 radicals by aerosol particles sampled from ambient air at Mts. Tai and Mang (China). *Atmospheric Chem. Phys.* **12**, 11907–11916 (2012).

66. Taketani, F., Kanaya, Y. & Akimoto, H. Kinetics of HO2 Uptake in Levoglucosan and Polystyrene Latex Particles. *J. Phys. Chem. Lett.* **1**, 1701–1704 (2010).

67. Taketani, F., Kanaya, Y. & Akimoto, H. Heterogeneous loss of HO2 by KCl, synthetic sea salt, and natural seawater aerosol particles. *Atmos. Environ.* **43**, 1660–1665 (2009).

68. Taketani, F., Kanaya, Y. & Akimoto, H. Kinetics of Heterogeneous Reactions of HO2 Radical at Ambient Concentration Levels with (NH4)2SO4 and NaCl Aerosol Particles. *J. Phys. Chem. A* **112**, 2370–2377 (2008).

69. Abbatt, J. P. D., Lee, A. K. Y. & Thornton, J. A. Quantifying trace gas uptake to tropospheric aerosol: recent advances and remaining challenges. *Chem. Soc. Rev.* **41**, 6555–6581 (2012).

70. Berkemeier, T. *et al.* Kinetic regimes and limiting cases of gas uptake and heterogeneous reactions in atmospheric aerosols and clouds: a general classification scheme. *Atmos Chem Phys* **13**, 6663–6686 (2013).

71. Davidovits, P., Kolb, C. E., Williams, L. R., Jayne, J. T. & Worsnop, D. R. Mass Accommodation and Chemical Reactions at Gas−Liquid Interfaces. *Chem. Rev.* **106**, 1323–1354 (2006).

72. Davidovits, P., Kolb, C. E., Williams, L. R., Jayne, J. T. & Worsnop, D. R. Update 1 of: Mass Accommodation and Chemical Reactions at Gas−Liquid Interfaces. *Chem. Rev.* **111**, PR76–PR109 (2011).

73. Fan, H., Tinsley, M. R. & Goulay, F. Effect of Relative Humidity on the OH-Initiated Heterogeneous Oxidation of Monosaccharide Nanoparticles. *J. Phys. Chem. A* **119**, 11182–11190 (2015).

74. Julin, J., Winkler, P. M., Donahue, N. M., Wagner, P. E. & Riipinen, I. Near-Unity Mass Accommodation Coefficient of Organic Molecules of Varying Structure. *Environ. Sci. Technol.* **48**, 12083–12089 (2014).

75. Katrib, Y., Mirabel, Ph., Le Calvé, S., Weck, G. & Kochanski, E. Experimental Uptake Study of Ethanol by Water Droplets and Its Theoretical Modeling of Cluster Formation at the Interface. *J. Phys. Chem. B* **106**, 7237–7245 (2002).

76. Kulmala, M. & Wagner, P. E. Mass accommodation and uptake coefficients — a quantitative comparison. *Mass Accommod. Uptake Coeff.* **32**, 833–841 (2001).

77. Shiraiwa, M., Ammann, M., Koop, T. & Pöschl, U. Gas uptake and chemical aging of semisolid organic aerosol particles. *Proc. Natl. Acad. Sci.* **108**, 11003–11008 (2011).

78. Herbst, E. Surface reactions in interstellar space. *Highlights Astron.* **12**, 55–57 (2002).

79. George, I. J. & Abbatt, J. P. D. Heterogeneous oxidation of atmospheric aerosol particles by gas-phase radicals. *Nat Chem* **2**, 713–722 (2010).

80. Winkler, P. M. *et al.* Mass and Thermal Accommodation during Gas-Liquid Condensation of Water. *Phys. Rev. Lett.* **93**, 075701 (2004).

81. Vesala, T., Kulmala, M., Rudolf, R., Vrtala, A. & Wagner, P. E. Models for condensational growth and evaporation of binary aerosol particles. *J. Aerosol Sci.* **28**, 565–598 (1997).

82. Pöschl, U., Rudich, Y. & Ammann, M. Kinetic model framework for aerosol and cloud surface chemistry and gas-particle interactions – Part 1: General equations, parameters, and terminology. *Atmos Chem Phys* **7**, 5989–6023 (2007).

83. Shiraiwa, M., Pfrang, C. & Pöschl, U. Kinetic multi-layer model of aerosol surface and bulk chemistry (KM-SUB): the influence of interfacial transport and bulk diffusion on the oxidation of oleic acid by ozone. *Atmos Chem Phys* **10**, 3673–3691 (2010).

84. Shiraiwa, M., Pfrang, C., Koop, T. & Pöschl, U. Kinetic multi-layer model of gas-particle interactions in aerosols and clouds (KM-GAP): linking condensation, evaporation and chemical reactions of organics, oxidants and water. *Atmos Chem Phys* **12**, 2777–2794 (2012).

85. Fuchs, N. & Sutugin, A. Highly dispersed aerosols. *Ann Arbor Sci Ann Arbor Mich* 105 pp (1970).

86. Wagner, P. E. A constant-angle mie scattering method (cams) for investigation of particle formation processes. *J. Colloid Interface Sci.* **105**, 456–467 (1985).

87. Caloz, F., Fenter, F. F., Tabor, K. D. & Rossi, M. J. Paper I: Design and construction of a Knudsen-cell reactor for the study of heterogeneous reactions over the temperature range 130–750 K: Performances and limitations. *Rev. Sci. Instrum.* **68**, 3172–3179 (1997).

88. Jayne, J. *et al.* Uptake of gas-phase aldehydes by water surfaces. *J. Phys. Chem.* **96**, 5452–5460 (1992).

89. Tang, M. J. *et al.* Heterogeneous Interaction of SiO2 with N2O5: Aerosol Flow Tube and Single Particle Optical Levitation–Raman Spectroscopy Studies. *J. Phys. Chem. A* **118**, 8817–8827 (2014).

90. Winkler, P. M. *et al.* Condensation of water vapor: Experimental determination of mass and thermal accommodation coefficients. *J. Geophys. Res. Atmospheres* **111**, (2006).

91. Symington, A. The Heterogeneous Interaction of Organic Acids with Ice Surfaces at Temperatures of the Upper Troposphere. *CPGS Diss. Newham Coll. Univ. Camb.* (2006).

92. Mao, J. *et al.* Chemistry of hydrogen oxide radicals (HOx) in the Arctic troposphere in spring. *Atmos Chem Phys* **10**, 5823–5838 (2010).

93. Gershenzon, Y. M. *et al.* Capture of HO2 Radicals by an NH4NO3 Surface at Low Temperatures. *Chem. Phys. Rep.* **18**, 79–90 (1999).

94. Thornton, J. & Abbatt, J. P. D. Measurements of HO2 uptake to aqueous aerosol: Mass accommodation coefficients and net reactive loss. *J. Geophys. Res. Atmospheres* **110**, (2005).

95. Matthews, P. S. Heterogeneous uptake of HO2 radicals onto atmospheric aerosols. (2014).

96. James, A. D. *et al.* The uptake of HO2 on meteoric smoke analogues. *J. Geophys. Res. Atmospheres* **122**, 554–565 (2017).

97. Moon, D. R. *et al.* Heterogeneous reaction of HO2 with airborne TiO2 particles and its implication for climate change mitigation strategies. *Atmos Chem Phys* **18**, 327–338 (2018).

98. Bedjanian, Y., Romanias, M. N. & El Zein, A. Interaction of OH Radicals with Arizona Test Dust: Uptake and Products. *J. Phys. Chem. A* **117**, 393–400 (2013).

99. Bertram, A. K., Ivanov, A. V., Hunter, M., Molina, L. T. & Molina, M. J. The Reaction Probability of OH on Organic Surfaces of Tropospheric Interest. *J. Phys. Chem. A* **105**, 9415–9421 (2001).

100. Park, J.-H., Ivanov, A. V. & Molina, M. J. Effect of Relative Humidity on OH Uptake by Surfaces of Atmospheric Importance. *J. Phys. Chem. A* **112**, 6968–6977 (2008).

101. George, I. J., Vlasenko, A., Slowik, J. G., Broekhuizen, K. & Abbatt, J. P. D. Heterogeneous oxidation of saturated organic aerosols by hydroxyl radicals: uptake kinetics, condensed-phase products, and particle size change. *Atmos Chem Phys* **7**, 4187–4201 (2007).

102. McNeill, V. F., Wolfe, G. M. & Thornton, J. A. The Oxidation of Oleate in Submicron Aqueous Salt Aerosols: Evidence of a Surface Process. *J. Phys. Chem. A* **111**, 1073–1083 (2007).

103. Che, D. L., Smith, J. D., Leone, S. R., Ahmed, M. & Wilson, K. R. Quantifying the reactive uptake of OH by organic aerosols in a continuous flow stirred tank reactor. *Phys. Chem. Chem. Phys.* **11**, 7885–7895 (2009).

104. Hearn, J. D. & Smith, G. D. A mixed-phase relative rates technique for measuring aerosol reaction kinetics. *Geophys. Res. Lett.* **33**, (2006).

105. Smith, J. D. *et al.* The heterogeneous reaction of hydroxyl radicals with sub-micron squalane particles: a model system for understanding the oxidative aging of ambient aerosols. *Atmos Chem Phys* **9**, 3209–3222 (2009).

106. Lambe, A. T., Miracolo, M. A., Hennigan, C. J., Robinson, A. L. & Donahue, N. M. Effective Rate Constants and Uptake Coefficients for the Reactions of Organic Molecular Markers (n-Alkanes, Hopanes, and Steranes) in Motor Oil and Diesel Primary Organic Aerosols with Hydroxyl Radicals. *Environ. Sci. Technol.* **43**, 8794–8800 (2009).

107. Bedjanian, Y., Nguyen, M. L. & Le Bras, G. Kinetics of the reactions of soot surface-bound polycyclic aromatic hydrocarbons with the OH radicals. *Atmos. Environ.* **44**, 1754–1760 (2010).

108. Villalta, P. W., Lovejoy, E. R. & Hanson, D. R. Reaction probability of peroxyacetyl radical on aqueous surfaces. *Geophys. Res. Lett.* **23**, 1765–1768 (1996).

109. Tong, C., Blanco, M., Goddard, W. A. & Seinfeld, J. H. Thermodynamic Properties of Multifunctional Oxygenates in Atmospheric Aerosols from Quantum Mechanics and Molecular Dynamics: Dicarboxylic Acids. *Environ. Sci. Technol.* **38**, 3941–3949 (2004).

110. Li, X., Hede, T., Tu, Y., Leck, C. & Ågren, H. Cloud droplet activation mechanisms of amino acid aerosol particles: insight from molecular dynamics simulations. *Tellus B Vol 65 2013* (2013).

111. Loukonen, V., Kuo, I.-F. W., McGrath, M. J. & Vehkamäki, H. On the stability and dynamics of (sulfuric acid) (ammonia) and (sulfuric acid) (dimethylamine) clusters: A first-principles molecular dynamics investigation. *Chem. Phys.* **428**, 164–174 (2014).

112. Zhang, C., Wang, Y., Liu, Y. & Yang, Y. A molecular dynamics study of water vapor nucleation in the presence of ions. *Chem. Eng. Sci.* **137**, 308–319 (2015).

113. Feng, Y.-J. *et al.* π-Hydrogen Bonding of Aromatics on the Surface of Aerosols: Insights from Ab Initio and Molecular Dynamics Simulation. *J. Phys. Chem. B* **120**, 6667–6673 (2016).

114. J. Gertner, B. & T. Hynes, J. Model molecular dynamics simulation of hydrochloric acid ionization at the surface of stratospheric ice. *Faraday Discuss.* **110**, 301–322 (1998).

115. Ma, X., Chakraborty, P., Henz, B. J. & Zachariah, M. R. Molecular dynamic simulation of dicarboxylic acid coated aqueous aerosol: structure and processing of water vapor. *Phys. Chem. Chem. Phys.* **13**, 9374–9384 (2011).

116. Darvas, M., Picaud, S. & Jedlovszky, P. Water adsorption around oxalic acid aggregates: a molecular dynamics simulation of water nucleation on organic aerosols. *Phys. Chem. Chem. Phys.* **13**, 19830–19839 (2011).

117. Darvas, M., Picaud, S. & Jedlovszky, P. Molecular dynamics simulations of the water adsorption around malonic acid aerosol models. *Phys. Chem. Chem. Phys.* **15**, 10942–10951 (2013).

118. Vardanega, D. & Picaud, S. Water and formic acid aggregates: A molecular dynamics study. *J. Chem. Phys.* **141**, 104701 (2014).

119. Radola, B., Picaud, S., Vardanega, D. & Jedlovszky, P. Molecular Dynamics Simulations of the Interaction between Water Molecules and Aggregates of Acetic or Propionic Acid Molecules. *J. Phys. Chem. B* **119**, 15662–15674 (2015).

120. Morita, A. Molecular dynamics study of mass accommodation of methanol at liquid–vapor interfaces of methanol/water binary solutions of various concentrations. *Chem. Phys. Lett.* **375**, 1–8 (2003).

121. Morita, A., Sugiyama, M., Kameda, H., Koda, S. & Hanson, D. R. Mass Accommodation Coefficient of Water: Molecular Dynamics Simulation and Revised Analysis of Droplet Train/Flow Reactor Experiment. *J. Phys. Chem. B* **108**, 9111–9120 (2004).

122. Morita, A., Kanaya, Y. & Francisco, J. S. Uptake of the HO2 radical by water: Molecular dynamics calculations and their implications for atmospheric modeling. *J. Geophys. Res. Atmospheres* **109**, (2004).

123. Julin, J. & Riipinen, I. Molecular dynamics simulations of mass accommodation and evaporation on surfaces of atmospheric interest. *AIP Conf. Proc.* **1527**, 437–440 (2013).

124. Julin, J. *et al.* Mass Accommodation of Water: Bridging the Gap Between Molecular Dynamics Simulations and Kinetic Condensation Models. *J. Phys. Chem. A* **117**, 410–420 (2013).

125. Garrett, B. C., Schenter, G. K. & Morita, A. Molecular Simulations of the Transport of Molecules across the Liquid/Vapor Interface of Water. *Chem. Rev.* **106**, 1355–1374 (2006).

126. Xu, W. & Zhang, R. Theoretical Investigation of Interaction of Dicarboxylic Acids with Common Aerosol Nucleation Precursors. *J. Phys. Chem. A* **116**, 4539–4550 (2012).

127. Hou, G.-L., Valiev, M. & Wang, X.-B. Deprotonated Dicarboxylic Acid Homodimers: Hydrogen Bonds and Atmospheric Implications. *J. Phys. Chem. A* **120**, 2342–2349 (2016).

128. Aloisio, S. & Francisco, J. S. Existence of a Hydroperoxy and Water (HO2·H2O) Radical Complex. *J. Phys. Chem. A* **102**, 1899–1902 (1998).

129. Clark, J., English, A. M., Hansen, J. C. & Francisco, J. S. Computational Study on the Existence of Organic Peroxy Radical-Water Complexes (RO2.H2O). *J. Phys. Chem. A* **112**, 1587–1595 (2008).

130. Tachikawa, H. & Abe, S. Direct ab initio MD study on the interaction of hydroperoxy radical (HOO) with water molecules. *Phys. Chem. Chem. Phys.* **12**, 3904–3909 (2010).

131. Tachikawa, H. Direct ab initio MD study on the electron capture dynamics of hydroperoxy radical (HOO)-water complexes. *J. Phys. Chem. A* **114**, 4951–4956 (2010).

132. Torrent- Sucarrat, M., Ruiz- Lopez, M. F., Martins- Costa, M., Francisco, J. S. & Anglada, J. M. Protonation of Water Clusters Induced by Hydroperoxyl Radical Surface Adsorption. *Chem. - Eur. J.* **17**, 5076–5085 (2011).

133. Martins- Costa, M. T. C., Anglada, J. M., Francisco, J. S. & Ruiz- Lopez, M. F. Reactivity of Atmospherically Relevant Small Radicals at the Air–Water Interface. *Angew. Chem. Int. Ed.* **51**, 5413–5417 (2012).

134. Zhang, T. *et al.* Role of the (H2O)n (n = 1–3) cluster in the HO2 + HO → 3O2 + H2O reaction: mechanistic and kinetic studies. *Phys. Chem. Chem. Phys.* **20**, 8152–8165 (2018).

135. Zhang, T., Wang, W., Li, C., Du, Y. & Lü, J. Catalytic effect of a single water molecule on the atmospheric reaction of HO2 + OH: fact or fiction? A mechanistic and kinetic study. *RSC Adv.* **3**, 7381–7391 (2013).

136. Zhang, T., Wang, W., Zhang, P., Lü, J. & Zhang, Y. Water-catalyzed gas-phase hydrogen abstraction reactions of CH3O2 and HO2 with HO2: a computational investigation. *Phys. Chem. Chem. Phys.* **13**, 20794–20805 (2011).

137. Zhou, D. D. Y. *et al.* Theoretical Determination of the Rate Coefficient for the HO2 + HO2 → H2O2+O2 Reaction: Adiabatic Treatment of Anharmonic Torsional Effects. *J. Phys. Chem. A* **116**, 2089–2100 (2012).

138. Iyer, S. *et al.* Computational Investigation of RO2 + HO2 and RO2 + RO2 Reactions of Monoterpene Derived First-Generation Peroxy Radicals Leading to Radical Recycling. *J. Phys. Chem. A* **122**, 9542–9552 (2018).

139. Mirivel, G., Riffault, V. & Galloo, J.-C. Analysis of phthalic, isophthalic and long-chain (C4–C12) dicarboxylic acids in atmospheric aerosols by UPLC/ESI/ToF-MS. *Anal. Methods* **3**, 1172–1179 (2011).

140. Crenn, V., Fronval, I., Petitprez, D. & Riffault, V. Fine particles sampled at an urban background site and an industrialized coastal site in Northern France — Part 1: Seasonal variations and chemical characterization. *Sci. Total Environ.* **578**, 203–218 (2017).

141. Vácha, R., Slavíček, P., Mucha, M., Finlayson-Pitts, B. J. & Jungwirth, P. Adsorption of Atmospherically Relevant Gases at the Air/Water Interface: Free Energy Profiles of Aqueous Solvation of N2, O2, O3, OH, H2O, HO2, and H2O2. *J. Phys. Chem. A* **108**, 11573–11579 (2004).

142. Chalmet, S. & Ruiz-López, M. F. The structures of ozone and HOx radicals in aqueous solution from combined quantum/classical molecular dynamics simulations. *J. Chem. Phys.* **124**, 194502 (2006).

143. Chung, L. W. *et al.* The ONIOM Method and Its Applications. *Chem. Rev.* **115**, 5678–5796 (2015).

144. *Advances in Atmospheric Chemistry*. vol. Volume 1 (World Scientific, 2016).

145. Brown, R. L. Tubular flow reactors with first-order kinetics. *J Res Natl Bur Stand* **83**, 1–8 (1978).

146. Keyser, L. F. High-pressure flow kinetics. A study of the hydroxyl + hydrogen chloride reaction from 2 to 100 torr. *J. Phys. Chem.* **88**, 4750–4758 (1984).

147. TSI | Precision Measurement Instruments. http://www.tsi.com/.

148. Mendez, M. *et al.* Reactive and Nonreactive Ozone Uptake during Aging of Oleic Acid Particles. *J. Phys. Chem. A* **118**, 9471–9481 (2014).

149. Bilde, M. *et al.* Saturation Vapor Pressures and Transition Enthalpies of Low-Volatility Organic Molecules of Atmospheric Relevance: From Dicarboxylic Acids to Complex Mixtures. *Chem. Rev.* **115**, 4115–4156 (2015).

150. Stull, D. R. Vapor Pressure of Pure Substances. Organic and Inorganic Compounds. *Ind. Eng. Chem.* **39**, 517–540 (1947).

151. Pentanedioic acid. https://webbook.nist.gov/cgi/cbook.cgi?ID=C110941&Mask=4.

152. Fuchs, H. *et al.* Intercomparison of peroxy radical measurements obtained at atmospheric conditions by laser-induced fluorescence and electron spin resonance spectroscopy. *Atmos Meas Tech* **2**, 55–64 (2009).

153. Whalley, L. K., Blitz, M. A., Desservettaz, M., Seakins, P. W. & Heard, D. E. Reporting the sensitivity of laser-induced fluorescence instruments used for HO2 detection to an

interference from RO2 radicals and introducing a novel approach that enables HO2 and certain RO2 types to be selectively measured. *Atmos Meas Tech* **6**, 3425–3440 (2013).

154. Hanke, M., Uecker, J., Reiner, T. & Arnold, F. Atmospheric peroxy radicals: ROXMAS, a new mass-spectrometric methodology for speciated measurements of HO2 and ∑RO2 and first results. *Int. J. Mass Spectrom.* **213**, 91–99 (2002).

155. Hornbrook, R. S. *et al.* Measurements of tropospheric HO2 and RO2 by oxygen dilution modulation and chemical ionization mass spectrometry. *Atmos Meas Tech* **4**, 735–756 (2011).

156. Wood, E. C. & Charest, J. R. Chemical Amplification - Cavity Attenuated Phase Shift Spectroscopy Measurements of Atmospheric Peroxy Radicals. *Anal. Chem.* **86**, 10266–10273 (2014).

157. Kundu, S. *et al.* Peroxy radical measurements by ethane – nitric oxide chemical amplification and laser-induced fluorescence during the IRRONIC field campaign in a forest in Indiana. *Atmospheric Chem. Phys.* **19**, 9563–9579 (2019).

158. Wood, E. C., Deming, B. L. & Kundu, S. Ethane-Based Chemical Amplification Measurement Technique for Atmospheric Peroxy Radicals. *Environ. Sci. Technol. Lett.* **4**, 15–19 (2017).

159. Verlet, L. Computer 'Experiments' on Classical Fluids. I. Thermodynamical Properties of Lennard-Jones Molecules. *Phys. Rev.* **159**, 98–103 (1967).

160. Abraham, M. J., van der Spoel, D., Lindahl, E., Hess, B. & the GROMACS development team. GROMACS User Manual version 2016.1. (2016).

161. Momany, F. A., McGuire, R. F., Burgess, A. W. & Scheraga, H. A. Energy parameters in polypeptides. VII. Geometric parameters, partial atomic charges, nonbonded interactions, hydrogen bond interactions, and intrinsic torsional potentials for the naturally occurring amino acids. *J. Phys. Chem.* **79**, 2361–2381 (1975).

162. Weiner, S. J. *et al.* A new force field for molecular mechanical simulation of nucleic acids and proteins. *J. Am. Chem. Soc.* **106**, 765–784 (1984).

163. Jorgensen, W. L. & Tirado-Rives, J. The OPLS [optimized potentials for liquid simulations] potential functions for proteins, energy minimizations for crystals of cyclic peptides and crambin. *J. Am. Chem. Soc.* **110**, 1657–1666 (1988).

164. Jensen, F. *Introduction to computational chemistry*. (John Wiley & Sons, 2013).

165. Bussi, G., Donadio, D. & Parrinello, M. Canonical sampling through velocity rescaling. *J. Chem. Phys.* **126**, 014101 (2007).

166. Berendsen, H. J. C., Postma, J. P. M., van Gunsteren, W. F., DiNola, A. & Haak, J. R. Molecular dynamics with coupling to an external bath. *J. Chem. Phys.* **81**, 3684–3690 (1984).

167. Fotsing Kwetche, C. R. Modélisation à l'échelle moléculaire de la réactivité des aérosols atmosphériques. (2018).

168. Darden, T., York, D. & Pedersen, L. Particle mesh Ewald: An N·log(N) method for Ewald sums in large systems. *J. Chem. Phys.* **98**, 10089–10092 (1993).

169. Brooks, B. R. *et al.* CHARMM: The Biomolecular Simulation Program. *J Comput Chem* **30**, (2009).

170. The Amber biomolecular simulation programs - Case - 2005 - Journal of Computational Chemistry - Wiley Online Library. https://onlinelibrary.wiley.com/doi/abs/10.1002/jcc.20290.

171. Ozboyaci, M., Kokh, D. B., Corni, S. & Wade, R. C. Modeling and simulation of protein–surface interactions: achievements and challenges. *Q. Rev. Biophys.* **49**, (2016).

172. Pérez, A. *et al.* Refinement of the AMBER force field for nucleic acids: improving the description of α/γ conformers. *Biophys. J.* **92**, 3817–3829 (2007).

173. Wang, J., Wolf, R. M., Caldwell, J. W., Kollman, P. A. & Case, D. A. Development and testing of a general amber force field. *J. Comput. Chem.* **25**, 1157–1174 (2004).

174. Vanommeslaeghe, K. *et al.* CHARMM general force field: A force field for drug-like molecules compatible with the CHARMM all-atom additive biological force fields. *J Comput Chem* **31**, (2010).

175. Berendsen, H. J. C., Grigera, J. R. & Straatsma, T. P. The missing term in effective pair potentials. *J. Phys. Chem.* **91**, 6269–6271 (1987).

176. Jorgensen, W. L., Chandrasekhar, J., Madura, J. D., Impey, R. W. & Klein, M. L. Comparison of simple potential functions for simulating liquid water. *J. Chem. Phys.* **79**, 926–935 (1983).

177. Mahoney, M. W. & Jorgensen, W. L. A five-site model for liquid water and the reproduction of the density anomaly by rigid, nonpolarizable potential functions. *J. Chem. Phys.* **112**, 8910–8922 (2000).

178. Vega, C., Abascal, J. L. F., Conde, M. M. & Aragones, J. L. What ice can teach us about water interactions: a critical comparison of the performance of different water models. *Faraday Discuss.* **141**, 251–276 (2009).

179. Poincaré, H. Sur le problème des trois corps et les équations de la dynamique. *Acta Math.* **13**, A3–A270 (1890).

180. Schuchardt, K. L. *et al.* Basis Set Exchange: A Community Database for Computational Sciences. *J. Chem. Inf. Model.* **47**, 1045–1052 (2007).

181. Roothaan, C. C. J. New Developments in Molecular Orbital Theory. *Rev. Mod. Phys.* **23**, 69–89 (1951).

182. Piela, L. *Ideas of quantum chemistry*. (Elsevier, 2006).

183. Ditchfield, R., Hehre, W. J. & Pople, J. A. Self- Consistent Molecular- Orbital Methods. IX. An Extended Gaussian- Type Basis for Molecular- Orbital Studies of Organic Molecules. *J. Chem. Phys.* **54**, 724–728 (1971).

184. Dunning, T. H. Gaussian basis sets for use in correlated molecular calculations. I. The atoms boron through neon and hydrogen. *J. Chem. Phys.* **90**, 1007–1023 (1989).

185. Cramer, C. J. Essentials of Computational Chemistry: Theories and Models, 2nd Edition. *Wiley.com* https://www.wiley.com/en-us/Essentials+of+Computational+Chemistry%3A+Theories+and+Models%2C+2nd+Edition-p-9780470091821.

186. Olsen, J., Christiansen, O., Koch, H. & Jörgensen, P. Surprising cases of divergent behavior in Möller–Plesset perturbation theory. *J. Chem. Phys.* **105**, 5082–5090 (1996).

187. Lewars, E. G. *Computational Chemistry: Introduction to the Theory and Applications of Molecular and Quantum Mechanics*. (Springer Netherlands, 2011).

188. Hohenberg, P. & Kohn, W. Inhomogeneous Electron Gas. *Phys. Rev.* **136**, B864–B871 (1964).

189. Perdew, J., Ruzsinszly, A. & Tao, J. Prescription for the design and selection of density functional approximations: More constraint satisfaction with fewer fits. *J. Chem. Phys.* **123**, 062201 (2005).

190. Mardirossian, N. & Head-Gordon, M. Thirty years of density functional theory in computational chemistry: an overview and extensive assessment of 200 density functionals. *Mol. Phys.* **115**, 2315–2372 (2017).

191. Goerigk, L. & Mehta, N. A Trip to the Density Functional Theory Zoo: Warnings and Recommendations for the User*. *Aust. J. Chem.* **72**, 563–573 (2019).

192. Goerigk, L. *et al.* A look at the density functional theory zoo with the advanced GMTKN55 database for general main group thermochemistry, kinetics and noncovalent interactions. *Phys. Chem. Chem. Phys.* **19**, 32184–32215 (2017).

193. Groenhof, G. Introduction to QM/MM Simulations. in *Biomolecular Simulations: Methods and Protocols* (eds. Monticelli, L. & Salonen, E.) 43–66 (Humana Press, 2013). doi:10.1007/978-1-62703-017-5_3.

194. Rivail, J.-L., Ruiz-Lopez, M. & Assfeld, X. *Quantum Modeling of Complex Molecular Systems*. vol. 21 (Springer, 2015).

195. Bielski, B. H. J., Cabelli, D. E., Arudi, R. L. & Ross, A. B. Reactivity of HO2/O−2 Radicals in Aqueous Solution. *J. Phys. Chem. Ref. Data* **14**, 1041–1100 (1985).

196. Frison, G. & Ohanessian, G. A comparative study of semiempirical, ab initio, and DFT methods in evaluating metal–ligand bond strength, proton affinity, and interactions between first and second shell ligands in Zn-biomimetic complexes. *J. Comput. Chem.* **29**, 416–433 (2008).

197. Houston, P. L. *Chemical kinetics and reaction dynamics*. (Courier Corporation, 2012).

198. Liu, Y. P. *et al.* Molecular modeling of the kinetic isotope effect for the [1,5]-sigmatropic rearrangement of cis-1,3-pentadiene. *J. Am. Chem. Soc.* **115**, 2408–2415 (1993).

199. Messiah, A. *Quantum mechanics*. vol. 2 (North-Holland Amsterdam, 1961).

200. Daniel Morton. Quantum Tunneling in Organic Chemistry. (21:42:53 UTC).

201. Brown, R. L. A Method of Calculating Tunneling Corrections for Eckart Potential Barriers. *J. Res. Natl. Bur. Stand.* **86**, 357–359 (1981).

202. Laulhé, C. Chapitre-IV Outils mathématiques : fonction de distribution de paires. http://hebergement.u-psud.fr/l3papp/wp-content/uploads/2016/02/Chapitre-IV.pdf.

203. Connolly, M. L. Analytical molecular surface calculation. *J. Appl. Crystallogr.* **16**, 548–558 (1983).

204. Cai, W., Zhang, M. & Maigret, B. New approach for representation of molecular surface. *J Comput Chem* **19**, 1805–1815 (1998).

205. Luzar, A. & Chandler, D. Effect of Environment on Hydrogen Bond Dynamics in Liquid Water. *Phys. Rev. Lett.* **76**, 928–931 (1996).

206. Radola, B., Picaud, S., Vardanega, D. & Jedlovszky, P. Analysis of Mixed Formic and Acetic Acid Aggregates Interacting With Water: A Molecular Dynamics Simulation Study. *J. Phys. Chem. C* **121**, 13863–13875 (2017).

207. Luzar, A. Resolving the hydrogen bond dynamics conundrum. *J. Chem. Phys.* **113**, 10663–10675 (2000).

208. Erbil, H. Y. & Avci, Y. Simultaneous Determination of Toluene Diffusion Coefficient in Air from Thin Tube Evaporation and Sessile Drop Evaporation on a Solid Surface. *Langmuir* **18**, 5113–5119 (2002).

209. Joshi, N., Romanias, M. N., Riffault, V. & Thevenet, F. Investigating water adsorption onto natural mineral dust particles: Linking DRIFTS experiments and BET theory. *Aeolian Res.* **27**, 35–45 (2017).

210. Atkinson, R. *et al.* Evaluated kinetic and photochemical data for atmospheric chemistry: Volume I - gas phase reactions of O_x, HO_x, NO_x and SO_x species. *Atmospheric Chem. Phys.* **4**, 1461–1738 (2004).

211. Ianni, J. C. *Kintecus*. (2017).

212. Cantrell, C. A. Technical Note: Review of methods for linear least-squares fitting of data and application to atmospheric chemistry problems. *Atmos Chem Phys* **8**, 5477–5487 (2008).

213. Wang, J., Wolf, R. M., Caldwell, J. W., Kollman, P. A. & Case, D. A. Development and testing of a General Amber Force Field. *J Comput Chem* **25**, 1157–1174 (2004).

214. Hess, B., Kutzner, C., van der Spoel, D. & Lindahl, E. GROMACS 4: Algorithms for highly efficient, load-balanced, and scalable molecular simulation. *J Chem Theory Comput* **4**, 435–447 (2008).

215. Frisch, M. J. *et al. Gaussian 16 Rev. B.01*. (2016).

216. Sousa da Silva, A. W. & Vranken, W. F. ACPYPE - AnteChamber PYthon Parser interfacE. *BMC Res. Notes* **5**, 367 (2012).

217. Bayly, C. I., Cieplak, P., Cornell, W. & Kollman, P. A. A well-behaved electrostatic potential based method using charge restraints for deriving atomic charges: the RESP model. *J. Phys. Chem.* **97**, 10269–10280 (1993).

218. Zielkiewicz, J. Structural properties of water: Comparison of the SPC, SPCE, TIP4P, and TIP5P models of water. *J. Chem. Phys.* **123**, 104501 (2005).

219. Bhattacharya, S., Saraswatula, V. G. & Saha, B. K. Thermal Expansion in Alkane Diacids—Another Property Showing Alternation in an Odd–Even Series. *Cryst. Growth Des.* **13**, 3651–3656 (2013).

220. Thalladi, V. R., Nüsse, M. & Boese, R. The Melting Point Alternation in α,ω-Alkanedicarboxylic Acids. *J. Am. Chem. Soc.* **122**, 9227–9236 (2000).

221. Scheuerman, R. F. & Sass, R. L. The crystal structure of valeric acid. *Acta Crystallogr.* **15**, 1244–1247 (1962).

222. Hagler, A. T., Lifson, S. & Dauber, P. Consistent force field studies of intermolecular forces in hydrogen-bonded crystals. 2. A benchmark for the objective comparison of alternative force fields. *J. Am. Chem. Soc.* **101**, 5122–5130 (1979).

223. Kerminen, V.-M., Lehtinen, K. E. J., Anttila, T. & Kulmala, M. Dynamics of atmospheric nucleation mode particles: a timescale analysis. *Tellus B* **56**, 135–146 (2004).

224. Pope, F. D., Dennis-Smither, B. J., Griffiths, P. T., Clegg, S. L. & Cox, R. A. Studies of Single Aerosol Particles Containing Malonic Acid, Glutaric Acid, and Their Mixtures with Sodium Chloride. I. Hygroscopic Growth. *J. Phys. Chem. A* **114**, 5335–5341 (2010).

225. Pruppacher, H. R., Klett, J. D. & Wang, P. K. *Microphysics of clouds and precipitation*. (1998).

226. Morita, A., Kanaya, Y. & Francisco, J. S. Uptake of the HO2 radical by water: Molecular dynamics calculations and their implications for atmospheric modeling. *J. Geophys. Res. Atmospheres* **109**, (2004).

227. Chai, J.-D. & Head-Gordon, M. Long-range corrected hybrid density functionals with damped atom–atom dispersion corrections. *Phys. Chem. Chem. Phys.* **10**, 6615–6620 (2008).

228. Weigend, F. & Ahlrichs, R. Balanced basis sets of split valence, triple zeta valence and quadruple zeta valence quality for H to Rn: Design and assessment of accuracy. *Phys. Chem. Chem. Phys.* **7**, 3297–3305 (2005).

229. Kozuch, S. & Martin, J. M. L. DSD-PBEP86: in search of the best double-hybrid DFT with spin-component scaled MP2 and dispersion corrections. *Phys. Chem. Chem. Phys.* **13**, 20104–20107 (2011).

230. Grimme, S., Ehrlich, S. & Goerigk, L. Effect of the damping function in dispersion corrected density functional theory. *J. Comput. Chem.* **32**, 1456–1465 (2011).

231. Nguyen, T. H., Hibbs, D. E. & Howard, S. T. Conformations, energies, and intramolecular hydrogen bonds in dicarboxylic acids: Implications for the design of synthetic dicarboxylic acid receptors. *J. Comput. Chem.* **26**, 1233–1241 (2005).

232. Canneaux, S., Bohr, F. & Henon, E. KiSThelP: A program to predict thermodynamic properties and rate constants from quantum chemistry results†. *J. Comput. Chem.* **35**, 82–93 (2014).

233. Nozière, B. & Hanson, D. R. Speciated Monitoring of Gas-Phase Organic Peroxy Radicals by Chemical Ionization Mass Spectrometry: Cross-Reactions between CH3O2, CH3(CO)O2, (CH3)3CO2, and c-C6H11O2. *J. Phys. Chem. A* **121**, 8453–8464 (2017).

234. Roose, A., Toubin, C., Dusanter, S., Riffault, V. & Duflot, D. Classical Molecular Dynamics Study of Small-Chain Carboxylic Acid Aerosol Particles. *ACS Earth Space Chem.* **3**, 380–389 (2019).

235. Paquet, E. & Viktor, H. L. Computational Methods for Ab Initio Molecular Dynamics. *Advances in Chemistry* https://www.hindawi.com/journals/ac/2018/9839641/ (2018) doi:10.1155/2018/9839641.

236. Cheng, T., Jaramillo-Botero, A., Goddard, W. A. & Sun, H. Adaptive Accelerated ReaxFF Reactive Dynamics with Validation from Simulating Hydrogen Combustion. *J. Am. Chem. Soc.* **136**, 9434–9442 (2014).

237. Chenoweth, K., van Duin, A. C. T. & Goddard, W. A. ReaxFF Reactive Force Field for Molecular Dynamics Simulations of Hydrocarbon Oxidation. *J. Phys. Chem. A* **112**, 1040–1053 (2008).

238. Liu, L., Liu, Y., Zybin, S. V., Sun, H. & Goddard, W. A. ReaxFF-lg: Correction of the ReaxFF Reactive Force Field for London Dispersion, with Applications to the Equations of State for Energetic Materials. *J. Phys. Chem. A* **115**, 11016–11022 (2011).

239. Fedorov, D. & Kitaura, K. *The fragment molecular orbital method: practical applications to large molecular systems*. (CRC press, 2009).

240. Nishimoto, Y., Fedorov, D. G. & Irle, S. Density-Functional Tight-Binding Combined with the Fragment Molecular Orbital Method. *J. Chem. Theory Comput.* **10**, 4801–4812 (2014).

241. Vaz, R. V., Gomes, J. R. B. & Silva, C. M. Molecular dynamics simulation of diffusion coefficients and structural properties of ketones in supercritical CO 2 at infinite dilution. *J. Supercrit. Fluids* **107**, 630–638 (2016).

242. Huang, Y.-L., Miroshnichenko, S., Hasse, H. & Vrabec, J. Henry's Law Constant from Molecular Simulation: A Systematic Study of 95 Systems. *Int. J. Thermophys.* **30**, 1791–1810 (2009).

243. Widom, B. Some Topics in the Theory of Fluids. *J. Chem. Phys.* **39**, 2808–2812 (1963).

244. Mohr, P. J., Taylor, B. N. & Newell, D. B. CODATA recommended values of the fundamental physical constants: 2010. *Rev. Mod. Phys.* **84**, 1527–1605 (2012).

APPENDICES

Appendix A: The continuum flux model

This section gives additional information about the continuum flux model describe in chapter 1 section II.1.1

The continuum mass flux I_c (kg s^{-1}) toward a particle is computed by equation 121 and the continuum heat flux Q_c (kJ s^{-1}) by equation 122.

$$I_c = C\frac{4\pi r_p M_v D_\infty p}{RT_\infty}\ln\left(\frac{1-X_\infty}{1-X_a}\right) \quad (121)$$

where r_p is the particle radius, M_v the molecular weight of the trace gas species, p the total pressure, X_∞ and X_a the mixing ratios far from and near the particle surface, T_∞ the temperature far from the particle, D_∞ the binary diffusion coefficient of the trace gas in the bath gas at temperature T_∞, R the ideal gas constant, and C a correction factor taking into account the diffusion temperature dependence. It allows the inclusion of the temperature gradient between the bath gas far from the particle surface and the particle surface.

$$Q_c = 2\pi r_p (K_a + K_\infty)(T_a - T_\infty) + H_v I_c \quad (122)$$

where K_a and K_∞ correspond to thermal conductivities of the binary mixture at the droplet temperature T_a and the gas temperature far from the droplet T_∞, respectively. H_v is the specific enthalpy of the trace gas.

As the transport of mass and energy is generally partially under kinetic control, some corrections are added to the continuum regime:

$$I_T = \beta_M I_c \quad (123)$$

$$Q_T = 2\pi r_p \beta_T (K_a + K_\infty)(T_a - T_\infty) + H_v \beta_M I_c \quad (124)$$

where I_T is the kinetic mass flux, Q_T the kinetic heat flux and

$$\beta_M = \frac{1+Kn_M}{1+\left(\frac{4}{3\alpha_M}+0.377\right)Kn_M + \frac{4}{3\alpha_M}Kn_M^2} \quad (125)$$

$$\beta_T = \frac{1+Kn_T}{1+\left(\frac{4}{3\alpha_T}+0.377\right)Kn_T + \frac{4}{3\alpha_T}Kn_T^2} \quad (126)$$

where Kn is the Knudsen number, which is the ratio of the mean free path (cf. equation 7) over the particle radius r_p, α_M the mass accommodation coefficient and α_T the thermal accommodation coefficient. The temperature T_a is computed by means of the heat balance equation (equation 127):

$$Q_T(r_p, T_a) - H_l(T_a) I_T(r_p, T_a) = 0 \quad (127)$$

where $H_l(T_a)$ is the specific enthalpy of the particle at temperature T_a. Once the temperature T_a is obtained, the mass flux $I_T(r_p, T_a)$ can be computed. Then by solving equation 128 where ρ_L is

the density of the particle at temperature T_a, and a_0 the initial particle size, we can obtain the time of nucleation as a function of the particle size using equation 128.

$$t(a) = \int_{a_0}^{a} \frac{4\pi\rho_L r^2}{I_T(r)} dr \qquad 128$$

The two accommodation coefficients can be found by fitting the experimental curve of the aerosol radius as a function of time by the theoretical function (Eq. 128) where these accommodation coefficients are adjustable parameters.

Appendix B: The kinetic flux model (model PRA)

This section provides additional information concerning the PRA model described in chapter 1 section II.1.3

For the gas-phase diffusion, Pöschl *et al.*[82] have considered an average distance from which the molecule has a straight trajectory to the particle surface. The concentration of the trace gas is considered as $[Xi]_{gs}$ within the distance d_p and $d_p + \Delta_{xi}$

Concerning the surface and the bulk processes, a simple double-layer surface was used to describe the physicochemical process (see Figure 115.A)

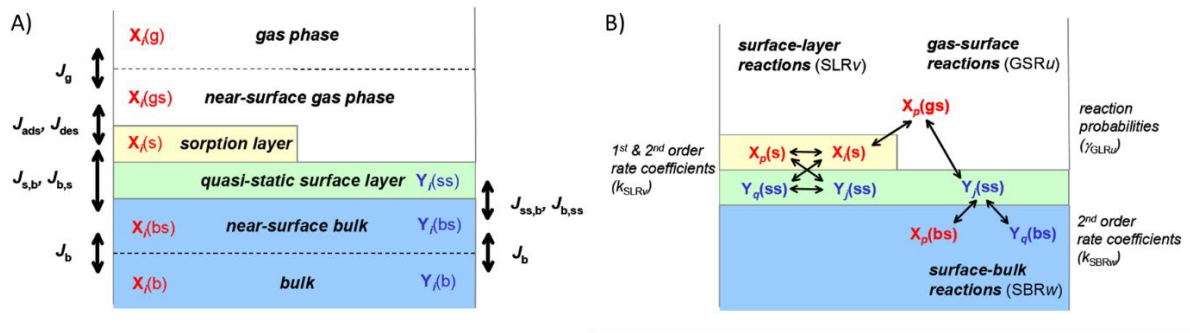

Figure 115: A) Double-layer surface model compartments and transport fluxes for the trace gas X_i (left) and non-volatile species Y_j (right) B) Classification of chemical reactions between volatile and non-volatile species at the surface.[82]

In this model, there are two monomolecular layers: a quasi-static surface layer composed of non-volatile species Y, and a sorption layer composed of the adsorbed trace gases X_i. Each species can diffuse through the layers but the contribution of X_i to the quasi-static surface layer is considered as negligible. The adsorption flux of the trace gas X_i to the surface J_{ads} is described by the multiplication of the surface accommodation coefficient $\alpha_{s,0}$ by the incoming flux of X_i (J_g). Furthermore, the authors have taken into account a Langmuir mechanism for the adsorption. In this mechanism, we consider that all adsorbate species compete for a single type of non-interfering sorption sites with an adsorption layer coverage θ_s on the quasi-static surface. For the desorption, the flux J_{des} corresponds to the adsorption layer coverage θ_s over the desorption lifetime τ_d times and the effective molecular cross section of X_i in the sorption layer σ_s (equation 129):

$$J_{des} = \frac{\theta_s}{\tau_d \sigma_d} \qquad 129$$

The reactions which occur at the surface have been split into three categories: the Gas-Surface Reactions (GSR), the Surface Layer Reactions (SLR) and the Surface Bulk Reactions (SBR) (see Figure 115.B).

For each layer, the difference between the production flux P and the loss flux L of molecules is computed. GSR reactions involve an Eley-Rideal mechanism whereas SLR ones are supposed to follow a Langmuir-Hinshelwood mechanism. In the Eley-Rideal mechanism, one gas phase species reacts with a surface adsorbed species, which contrasts to the Langmuir-Hinshelwood mechanism where two adsorbed species react together on the surface.

These reactions can play a very important role on the concentration of the species X_i in the case of reactive species. It is worth noting that the reaction fluxes may be larger than the diffusion flux through the particle surface.

So, the overall flux of net uptake can be computed from equation 130 when there is no bulk process (bulk reactions, bulk diffusion):

$$J_{net}=J_{ads}-J_{des}+L_{g,gsr}-P_{g,gsr} \quad (130)$$

where $L_{g,gsr}$ and $P_{g,gsr}$ are respectively the reactive loss flux and the reactive production flux of X_i at the gas-phase interface and quasi-static surface layer.

The uptake coefficient is then computed by equation 131:

$$\gamma=\frac{J_{ads}-J_{des}+L_{g,gsr}-P_{g,gsr}}{J_{coll}} \quad (131)$$

Applying the material balance equation (equation 132) for X_i at the sorption layer, we can replace the adsorption and desorption fluxes by equation 133.[82]

$$\frac{d[Xi]_s}{dt}=J_{ads}-J_{des}+P_s-L_s+J_{b,s}-J_{s,b} \quad (132)$$

$$J_{ads}-J_{des}=\frac{d[Xi]_s}{dt}-(P_s-L_s)+J_{b,s}-J_{s,b} \quad (133)$$

where $d[X_i]_s/dt$ is the time-dependent variation of X_i at the sorption surface, P_s and L_s the reactive production flux and the reactive loss flux of X_i at the sorption surface layer, $J_{b,s}$ the flux of X_i from the bulk to the sorption surface layer and $J_{s,b}$ the flux of X_i from the sorption surface layer to the bulk.

For the bulk processes, Shiraiwa *et al.* [83] have separated the bulk in n layers of size δ (Figure 116).

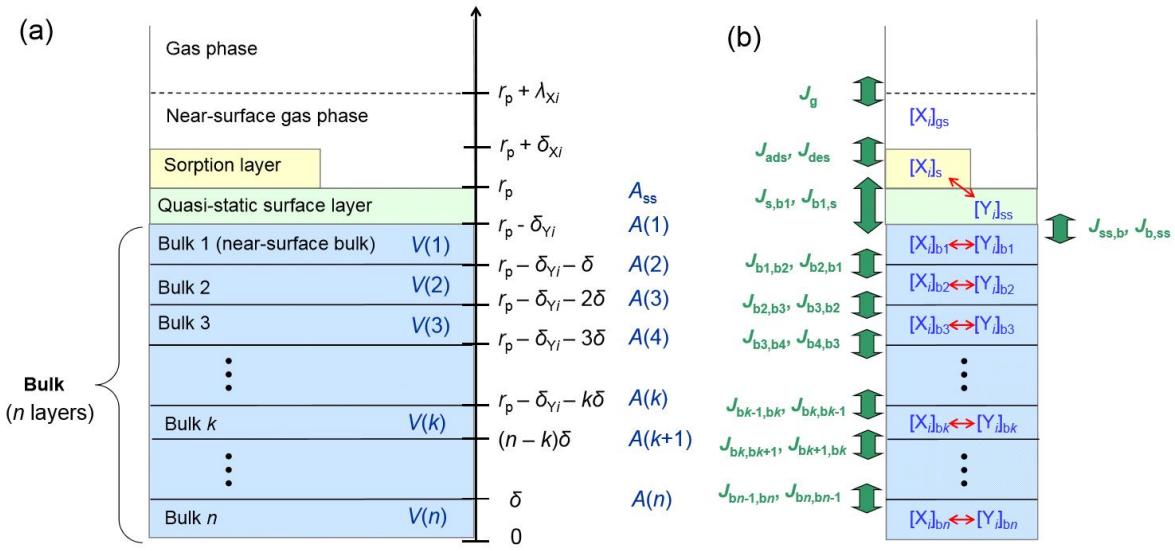

Figure 116: Kinetic multi-layer model (KM-SUB): (a) Model compartments and layers with corresponding distances from particle center ($r_p \pm x$), surface area (A) and volumes (V); λX_i is the mean free path of Xi in the gas-phase; δx_i and δY_j are the thicknesses of sorption and quasi-static bulk layers; δ is the bulk layer thickness. (b) Transport fluxes (green arrows) and chemical reactions (red arrows).[83]

The material balance equation is applied to each layer (equations 132, 134, 135 and 136):

$$\frac{d[X_i]_{bs}}{dt} = (J_{b2,bs} - J_{bs,b2})\frac{A(2)}{V(1)} + (J_{s,b} - J_{b,s})\frac{A(1)}{V(1)} + P_{bs,ss} - L_{bs,ss} + P_{bs,bs} - L_{bs,bs} \quad 134$$

$$\frac{d[X_i]_k}{dt} = (J_{bk+1,bk} - J_{bk,bk+1})\frac{A(k+1)}{V(k)} + (J_{bk-1,bk} - J_{bk,bk-1})\frac{A(k)}{V(k)} + P_{bk,bk} - L_{bk,bk} \quad 135$$

$$\frac{d[X_i]_n}{dt} = (J_{bn-1,bn} - J_{bn,bn-1})\frac{A(n)}{V(n)} + P_{bn,bn} - L_{bn,bn} \quad 136$$

where V(k) is the volume of the layer k and A(k) the interface area at the top of the layer. They can be computed by equations 137 and 138.

$$V(k) = \frac{4}{3}\pi[(r_b - (k-1)\delta)^3 - (r_b - k\delta)^3] \quad 137$$

$$A(k) = 4\pi(r_b - (k-1)\delta)^2 \quad 138$$

with $r_b = r_p - \delta_y$, the radius of the n-layers of the bulk.

The net flux of X_i between the sorption layer and the near surface bulk described by $J_{s,b}$ and $J_{b,s}$ is dependent on the diffusion of the species X_i within the bulk, D_b, and also the gas-particle equilibrium partitioning constant, $K_{sol,cc}$, or Henry's law constant. Then the flux of X_i species between each layer of the bulk $J_{b,b\pm1}$ depends only of the diffusion coefficient. The last process to be taken into account is the reactivity of the X_i species.

Finally, depending on the specific case studied, some approximations are done to simplify the computation of the uptake.[70,84]

Appendix C: Atomic Units

The atomic units (au) system has been defined in order to have the electron mass, the electron charge and the atomic momentum unit ħ equal to unity. This allows a simplification of the equation. This setting gives the following values as shown on Table 38.

Table 38: The atomic unit system. [244]

Bohr radius	a_0	0.52917721092(17). 10^{-10} m
Electron mass	m_e	9.10938291(40). 10^{-31} kg
Time	τ_0	2.418884326502(12) 10^{-17} s
Electron charge	e	1.602176565(35). 10^{-19} C
Energy (Hartree)	u.a.	4.35974434(19). 10^{-18} J
		219474.6313708(11) cm^{-1}
		657968.39207299(33) GHz
		3.1577504(29) . 10^5 K
		27.21138505(60) eV
Velocity	v_0	2.18769126379(71) . 10^6 $m.s^{-1}$
Atomic momentum	$\hbar$	1.054571628(53). 10^{-34} J.s
Bohr magneton	μ_B	1.854801830(46) .10^{-23} $J.T^{-1}$

Appendix D: Characterization of Cu-doped glutaric acid aerosol

In order to measure the HO_2 mass accommodation coefficient during uptake experiments, the glutaric acid aerosols can be doped with sufficient copper to catalyze the HO_2 consumption onto the aerosol surface (see Chapter 1 section II.2.2), which in turn will increase the uptake rate of HO_2 until the accommodation rate is reached.

The copper can be added by solubilizing copper sulfate in the solution of glutaric acid. Three copper-doped acid glutaric solutions where made in order to characterize their size distributions:

- two solutions where the concentration of copper was equal to the concentration of glutaric acid with a concentration of 5×10^{-3} M and 2.5×10^{-3} M.
- a solution where the concentration of copper was twenty times lower than the concentration of glutaric acid at 5×10^{-3} M.

A solution containing only 5×10^{-3} M of copper was also made for comparison.

Figure 117 compares the size distributions of the solutions cited previously to the size distribution of glutaric aerosols at an atomizer entrance pressure of 1 bar.

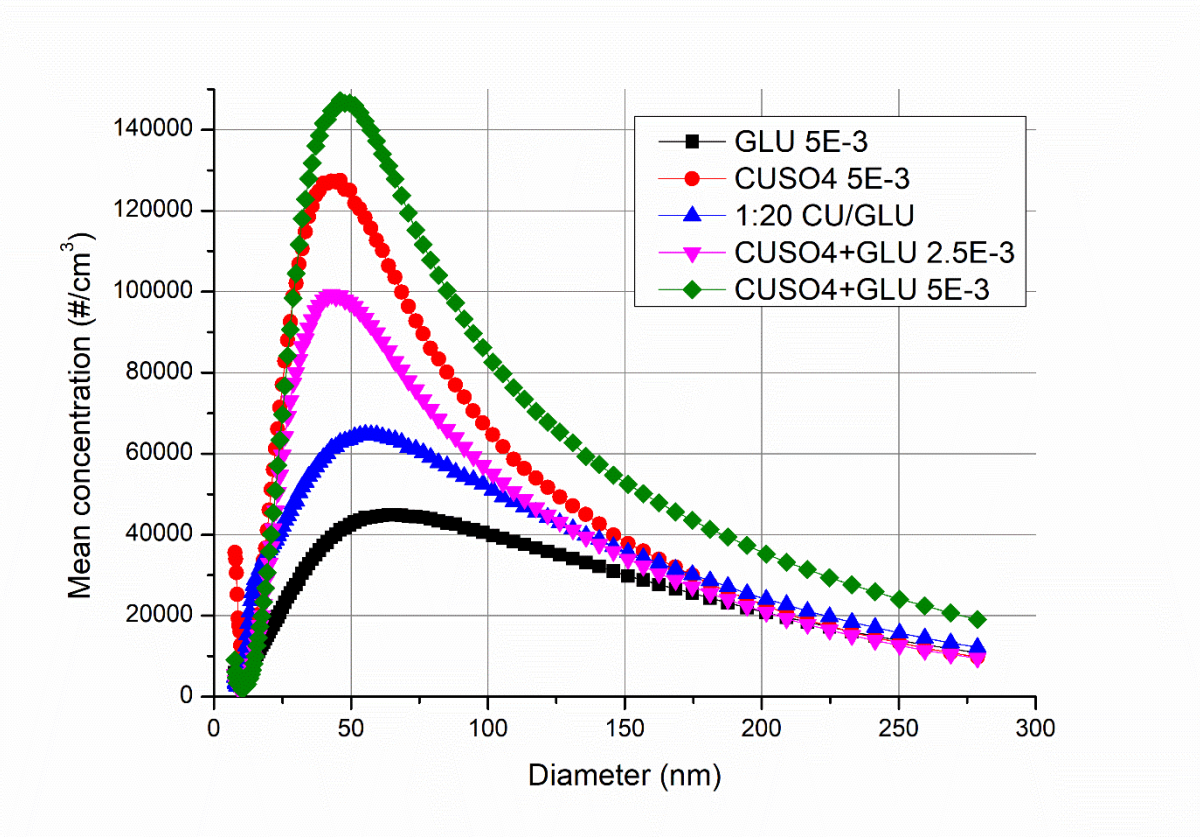

Figure 117: Size distribution of aerosols generated by atomization of a 5×10^{-3}M glutaric acid solution (black); a 5×10^{-3}M copper sulfate solution (red); a 1:20 Cu/Glutaric acid solution (blue), a solution made of 5×10^{-3}M glutaric acid and 5×10^{-3}M copper sulfate (magenta) a solution made of 5×10^{-3}M glutaric acid and 5×10^{-3}M copper sulfate (green).

The pure copper aerosol distribution is quite different of the pure glutaric acid aerosols as the concentration is higher and the mean diameter lower. Indeed, the pure glutaric acid size distribution has a total concentration of 2.55×10^{6} cm^{-3} and mean diameter of 82.1 nm while

the pure copper aerosol size distribution has a concentration of 5.95×10^6 cm^{-3} and a mean diameter equal to 62.7 nm. When the ratio of copper is increased, we get something closer to the shape of copper aerosol size distribution, while at a small copper ratio, the size distribution is closer to the glutaric acid aerosol size distribution. However, by adding more copper we tend to generate more pure copper aerosol and it may be the reason why the shape of the size distribution of copper-doped glutaric acid aerosol with a ratio 1:1 are close to the size distribution of the pure copper aerosol size distribution. Thus we cannot measure the mass accommodation coefficient on glutaric acid when there is an equivalent concentration of copper and glutaric acid. Finally it is interesting to note that the addition of a small amount of copper increases the aerosol concentration by a factor of 1.5 in the case of the ratio 1:20. At the same time the mean diameter decreases from 10 nm.

Appendix E: SPC/E water model parameters and AMBER GAFF Force Field parameters for glutaric and valeric acids

The following Table 39 and Table 40 introduce the AMBER GAFF Force field parameters used in this work

Table 39: Geometrical parameters used for water and carboxylic acids (glutaric and valeric). Bond distances are given in Ångströms and angles in degrees.

SPC/E water	d(O-H)	1.000
	H-O-H angle	109.47
Carboxylic acids	d(O-H)	0.974
	d(O-Cacid)	1.306
	d(O=Cacid)	1.214
	d(Cacid-C)	1.508
	d(C-C)	1.535
	d(C-H)	1.092
	O-Cacid=O	122.88
	O-Cacid-C	112.20
	O=Cacid-C	123.11
	Cacid-O-H	107.37
	Cacid-C-C	110.53
	C-C-H	110.05
	C-C-C	110.63
	Cacid-C-H	109.68
	H-C-H	108.35

Table 40: Parameters used for the coulombic interaction potential and the 12-6 Lennard-Jones potential

	Site	q/e	σ (Å)	ε (kJ mol^{-1})
SPC/E water	O	-0.8476	-	-
	H	0.4238	-	-
Glutaric acid	H(O-H)	0.3979	0.00000	0.00000
	O(O-H)	-0.6195	3.06647	0.88031
	O(C=O)	-0.5470	2.95992	0.87864
	Cacid	0.7524	3.39967	0.35982
	C(CH_2α)	-0.0707	3.39967	0.45773
	H(CH_2α)	0.0260	2.64953	0.06569
	C(CH_2β)	0.0163	3.39967	0.45773
	H(CH_2β)	0.0267	2.64953	0.06569
Valeric acid	H(O-H)	0.4440	0.00000	0.00000
	O(O-H)	-0.6141	3.06647	0.88031
	O(C=O)	-0.5500	2.95992	0.87864
	Cacid	0.6321	3.39967	0.35982
	C(CH_2α)	-0.1264	3.39967	0.45773
	H(CH_2α)	0.0807	2.64953	0.06569
	C(CH_2β)	-0.0804	3.39967	0.45773
	H(CH_2β)	0.0587	2.64953	0.06569
	C(CH_2γ)	-0.0794	3.39967	0.45773
	H(CH_2γ)	0.0397	2.64953	0.06569
	C(CH_3)	-0.0931	3.39967	0.45773
	H(CH_3)	0.0364	2.64953	0.06569

Appendix F: RESP charges of glutaric acid conformers

The following table introduce the RESP charges computed at the MP2/6-31+G** level.

*Table 41: RESP charges (MP2/6-31+G**) of the three glutaric acids conformers.*

	Conformer 1	Conformer 2	Conformer 3
H16	0.413	0.420	0.429
O1	-0.617	-0.603	-0.606
O3	-0.529	-0.545	-0.554
C8	0.731	0.716	0.729
H13	0.015	0.032	0.056
H14	0.015	0.032	0.056
C6	-0.046	-0.083	-0.015
H9	0.021	0.015	0.032
C4	-0.004	0.034	0.007
H10	0.021	0.015	0.032
C5	-0.046	-0.083	-0.015
H11	0.015	0.032	0.056
H12	0.015	0.032	0.056
C7	0.731	0.716	0.729
O2	-0.529	-0.545	-0.554
O0	-0.617	-0.603	-0.606
H15	0.413	0.420	0.429

Appendix G: HO2 parameters

The following table introduces the HO_2 parameters from Chalmet & Ruiz-López[142] and Vácha et al.[141] used in this work.

Table 42: HO_2 parameters.

Geometrical parameters		
	d(H-O)	0.983
	d(O-O˙)	1.326
	H-O-O˙	104.49

Non-bonded parameters			
Site	q/e	σ (Å)	ε (kJ mol^{-1})
O˙	-0.1700	2.62600	0.41210
O	-0.1400	2.62600	0.41210
H	0.3100	0.00000	0.00000

Appendix H: Van der Waals Complex of the H-abstraction of the glutaric acid by HO2

In this appendix, the geometries of the Van der Waals complexes of the H-abstraction of glutaric acid by HO_2 are introduced in Figure 118. The energies are introduced in Table 43.

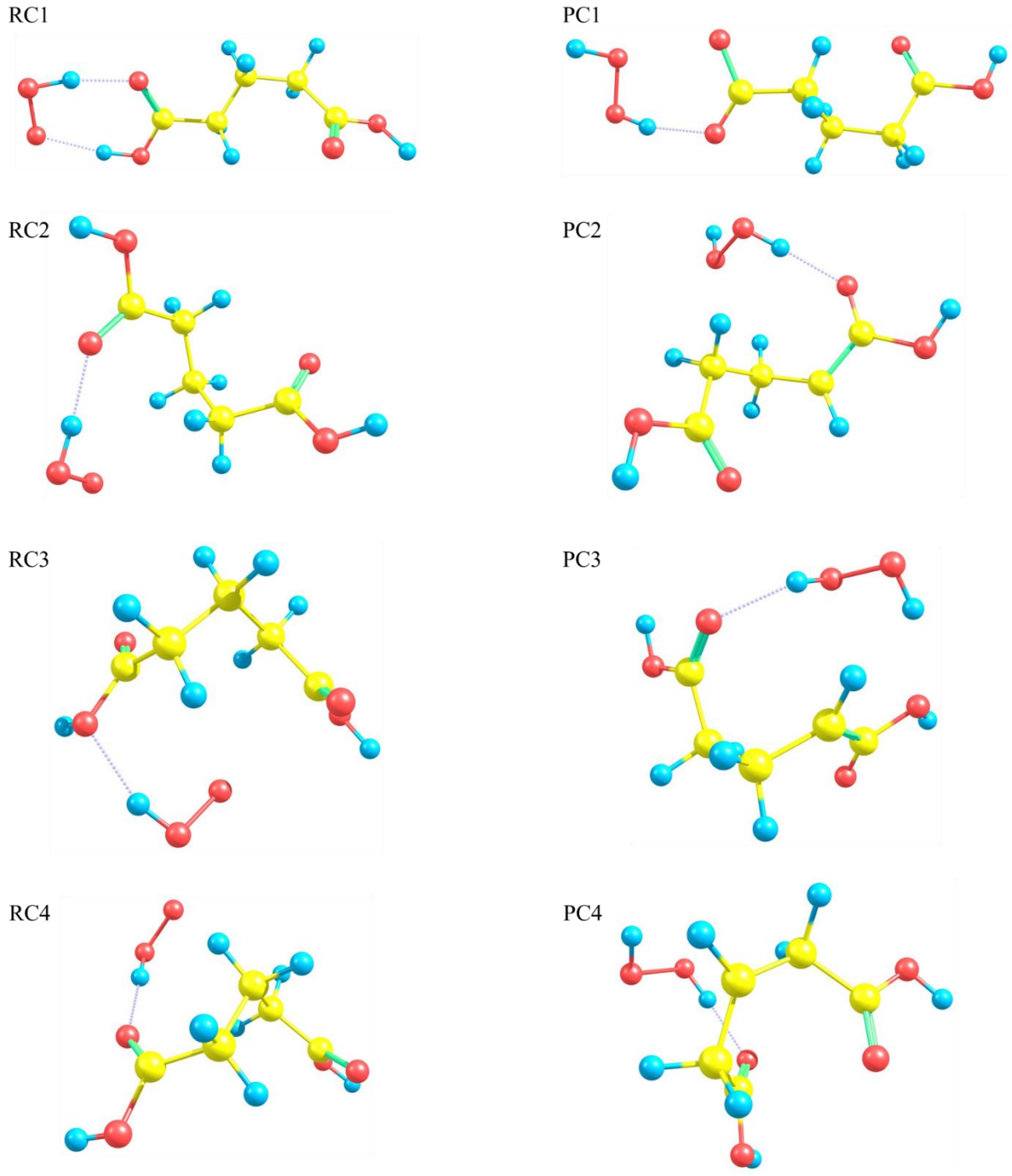

Figure 118: Geometries of the reactive Van der Waals complexes (RC) and product Van der Waals complex (PC) of the four different hydrogen environments.

Table 43: Energies (in kcal mol^{-1}) of the Van der Waals complexes of the glutaric acid H-abstraction by HO_2.

	ωB97X-D	DSD-PBEP86-D3(BJ)
RC1	-13.90	-14.11
RC2	-8.71	-8.60
RC3	-5.28	-6.08
RC4	-8.71	-8.60
PC1	22.82	22.30
PC2	2.59	0.59
PC3	3.70	1.50
PC4	10.59	7.58

RC accounts for Reactive Complex and PC for Product Complex

Appendix I: List of scientific contributions

Paper

A. ROOSE, C. TOUBIN, S. DUSANTER, V. RIFFAULT, D. DUFLOT, *Classical molecular dynamics study of small-chain carboxylic acid aerosol particles*, ACS Earth and Space Chemistry 3(3), 380-389 (2019), DOI 10.1021/acsearthspacechem.8b00172

International conference presentations

A. ROOSE, C. TOUBIN, S. DUSANTER, V. RIFFAULT, D. DUFLOT, *HO_2 accommodation on dicarboxylic acid aerosols: a combined experimental and theoretical study*, **Poster**, European Aerosol Conference, Göthenburg (Sweden), 25-30/08/2019.

A. ROOSE, S. DUSANTER, C. TOUBIN, D. DUFLOT, V. RIFFAULT, *Combined theoretical and experimental investigations of peroxy radical uptake on organic aerosols*, **Oral communication**, European Geoscience Union, Vienna (Austria), 08-12/04/2019.

A. ROOSE, C. TOUBIN, S. DUSANTER, V. RIFFAULT, D. DUFLOT, *Uptake of peroxy radicals on organic aerosols: Development of an Aerosol Flow Tube and molecular level characterization*, **Oral communication**, The 677 WE-Heraus-Seminar "Towards a molecular understanding of atmospheric aerosols", Bad Honnef (Germany), 26-31/08/2018.

A. ROOSE, S. DUSANTER, C. TOUBIN, D. DUFLOT, V. RIFFAULT, *Experimental and theoretical investigation of HO_2 sticking on dicarboxylic acid aerosols*, **Poster**, 25th international symposium on gas kinetics & related phenomena, Lille (France), 22-26/07/2018.

National conference presentations

A. ROOSE, D. DUFLOT, C. TOUBIN, V. RIFFAULT, S. DUSANTER, *Theoretical study of HO_2 sticking on glutaric acid aerosol surfaces*, **Poster**, Groupe Français de Cinétique et Photochimie, Douai, 20-21/06/2017.

Other communications

A. ROOSE, S. DUSANTER, C. TOUBIN, D. DUFLOT, V. RIFFAULT, *Combined theoretical and experimental investigations of peroxy radical uptake on organic aerosols*, **Oral communication**, Conseil scientifique du Labex CaPPA, 01/07/2019, Villeneuve d'Ascq.

A. ROOSE, D. DUFLOT, C. TOUBIN, V. RIFFAULT, S. DUSANTER, *Experimental and theoretical investigation of HO_2 sticking on dicarboxylic acid aerosols*, **Poster**, Atelier commun GDR EMIE & SUIE « Réactivité Hétérogène et Processus de Nucléation dans les Millieux Atmosphériques, Astrochimiques et en combustion », Villeneuve d'Ascq, 31/05 et 01/06 2019.

A. ROOSE, C. TOUBIN, S. DUSANTER, V. RIFFAULT, D. DUFLOT, *Experimental and theoretical investigation of organic aerosols*, **Oral communication**, 5ème journée scientifique

du labex CaPPA «atelier « Du gaz à la particule, comment se forment les suies ? les SOA ? les SIA ? », Villeneuve d'Ascq, 06/03/2019.

A. ROOSE, C. TOUBIN, S. DUSANTER, V. RIFFAULT, D. DUFLOT, *Experimental and theoretical investigation of HO_2 sticking on dicarboxylic acid aerosols*, **Oral communication**, GDR Suie, Villeneuve d'Ascq, 03-06/12/2018.

A. ROOSE, C. TOUBIN, S. DUSANTER, V. RIFFAULT, D. DUFLOT, *Experimental and theoretical investigation of HO_2 sticking on dicarboxylic acid aerosols*, **Oral communication**, Atelier thématique "Séparation phases gazeuse/particulaire de l'aérosol ", Villeneuve d'Ascq, 08/06/2018.

A. ROOSE, D. DUFLOT, C. TOUBIN, V. RIFFAULT, S. DUSANTER, *Experimental and theoretical investigation of HO_2 sticking on dicarboxylic acid aerosols*, **Poster**, 4ème journée scientifique du labex CaPPA, Villeneuve d'Ascq, 13/04/2018.

A. ROOSE, D. DUFLOT, C. TOUBIN, V. RIFFAULT, S. DUSANTER, *Theoretical and experimental study of uptake of peroxy radicals on organic aerosol surface*, **Oral communication**, WP2 Climibio meeting, Dunkerque, 26/01/2018.

ABSTRACT

Many uncertainties are still associated to chemical reaction mechanisms implemented in atmospheric models, especially for RO_x radicals (OH, HO_2, RO_2). Of particular interest, heterogeneous processes (uptake of radicals) occurring at the aerosol surface have yet to be better described in models. The objective of this work is to investigate the peroxy radical uptake onto organic aerosol surfaces. The uptake is investigated both experimentally (macroscale observation) and theoretically (molecular level description).

In the first part of this thesis an aerosol flow tube coupled to a peroxy radical measurement system (chemical amplification) has been developed and characterized. This system allows the measurement of HO_2 uptake onto organic aerosols and could be used to measure RO_2 uptakes as well. In this work, the uptake coefficient of HO_2 onto glutaric acid particles has been measured and compared to conflicting literature data.

The second part of this work consisted in the computation of fundamental processes driving the HO_2 uptake onto glutaric acid model particles, using molecular modelling tools (molecular dynamics (MM) and/or quantum mechanics (QM)). The accommodation coefficient has been determined and a preliminary investigation of heterogeneous reactions has been carried out using the hybrid QM/MM ONIOM method.

Keywords: organic aerosols; uptake coefficient; molecular dynamics; peroxy radical; modelling; aerosol flow tube

RÉSUMÉ

De nombreuses incertitudes sont encore associées aux mécanismes réactionnels utilisés dans les modèles de chimie atmosphérique, notamment sur la chimie des radicaux RO_x (OH, HO_2, RO_2). En particulier, l'absence ou une description approximative des processus hétérogènes (capture des radicaux) à la surface des aérosols représente un point à améliorer. L'objectif de cette thèse est de combiner une approche expérimentale (macroscopique) et théorique (point de vue moléculaire) de la capture de radicaux peroxyles à la surface d'aérosols organiques.

Dans la première partie de ce travail, un réacteur à écoulement laminaire couplé à un système de mesure de HO_2 et RO_2 par amplification chimique a été développé et caractérisé. Ce dispositif expérimental permet de mesurer la capture des radicaux HO_2 sur des aérosols organiques et également celle des radicaux RO_2 à terme. Dans le cadre de cette étude, la capture des radicaux HO_2 a été mesurée sur des aérosols d'acide glutarique et comparée aux données de la littérature qui présentaient des désaccords.

La deuxième partie de ce travail a consisté à utiliser des outils de modélisation moléculaire (dynamique moléculaire et/ou chimie quantique) afin de décrire les différents processus de la capture du radical HO_2 sur une particule modèle d'acide glutarique. Le coefficient d'accommodation a été déterminé et une première caractérisation de la réactivité hétérogène a été menée en utilisant la méthode hybride QM/MM (quantique/classique) ONIOM.

Mots clés : aérosols organiques ; coefficient de capture ; dynamique moléculaire ; radicaux peroxyles ; modélisation ; tube à écoulement